Engineering Rhodopsin-Based Artificial Photosynthesis



Weiming Tu

St Edmund Hall

University of Oxford

A thesis submitted for the degree of

Doctor of Philosophy

Trinity 2024

Acknowledgements

My DPhil journey has been a mix of joy, challenges and unexpected surprises. Four years ago, when I first arrived in the UK, I could never have imagined how much I would learn during my study here. I was fortunate to have excellent supervisors, Professor Wei Huang and Professor Ian Thompson, who introduced me to a novel and unexplored field. I'm impressed by Professor Wei Huang's dedication and passion for science. He always encourages me to aim high and has provided invaluable guidance. I am deeply grateful to Professor Ian Thompson as well; each of our routine meetings has left me feeling encouraged and confident.

I would like to thank the examiners of my transfer, confirmation and viva stages, Professor Aidong Yang, Professor Helen Townley, Professor Robert Carlisle and Professor Tom Bibby for their valuable comments that have significantly improved my work. I would also like to thank the collaborators at the University of Sheffield, Professor Neil Hunter and Dr. Paul Davison, for their important contributions to the work of Chapter 3.

I'm grateful to the members of the Begbroke family. Joseph Kennerley taught me how to run PCR and do gene assembly. Fariza Amman showed me how to use gas chromatography. Jiabao Xu taught me how to use Single-cell Raman spectroscopy. Simona Della Valle taught me how to work on *Ralstonia eutropha* strains. Samuel Putra showed me how to use electrochemical equipment. I would also like to thank Jochem Nielsen, Yutong Yin, Yun Dong, Jasmine Liu and all other lab members for their unconditional support to my DPhil project. I also want to thank the 4YP students Yip Shing Lee, Haris Saeed, Alfred Marriage Massey and Alexander Whitmarsh for their help with my experiments.

Additionally, I would like to express my gratitude to the friends I met in Oxford, including Yuan Zhang, Wenyu Chen and Yuxuan Lu. Although I haven't had many friends in Oxford, I truly value their friendship, and the summer of 2022 remains an unforgettable memory for me.

A very special thanks goes to Jiabao Xu. I could not have achieved this without your help. I would also like to extend my heartfelt thanks to Milky and Anda for your companionship. You have warmed my memories.

Finally, I would also like to give my deepest thanks to my parents. Four years ago, when I was deciding whether to stay in China or pursue a PhD abroad, my father encouraged me to go abroad to expand my horizons. Thanks to his advice and financial support, I enjoyed a wonderful journey during my studies in the UK. This experience will undoubtedly be one of the most valuable in my whole life.

Declaration

I declare that the work described in this thesis is my own, except where explicitly stated below, and that this thesis is my own composition.

Chapter 3

The plasmids construction as indicated in Table 3.1 was performed by Dr. Paul A. Davison. The Supplementary materials and methods, Supplementary Results, Table S3.2, Supplementary figure S3.1, S3.2 and S3.3 were provided by Dr. Paul A. Davison. Single-cell Raman spectroscopy data measurements and analysis were helped by Dr. Jiabao Xu.

Chapter 4

Single-cell Raman spectroscopy data measurements and analysis were helped by Dr. Jiabao Xu.

Lists of Publications

The work described in this thesis has led to the following publications:

1) **Tu, W.,** Xu, J., Thompson, I.P., Huang, W.E., 2023. Engineering artificial photosynthesis based on rhodopsin for CO_2 fixation. ***Nature Communications***, 14, 8012. (The Top 25 Life and Biological Sciences Articles of 2023 in *Nature Communications*, https://www.nature.com/collections/diiebagcjj)

2) **Tu, W.,** Thompson, I.P., Huang, W.E., 2024. Engineering bionanoreactor in bacteria for efficient hydrogen production. ***Proceedings of the National Academy of Science***,121(29), e2404958121.

3) **Tu, W**., Huang, W.E., 2023. Rhodopsin driven microbial CO_2 fixation using synthetic biology design. ***Environmental Microbiology***, 25(1), 126-130.

4) Davison, P.A.#, **Tu, W.# (co-first author)**, Xu, J., Valle, S.D., Thompson, I.P., Hunter, C.N., Huang, W.E., 2022. Engineering a rhodopsin-based photo-electrosynthetic system in bacteria for CO_2 fixation. ***ACS Synthetic Biology***, 11(11), 3805-3816.

5) **Tu, W.# (co-first author)**, Saeed, H., Huang, W.E., 2024. Rhodopsin-based light harvesting system for sustainable synthetic biology. ***Microbial Biotechnology***, 17(7), e14521.

Other contributions of the following studies completed during the DPhil are not covered in this thesis:

6) Yu, P., **Tu, W**., Wu, M., Wang, H., 2024. Evaluation of polyhydroxyalkanoate recovery from food waste by sequencing batch biofilm reactor with high mixed microbial biomass. ***Resources, Conservation and Recycling***, 205 (107536).

7) Tabish, T.A., Hussain, M.Z., Zervou, S., Myers, W.K., **Tu, W.,** Xu, J., Beer, I., Huang, W.E., Chandrawati, R., Crabtree, M.J., Winyard, P.G., 2024. S-nitrosocysteamine-functionalised porous graphene oxide nanosheets as nitric oxide delivery vehicles for cardiovascular applications. ***Redox Biology***, 72 (103144).

8) Valle, S.D., **Tu, W.,** Huang, W.E., 2023. Construction of microbial platform chassis for CO_2 fixation. ***Current Opinion in Systems Biology***, 37 (100489).

9) Wu, M., Liu, X., **Tu, W.,** Xia, J., Zou, Y., Gong, X., Yu, P., Huang, W.E., Wang, H., 2023. Deep insight into oriented propionate production from food waste: microbiological interpretation and design practice. ***Water Research***, 243 (120399).

10) Wu, M., Gong, X., Liu, X., **Tu, W.,** Yu, P., Zou, Y., Wang, H., 2023. A comprehensive techno-environmental evaluation of a pilot-scale PHAs production from food waste in China. ***Environmental Science & Technology***, 57 (1467-1478)

11) Xu, J., Luo, Y., Wang, J., **Tu, W.,** Yi, X., Xu, X., Song, Y., Tang, Y., Hua, X., Yu, Y. and Yin, H., Yang, Q., Huang, W. E., 2023. Artificial intelligence-aided rapid and accurate identification of clinical fungal infections by single-cell Raman spectroscopy. ***Frontiers in Microbiology***, 14 (1125676).

12) Zou, Y., **Tu, W.,** Wu, M., Liu, X., Wang, H., 2022. Fates of intracellular and extracellular antibiotic resistance genes during sludge anaerobic digestion with different pretreatments. ***Chemical Engineering Journal***, 454 (140356).

13) Zou, Y., Wu, M., Liu, J., **Tu, W.,** Xie, F., Yu, P., Zou, Y., Wang, H., 2022. Deciphering the extracellular and intracellular antibiotic resistance genes in multiple environments reveals the persistence of extracellular ones. ***Journal of Hazardous Materials***, 429 (128275).

14) Yu, P., **Tu, W.,** Wu, M., Zhang, Z., Wang, H., 2021. Pilot-scale fermentation of urban food waste for volatile fatty acids production: the importance of pH. ***Bioresource Technology***, 332 (125116).

15) Wu, M., Liu, X., Xiong, H., **Tu, W.,** Wang, H., 2021. Polyhydroxyalkanoate production from food waste coupled with aerobic nitrate reduction. ***ACS Sustainable Chemistry & Engineering***, 46 (15461-15468).

Table of Contents

Acknowledgements ... 1
Declaration ... 3
Lists of Publications ... 4
Table of Contents ... 6
Abstract ... 9
List of Abbreviations ... 11
Chapter 1 Introduction ... 13
1.1 Aim and objectives ... **13**
1.2 Structure of the thesis and key findings ... **14**
Chapter 2 Literature Review ... 17
2.1 Urgency of reducing carbon emissions ... **17**
2.2 Sustainable chemical engineering ... **18**
2.3 Microbial metabolism associated with H_2 synthesis and CO_2 fixation ... **19**
2.3.1 Microbial hydrogen synthesis ... 19
2.3.2 Microbial carbon dioxide fixation ... 20
2.4 Utilisation of renewable energy for sustainable biosynthesis ... **23**
2.4.1 Chlorophyll-based photosynthesis ... 23
2.4.2 Rhodopsin-based phototrophy ... 24
2.4.3 Electricity-driven electron transfer ... 26
2.5 Microbial production of biohydrogen from water and value-added products from CO_2 ... **28**
2.6 Synthetic biology as a tool to engineer cells ... **31**
2.6.1 Microbial chassis ... 31
2.6.2 Diverse products ... 33
2.6.3 Enhanced production ... 34
2.7 Outlook ... **35**
Chapter 3 Engineering a rhodopsin-based photo-electrosynthetic system in bacteria for CO_2 fixation ... 36
3.1 Summary ... **37**
3.2 Introduction ... **38**
3.3 Results ... **40**
3.3.1 Biosynthesis of β-carotene in *R. eutropha* ... 40
3.3.2 Biosynthesis of *Gloeobacter* rhodopsin in *R. eutropha* ... 42
3.3.3 Construction of a gene cluster for GR-retinal complex biosynthesis in *R. eutropha* ... 43
3.3.4 GR expression in *R. eutropha* H16 significantly enhances cell growth ... 44

3.3.5 CO_2 fixation by GR-expressing *R. eutropha* H16 46
3.3.6 Sources of reductant for light-driven autotrophic growth of *R. eutropha* 47
3.4 Discussion 51
3.5 Materials and methods 54
3.5.1 Bacterial strains and culture conditions 54
3.5.2 Plasmid construction 54
3.5.3 Single-cell Raman spectra (SCRS) measurements and analysis 55
3.5.4 Growth of *R. eutropha* strains under light and dark 56
3.5.5 Bicarbonate utilisation in *R. eutropha* growth 56
3.5.6 Microbial photoelectrochemical system apparatus 57
3.5.7 Counting colony forming units (CFU) to measure the concentration of viable cells in the cathode chamber 58
Chapter 3 Supplementary Information 60
Chapter 4 Engineering rhodopsin-based artificial photosynthesis for CO_2 fixation 84
4.1 Summary 85
4.2 Introduction 86
4.3 Results 89
4.3.1 Engineering a synthetic Mtr-mediated electron transport chain 89
4.3.2 Combination of the electron transport chain with a rhodopsin-based photosystem 91
4.3.3 Light-driven metabolism with CO_2 as the sole carbon source 92
4.3.4 Further enhancement of artificial photosynthesis 93
4.4 Discussion 97
4.5 Materials and methods 102
4.5.1 Bacterial strains, culture conditions and plasmid construction 102
4.5.2 Single-cell Raman spectra (SCRS) measurements and analysis 104
4.5.3 Analysis and quantification of intracellular biomolecules 104
4.5.4 Determination of NADH and NADPH levels 106
4.5.5 Fluorescence microscopy to visualize biofilm on the electrode 106
4.5.6 Microbial photoelectrochemical system 106
4.5.7 Electrochemically driven nitrate reduction 107
4.5.8 Electrochemically driven photosynthetic electron transport chain for reductant generation 107
4.5.9 The use of heavy water (D_2O) to probe phototrophic metabolisms 108
4.5.10 A hybrid system for light-driven CO_2 fixation into biomass 108
4.5.11 Calculations 109
Chapter 4 Supplementary Information 111
Chapter 5 Engineering bio-nanoreactor in bacteria for efficient hydrogen production 129

5.1 Summary **130**
5.2 Introduction **131**
5.3 Results **134**
5.3.1 Biogenic FeS nanoparticles assembled in periplasm of *S. oneidensis* MR-1 for enhanced inward electron transfer 134
5.3.2 Constructing a biologically reduced graphene oxide with *S. oneidensis* –FeS nanoparticles for H_2 production 136
5.3.3 Increasing proton pumping into the periplasm by expression of *Gloeobacter* rhodopsin and canthaxanthin 138
5.3.4 Enhanced H_2 production through efficient interactions of reactants within periplasmic nanoreactor 140
5.4 Discussion **143**
5.5 Materials and methods **146**
5.5.1 Bacterial strains, culture conditions and plasmid construction 146
5.5.2 Biosynthesis of FeS nanoparticles 146
5.5.3 Microbial reduction of GO to modify the electrode 146
5.5.4 Transmission electron microscope (TEM) characterisation 147
5.5.5 SDS-PAGE to validate overexpression of the periplasmic [FeFe]-hydrogenase . 147
5.5.6 Colony forming units (CFU) counting for quantification of viable cells on the electrode 148
5.5.7 Raman spectroscopy characterisation 148
5.5.8 Linear sweep voltammetry (LSV) analysis 149
5.5.9 Electrochemical test for fumarate reduction 149
5.5.10 Proton pumping capacity test of engineered cells in light 149
5.5.11 Light response test of the electrochemical systems with engineered cells 150
5.5.12 Cathodic hydrogen production 150
5.5.13 Calculations 150
Chapter 5 Supplementary Information 152
Chapter 6 Summary and Outlook 168
6.1 Summary **168**
6.2 Limitations of the work in the thesis **170**
6.3 Outlook **171**
References 175

Abstract

Carbon dioxide (CO_2) emissions are the key driving force of global climate change. Photosynthesis as the primary process to fix CO_2 and sustain life, holds immense significance in the natural world. With the sharp increase in CO_2 emissions over the past decades, understanding, improving and redesigning photosynthesis becomes an essential goal for achieving net-zero emissions.

The aim of this thesis is to engineer rhodopsin-based photosynthesis for two sustainable applications: CO_2 fixation and hydrogen (H_2) production. Microbial rhodopsin is a major light-harvesting photosystem in nature. Compared to chlorophyll-based photosystems, microbial rhodopsins have simple structural makeup, exceptional optical properties and high quantum efficiency, making them ideal biocomponents for engineering artificial photosynthesis. In this work, *Gloeobacter* rhodopsin (GR) was employed as an optogenetic tool to engineer *Ralstonia eutropha* H16 and *Shewanella oneidensis* MR-1 for CO_2 fixation and H_2 production, respectively. These two applications target to reduce carbon emissions from end-of-pipe biological carbon fixation and from the source to provide clean energy, respectively.

For CO_2 fixation, a GR-based photosynthetic electron transport chain was constructed in *R. eutropha* H16 to achieve proton-coupled electron transfer. By heterogeneously expressing the outer-membrane conduit MtrCAB and GR, extracellular electrons from an electrode and GR-driven proton motive force were integrated into *R. eutropha*'s native electron transport chain. The engineered photosynthetic electron transport chain powered the regeneration of ATP and NAD(P)H, driving the conversion of CO_2 to biomass with a maximum electron transfer efficiency of 45%.

For H_2 production, *S. oneidensis* MR-1 was employed as a biocatalyst on the cathode of an electrochemical system. Its periplasmic space was engineered to function as a bio-nanoreactor, loaded with conductive iron sulfide (FeS) nanoparticles and proton-pumping GR. FeS nanoparticles enhanced electron transfer, while light-powered GR improved the periplasmic proton concentration. The engineered bacterium concentrated protons and electrons in the periplasm, achieving efficient biohydrogen synthesis with an H_2 yield of 80.4 μmol/mg-protein/day with a faraday efficiency of 80% at a potential of −0.75 V vs. Standard hydrogen electrode (SHE).

In summary, this artificial photosynthesis system could revolutionise the field of microbial CO_2 fixation and green H_2 production, contributing to the achievement of net-zero emissions. In terms of ecological significance, microbial CO_2 fixation and H_2 metabolism are important processes associated with carbon and electron flows in natural ecosystems. Therefore, this novel system could unveil previously unrecognised photosynthetic mechanisms based on ubiquitous rhodopsins in nature, which may play a crucial role in the global carbon cycle and energy conversion.

List of Abbreviations

ATP – Adenosine triphosphate

ATPase – ATP synthase

CAN – Canthaxanthin

CBB cycle – Calvin-Benson-Bassham cycle

CFU – Colony forming units

CO_2 – Carbon dioxide

CV – Cyclic voltammetry

DC/4HB cycle – dicarboxylate/4-hydroxybutyrate cycle

D_2O – Heavy water (deuterium oxide)

E. coli – *Escherichia coli*

ETC – Electron transport chain

FeS – Iron sulfide

FMN – Flavin mononucleotide

GO – Graphene oxide

GR – *Gloeobacter* rhodopsin

H_2 – Hydrogen

H_2ase – Hydrogenase

LB – Lysogeny broth

LSV – Linear scanning voltammetry

Mtr – Metal-reducing pathway

MtrCAB – Metal-reducing pathway proteins MtrC, MtrA and MtrB

NAD^+ – Nicotinamide adenine dinucleotide

NADH – Reduced nicotinamide adenine dinucleotide

$NADP^+$ – Nicotinamide adenine dinucleotide phosphate

NADPH – Reduced nicotinamide adenine dinucleotide phosphate

PHB – Polyhydroxybutyrate

Rf – Riboflavin

rGO – Reduced graphene oxide

ROS – Reactive oxygen species

rTCA cycle – Reductive tricarboxylic acid cycle

R. eutropha – *Ralstonia eutropha*

SCRS – Single-cell Raman spectra

SDS-PAGE – Sodium dodecyl sulphate-polyacrylamide gel electrophoresis

SHE – Standard hydrogen electrode

S. oneidensis – *Shewanella oneidensis*

TEM – Transmission electron microscope

TSB – Tryptic soy broth

Vs. – versus

WL pathway – Wood-Ljungdahl pathway

3HP bicycle – 3-hydroxypropionate bicycle

3HP-4HB cycle – 3-hydroxypropionate-4-hydroxybutyrate cycle

Chapter 1 Introduction

Photosynthesis is a foundational process of the ecosystem, by which photosynthetic organisms convert solar energy into chemical energy supporting most living organisms. All known phototrophic metabolisms on Earth can be divided into chlorophyll-based and rhodopsin-based phototrophy mechanisms (1, 2). The significance of chlorophylls in capturing solar energy and driving carbon dioxide (CO_2) fixation has been studied for decades. Recent studies highlighted that microbial rhodopsins are major contributors to global light harvesting, potentially absorbing as much light energy as chlorophyll-based phototrophy (3, 4). Compared to the chlorophyll-protein complexes, rhodopsins are much simpler, involving a single membrane protein composed of seven transmembrane α-helices. Upon illumination, rhodopsins transform solar energy into an electrochemical gradient by pumping ions across the cell membrane (5). The inherently simple structure and mechanism of rhodopsins have opened avenues for engineering phototrophy in bacteria for light utilisation.

1.1 Aim and objectives

The main aim of this thesis is to engineer rhodopsin-based artificial photosynthesis in bacterial cells for sustainable chemical engineering, specifically focusing on carbon dioxide fixation (CO_2) and hydrogen (H_2) production (Figure 1.1).

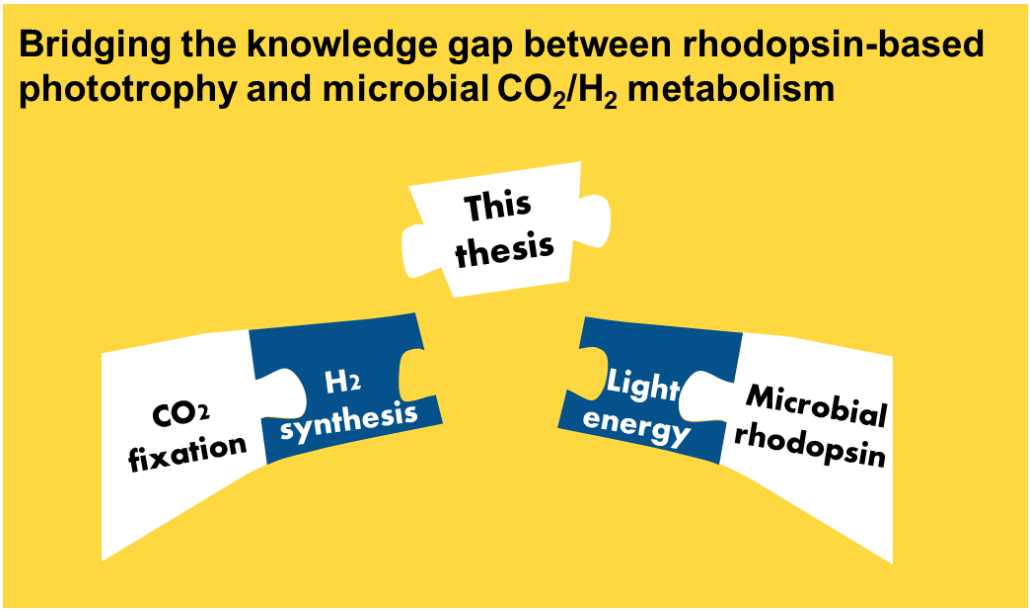


Figure 1.1. The aim of this thesis is to engineer rhodopsin-based photosynthesis to address the knowledge gap between rhodopsin-based photosystem and microbial CO_2 fixation/H_2 synthesis.

The detailed objectives of this thesis have been defined as follows:

- Express the outward proton-pumping *Gloeobacter* rhodopsin (GR) from *Gloeobacter violaceus* PCC7421 in non-native microbial hosts to enable light energy harvesting.
- Compare the growth performances of the GR-expressing *Ralstonia eutropha* H16 under light and dark to understand the impact of light-activated on cellular metabolism.
- Construct a photo-electrosynthetic system by combining the GR-expressing *R. eutropha* H16 with an electrochemical system for CO_2 fixation.
- Introduce outer membrane-bound cytochromes MtrCAB in *R. eutropha* H16 to improve its extracellular electron transfer efficiency.
- Couple GR-driven proton transport with the Mtr-mediated electron transfer for efficient CO_2 fixation in the photo-electrosynthetic system.
- Employ *Shewanella oneidensis* MR-1, an electroactive bacterium as a biocatalyst on the electrode to catalyse H_2 evolution via its periplasmic hydrogenases in an electrochemical water-splitting system.
- Engineer the periplasm of *S. oneidensis* MR-1 into a bioreactor, incorporating GR and self-assembled iron sulfate (FeS) nanoparticles for enhanced electron and proton transfer, respectively.
- Overexpress hydrogenases in *S. oneidensis* MR-1 for increased H_2 production.

1.2 Structure of the thesis and key findings

This thesis is presented in an **integrated format**, with most of its contents already published in scientific journals (Table 1.1).

Table 1.1. The contents and publications associated with this thesis

Chapters	Contents	Publications	My authorship
Chapter 1	Introduction	\	\
Chapter 2	Literature review	Partially published in *Environmental Microbiology* (2023)	First author
Chapter 3	GR-powered growth and CO_2 fixation by *R. eutropha*	Published in *ACS Synthetic Biology* (2022)	Co-first author
Chapter 4	Modular engineering of *R. eutropha* to enhance GR-driven CO_2 fixation	Published in *Nature Communications* (2023)	First author
Chapter 5	Efficient H_2 synthesis by engineered *S. oneidensis* with GR	Published in *Proceedings of the National Academy of Sciences* (2024)	First author
Chapter 6	Summary and outlook	Partially published in *Microbial Biotechnology* (2024)	Co-first author

The thesis structure and the key findings are summarised as follows:

Chapter 2 introduces the background of employing microbial platforms for sustainable chemical engineering, including the use of renewable energy sources for CO_2 fixation and H_2 production. The optimisations of bacterial energy harvesting systems and anabolic processes are reviewed with an emphasis on leveraging synthetic biology for efficient bioproduction.

Chapter 3 investigates the heterologous expression of GR-based photosystem in a model chemoautotrophic bacterium, *R. eutropha* H16. In this chapter, the growth performances of the GR-expressing *R. eutropha* H16 are compared under light and dark conditions to confirm the light-activated GR enhancing biomass growth. Furthermore, a photo-electrochemical system is established by integrating GR-expressing *R. eutropha* H16 with an external electrode and electron mediator riboflavin to form a closed redox loop, which drives rhodopsin-dependent CO_2 fixation.

Chapter 3's contribution to the field is as follows:

- It is the first time to transform a non-photosynthetic bacterium into a phototrophic organism using rhodopsin as a light-harvesting system to power CO_2 fixation. The breakthrough opens a new frontier to engineer novel photosynthetic microorganisms tailored for efficient light harvesting and CO_2 fixation.

Chapter 4 optimises the rhodopsin-based photo-electrosynthetic CO_2 fixation by three strategies. First, an Mtr-mediated extracellular electron transfer pathway for the passage of electrons over the cell envelope is expressed in the GR-expressing cells to facilitate the extracellular electron transfer; second, the carotenoid canthaxanthin is introduced as an antenna for GR to elevate its proton pumping capacity; third, a native carbonic anhydrase is overexpressed in the artificial photoautotroph for enhanced CO_2 fixation.

Chapter 4's contribution to the field is as follows:

- It demonstrates that rhodopsin-based artificial photosynthesis can be further improved by optimising extracellular electron transfer processes and proton motive force generation via rhodopsin with an antenna.

Chapter 5 equips an electroactive bacterium, *S. oneidensis* MR-1 with the GR-based photosystem for H_2 synthesis. In this chapter, the periplasm of *S. oneidensis* MR-1 is engineered into a bio-nanoreactor in which nano-material engineering is combined with synthetic biology to facilitate hydrogen production. The integration of reduced graphene oxide (rGO), native MtrCAB complex and iron sulfide (FeS) nanoparticles establishes an effective electron transfer chain from the electrode to the periplasm. The introduction of GR with canthaxanthin boosts proton pumping into the periplasm under light. This system, catalysed by the overexpression of [FeFe]-hydrogenase and powered by both electricity and light, achieves efficient H_2 production.

Chapter 5's contribution to the field is as follows:

- It proposes a bio-nanoreactor concept by engineering natural bacterial periplasm and applies it to enhance biochemical reactions, such as H_2 production.

The final **Chapter 6** provides a summary of the key findings of this thesis and concludes with an outlook.

Chapter 2 Literature Review

This chapter introduces the background of employing microbial cells to catalyse H_2 production and CO_2 fixation. It reviews microbial H_2 metabolism and CO_2 utilisation pathways. Also, it discusses using renewable energy sources to power microbial H_2 production and CO_2 fixation from the perspective of cellular energy metabolism, particularly highlighting the potential role of light-powered microbial rhodopsin in driving biosynthesis. Subsequently, this chapter summarises efforts in synthetic biology to enhance biohydrogen production and microbial carbon fixation as well as the engineering of metabolic pathways for various value-added chemicals. Finally, it provides an outlook on employing microbial cells for sustainable chemical engineering.

2.1 Urgency of reducing carbon emissions

The world is currently facing an unprecedented challenge because of the extreme rise in CO_2 emissions (6). The accumulation of greenhouse gases, mostly carbon dioxide, in the atmosphere, from industrialisation and human activities, has caused climate change and posed a severe threat to the economy and global health (7). The atmospheric CO_2 concentration has almost doubled from 200–280 ppm to 418 ppm in the past 50 years (8). If this increase continues, it is estimated that the CO_2 level will reach 500 ppm by 2045 (9), which may cause the Greenland and Antarctic ice sheets to melt, resulting in rising sea levels and extinctions of ~24% of plant and animal species (10). Hence, there is an urgent need to adopt strategies for mitigating CO_2 emissions.

There are two primary approaches to controlling CO_2 emissions. The first is to reduce emissions at the source by improving the energy structure and utilising clean energy. Hydrogen is the ultimate clean energy, releasing only water without CO_2 emissions when burned. However, current industrial H_2 production relies on fossil fuels, resulting in approximately 11.5–13.6 kilograms of CO_2 emissions per kilogram of H_2 produced (11). To reduce these emissions, H_2 produced by water electrolysis using renewable energy, known as green hydrogen, has recently attracted significant attention as an environmentally sustainable option for the low-carbon economy. The second approach is the end-of-pipe treatment of CO_2 emissions by employing carbon neutrality technologies to capture and fix CO_2. Many technologies, including physical, chemical and biological methodologies, have been developed for CO_2 removal from the

atmosphere (12-15). Physical-chemical methods, such as adsorption (16), water scrubbing (17), absorption (18) and membrane technology (19), have long been employed to remove CO_2. However, the physical-chemical processes are usually energy-intensive, complex and sometimes highly polluting (20). Moreover, physical-chemical CO_2 removal is limited in its ability to catalyse the formation of carbon–carbon bonds; thus, final products are mostly present as one-carbon compounds like formate and methanol. To overcome these bottlenecks, introducing biocatalysts had some success (21). The enzymatic reaction is specific, mild and efficient with no side reactions, which is usually used to complete some complex tasks that cannot be achieved by physical-chemical methods. Whole microbial cells are natural biocatalysts with specific enzymes for CO_2 conversion, which play a crucial role in the global carbon cycle (22). In the context of carbon neutrality, microbial CO_2 fixation is regarded as a promising approach to reducing CO_2 emissions (23), which can take place under mild conditions, with little environmental pollution and produce valuable bioproducts with carbon chains.

2.2 Sustainable chemical engineering

Sustainable chemical engineering is an important branch of chemical engineering that focuses on designing and optimising processes to minimise environmental impact, conserve resources and promote social and economic sustainability. Three elements are important for sustainable chemical engineering: building blocks, energy and catalysts (Figure 2.1). The C, H and O atoms in freely available building blocks CO_2, O_2 and H_2O are sufficient to build various and complex molecules. Energy sources are photons or electrons derived from solar energy or electricity. Microorganisms can serve as reproducible catalysts that catalyse H_2 synthesis and/or incorporate CO_2 into the biosynthetic pathways. In nature, microorganisms are divided into autotrophs and heterotrophs based on their ability to utilise inorganic carbon and into phototrophs and chemotrophs based on their ability to use different types of energy. With the development of new tools in synthetic biology, it is now possible to reconstruct, recombine and redesign carbon and energy modules in microorganisms, therefore converting heterotroph to autotrophy (24) and modifying chemotroph to phototroph (25). The building blocks, energy and catalyst form a sustainable platform, generating diverse outputs such as signals and products (Figure 2.1).

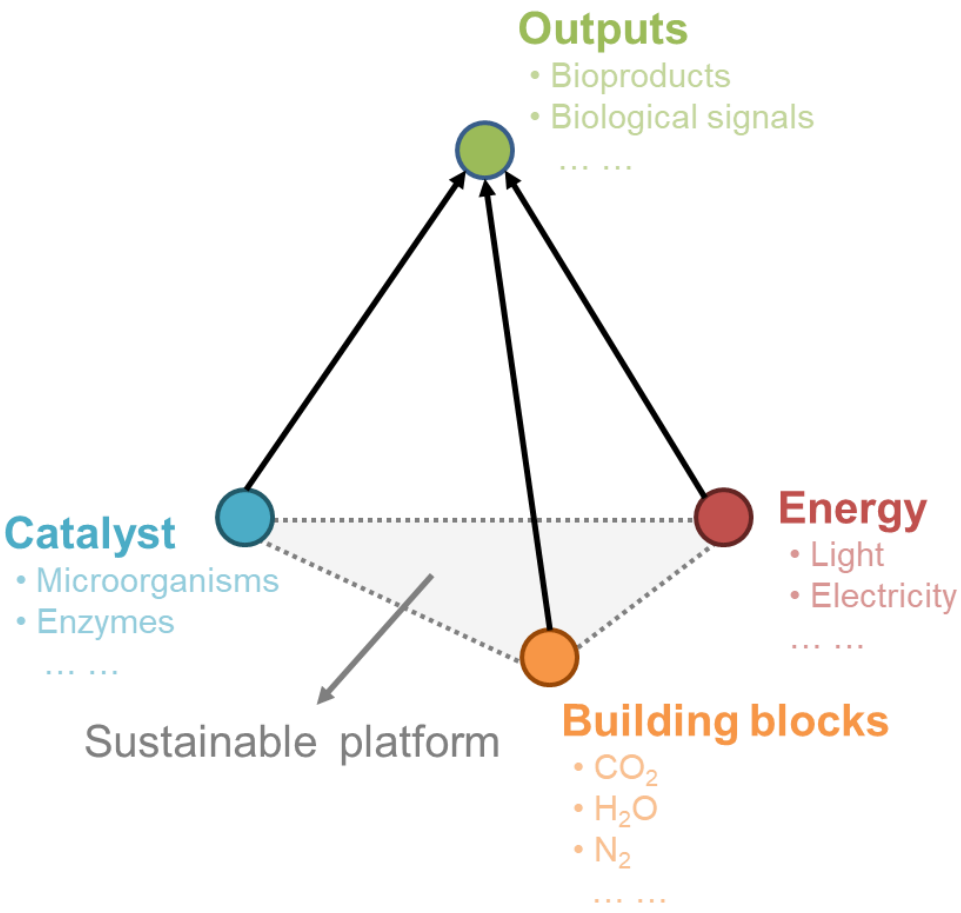


Figure 2.1. Schematic of sustainable bioprocesses in which building blocks, energy sources and catalysts form a triangle to achieve biosynthesis

2.3 Microbial metabolism associated with H_2 synthesis and CO_2 fixation

2.3.1 Microbial hydrogen synthesis

In sustainable chemical engineering, microbial cells are a promising catalyst for H_2 synthesis. Intracellular H_2 synthesis normally involves a straightforward enzymatic reaction. Specifically, bacteria employ hydrogenases or nitrogenases to catalyse H–H bond formation. Both hydrogenase and nitrogenase are metal enzymes, typically containing complex metal clusters and various cofactors (26). These enzymes can be classified into several groups (Table 2.1) based on their structures and cofactors.

Hydrogenase is significantly more efficient than nitrogenase in catalysing H_2 synthesis (26). For example, the turnover rates of [FeFe]-hydrogenases can reach up to 1000 times higher than those of nitrogenases (27, 28). Over the past decades, many species, including algae and bacteria, have been identified to have H_2 metabolism which efficiently generates hydrogen (29, 30). Two types of bacteria are commonly used as

the catalyst for H_2 production which are photosynthetic bacteria (31) and electroactive bacteria (32). Photosynthetic bacteria such as cyanobacteria split water via photosystem II and pass the electrons to hydrogenase via the photosynthetic electron transport chain for hydrogen evolution. Electroactive bacteria such as *S. oneidensis* MR-1 normally serve as the cathodic catalyst in an electrochemical water-splitting system to facilitate hydrogen production (32). Although bacteria are cost-effective catalysts and microbial H_2 metabolism has been proven feasible in H_2 synthesis, their inherent limitations such as the sensitivity of hydrogenase to oxygen and low electron-to-hydrogen yield hamper efficient H_2 production (33, 34). Further efforts in engineering biology are required to upgrade microbial cells into an efficient and robust catalyst for H_2 synthesis.

Table 2.1. Different types of hydrogenases and nitrogenases

Enzymes for H_2 synthesis	Cofactor	Fe–S Clusters	Example bacterium
[NiFe] hydrogenase	[NiFe] cluster	[4Fe–4S] and [3Fe–4S]	*Desulfovibrio gigas*
[FeFe] hydrogenase	H-cluster	[4Fe–4S] and [2Fe–2S]	*Clostridium pasteurianum*
[Fe] hydrogenase	FeGP	None	*Methanothermobacter marburgenis*
Molybdenum (Mo)-nitrogenase	M-cluster	P-cluster and [4Fe–4S]	*Rhodopseudomonas palustris*
Vanadium (V)-nitrogenase	V-cluster	P-cluster and [4Fe–4S]	*Azotobacter vinelandii*
Fe-nitrogenase	Fe-cluster	P-cluster and [4Fe–4S]	*Rhodobacter capsulatus*

2.3.2 Microbial carbon dioxide fixation

The exploitation of microorganisms as a biocatalyst for carbon capture is an economic, mild and sustainable strategy compared to metal catalysts. Compared to H_2 metabolism, microbial CO_2-fixing pathways are more complex, involving the synergy of energy metabolism and carbon fluxes. External energy input and internal carbon fixation pathway are two key elements for microorganisms to reduce CO_2. Based on the capacity to obtain external energy, CO_2-fixing microorganisms are generally classified into chemoautotrophs, accepting electrons from inorganic sources for energy generation, and photoautotrophs, using light as an energy source (35). The other classification is based on the different carbon fixation pathways. To date, at least six natural CO_2 fixation pathways have been identified (36). The Calvin–Benson–Bassham cycle (CBB

cycle) was the first discovered CO_2 fixation pathway (1948), followed by the discovery of the reductive tricarboxylic acid cycle (rTCA cycle, 1966), Wood-Ljungdahl pathway (WL pathway, 1972), 3-hydroxypropionate bicycle (3HP bicycle, 1993), dicarboxylate/4-hydroxybutyrate cycle (DC/4HB cycle, 2007) and 3-hydroxypropionate-4-hydroxybutyrate cycle (3HP-4HB cycle, 2008) (37-42). As shown in Table 2.2, the pathways can be divided into aerobic and anaerobic metabolism based on their tolerance to oxygen. CBB is the most widespread carbon fixation pathway that mainly exists in aerobic and facultative autotrophs. CBB cycle is inefficient and requires the most ATP input among all CO_2 fixation pathways. Despite the low efficiency and high energy requirement, more than 90% of CO_2 in nature is fixed by plants, algae and microorganisms using this fixation cycle (35). 3HP bicycle and 3HP-4HB pathway are the other aerobic pathways found in some aerobes. Unlike other carbon-fixating pathways using CO_2 molecule as the substrate, 3HP bicycle and 3HP-4HB pathway assimilate two moles of bicarbonate that can be dissolved intracellularly in much higher concentration than CO_2. In terms of evolution, the two significant traits are tolerance to oxygen and utilisation of bicarbonate, both of which provide a significant advantage (36). For anaerobic carbon fixation pathways, rTCA cycle and WL pathway are regarded as the most ancient carbon fixation metabolisms and can be completed by employing only 8 enzymes (43). After the appearance of oxygen in the earth's atmosphere, the once predominant anaerobic organisms with rTCA cycle and WL pathway gradually lost ground to aerobic organisms with the CBB cycle. Another anaerobic carbon reduction pathway is via the DC/4HB cycle which fixes one mole of CO_2 and one mole of bicarbonate in a cycle. The anaerobic carbon fixation pathways require less energy input than the aerobic ones due to the limited energy supply, whilst aerobic processes are thermodynamically more favourable than the anaerobic ones (44). This diversity of natural pathways provides the basis and opportunity for the design and construction of hybrid and synthetic carbon fixation systems.

Table 2.2. Characteristics of the six natural CO_2 fixation pathways

Pathways	Energy sources	Electron sources	Total enzyme numbers	Carbon fixation enzymes	Inputs	Outputs	Typical microorganisms	Reference
	Aerobic metabolism							
CBB cycle	Light, inorganic chemical substances	Water, hydrogen, sulfur	11	Ribulose-1,5-bisphosphate carboxylase-oxygenase	3 CO_2, 9 ATP, 6 NAD(P)H	Glyceraldehyde-3-phosphate	*Synechococcus elongatus*, *Ralstonia eutropha*	(42)
3HP bicycle	Light	Water	18	Acetyl-CoA and propionyl-CoA carboxylase	3 HCO_3^-, 5 ATP, 5NAD(P)H	Pyruvate	*Chloroflexus aurantiacus*	(39)
3HP-4HB	Inorganic chemical substances	Hydrogen, sulfur	15	Acetyl-CoA and propionyl-CoA carboxylase	2 HCO_3^-, 4 ATP, 4 NAD(P)H	Acetyl-CoA	*Metallosphaera sedula*	(37)
				Anaerobic metabolism				
rTCA	Light, inorganic chemical substances	Water, sulfur	8	α-ketoglutarate synthase and isocitrate dehydrogenase	2 CO_2, 2 ATP, 4 NAD(P)H	Acetyl-CoA	*Aquifex aeolicus*	(41)
WL pathway	Inorganic chemical substances	Hydrogen	8	Formate dehydrogenase and CO dehydrogenase	2 CO_2, 1 ATP, 4 NAD(P)H	Acetyl-CoA	*Desulfotignum phosphitoxidans*	(40)
DC/4HB cycle	Inorganic chemical substances	Hydrogen, sulfur	14	Pyruvate synthase and phosphoenolpyruvate carboxylase	1 CO_2, 1 HCO_3^-, 3 ATP, 4 NAD(P)H	Acetyl-CoA	*Ignicoccus hospitalis*	(38)

2.4 Utilisation of renewable energy for sustainable biosynthesis

2.4.1 Chlorophyll-based photosynthesis

Photosynthesis is an ancient process of energy conversion and carbon fixation by which photosynthetic organisms synthesise carbohydrates from CO_2 exploiting light as an energy source. Photosynthesis can be classified into oxygenic and anoxygenic photosynthesis. Oxygenic photosynthesis begins with the oxidation of water to oxygen, a light-dependent reaction catalysed by photosystem II. In contrast, anoxygenic photosynthesis is a phototrophic process in which light energy is captured by bacteriochlorophyll and rhodopsin without producing oxygen. The standard, near-universal type of chlorophyll-based photosynthesis is oxygenic and involves two successive stages, 1) light-dependent reactions for conversion of light energy to chemical energies of ATP and NAD(P)H, and 2) light-independent reactions (also CBB cycle) leading to the assembly of carbohydrate molecules from CO_2, driven by the chemical energy generated in the first stage. The energy generated by light-dependent reactions can also be used to synthesise biohydrogen. For example, in cyanobacteria systems, when the Clavin cycle is not activated, the hydrogenases accept surplus electrons from the photosynthetic electron transport chain to synthesise H_2 (45, 46).

Microorganisms with chlorophyll play a vital role in the cycling of carbon on earth, and with the development of biotechnology over the last decade, they have been widely used for bio-manufacturing employing CO_2 as the carbon source (47). Photosynthetic microorganisms are recognized as promising cell factories for bio-production, and their photosynthetic capacity combined with high cell-density fermentation offers an attractive avenue to fixate CO_2 into biofuels (48). However, the microbial photosynthesis efficiency is lower than 3% (49), impeding the broad applications of light-driven production. A key factor leading to low photosynthesis efficiency is the energy loss during light harvesting (35). Photosynthetic microorganisms generally use photosystem I and II to take photons of light wavelengths between 400 and 700 nm (50), resulting in the dissipation of light energy outside the range. In recent years, some near-infrared absorbing chlorophylls, such as chlorophyll f and d, were discovered and identified in cyanobacteria, by which light above 700 nm can be captured (51). This provides the prospect of extending the spectrum of light for more utilisation of solar energy. The large size of chlorophyll antenna molecules is also responsible for light energy loss, especially in high-density fermentation. Incoming light is absorbed by chlorophyll antenna molecules of the cells at the top layers and barely penetrates the lower layers, thereby causing unbalanced energy distribution in space for a fermentation system (52). Most light energy can be dissipated via non-photochemical quenching when photosynthesis of the top cells reaches saturation. To overcome the bottleneck, some studies have been devoted to minimising the size of chlorophyll

antenna by genetic engineering and demonstrated an improvement in photosynthesis due to a truncated chlorophyll antenna (52). Another significant energy loss occurs at a high intensity of sunlight due to saturation. Photosystems become saturated at only 20% of full sunlight, leaving 80% of the light unused (53). Moreover, high light intensities can cause photodamage of the photosystem II. Fortunately, the advent of photovoltaic technology opens up the potential to reshape the light-harvesting process of photosynthesis (54). Some significant developments in photovoltaic materials have achieved a solar-to-electricity conversion efficiency of more than 20%, surpassing the theoretical maximum efficiency of approximately 11% for bio-photosystems (55). Photovoltaic-electrochemical systems can replace photosystem II to generate electrons. The integration of the photo-electrochemical system with cyanobacteria lacking photosystem II has shown improved photosynthetic performance at high light intensities (56).

2.4.2 Rhodopsin-based phototrophy

In nature, there are two major systems for capturing solar energy, chlorophyll- and rhodopsin-based light absorbance systems (1, 2). Microbial rhodopsin, as a light-activated ion transporter, is globally abundant and widely distributed in bacteria (1, 57-63) and eukaryotic photosynthetic plankton including diatoms (64). It utilises light at a peak wavelength of ~530 nm, complementary to chlorophyll in light absorption (65) (Figure 2.2A). A recent survey in the Mediterranean Sea and the Eastern Atlantic Ocean suggested that microbial rhodopsin-based systems could contribute the same amount of light energy harvesting as chlorophyll-based systems (3).

Microbial rhodopsins have significant structural diversity, despite their conserved structural motif of seven transmembrane alpha helices attached to a retinal chromophore (66-69) (Figure 2.2B). In general, microbial rhodopsins can be divided into light-driven pumps and light-gated channels (5). Among them, proton-pumping rhodopsins such as proteorhodopsin and *Gloeobacter* rhodopsin are most well-studied and clearly understood. They act as a light-activated proton pump, harvesting solar energy to pump out protons for the generation of a proton motive force which supports ATP synthesis (70), biomass growth (71), substrate uptake (72) and bacterial survival (73). The simple structure and mechanism of rhodopsin offer a new approach to genetically engineering non-phototrophic cells for harvesting light energy. Engineered *E. coli* with rhodopsin was reported to have long-term viability (74), enhanced biomass growth (75), accelerated target compound biosynthesis (76) and elevated H_2 production (77).

Rhodopsin cannot solely drive CO_2 fixation. Unlike chlorophyll-based photosynthesis, rhodopsin is independent of electron transfer and does not involve any known redox processes. The conventional concept of rhodopsin phototrophy is based on light-driven extra energy supply, such as increasing

ATP to promote microbial carbon fixation (Figure 2.3). It has been reported that proteorhodopsin-powered anaplerotic CO_2 fixation could occur in *Dokdonia sp*. MED134 (78) and in marine bacteria (79-86). These studies suggest that rhodopsin's role in the carbon cycle is likely indirect through affecting microbial metabolism. There is a lack of evidence to demonstrate a direct relationship between rhodopsin and microbial autotrophic carbon fixation in natural environments.

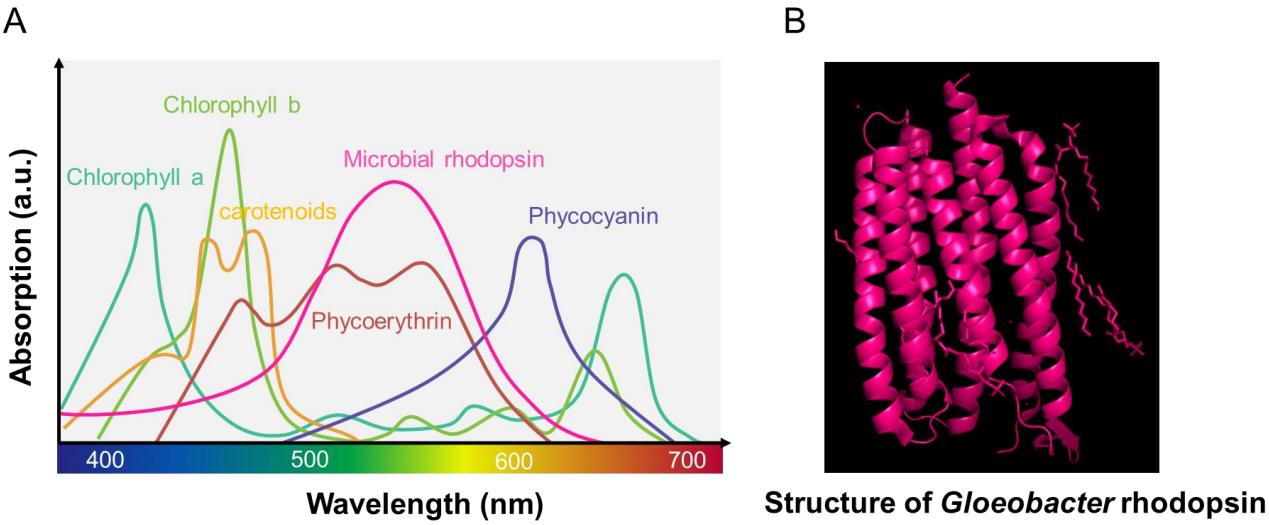


Figure 2.2. (A) Light absorptions of chlorophyll-based photosystem, rhodopsin-based photosystem and some common pigments including carotenoids, phycoerythrin and phycocyanin. (B) 3D structure of typical microbial rhodopsin, *Gloeobacter* rhodopsin (GR), which is performed by an available crystal structure database GR (PDB code: 6NWD) in the PyMOL program.

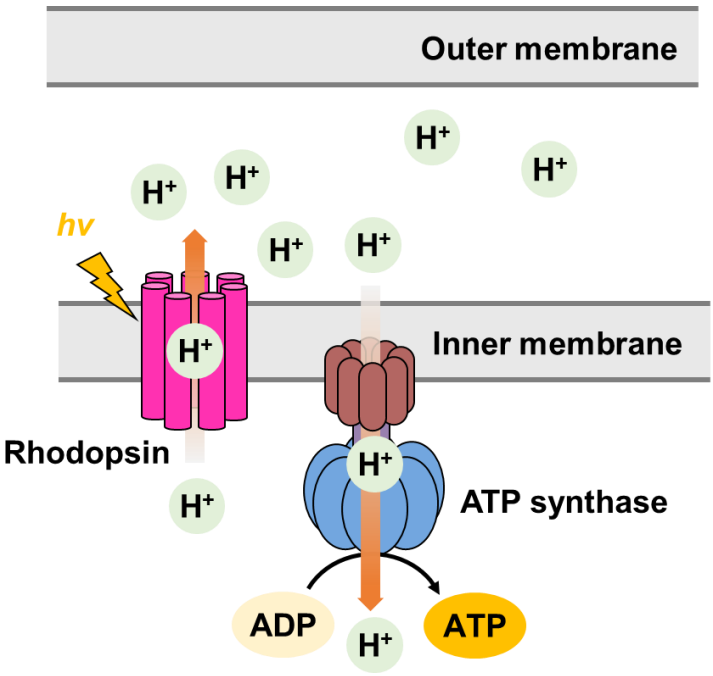


Figure 2.3. Schematic of proton-pumping rhodopsin generating proton motive force in light to drive ATP synthesis.

2.4.3 Electricity-driven electron transfer

Microbial electrosynthesis (MES) is an emerging technology that converts electrical energy to chemical energy, with the microorganisms utilising the cathode as the electron donor to drive biosynthesis (87). Figure 2.4 shows four possible electron transfer mechanisms in MES. Direct electron transfer only occurs in electroactive microorganisms. A direct extracellular electron transfer mechanism typically involves outer-membrane bound cytochromes such as the multi-heme protein complex MtrCAB of *S. oneidensis* MR-1 and PioABC of *Rhodopseudomonas palustris* TIE-1 that can interact with electrodes to transport extracellular electrons bidirectionally (88). Through the extracellular electron transport pathway, *S. oneidensis* MR-1 can directly obtain electrons from the cathode to reduce protons for H_2 synthesis, while *R. palustris* TIE-1 can directly accept electrons from the cathode to power its CO_2 fixation pathway.

In addition to direct electron transfer, the electroactive bacteria can also obtain electrons from the electrode indirectly mediated by electron shuttling molecules such as flavin. For example, the electroactive bacterium *S. oneidensis* MR-1 is able to synthesise and secret flavin to facilitate extracellular electron transfer, and the flavin-dependent processes account for ~80% of the total electron transfer (89). Indirect electron transfer can also be applied to non-electroactive bacteria in the presence of electron mediators (Figure 2.4). Engineered *E. coli* with heterologous hydrogenase can synthesise H_2 by obtaining electrons from the cathode mediated by methylviologen (90). Chemoautotrophic *R. eutropha* can fix CO_2 into polyhydroxybutyrate by accepting electrons from the cathode mediated by neutral red (91). Additionally, electrochemically synthesised molecules such as H_2 or formate can be used as electron mediators to power CO_2 fixation (92, 93). Hydrogen autotrophic or formatotrophic species utilise H_2 or formate by hydrogenase or formate dehydrogenase to generate reducing equivalents NAD(P)H, driving CO_2 reduction.

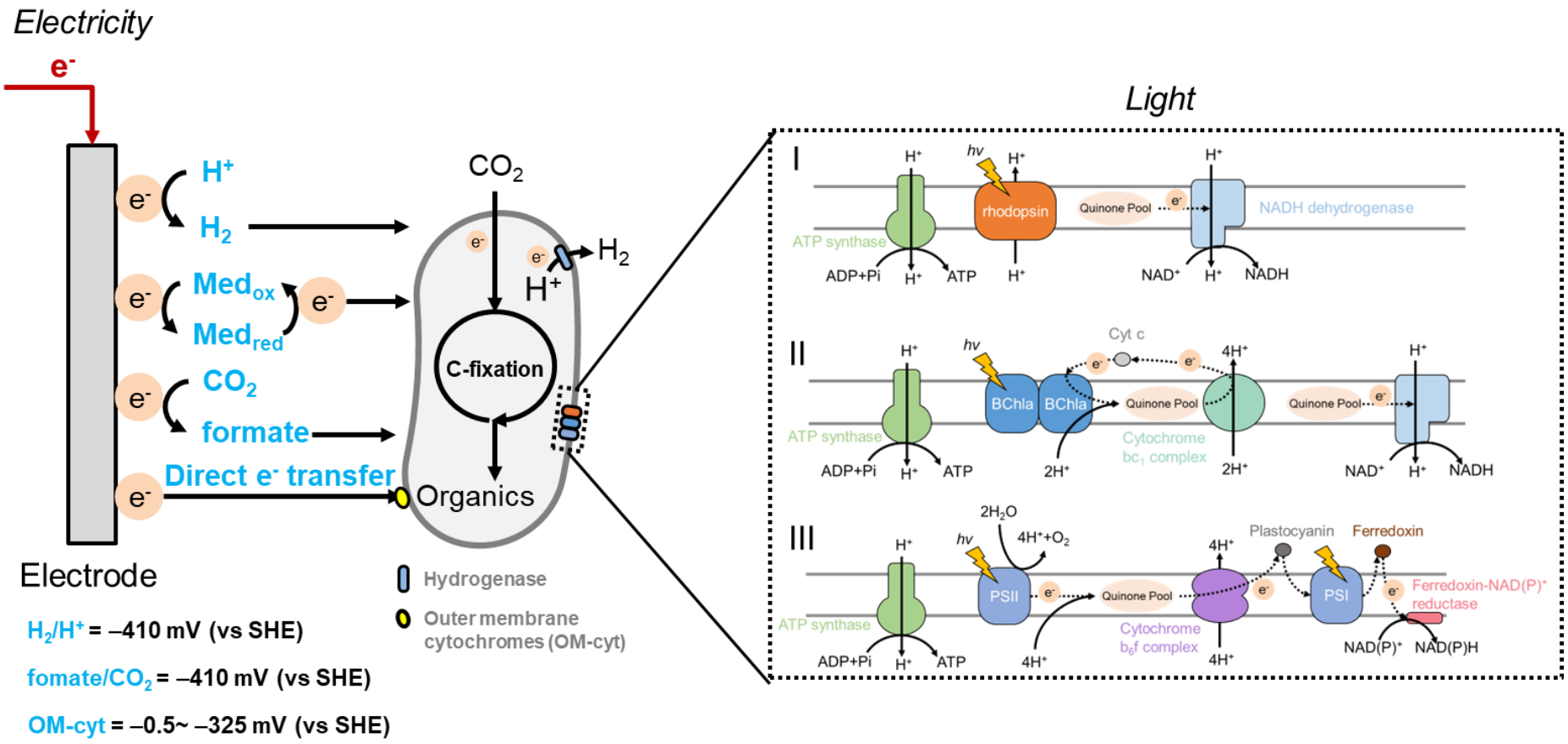


Figure 2.4. Schematic of microbial energy harvesting. Three types of photosynthesis, I. rhodopsin-based photosynthesis, II. anoxygenic photosynthesis and III. oxygenic photosynthesis, are shown in the dotted box. Abbreviations: Med_{ox}, oxidised mediator; Med_{red}, reduced mediator; C-fixation, carbon dioxide fixation pathway; BChla, bacteriochlorophyll a; PSI, photosystem I; PSII, photosystem II.

2.5 Microbial production of biohydrogen from water and value-added products from CO_2

Water splitting is regarded as one of the most promising approaches to generating green hydrogen. In general, biohydrogen production via water splitting can be divided into microbial electrosynthesis of H_2 and photosynthetic hydrogen production. As outlined in Table 2.3, the photosynthetic hydrogen production is primarily achieved by algae and cyanobacteria, and the microbial electrosynthesis is mainly achieved by electroactive bacteria. In microbial electrosynthesis, the electrochemical system is used to mimic photosystem II in photosynthetic H_2 production. An advantage of this approach is that a dual-chamber electrochemical bioreactor can separate the hydrogen production reaction from oxygen evolution at the anode, thereby improving efficiency. However, the disadvantage is that proton and electron transfer efficiency could be sacrificed compared to the integrated processes in the photosynthetic electron transport chain.

Table 2.3. Some examples of biohydrogen production by electroactive bacteria and photosynthetic bacteria

Energy source	Bacteria	H_2 yield	Reference
Electricity	*Shewanella oneidensis*	24.5 mL/m^3/d	(94)
Electricity	*Desulfovibrio paquessi*	0.12 m^3/m^3/d	(95)
Electricity	Mixed cultures (dominant by hydrogenotrophic bacteria)	0.148 m^3/m^3/d	(96)
Electricity	Mixed cultures (dominant by sulphate-reducing bacteria)	1.85 m^3/m^3/d	(97)
Light	*Synechocystis* PCC 6803	6.55 μmol/mg chl/h	(98)
Light	*Chlamydomonas reinhardtii*	0.44 μmol/mg chl/h	(99)
Light	*Anabaena variabilis*	~20.26 μmol/mg chl/h	(100)

Table 2.4. Some recent examples of value-added product biosynthesis from CO_2

Energy source	Culture	CO_2 fixation pathway	Product	Productivity/ yield	Reference
H_2 produced from water electrolysis	Mixed cultures dominated by *Acetobacterium*	Wood-Ljungdahl; CBB cycle	Acetate	11.0 ± 1.6 mM/d	(101)
H_2 produced from water electrolysis	Mixed cultures dominated by *Clostridium*	Wood-Ljungdahl	Butyrate	1.8 mMC/d	(94)
H_2 produced from water electrolysis	*Acetobacterium woodii* and *Acinetobacter*	Wood-Ljungdahl	Alkanes	8.2 μg/L/h	(102)
H_2 produced from water electrolysis	Engineered *Ralstonia eutropha*	CBB cycle	Polyhydroxybutyrate (PHB)	~700 mg/L	(93)
H_2 produced from water electrolysis	Engineered *Ralstonia eutropha*	CBB cycle	Lycopene	1.73 mg/L	(103)
Formate produced from electrosynthesis	Engineered *Ralstonia eutropha*	CBB cycle	Isobutanol and 3-methyl-1-butanol	1.4 g/L	(92)
Light	*Chlorella vulgaris*	CBB cycle	Neutral lipids	516.6 mg/L/d	(104)
Light	Engineered *Synechocystis*	CBB cycle	Ethylene	718 μL/L/h	(105)
Light	*Parachlorella kessleri*	CBB cycle	Carotenoid	0.030 μg /mL	(106)
CO and H_2	Engineered *Clostridium autoethanogenum*	Wood-Ljungdahl	Acetone and isopropanol	~3 g/L/h	(107)
H_2	*Clostridium ljungdahlii*	Wood-Ljungdahl	Ethanol	0.301 g/L/h	(108)
H_2	Engineered *Ralstonia eutropha*	CBB cycle	Trehalose	0.47 g/L	(109)
H_2	Engineered *Ralstonia eutropha*	CBB cycle	Polyhydroxyalkanoates (PHA)	20–60% of dry cell weight	(110)
H_2	Engineered *Ralstonia eutropha*	CBB cycle	Lipochitooligosaccharides (LCO)	1.4 mg/L	(110)

CO_2 is cheap, renewable, abundant and nontoxic carbon feedstock for bioproduction (111). As shown in Figure 2.5, biofuel production from CO_2 is mainly achieved by gas

fermentation employing microbes as a biocatalyst. Gas-driven fermentation is a traditional mode to produce bioenergies from CO_2 or syngas (112), which usually uses light or H_2 as energy sources. While renewable electricity is increasingly employed in industry, microbial electrosynthesis may represent the future of biochemical production from CO_2. Table 2.4 lists some recent examples of bioproduction processes from CO_2. The most common carbon fixation pathways utilised by microbial strains and most widely used in industry are the CBB cycle and Wood-Ljungdahl pathways; the former is the most common in autotrophs and the latter is the most efficient. As for the types of final products, they are determined by the metabolic pathways of the fermenting microorganisms. For example, *R. eutropha* has a natural pathway for polyhydroxybutyrate (PHB) synthesis, which is widely exploited in industry. In order to generate products that cannot be directly synthesised by wild-type CO_2-fixating microorganisms, industrial CO_2-fixating strains can be genetically engineered for production, or the production can be alternatively achieved in two stages, i) CO_2 is electro-reduced to acetate or formate, and ii) the reduced products are further transformed by other functional strains (113). The two-stage process can be completed in a cathode chamber (92) or spatially decoupled into two reactors (114). The integrated microbial electrochemical system is convenient and can achieve *in situ* conversion of electrons to final products. However, recent research suggests that the spatially decoupled electro-biosystem highly boosts CO_2 electro-biofixation because it can largely avoid disparities between electrochemical and microbial processes (115).

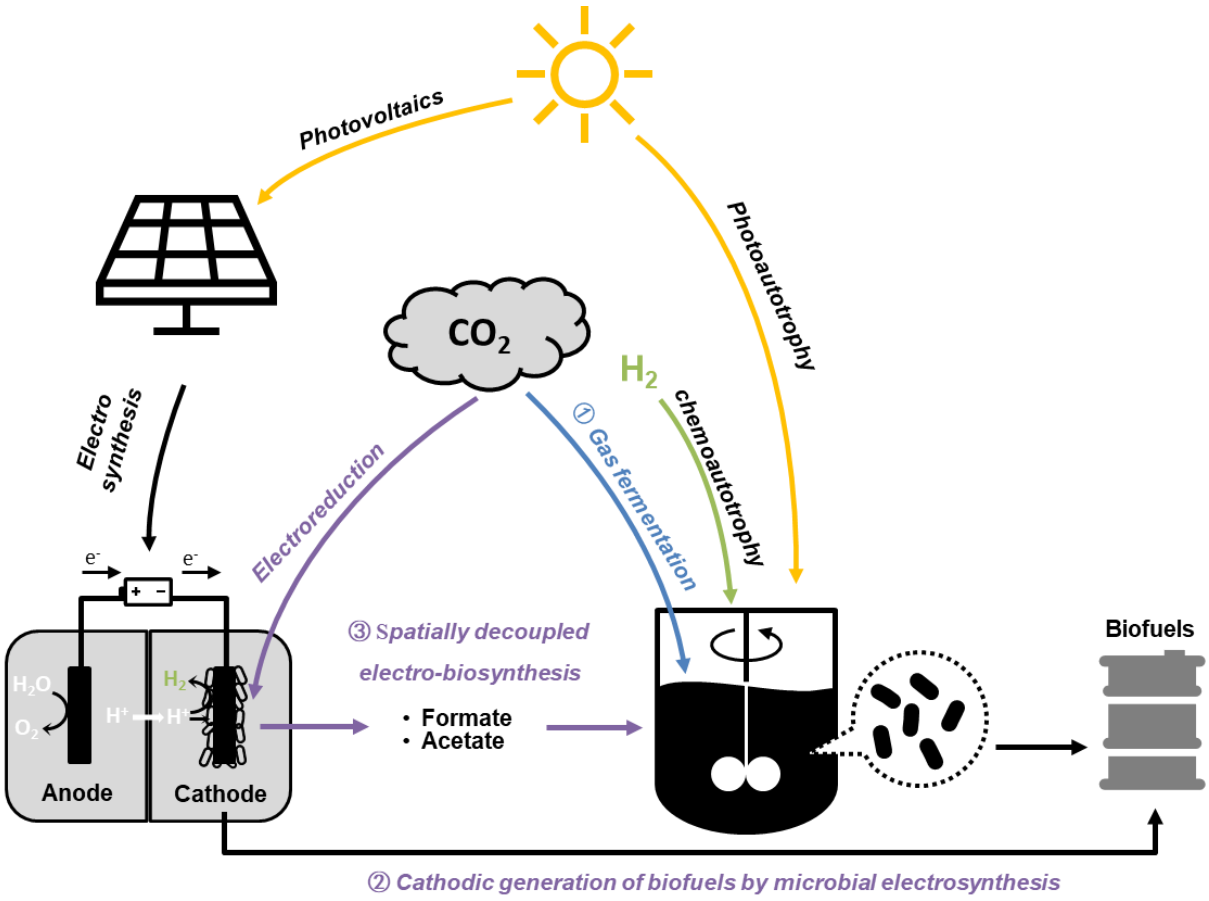


Figure 2.5. Schematic of biofuel production from CO_2 by microbes powered by light, hydrogen and electricity.

2.6 Synthetic biology as a tool to engineer cells

Engineering cells through synthetic biology is a significant potential means of improving bioproduction. Synthetic cell factories enable precise steering to achieve target production with high efficiency. Efficient biohydrogen synthesis can be achieved by engineering microbial cells with high oxygen tolerance and improved electron flux to hydrogen. For biofuel production, synthetic biology not only enables the formation of a wide range of high-value products but also makes the biosynthetic pathways controllable for directing carbon towards the desired products thereby improving the overall efficiency and productivity (35).

2.6.1 Microbial chassis

Although there are many microbial species able to fix CO_2, only a few strains are currently used as chassis for commercial production and industrial-scale applications

(Table 2.5). In synthetic biology, a chassis refers to a biological platform, such as a cell or an organism, which acts as a framework supporting genetic components and providing all the resources to be functional (116, 117). In the context of biofuel production from CO_2, an ideal microbial chassis should have high growth rates, CO_2-fixing efficiency and natural pathways for biofuel synthesis. However, few species currently meet these conditions. Chemoautotroph *R. eutropha*, chemoautotroph (specifically electroautotroph) *Clostridium ljungdahlii*, and photoautotroph *Synechococcus elongatus* are the most-studied chassis available for synthetic biology in the conversion of CO_2 to value-added chemicals. This is attributed to their metabolic versatility, the native capability of utilising CO_2, and the relatively high efficiency of CO_2 fixation (118, 119). In the last few years, genetically engineering industrially relevant heterotrophic organisms to become autotrophs has attracted a broad interest because it could provide more choices in terms of chassis. Indeed, there have already been several reported studies where *E. coli*, one of the most common hosts for engineering chassis, have been converted to autotrophy (24, 120), which demonstrates the potential to expand the spectrum of microorganisms available for industrial exploitation of biological carbon fixation.

Common microbial platforms for H_2 production primarily include photosynthetic microorganisms and electroactive bacteria. Photosynthetic microorganisms such as eukaryotic algae and cyanobacteria utilise photosystem II for water splitting to achieve photosynthetic H_2 production, while electroactive bacteria can be integrated with electrochemical systems to catalyse H_2 evolution at the cathode. The green alga *Chlamydomonas reinhardtii*, in particular, has been used as a chassis for synthetic biology to enhance biological H_2 production from sunlight (121, 122). Although synthetic biology for electroactive bacteria has made progress in improving electricity generation (123) and biosynthesis (124), engineering electroactive bacteria for efficient H_2 production remains largely unexplored.

Table 2.5 Common industrial strains platforms of synthetic biology for CO_2 fixation

Model species	Energy metabolism	Native Carbon fixation pathway	Common energy sources for CO_2 fixation	By-product	Comments
Ralstonia eutropha	Facultative	CBB cycle	Formate and H_2	PHB	Non-pathogenic (qualified presumption of safety as a source of single-cell protein); has a high-flux carbon storage pathway
Clostridium autoethanogenum	Anaerobic	Wood-Ljungdahl	H_2, CO and electricity	Ethanol	Biomass is nutritionally valuable; Model acetogen used for syngas fermentation and microbial electrosynthesis
Synechococcus elongatus	Aerobic	CBB cycle	Light	Oxygen	Rapid autotrophic growth; high tolerance to stress

2.6.2 Diverse products

Engineering microbial cells to synthesise diverse products is a key objective in establishing a versatile biosynthetic platform. CO_2-fixing microorganisms can be engineered to produce various commodity chemicals, such as alcohols, bioplastics, organic acids and sugars. The process of the conversion of CO_2 to reduced products can be divided into two stages, 1) from CO_2 to central carbon metabolites and 2) from central metabolites to targeted chemicals. The process of stage 1 is fixed and depends on the carbon fixation pathway while stage 2 is flexible and determines the types of bioproduct. Pyruvate and acetyl-CoA are the essential metabolites of carbon fixation. If the anabolism based on CO_2 is the main road in a traffic network, pyruvate and acetyl-CoA would be the crossroads connecting different branches (i.e., pathways). Pyruvate is the precursor of butanol and propanol while acetyl-CoA, one of the downstream metabolites of pyruvate, further leads to acids and polymer accumulation (20). To date, synthetic biology has been mostly used to adjust the direction of metabolic conversions by introducing new metabolic pathways or deleting native genes. For example, *R. eutropha* was engineered to produce isobutanol and 3-methyl-1-butanol by knocking the PHB synthesis genes out whilst incorporating genes for alcohol production (92). Alternatively, synthetic biology can be employed to make non-CO_2-fixing cell factories able to reduce CO_2 by introducing appropriate gene clusters. For instance, *E. coli* can

be engineered to convert CO_2 into the central building block acetyl-CoA, making it a versatile platform for the synthesis of various compounds from CO_2 (125).

2.6.3 Enhanced production

Aiming to enhance the efficiency of biofuel production from CO_2, synthetic biology mainly focuses on gene overexpression and deletion to enable redirection of the carbon flux. Overexpressing specific enzymes is a straightforward strategy to increase the level of functional enzymes, thereby promoting the reactions (126). In addition, the heterologous expression of a more efficient enzyme can achieve the same effect. The exploitation of *R. eutropha* for CO_2 fixation is limited by the low efficiency of the Rubisco enzyme. The overexpression of Rubisco derived from *Synechococcus elongatus* PCC7942 in *R. eutropha* has been confirmed to be effective in improving the CO_2 fixation process (91). H_2 is a common chemical energy source for carbon fixation by chemoautotrophs. *R. eutropha* as a chemolithoautotrophic bacterium can obtain electrons from H_2 via hydrogenases to reduce CO_2. Expression of hydrogenases demonstrated an improvement in the growth of *R. eutropha* on CO_2, suggesting that high utilisation efficiency of energy leads to enhanced bioprocesses (127). Deleting unwanted pathways that divert from the target products also improves the yield. For example, acetyl-CoA is a key precursor in carbon metabolism for most microorganisms. When the genes associated with ethanol synthesis (i.e. *adhE1* and *adhE2*) were deleted (128) from *C. ljungdahlii* acetate yield on CO_2 was significantly enhanced by the deletion. Thus, redirection of the carbon flux from biomass synthesis specifically to the production of high-value chemicals holds great potential. One potential target is biofuel synthesis which is independent of microbial growth, suffering from suboptimal production because most of the flux is channelled into biomass production. However, by knocking out the genes related to biomass synthesis or by stringently controlling their expression by replacing a strong inducible promoter (119) the carbon flux can be directed more towards production.

The synthetic biology strategies for improving biohydrogen production focus on overcoming the oxygen sensitivity of hydrogenases and improving the electron flow to H_2 production. Oxygen poses a significant challenge to cyanobacterial and algal photosynthetic H_2 production because the oxygen generated from photoreaction could inactivate hydrogenases. One straightforward strategy to improve resistance to oxygen

is to introduce oxygen-tolerant hydrogenases (129). Another approach involves increasing oxygen consumption to mitigate the effect of oxygen evolution on H_2 production. For example, introducing pyruvate oxidase from *E. coli* into the chloroplast of *C. reinhardtii* was reported to facilitate the decarboxylation of pyruvate to acetyl-phosphate and CO_2, thereby increasing oxygen consumption and enhancing hydrogen production. Besides oxygen sensitivity, the low utilisation of electrons also contributes to inefficient hydrogen production because of the competition between the CO_2 fixation process and hydrogen production. Inhibition of the CO_2 fixation pathway of algae has been reported to promote and prolong H_2 production (130). Recent efforts have focused on directly coupling hydrogenase to photosynthesis by fusing the enzyme to photosystem I, directing more electrons toward H_2 synthesis and allowing sustained H_2 generation (31).

2.7 Outlook

With the accelerating drive for sustainability, there is a growing realization that microorganisms have the potential to be ideal platforms to produce green hydrogen from splitting water and carbon-based products from carbon fixation. For this to be a realistic option, the ability of microorganisms to utilise light and electricity more effectively is essential as this is a primary pinch-point. The rapidly developing field of synthetic biology offers the most promising route to engineering to maximise microbial energy utilisation for biohydrogen production or carbon fixation. Synthetic biology has the potential to assemble different energy-harvesting systems such as the rhodopsin-based photosystem to power the targeted bioprocess. Further optimisation of energy harvesting may require the assistance of abiotic systems, for example, the incorporation of materials such as photovoltaic cells and nanoparticles. Besides energy utilisation, carbon allocation is another key factor determining the conversion yield of products from the assimilation of CO_2. Considerable effort has been devoted to optimising carbon metabolism, and equal attention should also be directed toward the synergy between the energetic and carbon fixation modules. In the future, an efficient, versatile and sustainable microbial platform capable of effective H_2 synthesis or carbon fixation holds significant promise in reducing carbon and energy loss, thereby contributing to a greener world.

Chapter 3

ACS SyntheticBiology

Engineering a Rhodopsin-Based Photo-Electrosynthetic System in Bacteria for CO_2 Fixation

Paul A. Davison [a#], Weiming Tu [b#] Jiabao Xu [b], Simona Della Valle [b], Ian P. Thompson [b], C. Neil Hunter [a] and Wei E. Huang [b*]

[a] Plants, Photosynthesis and Soil, School of Biosciences, University of Sheffield, Sheffield S10 2TN, United Kingdom.

[b] Department of Engineering Science, University of Oxford, Oxford OX1 3PJ, United Kingdom.

[*]Corresponding author: Department of Engineering Science, University of Oxford, Parks Road, OX1 3PJ, Oxford, United Kingdom. Email wei.huang@eng.ox.ac.uk Tel: +44 1865 283786.

[#] P.A.D and W.T. contributed **equally** to this work.

Chapter adapted from publication: ***ACS Synthetic Biology*** (2022)

DOI: 10.1021/acssynbio.2c00397

3.1 Summary

This chapter focuses on one of the core objectives of the thesis: engineering a light-driven biological system that integrates rhodopsin with electron-transfer processes to power CO_2 fixation. In this chapter, a light-driven proton pump comprising *Gloeobacter* rhodopsin (GR) and its cofactor retinal have been assembled in *Ralstonia eutropha* (*Cupriavidus necator*) H16. In the presence of light, this strain fixed inorganic carbon (or bicarbonate) leading to 20% growth enhancement, when formate was used as the electron donor. We found that an electrode from a solar panel can replace organic compounds to serve as the electron donor, mediated by the electron shuttle molecule riboflavin. In this new autotrophic and photo-electrosynthetic system, GR is augmented by an external photocell for reductive CO_2 fixation. We demonstrated that this hybrid photo-electrosynthetic pathway can drive the engineered *R. eutropha* strain to grow using CO_2 as the sole carbon source. In this system, a bioreactor with only two inputs, light and CO_2, enables the *R. eutropha* strain to perform a rhodopsin-dependent autotrophic growth. Light energy alone, supplied by a solar panel, can drive the conversion of CO_2 into biomass with a maximum electron transfer efficiency of 20.4%.

Keywords: *Ralstonia eutropha*, β-carotene, proteorhodopsin, Gloeobacter rhodopsin, biosynthesis, synthetic biology, CO_2 fixation, photoautotrophy,

3.2 Introduction

One vital challenge in the 21st century is the sustainable production of chemicals and fuels from CO_2, using a biocatalyst and driven by a renewable energy source, for example from sunlight (131, 132). Harnessing the biological fixation of CO_2 for sequestering biomass is an ideal outcome in terms of mitigating rising levels of atmospheric CO_2, even more so if useful products such as chemicals and fuels could be generated. Recent important advances in synthetic biology have demonstrated that *Escherichia coli* can be genetically engineered to grow on CO_2 while reducing power and energy are obtained by oxidising a supplied organic compound (e.g., pyruvate and formate) (24, 133, 134). Other approaches harnessed the native CO_2 fixation pathway of the chemolithotroph *Ralstonia eutropha* H16, coupled to an electrochemical supply of the required reducing power (92, 135). The solar-powered electrochemical systems producing H_2 or formate combined with *Ralstonia eutropha* H16 can drive the artificial photosynthetic process for carbon fixation into biomass and biofuels (93).

The engineering of photoautotrophic growth into a synthetic biology chassis would represent the next level of metabolic engineering, in terms of using synthetic biology for sustainable production of biomass, chemicals and fuels. Engineering photoautotrophy would require exploitation of one of the light-driven systems that have naturally evolved, which are based on either chlorophyll or rhodopsins (1-3). Chlorophyll-based photosynthesis requires a large and relatively complex network of components for light-harvesting, charge-separation, then electron and proton transfers, for driving CO_2 fixation in cells. In contrast, rhodopsin-based utilisation of light is simpler, involving only one membrane protein (65) that usually comprises seven transmembrane α-helices. Microbial rhodopsins are widespread amongst the microbial inhabitants of sunny environments such as the upper ocean (136), and their functions have been dissected by heterologous production in *E. coli* (57, 63). These studies demonstrated that retinal-binding proteorhodopsin (PR) generates a proton gradient that can be used for the production of biologically available energy in the form of ATP (63). Although microbial rhodopsins have been reported as major contributors to solar energy capture in the sea (3), there is no report of rhodopsin-driven autotrophic growth in microbes, likely due to the lack of electron donors required for reductive assimilation of CO_2. In contrast, chlorophyll-based photoautotrophic systems obtain electron donors from light-driven water splitting by photosystem II, and photosystem

I uses light to generate a proton-motive force for ATP generation. Inspired by chlorophyll-based photoautotrophy (137), we hypothesised that a closed redox loop can be constructed by integrating rhodopsin with an electron donor. If the electron donor can be supplied by an electrode powered by a solar panel, a rhodopsin-based photo-electrosynthetic system could drive the autotrophic growth of bacteria using CO_2 as the sole carbon source, and with light as the only energy input.

To test this hypothesis, we engineered a light-powered electromicrobial system for CO_2 fixation (Figure 3.1). The chosen bacterium, *Ralstonia eutropha* (*Cupriavidus necator*) H16, lacks the capacity to use light as an energy source, but its native CO_2 fixation pathway is encoded on two operons of the Calvin-Benson-Bassham (CBB) cycle, one on chromosome 2 and the other on its pHG1 megaplasmid (138). In this study, *R. eutropha* H16 was engineered to synthesise rhodopsin that harvests light energy to generate ATP, while an electron-carrying molecule is required for the electron transfer from an electrode to cells. *R. eutropha* H16 commonly utilises H_2 generated from water splitting to drive CO_2 reduction (139). Nevertheless, the generation of H_2 (or formate) is generally catalysed by an abiotic electrode and the metallic catalysts usually dissolve into the medium and produce toxic compounds to inhibit biosynthesis or growth of *R. eutropha* H16. In this study, the biocompatible and less toxic molecule riboflavin was introduced as an electron shuttle to mediate the electron transfer from an electrode. This bioenergetic system has only two inputs, light and CO_2. The bioenergy for *R. eutropha* H16 growth is supplied by installing *Goleobacter* rhodopsin (GR), augmented by an external photocell that serves as the electron donor (Figure 3.1). This engineered bacterium performs a hybrid form of photoautotrophy, which uses light to convert CO_2 into biomass.

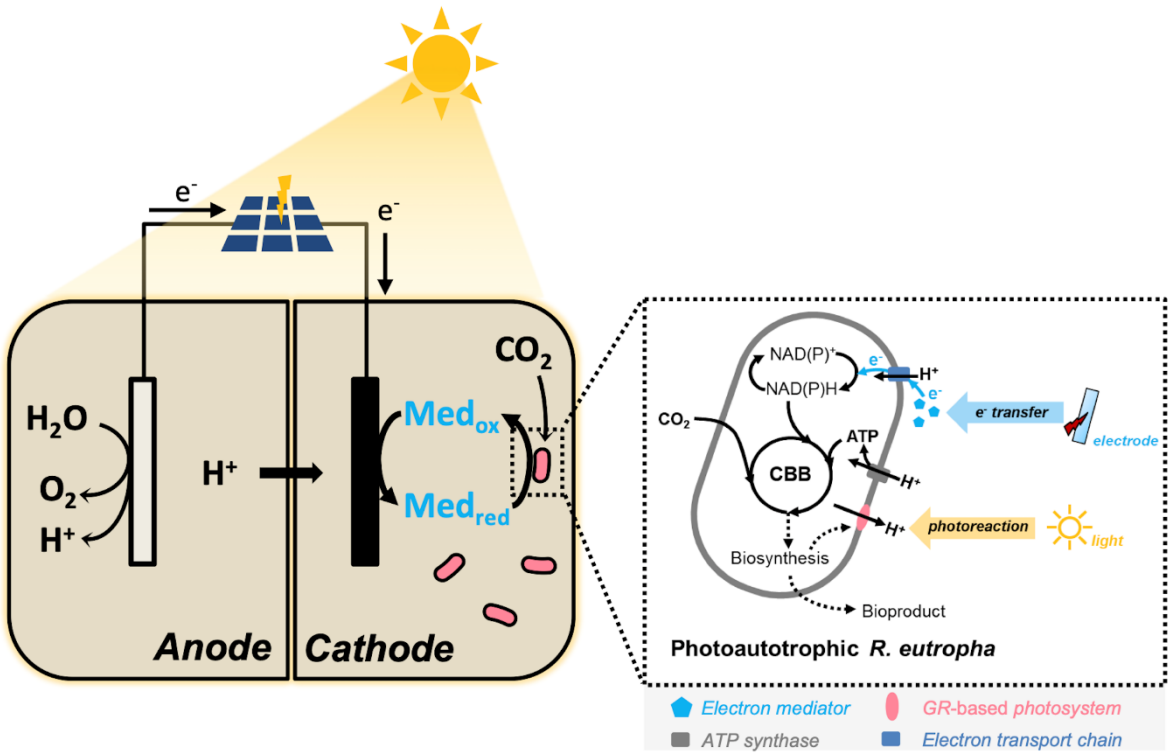


Figure 3.1. A rhodopsin-based photoautotrophic system is able to fix CO_2. Light can be used to activate rhodopsin and generate electricity. Light-activated rhodopsin pumps protons, and when coupled with ATP synthase, generates ATP. An electrode, mediated by riboflavin, can serve as an electron donor to supply electrons. The closed redox loop drives CO_2 fixation.

3.3 Results

3.3.1 Biosynthesis of β-carotene in *R. eutropha*

Biosynthesis of carotenoids requires the supply of the geranylgeranyl diphosphate (GGPP) precursor, followed by phytoene desaturation and subsequent modifications such as cyclisation or introduction of keto groups (140). The carotenoid β-carotene is the precursor of retinal, which is the essential cofactor for the light driven proton pump rhodopsin. The entire *crtEXYIB* operon for β-carotene synthesis, including the *crtE* promoter region (*crt* operon), from the pORANGE plasmid (141), was cloned into the pLO11a plasmid to make pCRT (Table 3.1 and Suppl Fig. S3.1A). The resulting production of β-carotene by *R. eutropha* H16 can be enhanced by overexpression of the *dxr* gene in pDxrCRT (Table 3.1 and Suppl Fig. S3.1B). A biosynthetic pathway for β-carotene synthesis in *R. eutropha* H16 is shown in Figure 3.2A. Detailed information about the production of β-carotene in *R. eutropha* H16 (strain H16 pDxrCRT) is given in Suppl Fig. S3.2.

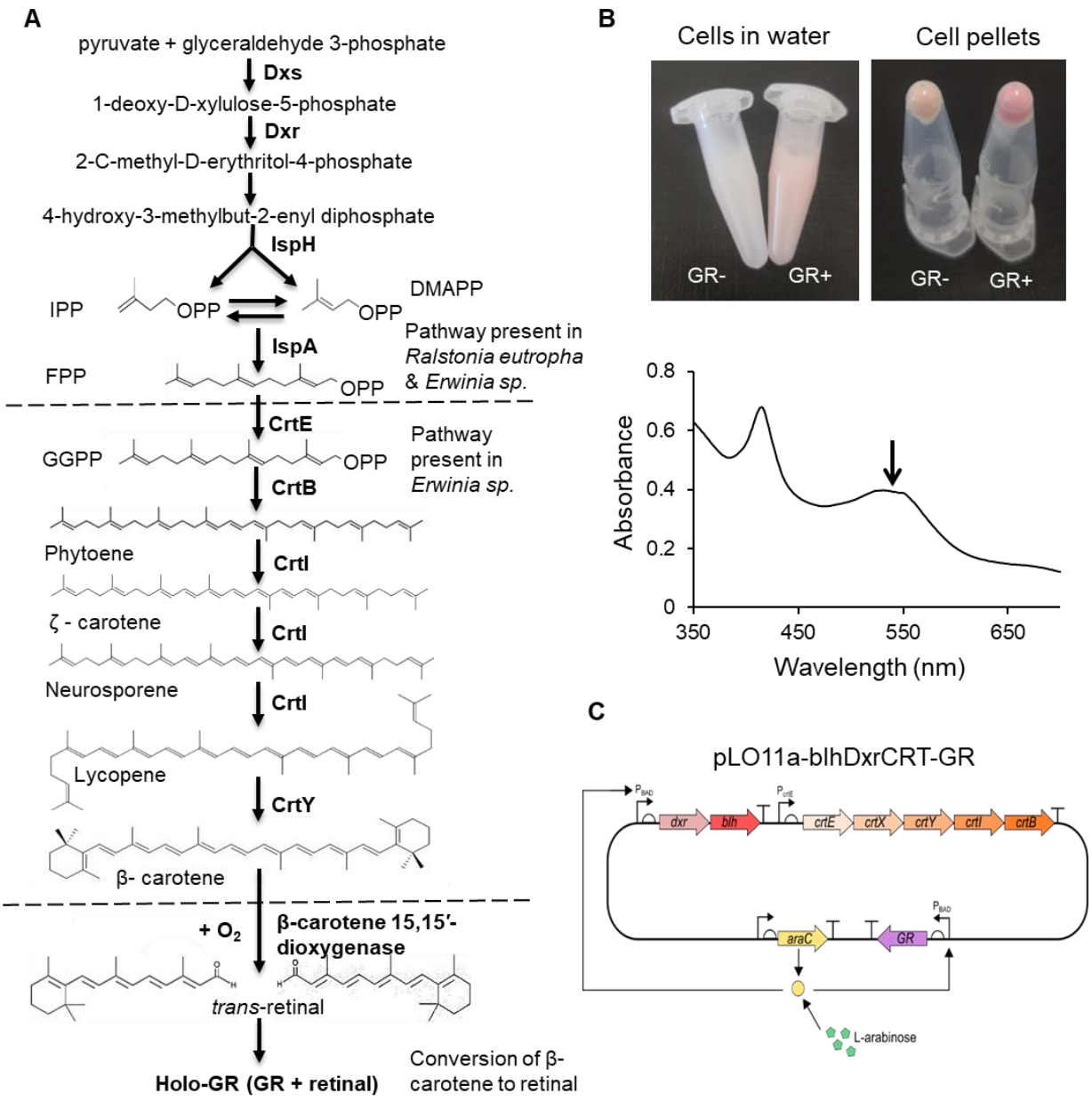


Figure. 3.2. (A) Pathway showing the synthesis of β-carotene from pyruvate and glyceraldehyde 3-phosphate and its conversion to retinal by β-carotene 15,15'-dioxygenase (product key: IPP, isopentenyl diphosphate; DMAPP, dimethylallyl pyrophosphate; FPP, farnesyl diphosphate; GGPP, geranylgeranyl diphosphate). The parts of the pathway common to both *Ralstonia eutropha* and *Erwinia sp.* and unique to *Erwinia sp.* are indicated. The enzyme key is as follows: Dxs, 1-deoxy-D-xylulose-5-phosphate synthase; Dxr, 1-deoxy-D-xylulose 5-phosphate reductoisomerase; IspH, 4-hydroxy-3-methylbut-2-enyl diphosphate reductase; crtE, geranylgeranyl diphosphate synthase; crtB, phytoene synthase; crtI, phytoene desaturase; crtY, lycopene cyclase. (B) GR expression in *R. eutropha* H16 causes a distinct pink colouration. Absorbance scan of isolated membranes from the induced H16 GR cells shows absorption at 540 nm (arrowed), a light wavelength that is not absorbed by chlorophyll. (C) The gene-circuit design shows the arrangement of the pLO11a-blhDxrCRT-GR construct. This contains the crt operon (*crtEXYIB*) plus an 879bp upstream region containing the *crtE* endogenous promoter (P_{crtE}) and the *dxr*, *blh* and *GR* genes (with upstream ribosome binding site shown as semi-circles) under the control of the arabinose inducible P_{BAD} promoter.

Table 3.1. Strains and plasmids used in this study

Strains	**Comments**
***E. coli* JM109**	Commercially obtained (Promega, UK)
***Ralstonia eutropha* H16 (ATCC 17699)**	Wild-type strain
***Ralstonia eutropha* H16 Δ*pha* (RHM5)**	Wild-type strain with *phaCAB* operon encoding genes required for conversion of acetyl-CoA to polyhydroxybutyrate (PHB) deleted (gift from Min-Kyu Oh, Korea University, S. Korea).
Plasmids	**Comments**
pLO11a (Tc^r, RK2 *ori*, Mob^+)	Expression vector for use in *R. eutropha* with P_{BAD} promoter and downstream cloning sites (gift from Oliver Lenz, Technische Universität Berlin, Germany).
pLO11a-CrtYI	pLO11a containing *crtY* and *crtI* from *Erwinia herbicola*
pLO11a-CRT	pLO11a containing constitutive *crtEXYIB* operon from *Erwinia uredovora*
pLO11a-Dxr	pLO11a containing *dxr* from *R. eutropha*
pLO11a-DxrCRT	pLO11a containing *dxr* from *R.eutropha* downstream of P_{BAD} promoter and upstream of *crtEXYIB* operon from *E. uredovora*
pLO11a-GR	pLO11a containing the gene for GR rhodopsin from *Gloeobacter violaceus* PCC7421
pLO11a-blh	pLO11a containing *blh* from the uncultured marine bacterium 66A03 (GenBank: DQ065755.1) codon optimised for *R. eutropha*
pLO11a-Dxr-blh	pLO11a containing *dxr* and *blh* genes separated by a ribosome binding site
pLO11a-blhDxrCRT	pLO11a containing *dxr* and *blh* genes separated by a ribosome binding site downstream of P_{BAD} promoter and upstream of *crtEXYIB* operon from *E. uredovora*
pLO11a-blhDxrCRT-GR	pLO11a-blhDxrCRT containing the *GR* gene downstream with its own P_{BAD} promoter

3.3.2 Biosynthesis of *Gloeobacter* rhodopsin in *R. eutropha*

GR is a rhodopsin from the cyanobacterium *Gloeobacter violaceus* PCC7421 (Genbank: BAC88139) (142, 143). Transfer of the plasmid pLO11a-GR into *R. eutropha* H16 resulted in a distinct pink colour after growth to log phase and overnight induction in the presence of 0.1% (w/v) L-arabinose and exogenous 5 μg ml^{-1} retinal (Figure 3.2B). To examine the GR-retinal complex present in the cytoplasmic membrane, a cell pellet from a 500 ml arabinose and retinal supplemented culture of *R. eutropha* H16 containing pLO11a-GR was disrupted using a French press and the membrane fraction purified on a sucrose density gradient. The fractionated cell extract

from arabinose-induced cells generated a diffuse, highly coloured membrane band in the middle of the gradient. An absorbance spectrum (Figure 3.2B) recorded on a sample harvested from the middle of this band revealed a peak at around 540 nm (arrowed) which is consistent with the published value for the GR-retinal complex (144).

3.3.3 Construction of a gene cluster for GR-retinal complex biosynthesis in *R. eutropha*

Following the construction of two *R. eutropha* strains that separately produce β-carotene (H16 pDxrCRT) and GR (H16 GR), these new attributes were combined within a single strain to enable the assembly of a functional rhodopsin that confers the capacity for ATP synthesis in the light. The *blh* gene from the uncultured marine bacterium 66A03 encodes the β-carotene 15, 15'-dioxygenase enzyme (EC:1.13.11.63), which cleaves one molecule of β-carotene into two molecules of retinal (Figure 3.2A) in the presence of oxygen (145). Although the H16 pDxrCRT strain successfully makes β-carotene, the conversion of this into retinal is a potentially rate limiting step so the *blh* gene was codon optimised for *R. eutropha* to ensure the best chance of expression and cloned into pDxrCRT to create pLO11a-blhDxrCRT (Table 3.1), an expression vector for retinal production. The *GR* gene, under the control of a separate P_{BAD} promoter, was then inserted into this vector to create pLO11a-blhDxrCRT-GR, for the production of GR holoprotein (Figure 3.2C and Table 3.1). This construct was transferred by conjugation into *R. eutropha* H16 to create *R. eutropha* H16 blhDxrCRT-GR (henceforth *R. eutropha*-GR), which acquired a pink colour in the presence of 0.1% arabinose inducer, indicating assembly of a GR-retinal holocomplex. Solvent extraction of the pellets followed by HPLC analysis showed that the uninduced sample contained no β-carotene (Suppl Fig. S3.3A, broken line) or retinal (Suppl Fig. S3.3B, broken line) but upon induction a small amount of β-carotene (Suppl Fig. S3.3A, solid line) and a larger amount of retinal, appearing as an elution peak at approximately 8 minutes under these running conditions, could be detected (Suppl Fig. S3B, solid line). This peak had an absorbance spectrum identical to that seen for all *trans*-retinal with an absorbance maximum at 380 nm (Suppl Fig. S3.3C, solid line). Following induction two further peaks appeared at 8.9 and 9.2 minutes (Suppl Fig. S3B labelled 1 and 2, respectively) with absorbance spectra (Suppl Fig S3.3C, broken lines) similar to all *trans*-retinal but with shifted absorbance maxima of 386 nm (peak 1) and 395 nm (peak 2). It is not known if these are isomers or derivatives

of *trans*-retinal though expression of mouse β-carotene 15, 15'-dioxygenase in a β-carotene expressing *E.coli* strain also resulted in the appearance of extra peaks in addition to that seen for retinal (146). Raman micro-spectroscopy was used to examine GR-retinal complexes in *R. eutropha* H16 and *E. coli* JM109. Single-cell Raman spectra (SCRS) of cells synthesising GR display a unique band at 1530 cm^{-1} (Suppl Fig. S3.4), which is a characteristic biomarker for the retinal-GR holoenzyme, similar to that previously reported for the retinal-PR holoenzyme (74).

3.3.4 GR expression in *R. eutropha* H16 significantly enhances cell growth

Initially, formate was used as the organic electron donor to investigate the light-dependent growth of the engineered *R. eutropha*-GR strain. Figure 3.3A shows that when arabinose was added as the inducer under micro-aerobic conditions, the *R. eutropha*-GR strain illuminated by white LED light showed enhanced growth with the biomass increased up to 24% compared to that seen in the dark, or in uninduced or dark-grown cells. Given the likely consumption of formate in the earlier stages of this experiment (147) the final increase in biomass at the later time points is ascribed to light-driven turnover of GR and subsequent production of ATP and NADPH for CO_2 fixation. The micro-aerobic growth rate of *R. eutropha*-GR has increased to 0.022 h^{-1} in the light, compared to 0.015 h^{-1} in the dark. Light-enhanced growth was maintained over the five-day time course of the experiment, indicating a significant light-dependent increase in biomass of the *R. eutropha*-GR strain. Control strains grown in the presence of arabinose alone (no formate) did not show any growth (Figure 3.3A), ruling out the possibility that the inducer could be used as a carbon source. *R. eutropha* H16 with no GR expression (containing pLO11a-blhDxrCRT-GR but no arabinose induction) showed no detectable growth difference between light and dark conditions (Figure 3.3A). Thus, this is evidence that holo-GR produced in *R. eutropha*-GR can capture light energy to increase cell growth in the presence of formate. The light energy harvested by GR significantly enhanced PHB accumulation in *R. eutropha*-GR when formate was used as the sole carbon source (Suppl Fig. S3.5). This also confirms that energy from light-driven proton pumping by GR stimulates biosynthesis.

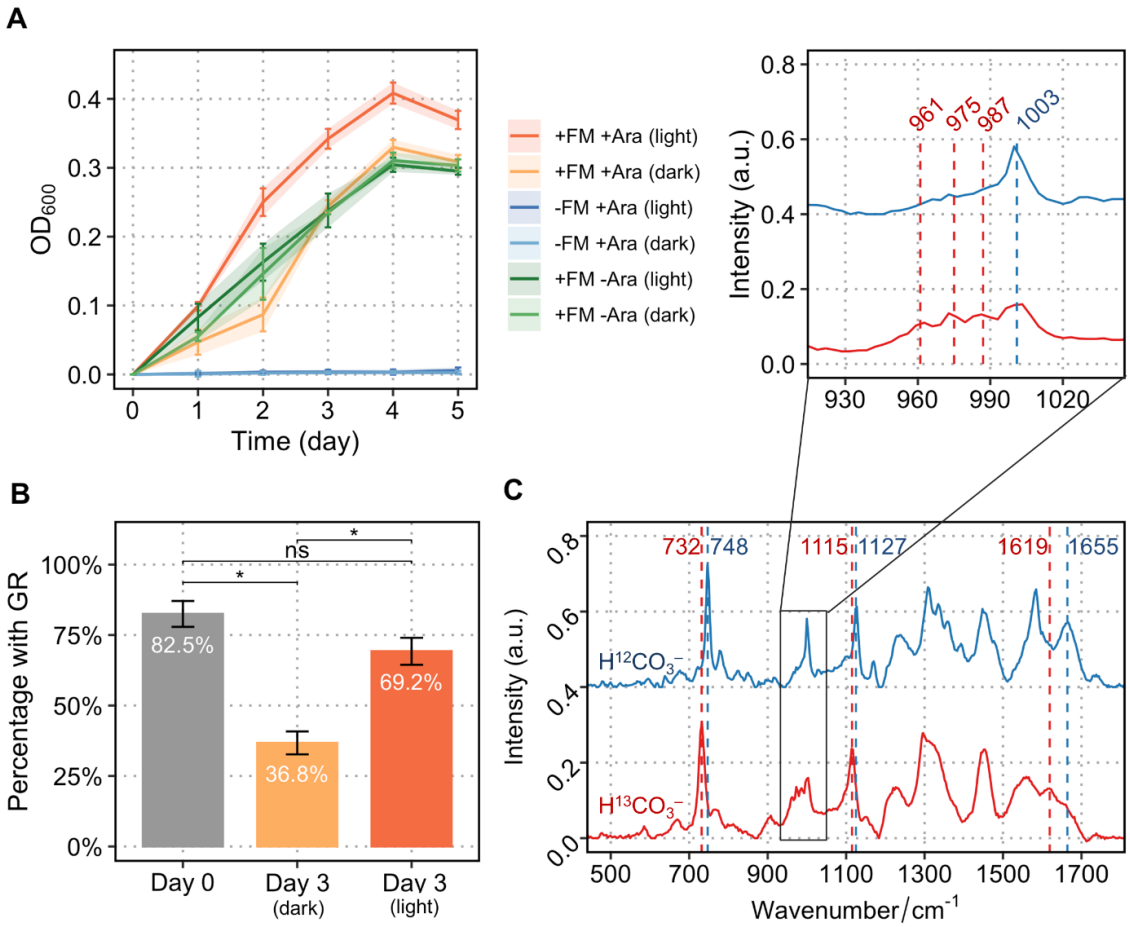


Figure 3.3. (A) Growth curves, represented by OD_{600}, of *R. eutropha* H16 with pLO11a-blhDxrCRT-GR (*R. eutropha*-GR) grown under micro-aerobic conditions in minimal medium with and without formate, with and without light and with and without induction of GR expression. Data show means ± SD, n = 3. (B) Bar chart showing the percentage of the *R. eutropha*-GR cell population grown in the presence of formate expressing GR at day 0 and after 3 days in the light and dark. Independent t tests were performed: *P < 0.05. Data show means ± SD, n = 3. (C) SCRS of cells of *R. eutropha*-GR grown under light in either ^{12}C-bicarbonate (blue) or ^{13}C-bicarbonate (red). Cells grown in ^{13}C-bicarbonate exhibited isotopic Raman shifts from 1655 to 1619 cm^{-1} (Amide I of proteins), 1127 to 1115 cm^{-1} (cytochrome *c*), 748 to 732 cm^{-1} (cytochrome *c*) and 1002 to 987, 975 and 961 cm^{-1} (phenylalanine).

Raman micro-spectroscopy was employed to examine cells containing GR. After growth of *R. eutropha*-GR in minimal medium (MM) with formate in the dark or light for 3 days, the position of the 1530 cm^{-1} Raman band, characteristic for GR, remained the same (Suppl Fig. S3.6). We further measured SCRS of the bacterial population (200 or 400 single cells) and calculated the percentage of the sub-population expressing GR, i.e. with the 1530 cm^{-1} GR band (Table S3.1 and Figure 3.3B). At the outset 83% of the *R. eutropha* H16 population synthesised holo-GR (Figure 3.3B); this proportion declined only to 69% by day 3 under micro-aerobic conditions in the light, in the

absence of antibiotic selection pressure, whilst it dropped to 37% in the dark (Table S3.1 and Figure 3.3B). This indicates that *R. eutropha*-GR in the light had a growth advantage over the cells without GR, leading to an enrichment of those cells with GR. Micro-aerobic conditions were used in this study to reduce the risk of overproduction of reactive oxygen species (ROS) (148). The Raman analysis at the single cell level showed that the percentage of GR containing cells under microaerobic conditions was higher than that seen under aerobic conditions (Table S3.1).

3.3.5 CO_2 fixation by GR-expressing *R. eutropha* H16

Stable isotope probing was used to examine CO_2 fixation by the *R. eutropha*-GR strain. Formate (40 mM) or bicarbonate (40 mM) were used under three differing conditions: (i) ^{12}C-formate + ^{12}C-bicarbonate; (ii) ^{13}C-formate + ^{12}C-bicarbonate; and (iii) ^{12}C-formate + ^{13}C-bicarbonate. Under these three labelling conditions illumination for 3 days improved growth by 18% (Suppl Fig. S3.7A), 20% (Suppl Fig. S3.7B) and 20% (Suppl Fig. S3.7C), respectively. Incorporation of a ^{13}C-substrate was detected via shifted Raman bands in SCRS (149), as shown in Figure 3.3C for *R. eutropha*-GR grown in ^{13}C-formate and ^{13}C-bicarbonate, compared to ^{12}C substrates. In particular, two Raman bands corresponding to cytochrome *c* (150-152) at 748 (pyrrole breathing mode) and 1127 cm^{-1} (υ (CN) stretching vibrations), and a band arising from proteins at 1655 cm^{-1} (Amide I), are shifted to 732, 1115, and 1619 cm^{-1}, respectively (Figure 3.3C). The single band at 1003 cm^{-1} is characteristic of the phenyl ring of ^{12}C-phenylalanine which becomes three bands at 987, 975 and 961 cm^{-1} in the ^{13}C amino acid (Fig. 3.3C), in good agreement with the ^{13}C-Raman shifts observed in previous work (153). Isotope labelling with ^{13}C-bicarbonate (Figure 3.3C) confirms CO_2 fixation by *R. eutropha*-GR, and subsequent incorporation into biomass. After 3 days of culture in the light, *R. eutropha*-GR cells showed a full utilisation of the bicarbonate whilst intracellular bicarbonate was observed in most of the cells under the dark conditions (Suppl Fig. S3.8).

We further sought to compare the extent of ^{13}C incorporation from ^{13}C-bicarbonate and ^{13}C-formate in the light (Suppl Fig. S3.9). The Raman band for pyrrole ring breathing in cytochrome *c*, originally at 748 cm^{-1} (Suppl Fig. S3.9), exhibited a larger downshift to 732 cm^{-1} in cells grown with ^{13}C-bicarbonate relative to that observed with ^{13}C-formate (Suppl Fig. S3.9), suggesting that *R. eutropha*-GR preferentially uses carbon

from the ^{13}C-bicarbonate over that from ^{13}C-formate. We also quantified the newly synthesised proteins in single cells by calculating the area ratio of the 1655 cm^{-1} to 1619 cm^{-1} bands and found higher amounts of these proteins with ^{13}C-bicarbonate relative to ^{13}C-formate ($p < 0.0001$) (Suppl Fig. S3.9). These results suggest that *R. eutropha*-GR could also fix bicarbonate with formate acting as an organic electron donor. When formate acts as the carbon source it is converted into CO_2 and NADH by *R. eutropha* H16 (92), with the CO_2 being fixed via the Calvin-Benson-Bassham (CBB) cycle and the NADH transformed into NADPH, via a proton-translocating transhydrogenase, to support cell growth (138, 154). When extra energy is available via the light-harvesting GR, *R. eutropha*-GR fixed more CO_2 from bicarbonate rather than from formate.

3.3.6 Sources of reductant for light-driven autotrophic growth of *R. eutropha*

A hybrid form of a photoautotrophic system was established to grow *R. eutropha*-GR, (Suppl Fig. S3.11) using CO_2 and light as the inputs, and biomass generation as the output. The light source serves two purposes: driving the solar panel to produce electricity for electron supply and activating intracellular GR in the cathode chamber to generate ATP (Suppl Fig. S3.11).

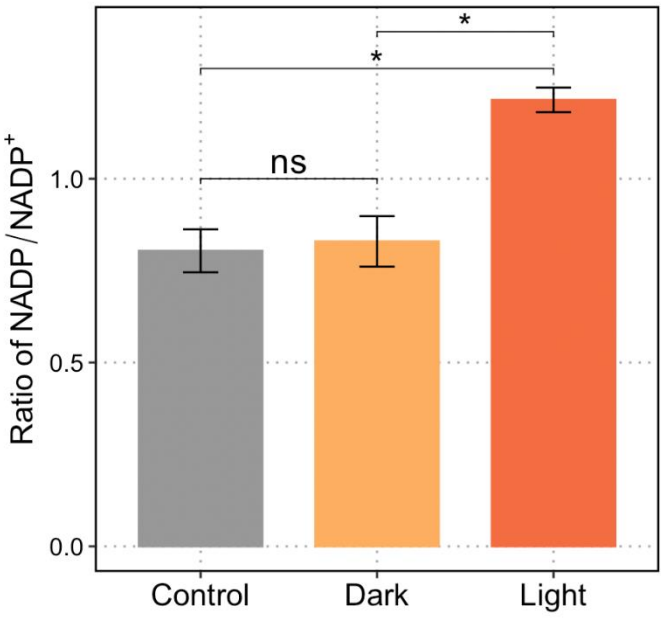


Figure 3.4. The intracellular NADPH/$NADP^+$ ratios of *R. eutropha* H16 with pLO11a-blhDxrCRT-GR in different conditions. Independent t tests were performed: *$P < 0.05$. Data show means ± SD, n = 3. The NADPH/$NADP^+$ ratio in the light was higher than that in the dark or a day-0 control.

Rather than using formate, a carbon cloth electrode can also be directly used as the electron donor for CO_2 fixation which requires an electron shuttle to transfer electrons from the cathode to the cells. We used riboflavin-mediated electron transfer from an electrode in a bioreactor with CO_2 as the sole source of carbon. Riboflavin (−400 mV vs Ag/AgCl) is a common electron shuttling molecule used in microbial electrochemical systems (155-157). For some electroactive species, riboflavin interacts with cytochrome c and can transfer electrons from bacteria to an electrode (158); the reverse process however, is thermodynamically unfavourable (91). Interestingly we found that in this system riboflavin is able to transfer electrons from the cathode to bacterial cells when a light-driven proton pump (such as the GR) is present to overcome the energy hurdle. A microbial photoelectrochemical system was set up to confirm that GR-expressing cells are able to generate reducing equivalent from electrode-supplied electrons in the presence of riboflavin and light. In the light, the NADPH/$NADP^+$ ratio significantly increased compared to a control group and a dark group (Figure 3.4), indicating that NADPH can be synthesised in the absence of organic electron donors. Figure 3.5 illustrates the electron transport chain for the reductive fixation of CO_2, which operates by reversing electron flow from the quinol pool to NADH dehydrogenase. In this electron transport chain, a proton-translocating transhydrogenase is required, which couples the reduction of $NADP^+$ by NADH to the inward translocation of protons across the cytoplasmic membrane (154, 159). Thus, the transmembrane proton gradient created by the light-driven turnovers of GR enables electron shuttling via riboflavin, leading to NADPH formation and ATP production by the ATP synthase (Figure 3.5).

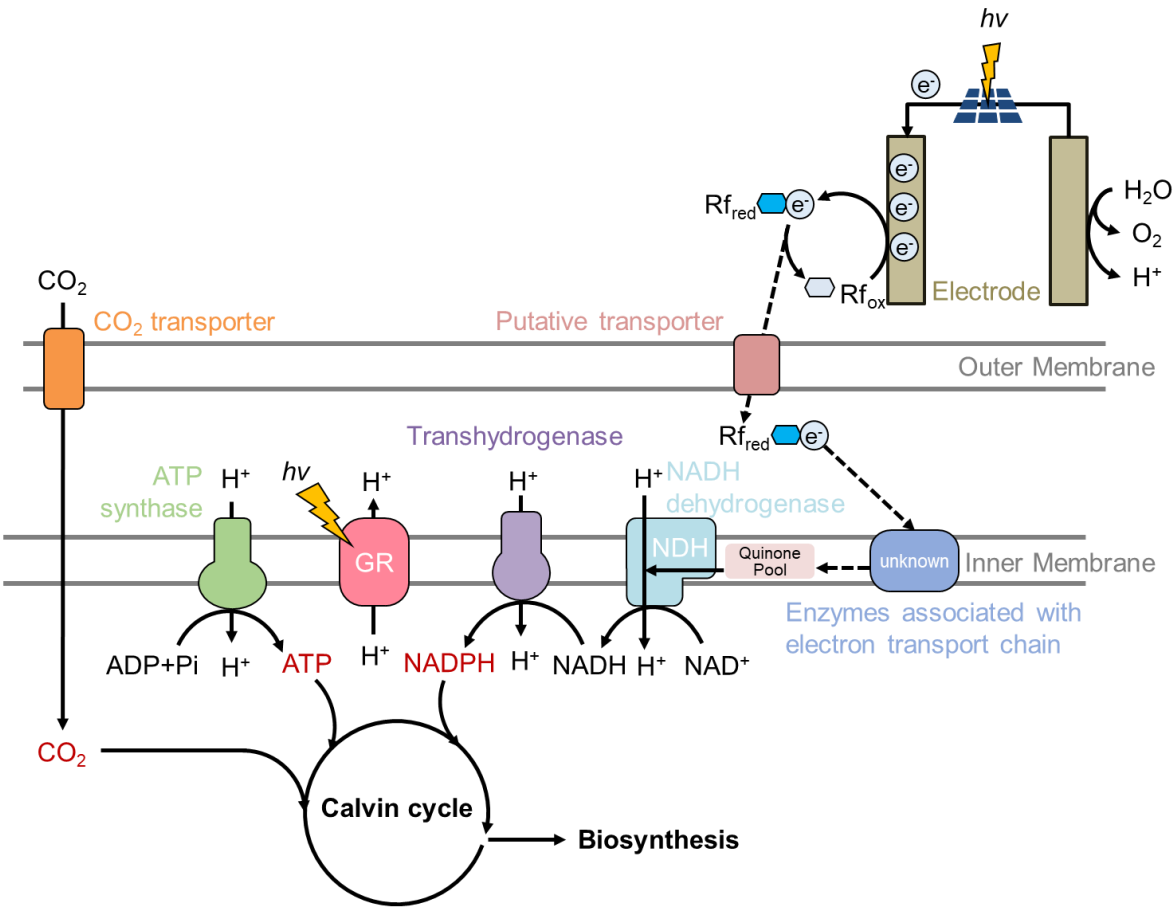


Figure 3.5. Photoelectrochemical CO_2 fixation bioreactor system. A light source generates electricity, and electrons are transferred from electrode to cells mediated by riboflavin. The light activated GR system with a complete redox loop can drive autotrophic growth of bacteria via light-driven ATP synthesis. NADH is generated by an electron transfer from the quinol pool to NAD^+ and is then converted into NADPH catalysed by membrane-bound transhydrogenase. The mechanism by which riboflavin transfer electrons to *R. eutropha* is unclear and is represented by a dashed line.

The reversible redox reactions of riboflavin were used to shuttle electrons from the electrode to the cell. We used cyclic voltammetry (CV) to verify these redox reactions at the electrode, which was made from carbon cloth. The cyclic voltammogram in Figure 3.6A shows typical oxidative and reductive peaks, indicating the suitability of the electrode material, and yielding a midpoint potential for riboflavin of –0.39 V versus an Ag/AgCl standard electrode (Figure 3.6A). It also shows that when carbon cloth is used as the cathode electrode without riboflavin, it could not transfer electrons.

We used the bioreactor to demonstrate that *R. eutropha*-GR could perform photoautotrophic growth in the presence of the cathode at the potential of –0.6 V vs. Ag/AgCl, driven by light-activated GR and in the absence of formate (Figure 3.6B). Several negative controls show there was no detectable growth in the dark, even though

the electrode potential, riboflavin and GR were available, nor in uninduced cells lacking GR but with riboflavin and the electrode potential (Figure 3.6B), nor in the absence of riboflavin (Figure 3.6B). Although *R. eutropha* is able to use H_2 as an energy source and will grow in its presence the lack of cell growth in the negative controls should rule out the possibility of H_2 generation from the cathode. Electrosynthesis of H_2 requires a sufficient voltage potential, but the potential of the cathode (–0.6 V vs. Ag/AgCl) in this study is insufficient for carbon cloth without coating catalysts to produce H_2.

Autotrophic growth of *R. eutropha*-GR in the bioreactor was assessed using cell counts (Figure 3.6C) and verified by isotope labelling with $^{13}CO_2$ as the sole carbon source for 4 days (Figure 3.6C). SCRS was used to analyse 200 single cells of *R. eutropha*-GR, which revealed multiple Raman shifts arising from integration of $^{13}CO_2$ into cellular biomass. Raman bands corresponding to cytochrome *c* at 748 (pyrrole breathing mode) and 1127 cm^{-1} (CN stretching vibrations), and a band arising from proteins at 1655 cm^{-1} (Amide I), shifted to 728, 1113, and 1623 cm^{-1}, respectively (Figure 3.6C). SCRS was also used to quantify the number of GR-containing bacterial cells from the bioreactor (Suppl Fig. S3.9), which showed no significant change after 4 days (Figure 3.6D), reflecting a likely selective advantage conferred by GR, despite the absence of antibiotics.

The overall voltage to drive photo-electrosynthetic growth of *R. eutropha*-GR in the bioreactor was 1.6-1.8 V. The corresponding light intensity on the solar panel was only 2 µmol m^{-2} s^{-2} (Suppl Fig. S3.12), suggesting the bioreactor could operate in weak daylight. During the exponential growth phase (day 3-4 in Figure 3.6C), the maximal electron conversion efficiency from electricity to biomass was 20.4%.

Collectively, the results suggest that *R. eutropha*-GR can utilise light as an energy source to drive the CO_2 fixation pathway for cell growth, in effect converting *R. eutropha* from chemolithoautotrophy to a new growth mode that is a hybrid form of photoautotrophy that could be termed photoelectroautrophy.

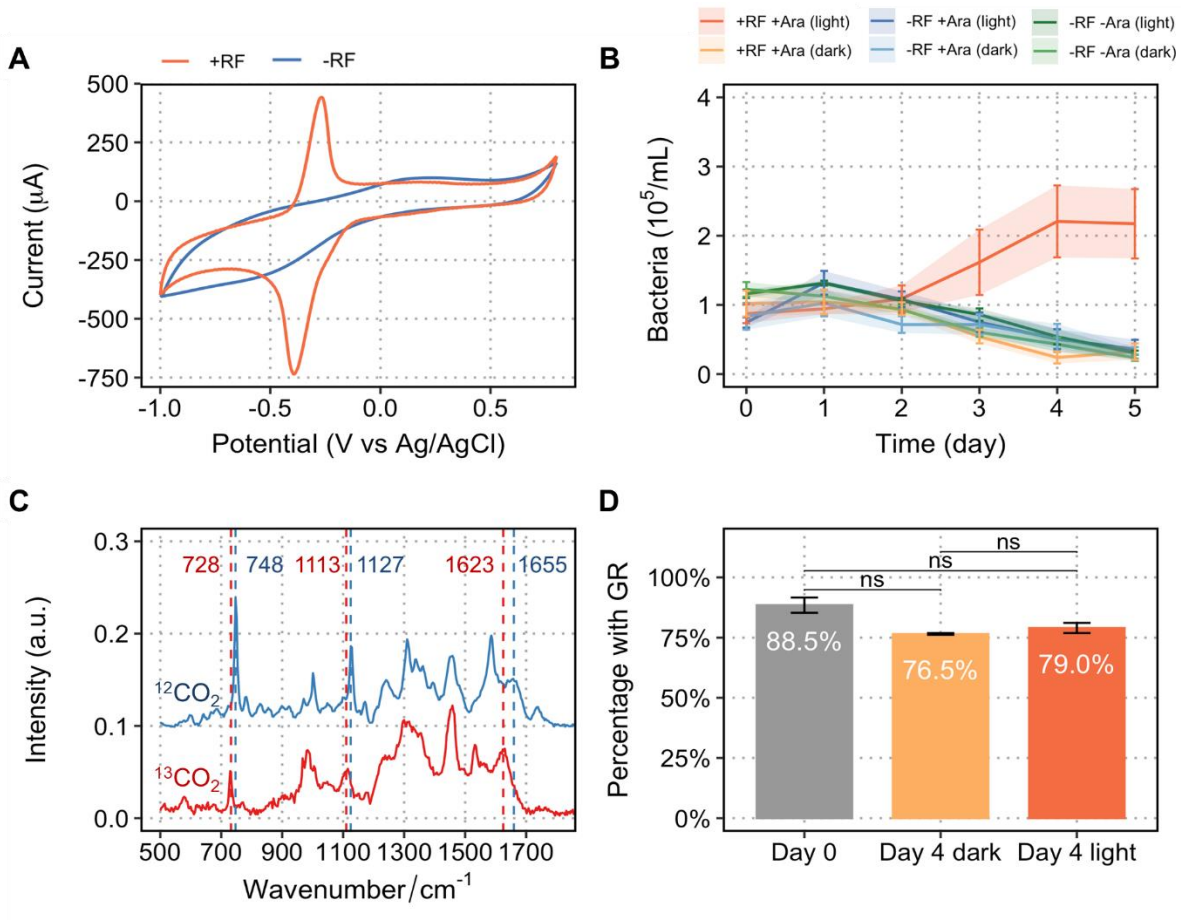


Figure 3.6. (A) Cyclic voltammetry (CV) analysis of the abiotic electrochemical system with or without 50 μM riboflavin (RF) using carbon cloth as the working electrode. CVs were conducted with a scan rate of 0.05 V/s within a potential range between -1.0 V and 0.8 V versus Ag/AgCl electrode. (B) Growth of engineered *R. eutropha*-GR with CO_2 as the sole carbon source, driven by light-activated GR and electricity (data show means ± SD, n = 3). (C) SCRS of cells of photoelectroautrophic *R. eutropha*-GR grown on ^{12}C-CO_2 (blue) and ^{13}C-CO_2 (red). Cells grown on ^{13}C-CO_2 exhibited isotopic Raman shifts from 1655 to 1623 cm^{-1} (Amide I of proteins), 1127 to 1113 cm^{-1} (cytochrome *c*), and 748 to 728 cm^{-1} (cytochrome *c*). (D) Bar chart showing the percentage of *R. eutropha*-GR cells that maintained high levels of GR after 4 days incubation in the light and dark, without antibiotic selection pressure.

3.4 Discussion

The results of this study confirm that *R. eutropha*-GR can be engineered to grow autotrophically, using light to supply energy for GR to pump protons and for riboflavin to mediate electron transfers (Figure 3.5C). Thus, *R. eutropha* has been engineered to perform a type of hybrid photosynthesis, in which GR acts as a light-driven proton pump. The study supports the assumption that the proton gradient from GR was able to reverse the NADH dehydrogenase activity to make NADH from NAD^+. PR-driven NADH dehydrogenase reversion has previously been reported in *Shewanella oneidensis* MR-1 (124) and in this study, we show that it can also occur in *R. eutropha*.

The resulting proton motive force drives the transhydrogenase that forms NADPH, used for reductive fixation of CO_2, as well as driving ATP synthase to produce ATP. Electrons required for the reductive assimilation of CO_2 using the native Calvin-Benson-Bassham (CBB) cycle can be provided by either an electrode (mediated by riboflavin) or an organic compound such as formate (Figure 3.1). Accordingly, biomass production in the light can be enhanced by 20% when formate is used as the electron donor (Figure 3.3A), but biomass can also be produced in a bioreactor with a CO_2 carbon supply and a light source as the only inputs (Figure 3.6B). The biomass of *R. eutropha* H16 is a good source of single-cell protein for animal feed due to its high protein content, and it has been awarded a qualified presumption of safety (QPS) in the EU (160, 161).

The results show that riboflavin can mediate electron transfer between cells and the electrode. Although the mechanism of riboflavin delivering the electrons to the electron transport chain is still unknown, we have shown that riboflavin is able to serve as an electron shuttling molecule to transfer electrons between *R. eutropha* and an electrode (Figure 3.6). We speculate that *R. eutropha* has a putative transporter for riboflavin-like molecules to enable riboflavin to pass through the outer membrane allowing riboflavin to be oxidised by enzymes that could be associated with the electron transport chain. A series of enzymes involved in the electron transport chain have been reported relevant to electron shuttle-mediated electron transfer of *R. eutropha*. The hydrogenase in *R. eutropha* is able to interact reversibly with electron shuttles such as flavin (162). The nitrate respiration chain was also upregulated in the presence of an electron mediator (163).

The conversion of *R. eutropha* H16 from chemolithoautotrophy to a hybrid form of photoautotrophy has required the introduction of β-carotene biosynthesis, via the insertion of a four-gene biosynthetic pathway and overexpression of the *dxr* gene, and its subsequent conversion into retinal by adding a gene encoding β-carotene 15 15'-dioxygenase. The introduction of the gene encoding the GR creates a photosynthetic system built from a single rhodopsin protein, compared to one that relies on a series of chlorophyll protein complexes. As GR has a pKa=~4.8 (164), compared to PR which has a pKa=~7.5 (165), GR is functional at a lower pH, a situation often found in *R. eutropha* H16 growing using formate or CO_2 as the sole carbon source. GR is originally from thylakoid-less *Gloeobacter violaceus* PCC7421 (166), its high efficiency of

proton pumping and rapid photocycle is probably to compensate for its reduced energy generation as compared to that from chlorophyll-based photosynthesis (143). It has been reported that GR expression in *E. coli* has increased biomass growth in the light (75) and GR also has a higher molecular proton pumping rate than PR (167). However, the excess energy resulting from GR activity could also lead to the overproduction of reactive oxygen species (ROS). It has been reported that GR-expressing *E. coli* showed elevated energy (i.e. ATP) levels but also increased ROS under aerobic conditions, resulting in a slower growth rate (148). Therefore, in this study, micro-aerobic conditions were used for the growth experiments. In the microbial photoelectrochemical system, oxygen limitation is an even more critical factor when taking into account both the ROS associated with the GR function and the cathode-derived ROS (139). As a result, the cathode chamber was only bubbled with CO_2 to create anoxic conditions, which will limit both biomass growth and retinal production from β-carotene as the 15,15'-dioxygenase enzyme requires oxygen. In addition, riboflavin could be another limiting factor for biomass growth, possibly because of the low electron delivery rates directed from riboflavin to *R. eutropha* cells. Despite the low biomass growth rate, this study is the first proof of concept for rhodopsin-based photoelectrosynthesis.

In this study, we demonstrate that we can design a light-dependent electron transfer chain to drive photo-electrosynthesis using a rhodopsin-based system. Such a system only requires a rhodopsin and an electron mediator such as riboflavin. Microbial rhodopsin is a simple light-driven proton pump found broadly distributed in nature (3), and it can also be easily engineered into different bacterial hosts (57, 63). Furthermore, GR has been shown to combine with other retinal analogues to absorb near-infrared light (850-950 nm) (168), which can significantly extend the light-harvesting spectrum and maximise energy harvesting per surface area (169). The recyclable electron mediator riboflavin can be readily synthesised by bacteria (170) or manually added into the reactor. Hence, the application of such a rhodopsin-based light-harvesting system would enable the conversion of various naturally heterotrophic bacteria into photoautotrophs that are able to use light for CO_2 fixation. In natural oxygenic photosynthesis, a chlorophyll-based photosystem splits water and provides electrons to the redox reaction. The hybrid photoelectro-autotrophic system shown here mimics photosynthesis using GR to generate a proton gradient and electricity as the electron

donor. The result is that a new mode of photosynthetic growth has been engineered, enabling *R. eutropha* H16 to use solar energy to convert CO_2 into biomass.

3.5 Materials and methods

3.5.1 Bacterial strains and culture conditions

E. coli strains were grown in LB broth at 37 °C under aeration by shaking at 200 rpm. *R. eutropha* strains were grown in LB broth at 30 °C under aeration by shaking at 150 rpm. If required, antibiotics (Sigma-Aldrich) were added as follows: 10 μg ml^{-1} gentamicin, 10 μg ml^{-1} tetracycline, 400 μg ml^{-1} kanamycin and 500 μg ml^{-1} ampicillin for *R. eutropha*; 12.5 μg ml^{-1} tetracycline and 50 μg ml^{-1} kanamycin for *E. coli*. Induction of strains transformed with the pLO11a expression vector containing the arabinose-inducible P_{BAD} promoter was carried out by growth to log phase and the addition of 0.1% (w/v) L-arabinose (Sigma-Aldrich) and overnight growth at 30 °C for *R. eutropha* and 0.2% (w/v) L-arabinose and overnight growth at 37 °C for *E. coli*. Where required, induction of GR expression was accompanied by the addition of exogenous *trans*-retinal (Sigma-Aldrich) to a final concentration of 5 μg ml^{-1}.

All constructs were assembled and expressed in a commercially obtained, chemically competent *E. coli* JM109 strain (Promega, UK). Two gentamicin-resistant *R. eutropha* strains, namely H16 (ATCC 17699) and its derivative strain RHM5 (gift from Min-Kyu Oh, Korea University, South Korea; hereafter H16Δ*pha*) in which the *phaCAB* operon encoding the genes required for the conversion of acetyl-CoA to polyhydroxybutyrate (PHB) have been deleted (171), were used for expression of constructs. Recombinant plasmids were transformed into the *E. coli* S17-1 strain (172), made chemically competent using standard techniques (173). For conjugative plasmid transfer into *R. eutropha*. 1 ml overnight culture pellets of *E. coli* S17-1 and *R. eutropha* were mixed together in 100 μl LB media and spot dried onto a Luria-Bertani (LB)-agar plate, left overnight at 30°C and streaked to single colonies on a LB-agar plate containing gentamicin and appropriate selection antibiotics.

3.5.2 Plasmid construction

Common cloning procedures were performed according to standard protocols (173). Polymerase chain reaction (PCR) was carried out using Q5 DNA polymerase (NEB, UK) and synthesised primers (Sigma-Aldrich) according to the manufacturer's

instructions, and all PCR products were checked by DNA sequencing (Eurofins, Germany). A list of the plasmids and primers used in this study are shown in Table 1 and Suppl Table S3.2 respectively and details of plasmid construction are given in Supporting Information.

3.5.3 Single-cell Raman spectra (SCRS) measurements and analysis

Bacterial cells were washed three times with distilled water to remove traces of the culture medium prior to measurements. Samples were diluted until individual bacterial cells could be observed under a 100×/0.75 microscope and a 1.5 µl suspension was dropped onto an aluminium-coated slide and air dried. SCRS were obtained using a 532-nm neodymium-yttrium aluminium garnet laser with a 300 grooves mm^{-1} diffraction grating (LabRAM HR Evolution, HORIBA, UK) and were acquired in the range of 100–3200 cm^{-1}. The laser power was set at ~30 mW which was attenuated by neutral density (ND) filters before focusing onto the samples. For the measurements of the *Gloeobacter violaceus* PCC7421 rhodopsin complexes, 1% power filter and 1-second acquisition time were used; the low power and short acquisition time were used to prevent photobleaching of the chromophores. Each condition was measured with two biological replicates; each replicate was measured with more than 150 and 100 single cells in induced and uninduced samples, respectively, or 200 and 400 single cells before and after growth, respectively, under microaerobic conditions. Cells with GR complexes were identified by a band at ~1530 cm^{-1}. Intracellular polyhydroxybutyrate (PHB) was identified and quantified by the band at 1735 cm^{-1} (150). Raman bands at 748 (pyrrole breathing mode), 1128 (υ(CN) stretching vibrations), 1312 (δ (CH) deformations) and 1584 cm^{-1} (υ (CC) skeletal stretches) were used for quantifying the resonance Raman spectrum of cytochrome c, of which the vibrational modes with the porphyrin π-π* transitions are in resonance with the incident Raman laser at 532 nm, thereby greatly enhancing the signals (150, 174). As in the measurements for determining utilisation of formate, bicarbonate and carbon dioxide, 25% power filter and 3 to 5-second acquisition time were used to acquire spectra with high signal-to-noise ratios. Each condition was measured with two to three biological replicates, each with more than 30 to 50 single cells acquired. Spectra were recorded with LABSPEC 6 software (HORIBA, UK). All raw spectra were pre-processed by cosmic ray correction, polyline baseline fitting and subtraction and vector normalisation of the entire spectral

region. Quantification of biomolecules was done by integrating the area of the corresponding Raman bands. All analysis and plotting were done under a R 4.0.0 environment.

3.5.4 Growth of *R. eutropha* strains under light and dark

Growth characterization experiments of *R. eutropha* with pLO11a-blhDxrCRT-GR were conducted under light and dark conditions, with and without induction, respectively. Before the experiments, *R. eutropha* strains harbouring the plasmid were pre-cultivated overnight in tryptic soy broth (TSB) medium (17 g/L casein peptone, 2.5 g/L dipotassium hydrogen phosphate, 2.5 g/L glucose, 5 g/L sodium chloride, 3 g/L soya peptone) with 10 µg/ml of tetracycline, 5 µg/ml of *trans*-retinal and 0.2% (w/v) L-arabinose at 30 °C under aeration by shaking at 150 rpm. After TSB preculture, cells were harvested by centrifugation at 3000 g for 5 min. The supernatant was discarded, and cells were washed three times with a minimal medium (MM: 6.74 g/L $Na_2HPO_4 \cdot 7H_2O$, 1.5 g/L KH_2PO_4, 1.0 g/L $(NH_4)_2SO_4$, 1 mg/L $CaSO_4 \cdot 2H_2O$, 80 mg/L $MgSO_4 \cdot 7H_2O$, 0.56 mg/L $NiSO_4 \cdot 7H_2O$, 0.4 mg/L ferric citrate, 200 mg/L $NaHCO_3$, and pH 7.0) (91). Cells were grown under eight different conditions: MM with and without 80 mM formate in normal aerobic and micro-aerobic environments; MM containing 0.2% (w/v) L-arabinose as the inducer, with and without formate in micro-aerobic environment which were created in 15 mL tubes filled with 12 mL medium. Neither antibiotics nor exogenous *trans*-retinal was added in any of these conditions. Each growth condition was illuminated with a white LED light (~50 µmol/s/m^2) and dark wrapped in foil. In total, 6 growth conditions were analysed with each condition having three replicates. Cells were initially resuspended in the MM to a final optical density (OD) of ~0.01 and grown at 30 °C with shaking at 150 rpm.

3.5.5 Bicarbonate utilisation in *R. eutropha* growth

R. eutropha with pLO11a-blhDxrCRT-GR was grown in MM containing 0.2% (w/v) L-arabinose micro-aerobically, using 40-mM formate and 40-mM bicarbonate as carbon sources. In order to investigate inorganic carbon fixation and the impact of bicarbonate utilisation on biomass synthesis, ^{13}C isotope-labelled formate and bicarbonate were used for growth experiments under the following isotopic conditions: (i) ^{12}C-formate + ^{12}C-bicarbonate; (ii) ^{13}C-formate +^{12}C-bicarbonate; and (iii) ^{12}C-formate + ^{13}C-bicarbonate. Each experiment was carried out under light or dark

conditions, and no antibiotics were added. Single cell Raman spectroscopic measurements were carried out for the isotopic analysis.

3.5.6 Microbial photoelectrochemical system apparatus

A dual-chamber bioreactor (70 mL for each chamber) separated by a Nafion membrane (only allowing proton transfer) was used as a bio-photoelectrochemical system for microbial growth experiments. For the anode chamber, carbon cloth (H23, 95 g m^{-2}; 2.5 × 4.0 cm^2; Quintech, Gloucestershire, UK) with a platinum catalyst (1 mg cm^{-2}, PtC 60%; FuelCellStore) was used as the counter electrode. For the cathode chamber, the working electrode was made of 3.0 × 3.0 cm^2 carbon cloth and an Ag/AgCl reference electrode (3M KCl, RE-5B, BASi, USA) was installed for measuring the potentials. MM medium (as above) was added in both chambers. For the test of reducing power generation from electrode-supplied electrons, *R. eutropha* with pLO11a-blhDxrCRT-GR was grown overnight in MM medium with 80 mM formate, and the culture cells were collected and washed as above with the MM medium to give an initial OD_{600} of ~0.1 before being injected into the cathode chamber. An electron shuttle (50 μM riboflavin) was then added to the chamber as the electron mediator. A polycrystalline solar panel (1.5W, 140 mm×180 mm, RS, UK) was used to generate electricity powered by light. Photovoltaic characterisation of the solar panel is shown in Suppl Fig. S3.11. The potential of the working electrode was controlled by a designed potentiostat. In the experiments, the potential was kept at –0.6 V [versus Ag/AgCl]. The cathode chamber was first bubbled with N_2 to remove oxygen, and then illuminated with white LED light (~50 μmol/s/m^2), operated at 30 °C, and agitated at 150 rpm. Cells were maintained overnight and collected for measurement of NADPH levels using a $NADP^+$/NADPH quantification kit (Sigma-Aldrich) The $NADP_{total}$ and NADPH were extracted and quantified according to the manufacturer's protocol. The amount of NADP+ was calculated by the difference between $NADP_{total}$ and NADPH, and then the NADPH/$NADP^+$ ratio was obtained. Suppl Fig. S3.10 showed the calibration curve between NADPH amount and absorbance at 450 nm.

For the test of light-driven autotrophic growth, *R. eutropha* with pLO11a-blhDxrCRT-GR was grown overnight in TSB and pretreated as above with the MM medium to give an initial OD_{600} of ~0.01 before being injected into the cathode chamber. The cathode chamber was bubbled with CO_2 at a flow rate of 20 mL/min, illuminated with white

LED light (~50 μmol/s/m^2), operated at 30 °C, and agitated at 150 rpm. Pictures of microbial photoelectrochemical system apparatus can be found in Suppl Fig. S3.11.

The electron transfer efficiency of the biomass formation could be calculated by the equation,

$$\eta = \frac{nzF}{\text{Charge passed (C)}} \qquad (1)$$

where n is the amount of biomass (using classic formula $CH_{1.4}N_{0.2}O_{0.4}$) product (mol), z is the number of transferred electrons (z = 4 for CO_2 conversion to $CH_{1.4}N_{0.2}O_{0.4}$), F is the Faraday constant (96,485 C/mol). The average current is calculated by dividing time into charges. In the solar panel system with riboflavin, the average electricity current was −11.2 μA under stable operation in the presence of GR-expressing cells, and −9.7 μA in the presence of cells without induction.

3.5.7 Counting colony forming units (CFU) to measure the concentration of viable cells in the cathode chamber

The viable cells in the cathode chamber consist of the cells on the electrode and in the supernatant. For the counting of the cells attached on the electrode, the carbon cloth electrode was placed in a 50 ml test tube containing 5 ml of 0.9% sterile NaCl solution and vortexed for 2 min. A series of diluted solutions were spread onto LB agar plates, which were then incubated at 30 °C for 48 h. CFU was counted to estimate the total number of viable cells on the electrode. For the counting of the cells in the supernatant, 1 mL of mixture was collected from the cathode chamber and a series of diluted solutions were spread onto LB agar plates, which were then incubated at 30 °C for 48 h prior to CFU counting. In this way, the total number of viable cells in the cathode chamber (cells on the electrode plus cells in the supernatant) was calculated and then divided by the working volume to estimate the concentration of viable cells.

Data Availability Statement: All data discussed in the paper will be made available to readers.

Author contributions: W.E.H conceived original idea; W.T., P.A.D., C.N.H. and W.E.H. designed research; W.T., P.A.D. and J.X. performed research; S.D.V. and I.P.T.

contributed new reagents/analytic tools; W.T., P.A.D. and J.X. and W.E.H. analysed data; and W.T., P.A.D., C.N.H. and W.E.H. drafted the manuscript. All authors revised the manuscript.

Conflict of interest statement: The authors declare no competing financial interest.

Acknowledgements

W.E.H. thanks EPSRC (EP/M002403/1 and EP/N009746/1) for support. P.A.D., W.E.H., and C.N.H. gratefully acknowledge funding (BB/M000265/1) from the Biotechnology and Biological Sciences Research Council (United Kingdom). P.A.D. and C.N.H. are supported by European Research Council Synergy Award 854126. The authors thank Dr. Craig McGregor-Chatwin and Dr. Andrew Hitchcock for technical assistance. We thank Prof Kwang-Hwan Jung at Sogang University for providing plasmids of beta-carotene and GR and had helpful discussions. We also thank Oliver Lenz, Technische Universität Berlin Germany, for providing plasmid pLO11a and *Ralstonia eutropha* wild-type strain.

Chapter 3 Supplementary Information

ACS SyntheticBiology

Engineering a Rhodopsin-Based Photo-Electrosynthetic System in Bacteria for CO_2 Fixation

Paul A. Davison [a#], Weiming Tu [b#] Jiabao Xu [b], Simona Della Valle [b], Ian P. Thompson [b], C. Neil Hunter [a] and Wei E. Huang [b*]

[a] Plants, Photosynthesis and Soil, School of Biosciences, University of Sheffield, Sheffield S10 2TN, United Kingdom.

[b] Department of Engineering Science, University of Oxford, Oxford OX1 3PJ, United Kingdom.

[*]Corresponding author: Department of Engineering Science, University of Oxford, Parks Road, OX1 3PJ, Oxford, United Kingdom. Email wei.huang@eng.ox.ac.uk Tel: +44 1865 283786.

[#] P.A.D and W.T. contributed **equally** to this work.

Chapter adapted from publication: ***ACS Synthetic Biology*** (2022)

DOI: 10.1021/acssynbio.2c00397

Materials and methods

Plasmid construction

The detailed information about primers used in this study is shown in Supplementary Table S3.2.

A modified version of the pLO11 (Tc^r, RK2 *ori*, Mob^+) vector specifically designed for expression in *R. eutropha* (175), with the acetoin promoter replaced by the *araC* gene and the arabinose inducible P_{BAD} promoter (henceforth called 'pLO11a') was used for the expression of heterologous genes (gift from Oliver Lenz, Technische Universität Berlin, Germany).

The *crtY* and *crtI* genes were isolated by PCR as a single fragment from the pRER1B plasmid that contains the *crtY* and *crtI* genes from *Erwinia herbicola* (*Pantoea agglomerans)* (176) using the primers CrtYI_F and CrtYI_R and cloned into the *Nco*I-*Hin*dIII sites of pLO11a to create pLO11a-CrtYI.

The *Erwinia uredovora* (*Pantoea ananatis) crtEXYIB* operon responsible for conversion of GGPP to β-carotene in *E. coli*, including the 879 bp upstream region required for constitutive β-carotene expression, was isolated by PCR as a single fragment from the pORANGE (141) plasmid (gift from Kwang-Hwan Jung, Sogang University, S.Korea) using the primers CRT_F and CRT_R and cloned into the *Sac*I-*Bgl*II sites of pLO11a to create pLO11a-CRT.

The *dxr* gene from *R. eutropha* (GenBank: CP039287.1) was synthesised (Integrated DNA Technologies, USA) and isolated by PCR using the primers SacDxr_F and SacDxr_R and cloned into the *Sac*I site of the pLO11a-CRT plasmid to create plasmid pLO11a-DxrCRT. It was also isolated by PCR using the primers NcoDxr_F and HindDxr_R and cloned into the *Nco*I-*Hind*III sites of pLO11a to create pLO11a-Dxr.

The gene encoding the *Gloeobacter violaceus* PCC7421 rhodopsin, GR, (gift from Kwang Hwan-Lung, Sogang University, S.Korea; Genbank: BA000045) was isolated by PCR using the primer pair GR_F and GR_R and cloned into the *Nco*I and *Bgl*II sites of pLO11a.

The β-carotene 15, 15'-dioxygenase gene (*blh*) from the uncultured marine bacterium 66A03 (GenBank: DQ065755.1) previously shown to produce retinal in *E. coli* (145) was codon optimised for *R. eutropha* and synthesised (Integrated DNA Technologies,

USA) flanked by *Nco*I-*Hind*III sites and cloned into pLO11a to create pLO11a-blh. The *blh* gene with an upstream ribosome binding site was created by PCR from pLO11a-blh using primers Rbsblh_F and LOterm_R and inserted into the *Hind*III site of pLO11a-Dxr to create pLO11a-Dxr-blh. The *dxr-blh* operon was created by PCR from pLO11a-Dxr-blh using primers Dxr_F and Blh_R and inserted into the *Hind*III site of pLO11a-CRT to create pLO11a-blhDxrCRT. The *GR* gene with its own P_{BAD} promoter was created by PCR from pLO11a-GR using primers pBAD_F and LOterm_R and inserted into the *Eco*RI site of pLO11a-blhDxrCRT to create pLO11a-blhDxrCRT-GR.

Carotenoid extraction and analysis

Strains transformed with the pLO11aa expression vector constructs were grown in 50ml LB with 12.5 µg ml^{-1} tetracycline to log phase and either induced with 0.1% (w/v) L-arabinose (Sigma-Aldrich) and overnight growth at 30 °C for *R. eutropha* or 0.2% (w/v) L-arabinose and overnight growth at 37 °C for *E. coli*. Carotenoids were solvent extracted from the 50ml cell culture pellets with 1 ml of 7:2 acetone:methanol (v/v), clarified by centrifugation and an absorption spectrum taken using an Agilent Cary 60 UV-Vis spectrophotometer. For more detailed analysis the solvent extract was dried down under nitrogen, re-dissolved in methanol and carotenoids separated by reversed-phase HPLC on an Agilent 1100 HPLC system using a Supelco Discovery HS C18 column as previously described (177). Elution of β-carotene and retinal were monitored at 450 nm and 380 nm respectively. An all-*trans*-β-carotene standard (Sigma-Aldrich) of known concentration was used for the quantification of integrated peak areas. A pure all-*trans*-retinal standard (Sigma-Aldrich) was used to assign the retinal peak.

Membrane purification

A 20 ml LB overnight culture with appropriate antibiotic selection of *R. eutropha* was used to inoculate 500 ml LB with selection in a 2.5 L conical flask. This was grown at 150 rpm and 30ºC to OD_{600} = 0.5 - 07, induced with 0.1% (w/v) L-arabinose and 5 µg ml^{-1} all-*trans*-retinal and grown overnight at 30ºC. The culture was pelleted and resuspended in approximately 10 ml of buffer A (25 ml K_2HPO_4/KH_2PO_4 pH 7.4) and lysed by two cycles of French pressing at a pressure of 18 000 psi. Membrane fractions were isolated on a 10-50% continuous sucrose gradient (the sucrose was made up in buffer A and 1.5 ml broken cells loaded per gradient) spun at 30,000 rpm for 2 hours at 4°C. A 1 ml membrane fraction was removed, and an absorption spectrum was taken

using an Agilent Cary 60 UV-Vis spectrophotometer.

PHB accumulation from formate in the light and dark

The engineered *R. eutropha* precultured in TSB with 100 µg/mL kanamycin was centrifuged and washed three times with a nitrogen-limited minimal medium (3.57 g/L Na_2HPO_4, 1.5 g/L KH_2PO_4, 0.1 g/L $(NH_4)_2SO_4$, 0.08 g/L $MgSO_4 \cdot 7H_2O$, 0.2 g/L $NaHCO_3$, 1 mg/L $CaSO_4 \cdot 2H_2O$, 0.56 mg/L $NiSO_4 \cdot 7H_2O$, 0.4 mg/L ferric citrate, and pH 7.0) to remove TSB medium. Subsequently, the cell pellet was resuspended in the nitrogen-limited minimal medium, and the OD was adjusted to 1 before being transferred into flasks with a total volume of 250 mL. Formate (80 mM) was added into baffled flasks with a working volume of 200 mL for micro-aerobic PHB synthesis. The flasks were illuminated with a white LED light (~50 µmol/s/m^2) and dark wrapped in foil. Unless otherwise stated, all cultures were grown at 30 °C and 150 rpm.

Results

Identification of genes for beta-carotene synthesis in *R. eutropha* H16

Analysis of the KEGG pathway for *R. eutropha* H16 (*Cupriavidus nectar* H16; https://www.genome.jp/kegg-bin/show_pathway?reh00906) shows that it contains homologues of *crtE* and *crtB* (Genbank accession numbers CAJ92601.1 and CAJ93812.1 respectively) but not *crtI* and *crtY*. To see whether these homologous *crtE* and *crtB* genes were functional, and their products could be combined with exogenous CrtY and CrtI enzymes to make β-carotene, the *crtY* and *crtI* genes were isolated as one fragment by PCR from the *crt* operon of *Erwinia herbicola*, where they are situated adjacent to each other in the *crt* operon, and inserted into the modified pLO11 (Tc^r, RK2 *ori*, Mob^+) vector containing the arabinose inducible P_{BAD} promoter (pLO11a) specifically designed for expression in *R. eutropha* (175). This plasmid pLO11a-CrtYI (Table 3.1) was transformed into wild-type *R. eutropha* H16 by conjugation, the subsequent strain grown to log phase in LB with 12.5 µg ml^{-1} tetracycline, grown overnight in the presence and absence of arabinose and the cell pellets subjected to solvent extraction and HPLC analysis. No β-carotene could be detected by HPLC in either the negative control consisting of *R. eutropha* H16 transformed with the empty

pLO11a vector or the strain containing pLO11a-CrtYI in either the absence or presence of arabinose (results not shown). This suggests that the native *crtE* and *crtB* genes in *R. eutropha* H16 are not functional in the β-carotene biosynthetic pathway.

The pORANGE plasmid, which gives constitutive β-carotene expression in *E. coli* JM109 (141), was used in attempts to synthesise this carotenoid in *R. eutropha* H16. DNA sequencing revealed that this plasmid encodes the carotenoid biosynthesis gene cluster (*crtE*, *crtX*, *crtY*, *crtI*, *crtB;* the *crtX* gene encodes the zeaxanthin glucosyltransferase enzyme which is not involved in β-carotene synthesis) from *Pantoea ananatis* (*Erwinia uredovora*) and an 879 bp region upstream of *crtE* that contains the putative 240 bp promoter region (Genbank: D90087) required for constitutive expression of this operon in *E. coli* JM109. The entire *crtEXYIB* operon, including the *crtE* promoter region (*crt* operon), was isolated by PCR from pORANGE and cloned into the pLO11a expression plasmid to create pLO11a-CRT (designated pCRT; plasmid map shown in Suppl Fig. S1A).

Overexpression of the *dxr* gene in *R. eutropha* enhanced β-carotene production

Isopentenyl diphosphate (IPP) is the common, five-carbon building block in the biosynthesis of all carotenoids with the second reaction in its synthesis being the reduction of 1-deoxy-D-xylulose 5-phosphate (DXP) to 2-C-methyl-D-erythritol-4-phosphate, catalysed by DXP reductoisomerase and encoded by *dxr* (Fig. 3.2A). Overexpression of the *Synechocystis dxr* gene in tobacco and the maize *dxr* gene in *Zea mays* has been shown to increase carotenoid content in tobacco and maize plants (178, 179). In order to try and increase the levels of β-carotene in *R. eutropha* H16 an attempt was made to overexpress the native *dxr* gene that encodes DXP reductoisomerase (EC:1.1.1.267), the homologue of *E. coli dxr*, in conjunction with the *crt* operon. The *dxr* gene was synthesised and cloned into the pLO11a-CRT plasmid to create plasmid pLO11a-Dxr-CRT (designated pDxrCRT; plasmid map shown in Suppl Fig. S3.1B) in which expression was induced by arabinose. When this construct was transformed into *E. coli* JM109 the cells turned yellow without arabinose induction (Suppl Fig. S3.2A), whilst transformed *R. eutropha* H16 cells only appeared slightly yellow in the presence of arabinose (Suppl Fig. S3.2B). Subsequent solvent extraction of *R. eutropha* H16 pDxrCRT cells and HPLC analysis showed that β-carotene was produced after induction (Suppl Fig. S3.2C, solid line), whilst no β-carotene was detectable in the

absence of arabinose (Suppl Fig. S3.2C, broken line). A negative control strain of *R. eutropha* H16, containing only the *dxr* gene cloned by PCR into the pLO11a expression plasmid produced no β-carotene in the absence or presence of arabinose (results not shown).

Redirection of carbon flux promoted β-carotene production in *R. eutropha*

The pDxrCRT construct was transformed into the RHM5 Δ*phaCAB* strain (henceforth referred to as H16Δ*pha*) as it has been shown that deleting the *phaCAB* operon encoding the three metabolic pathway genes from acetyl-CoA to polyhydroxybutyrate (PHB) increases production in *R. eutropha* of ethanol from acetate (178, 179). The resulting strain looked demonstrably more yellow after induction with arabinose (Suppl Fig. 3.2D) and β-carotene could easily be extracted into solvent and detected using an absorbance scan (Suppl Fig 3.2E) where the effect of induction on β-carotene production was clearly observable; subtraction of the uninduced scan from the induced gave a difference spectrum identical to that of β-carotene (Suppl Fig. 4F); HPLC analysis confirmed the presence in the solvent extract of *trans*- and *cis*-β-carotene observed as peaks eluting at about 16.9 minutes and 17.1 minutes respectively (Suppl Fig. 3.2G).

Three weighed cell pellets from 50-ml cultures of *R. eutropha* H16 pCRT and H16 pDxrCRT were each solvent extracted, the extract analysed by HPLC to determine the mean integrated β-carotene peak areas (as determined by Agilent ChemStation HPLC software) and compared against the peak areas obtained from several dilutions of a 1 mg/ml β-carotene standard dissolved in methanol. Yield values for *R. eutropha* H16 pCRT and pDxrCRT of approximately 0.6 ± 0.2 µg and 0.9 ± 0.1 µg β-carotene per g wet weight of pellet respectively were obtained showing that more β-carotene was produced in the presence of *dxr*. A further improvement in yield was obtained with *R. eutropha* H16Δ*pha* pDxrCRT where a value of approximately 2 ± 0.5 µg β-carotene per g wet weight of pellet was obtained (Suppl Fig. 3.2H).

Validation of GR biosynthesis in *E. coli* and *R. eutropha* H16 using single-cell Raman microspectroscopy

In order to determine the presence *in vivo* of the GR-retinal complex in cells expressing the *GR* gene, samples of uninduced and arabinose induced H16Δ*pha* GR, JM109 blhDxrCRT-GR and H16Δ*pha* blhDxrCRT-GR strains were examined at a single-cell level by Raman spectroscopy. Induction of H16Δ*pha* GR included the addition of exogenous retinal whereas induction of JM109 blhDxrCRT-GR, H16Δ*pha* blhDxrCRT-GR and H16 blhDxrCRT-GR did not as these strains make their own endogenous retinal. Single-cell Raman spectra (SCRS) were obtained ($n > 150$ in each induced sample and $n > 100$ in each uninduced sample) and the averaged spectra are shown in Suppl Fig. S3.4A. A prominent band at 1530 cm^{-1} was present in all induced samples of H16Δ*pha* GR (labelled H16-GR), JM109 blhDxrCRT-GR (labelled JM109) and H16Δ*pha* blhDxrCRT-GR (labelled H16); this band was also present in the H16 blhDxrCRT-GR strain (where the *pha* operon has not been deleted), appearing upon arabinose induction (Suppl Fig S3.4B). This characteristic Raman band was attributed to ethylenic stretching ($\nu_{C=C}$) vibrations in retinal-protein complexes(74), which depending on the carbon chain length and structure, can shift between 1505–1530 cm^{-1} (180). To date, Raman spectroscopy has only been carried out on purified GR protein either as crystals (181) or reconstituted into liposomes (182) where the ethylenic stretching ($\nu_{C=C}$) band was typically seen between 1524-1535 cm^{-1} depending on the pH conditions.

The percentage of cells expressing GR-retinal in a population was calculated by counting the number of SCRS that contained the 1530 cm^{-1} GR band (Table S3.2). The induced JM109 blhDxrCRT-GR sample had 41% of its population present with GR-retinal whilst 9% of the uninduced population also had GR-retinal present which is presumably a reflection of some 'leakiness' in the P_{BAD} promoter. Induced samples of H16Δ*pha* blhDxrCRT-GR and H16Δ*pha* GR showed 8% and 89% respectively of the populations expressing GR-retinal; no Raman band at 1530 cm^{-1} was observed in the uninduced samples. The percentage of cells expressing GR-retinal (Table S3.2) was highest in the H16Δ*pha* GR strain, to which exogenous retinal had been added, and is presumably a reflection of the reduced amount of endogenous retinal produced in *E. coli* JM109 and *R. eutropha* H16Δ*pha* by the pLO11a blhDxrCRT-GR construct, although the higher percentage of cells in the former indicates better expression of the construct in *E. coli*. As the amount of endogenous retinal is the limiting factor in the production of GR-retinal there is certainly more scope for improving its production, for

example, through codon optimisation of all the genes, the use of different promoters with differing induction conditions and molecular evolution/screening techniques.

Supplementary Tables and Figures

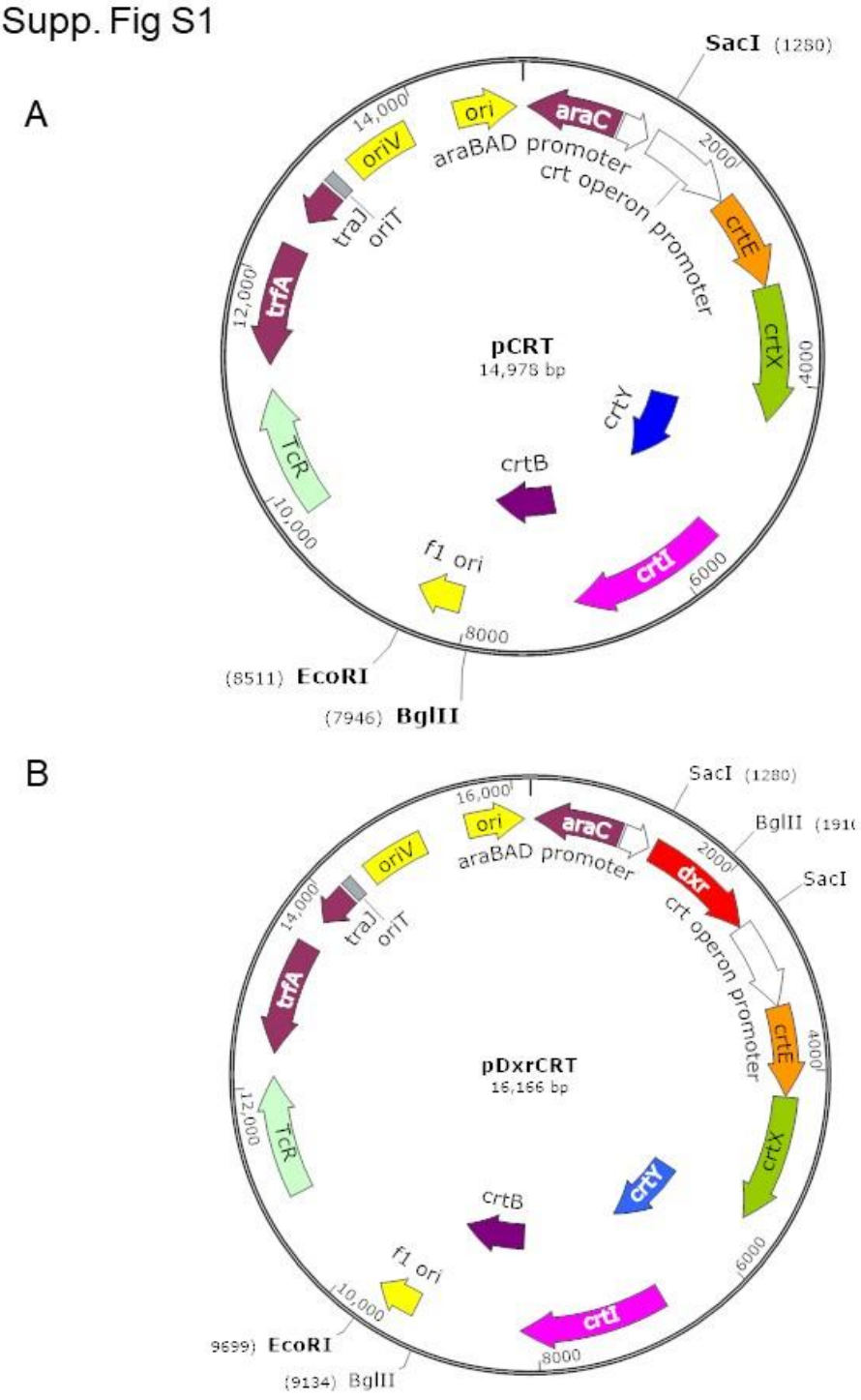
Table S3.1. The percentage of cells with GR in *Ralstonia eutropha* H16 blhDxrCRT-GR under microaerobic or aerobic conditions before and after growth for 72 h without antibiotics.

Conditions	Total cells measured by Raman	Cells with GR	Percentage
0 h	200	165	82.5%
Microaerobic 72 h light	400	277	69.2%
Microaerobic 72 h dark	400	148	36.8%
Aerobic 72 h light	400	86	26.2%
Aerobic 72 h dark	400	143	35.8%

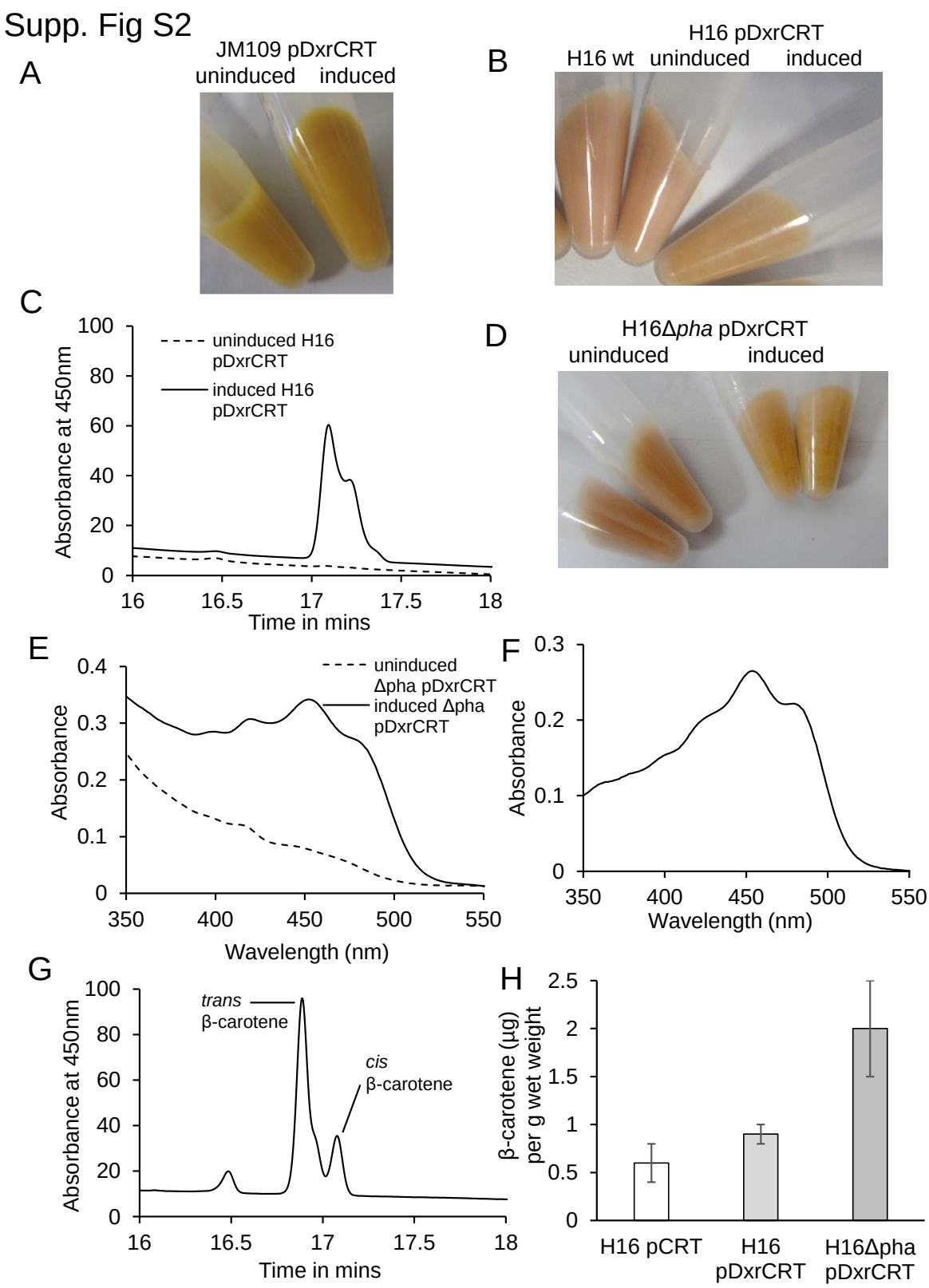
Table S3.2. Primers used in this study

Primer name	Sequence
CrtYI_F	GATCCATGGGAAGGGATCTGATTTTAGTCGGC
CrtYI_R	GATAAG CTTGCTCATTGCAGATCCTCAATCA
CRT_F	GCTCTAGAGCTCGATCTCAAACAGGATTGGGC
CRT_R	GCTCTAGATCTGACGCTCCGGGAAAGAC
SacDxr_F	GCGGAGCTCATG CATCGCATTACCATCCTG
SacDxr_R	GCGGAGCTCTCAGCGCTTTGCAGCC
NcoDxr_F	GCACCATGGGCCATCGCATTACCATCCTGGG
HindDxr_R	GCAAAGCTTCAGCGCTTTGCAGCC
pBAD_F	GCAGATCTGAATTCAAGAAACCAATTGTCCATATTGCATC
LOterm_R	GCTGAATTCAGATCTGTGACGCAGTAGCGGTAAACG
GR_F	CATGCCATGGGTTTGATGACCGTATTTTCTTC
GR_R	GCAGATCTGCGGCCGCTAGGAGATAAGACTGCCTCCCG
Rbsblh_F	GCGAAGCTTAAGGAGGAGACCCCATGG
Dxr_F	GCGGAGCTCATGGGCCATCGCATTACCATC
Blh_R	GCGGAGCTCTTATTAATGGTGATGGTGATGATGGC

Supp. Fig S1



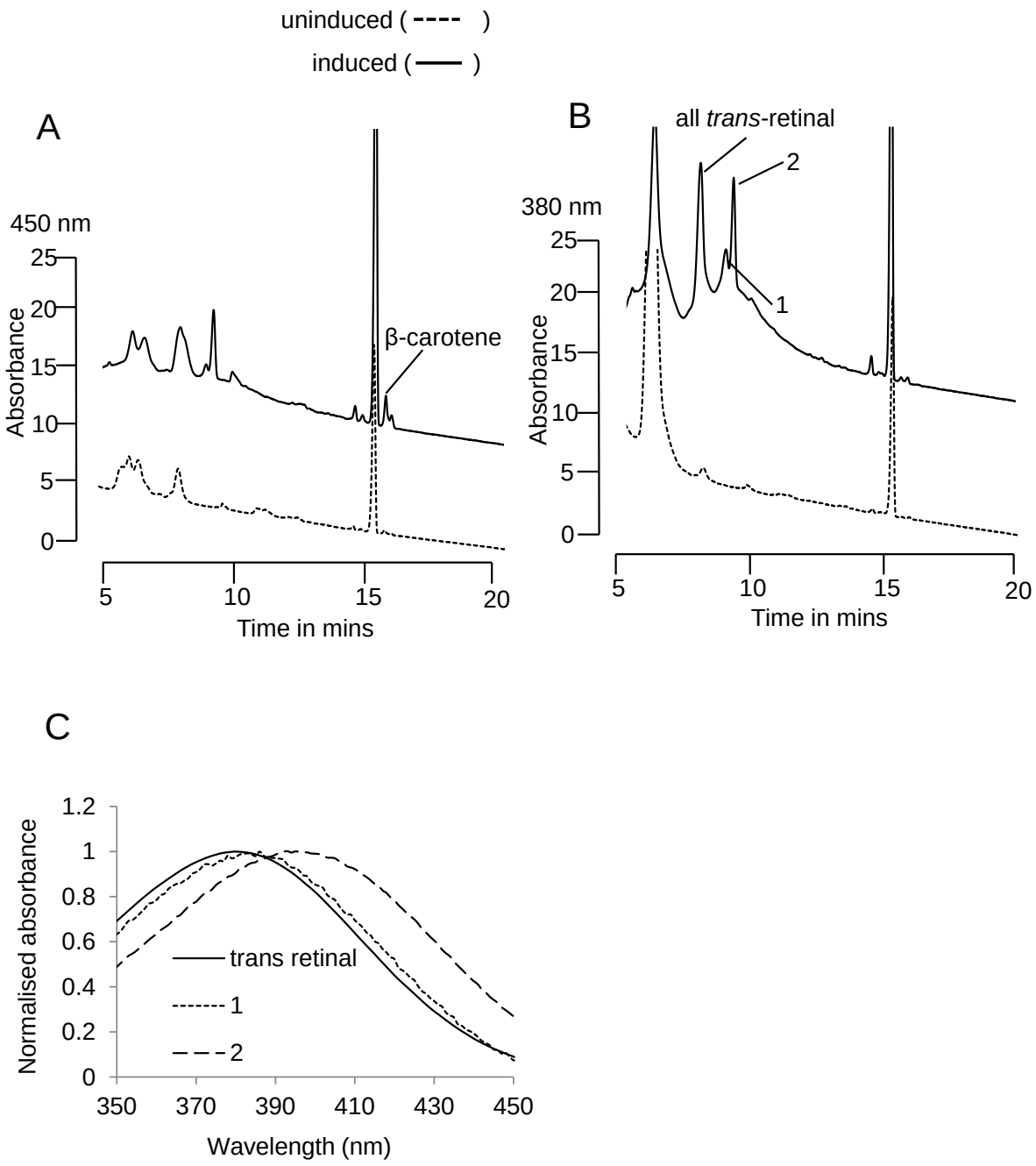
Supplementary figure S3.1. Plasmid maps of (A) pCRT and (B) pDxrCRT. The genes with their associated proteins are as follows: dxr, 1-deoxy-D-xylulose 5-phosphate reductoisomerase; crtE, geranylgeranyl diphosphate synthase; crtX, zeaxanthin glucosyltransferase; crtB, phytoene synthase; crtI, phytoene desaturase; crtY, lycopene cyclase. The plasmid backbone in both cases is pLO11a.



Supplementary figure S3.2. (A) Cell pellets of 50 ml cultures of *E. coli* JM109 transformed with the pLO11a-Dxr-crt (pDxrCRT) construct grown in the absence (uninduced) and presence (induced) of arabinose. (B) Cell pellets of 50 ml cultures of *R. eutropha* H16 wild-type cells (wt) and cells transformed with pDxrCRT grown in the presence and absence of arabinose. (C) HPLC elution profiles at 450nm of solvent extracted uninduced (broken line) and induced (solid

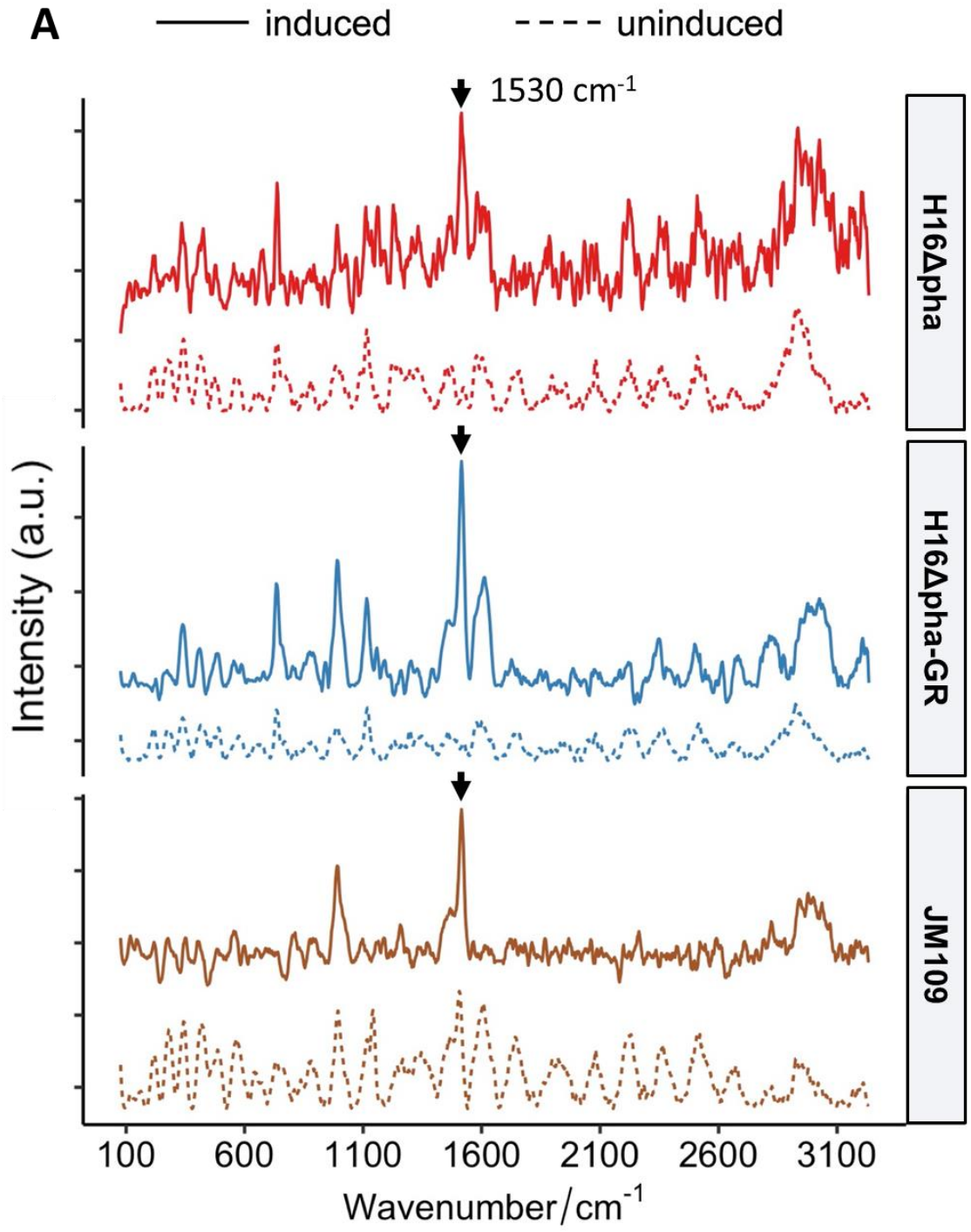
line) *R. eutropha* H16 pDxrCRT cells. (D) Cell pellets of 50 ml cultures of *R. eutropha* H16Δ*pha* cells transformed with the pDxrCRT construct grown in the absence (uninduced) and presence (induced) of arabinose. (E) Absorbance scan of solvent extracted uninduced (broken line) and induced (solid line) H16Δ*pha* pDxrCRT cells and the resulting difference absorbance scan (F). (G) HPLC elution profile at 450nm of solvent extracted induced H16Δ*pha* pDxrCRT cells with the *trans*- and *cis*-β-carotene peaks indicated. (H) Yield of β-carotene (expressed as µg per g of wet weight pellet) in induced *R. eutropha* H16 pCRT, H16 pDxrCRT and H16Δ*pha* pDxrCRT.

Supp. Fig S3

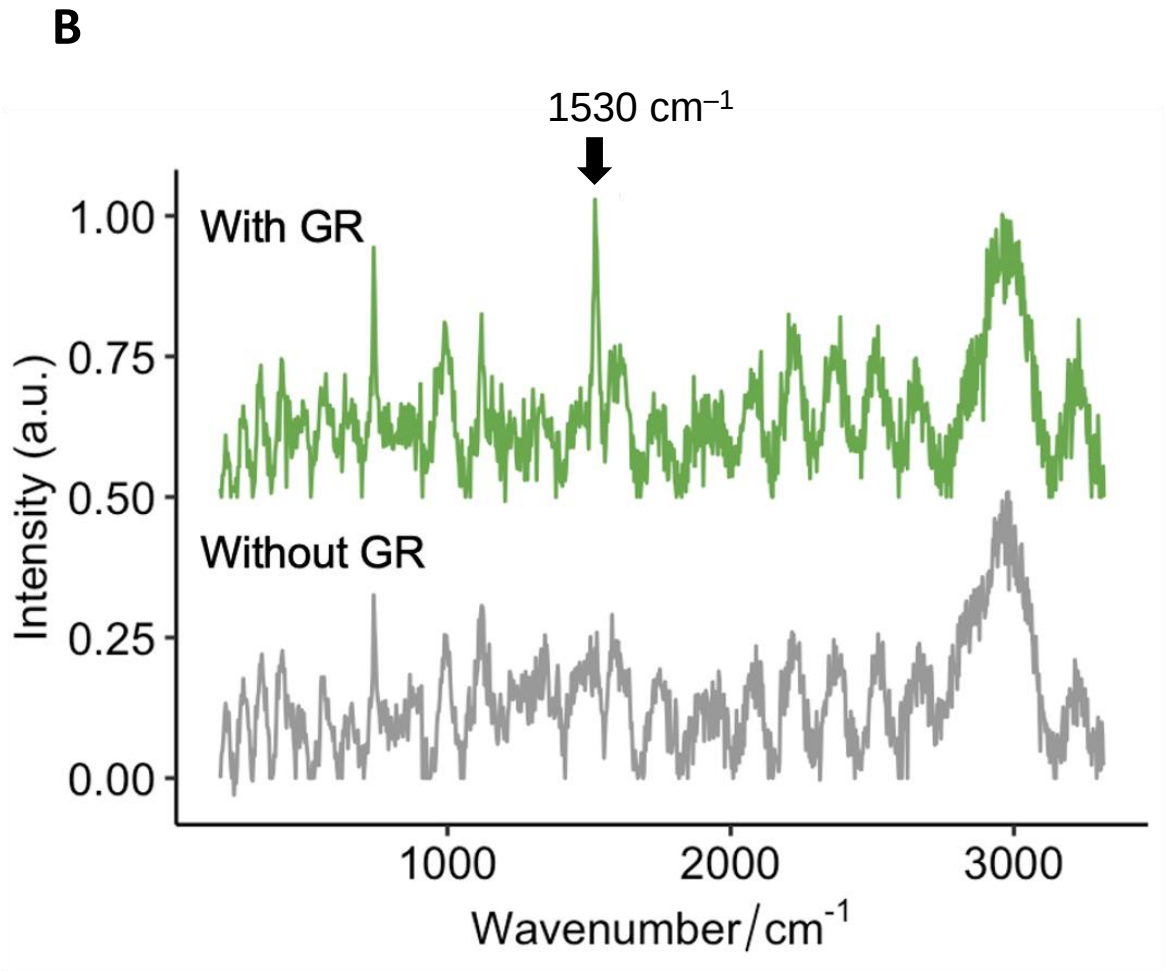


Supplementary figure S3.3. HPLC elution profiles at 450nm (A) and 380nm (B) of solvent extracted H16Δ*pha* blhDxrCRT-GR uninduced (solid line) and induced (broken line) cell pellets with the β-carotene and retinal peaks shown arrowed; two unknown peaks appearing after induction are labelled 1 and 2 with their normalised absorbance spectra shown compared to that of the *trans*-retinal peak (C).

Suppl Fig S4

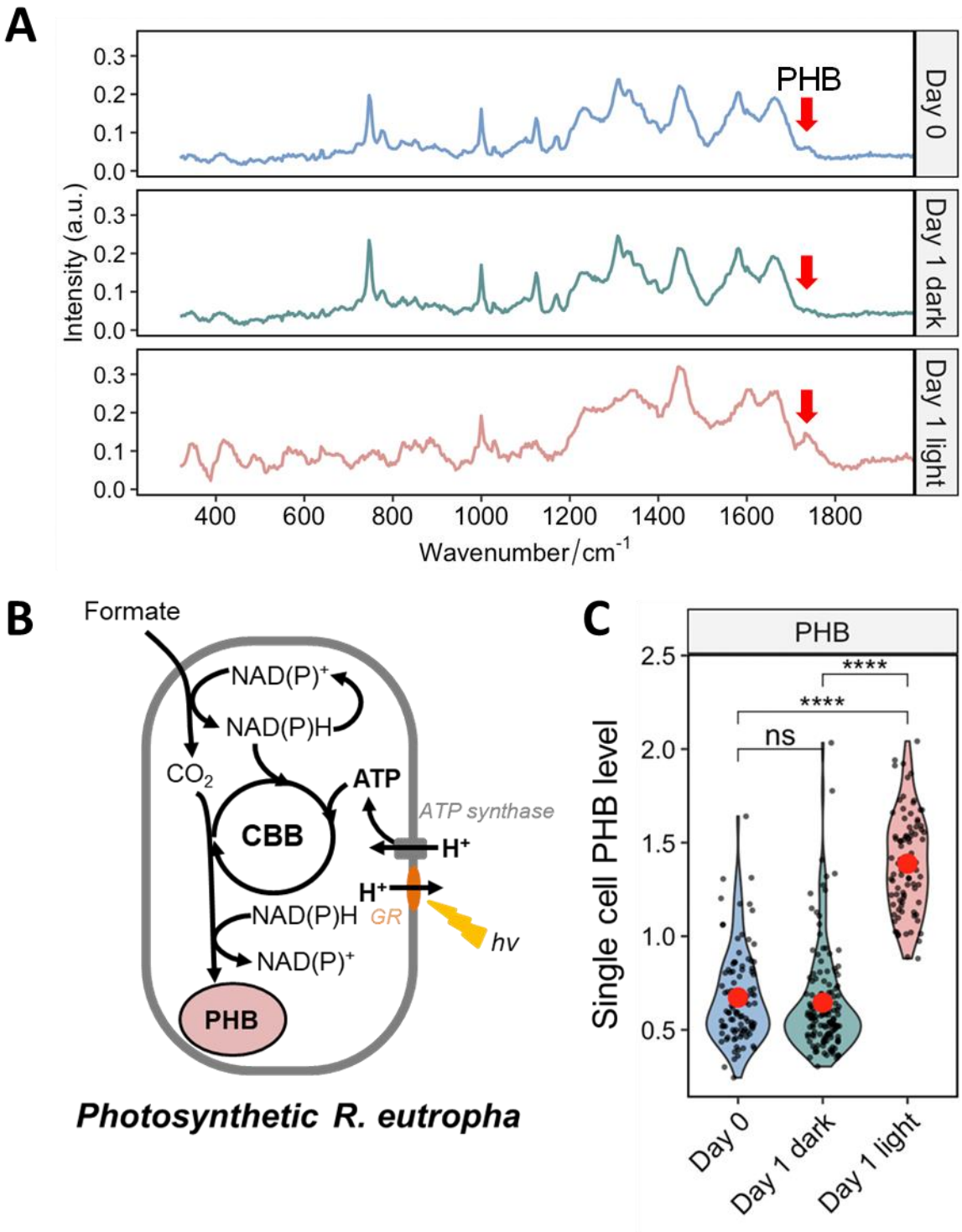

A
induced
uninduced
1530 cm-1
H16Δpha
H16Δpha-GR
JM109
Intensity (a.u.)
100
600
1100
1600
2100
2600
3100
Wavenumber/cm-1

Supp. Fig S4



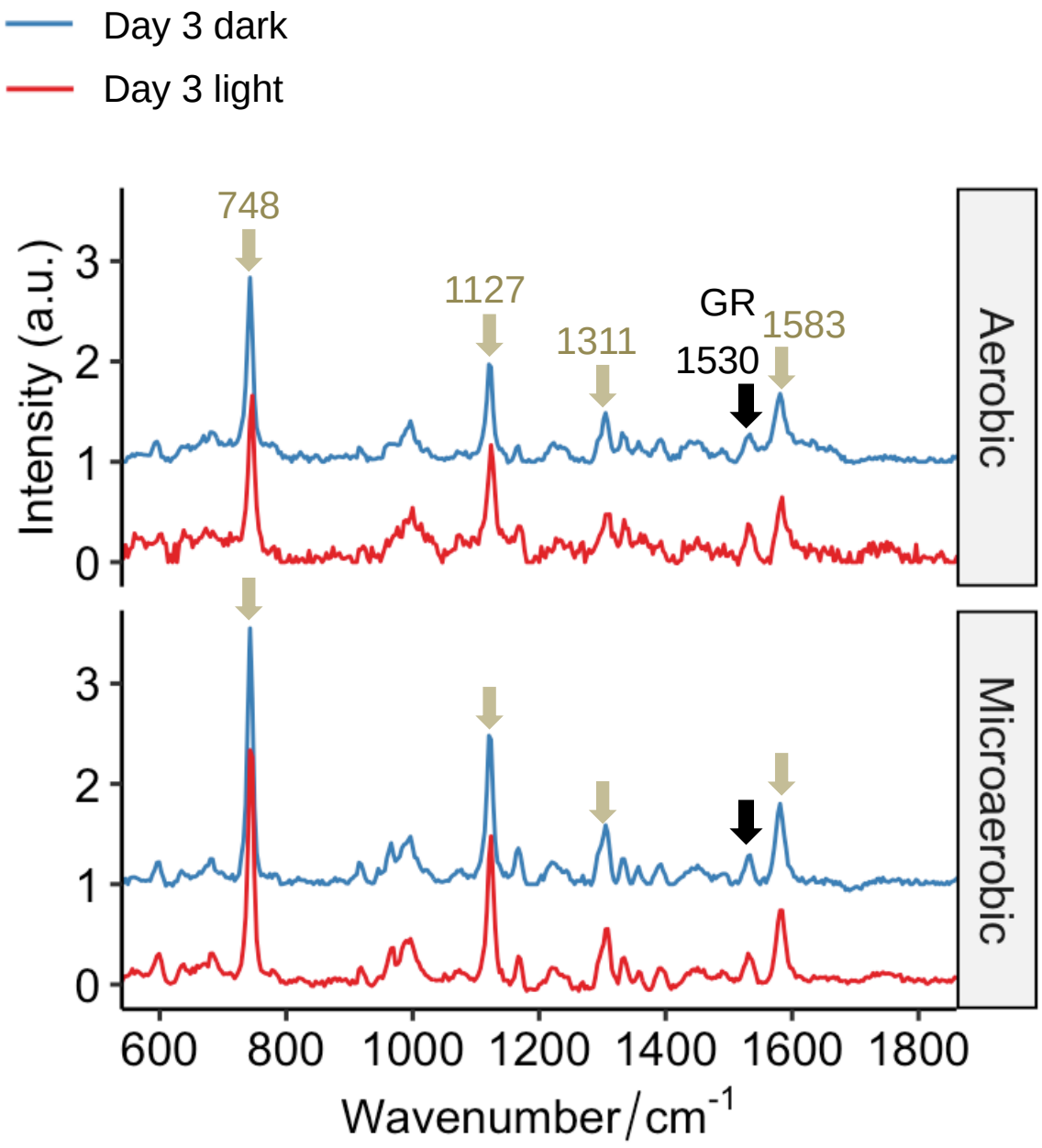
Supplementary figure S3.4. (A) SCRS of GR in *E. coli* JM109 blhDxrCRT-GR (JM109), *R. eutropha* H16Δ*pha* GR (H16-GR) and *R. eutropha* H16Δ*pha* blhDxrCRT-GR (H16) without induction (broken line) and after induction with arabinose (solid line); strain H16Δ*pha* GR also contained exogenous retinal. (B) SCRS of *R. eutropha* H16 blhDxrCRT-GR without induction (grey trace) and after induction with arabinose (green trace). The Raman signal at 1530 cm^{-1} (arrowed) is indicative of retinal bound within GR.

Suppl Fig S5



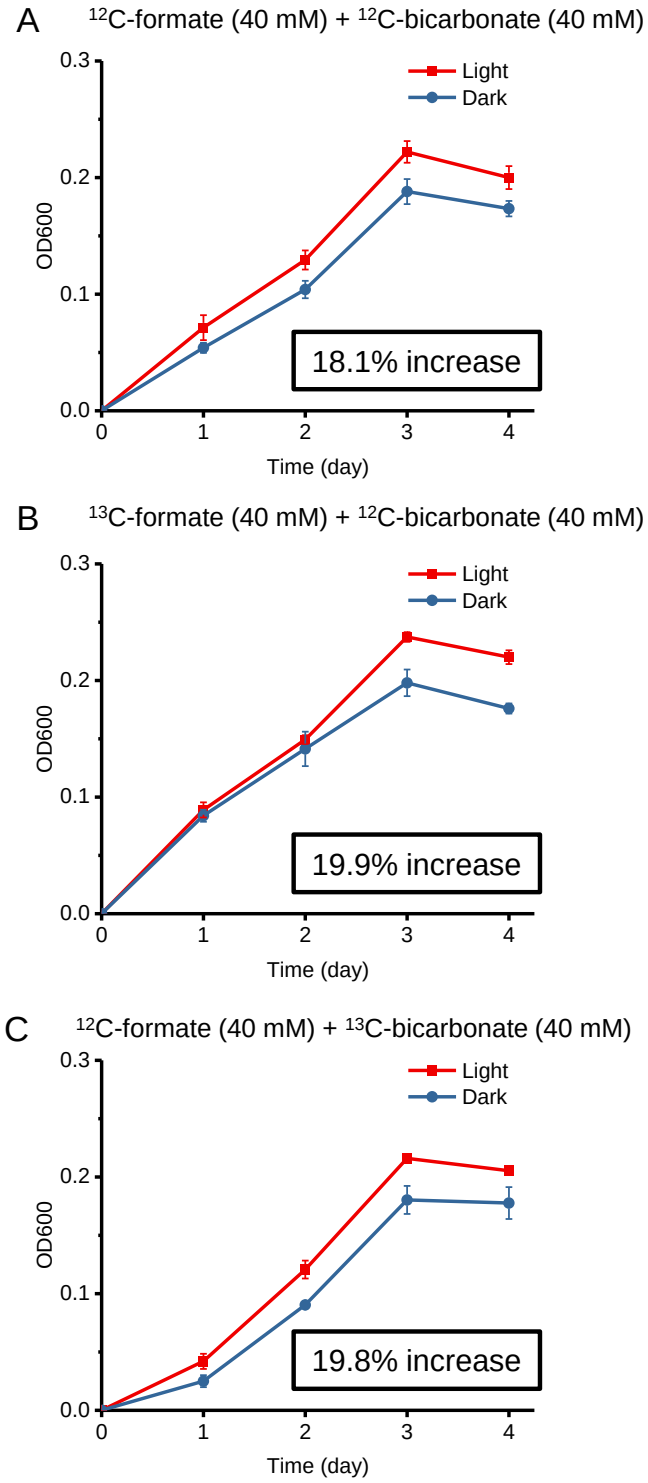
Supplementary figure S3.5. (A) PHB synthesis from formate by GR-expressing *R. eutropha* H16 (B) Comparisons of single-cell PHB content in the dark and light.

Supp. Fig S6



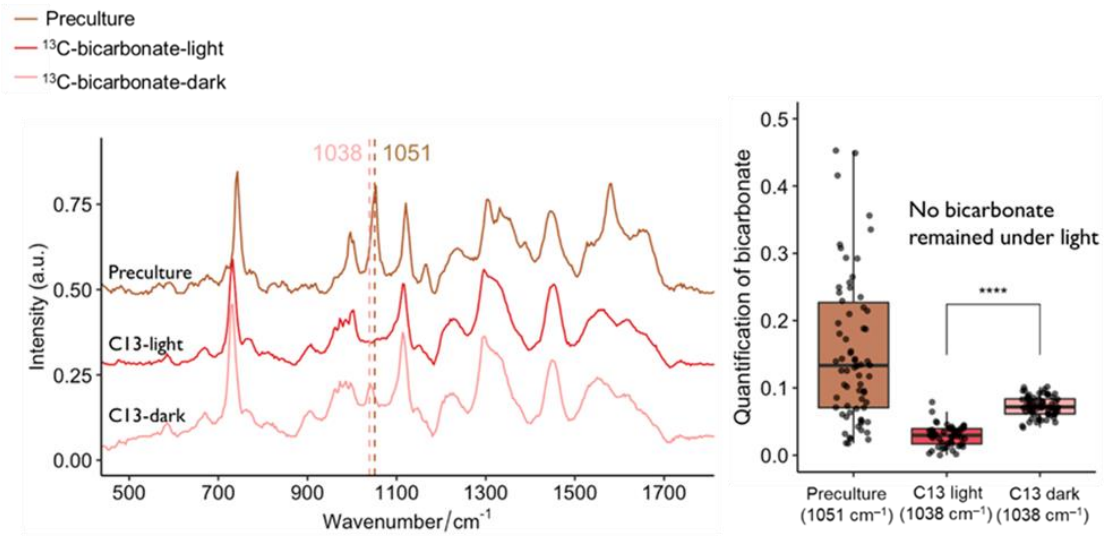
Supplementary figure S3.6. SCRS of *R. eutropha* H16 Δ*pha* with pLO11a-blhDxrCRT-GR after aerobic and microaerobic growth in MM media containing formate for 72 h under light (red line) or in the dark (blue line). Raman bands representative of the resonant cytochrome *c* molecules are labelled at 1583, 1311, 1123, and 750 cm^{-1}.

Supp. Fig S7



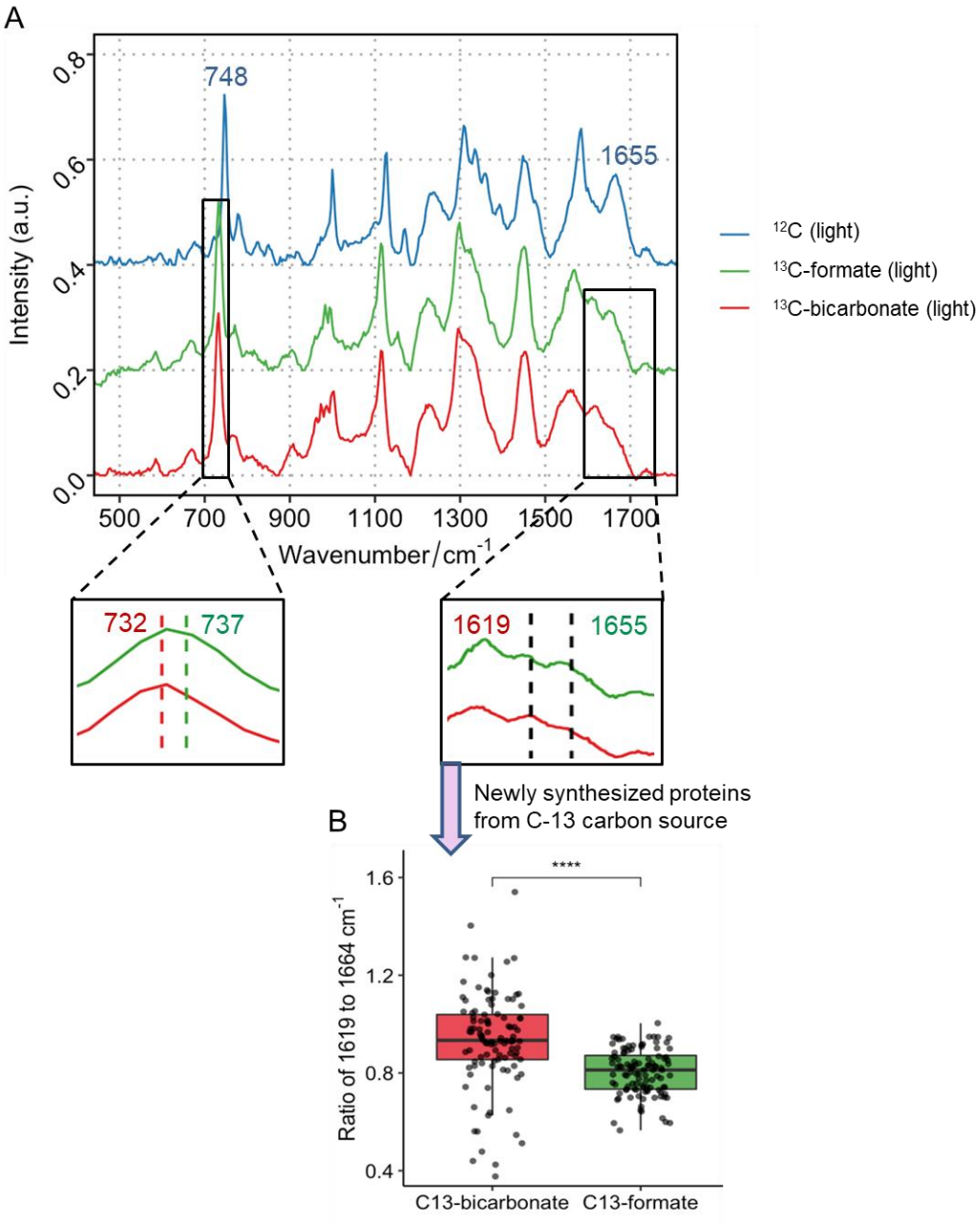
Supplementary figure S3.7. Growth curves, represented by OD_{600}, of *R. eutropha* H16Δ*pha* with pLO11a-blhDxrCRT-GR grown in (A) ^{12}C-formate + ^{12}C-bicarbonate, (B) ^{13}C-formate +^{12}C-bicarbonate and (C) ^{12}C-formate + ^{13}C-bicarbonate, under microaerobic conditions either in the light or in the dark. The percentage increases under light compared with the dark at the maximum growth point (day 3) are shown for each substrate condition.

Suppl Fig S8



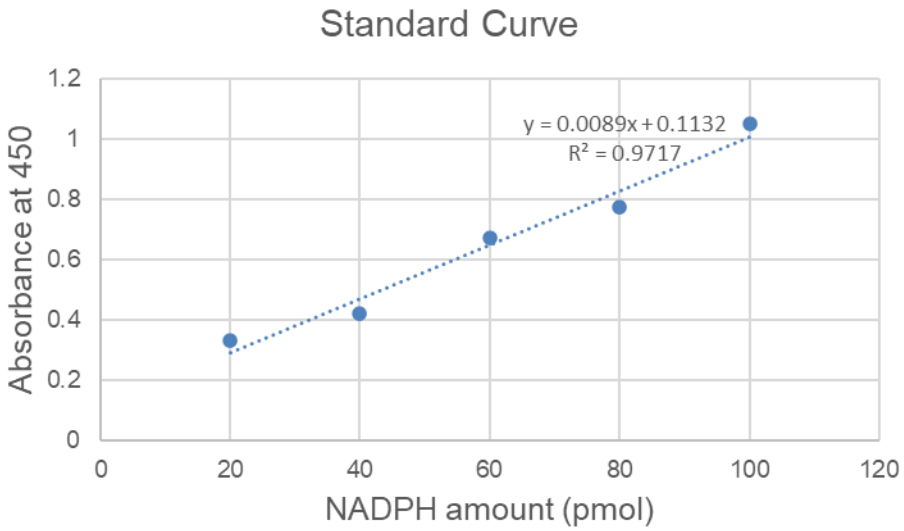
Supplementary figure S3.8. (A) Single cell Raman spectra of *R. eutropha* H16 with pLO11a-blhDxrCRT-GR at the preculture stage and after 3 days growth with 12C-formate + 13C-bicarbonate under light and dark conditions. The Raman signals at 1051 cm^{-1} and 1038 cm^{-1} are indicative of ^{12}C-bicarbonate and ^{13}C-bicarbonate, respectively. (B) Quantification of cells at the single-cell level that contain bicarbonate. Statistical significance was calculated based on Student's t test ($p < 0.0001$).

Suppl Fig S9



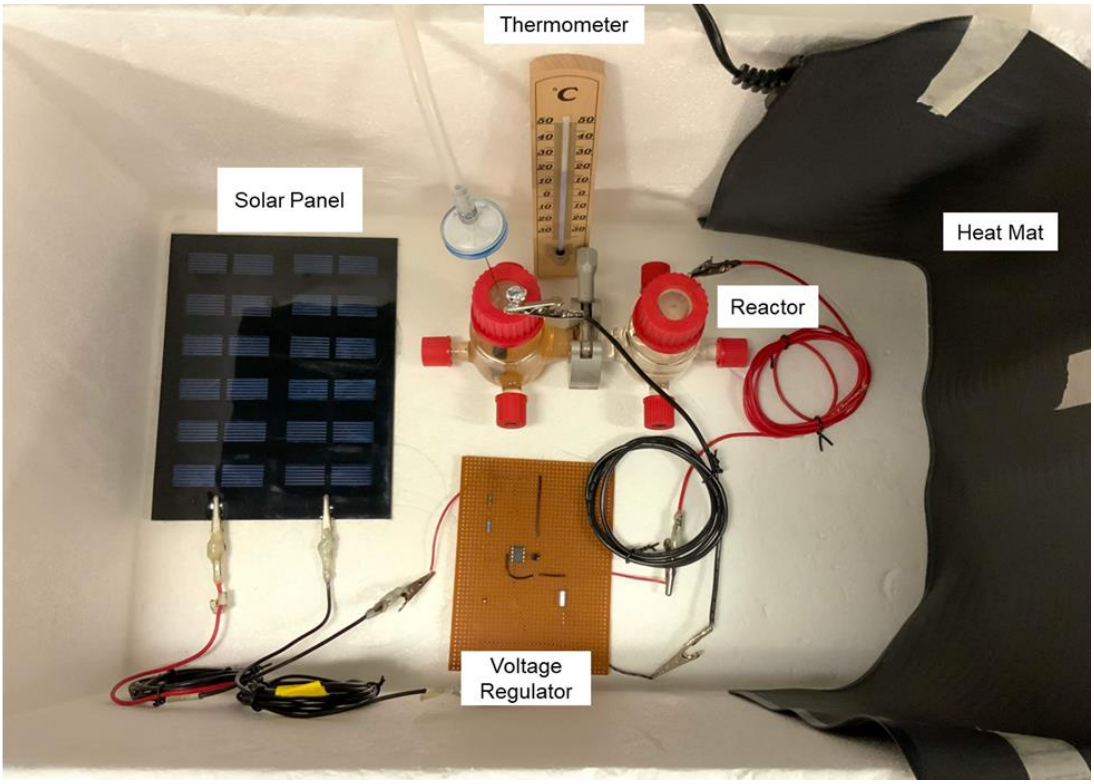
Supplementary figure S3.9. (A) Single cell Raman spectra of *R. eutropha* H16Δ*pha* with pLO11a-blhDxrCRT-GR grown under light with ^{13}C-formate + ^{12}C-bicarbonate (green) or ^{12}C-formate + ^{13}C-bicarbonate (red). Raman shifts were observed at 737 (^{13}C-formate) and 732 (^{13}C-bicarbonate), and from 1664 to 1619 (both ^{13}C-formate and ^{13}C-bicarbonate). (B) Quantification of newly synthesised proteins at the single-cell level from ^{13}C-formate (green) or ^{13}C-bicarbonate (red) by calculating the ratio of the areas of the 1619-cm^{-1} band to the 1664-cm^{-1} band. Statistical significance was calculated based on Student's t test ($p < 0.0001$).

Suppl Fig S10



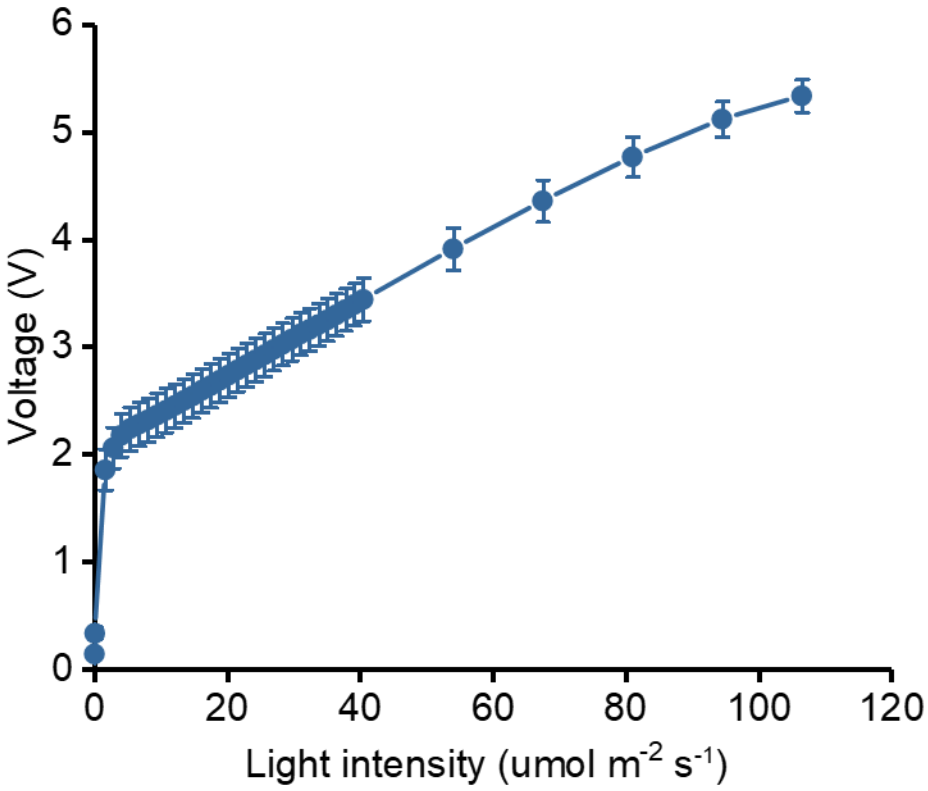
Supplementary figure S3.10. A standard calibration curve for NADPH based on absorbance at 450 nm using the NADP/NADPH quantification kit (Sigma-Aldrich).

Suppl Fig S11



Supplementary figure S3.11. The setup of the photo-electrosynthetic system.

Suppl Fig S12



Supplementary figure S3.12. The electricity production from the solar panel.

Chapter 4



Engineering Rhodopsin-Based Artificial Photosynthesis for CO_2 Fixation

Weiming Tu, Jiabao Xu, Ian P. Thompson and Wei E. Huang*

Department of Engineering Science, University of Oxford, Oxford OX1 3PJ, United Kingdom.

*Corresponding author: Wei E. Huang. Email: wei.huang@eng.ox.ac.uk. Tel: +44 1865 283786.

Chapter adapted from publication: ***Nature Communications*** (2023)

DOI: 10.1038/s41467-023-43524-4

4.1 Summary

Building on the work in Chapter 3, this chapter optimises the electron transfer process to enhance CO_2 fixation efficiency. Here, we construct an artificial photosynthesis system which combines the proton-pumping ability of rhodopsin with an extracellular electron uptake mechanism, establishing a pathway to drive photoelectrosynthetic CO_2 fixation by *Ralstonia eutropha* (also *Cupriavidus necator*) H16. *R. eutropha* is engineered to heterologously express an extracellular electron transfer pathway of *Shewanella oneidensis* MR-1 and *Gloeobacter* rhodopsin (GR). Employing GR and the outer-membrane conduit MtrCAB from *S. oneidensis*, extracellular electrons and GR-driven proton motive force are integrated into *R. eutropha*'s native electron transport chain (ETC). Inspired by natural photosynthesis, the photo-electrochemical system splits water to supply electrons to *R. eutropha* via the Mtr outer-membrane route. The light-activated proton pump - GR, supported by canthaxanthin as an antenna, powers ATP synthesis and reverses the ETC to regenerate NADH/NADPH, facilitating *R. eutropha*'s biomass synthesis from CO_2. Overexpression of carbonic anhydrase further enhances CO_2 fixation. This innovative artificial photosynthesis system has the potential to advance the development of efficient photosynthesis, redefining our understanding of the ecological role of rhodopsins in nature.

Keywords: rhodopsin, artificial photosynthesis, solar energy, splitting water, CO_2 fixation, electron transport chain, Mtr

4.2 Introduction

Microbial carbon dioxide (CO_2) fixation through photosynthesis is one of the foundations of the global carbon cycle (183, 184). Photosynthetic microbes harvest solar radiation to convert CO_2 and water into organic compounds, contributing around 50% of primary productivity on earth (185). In nature, almost all known light-harvesting mechanisms in microorganisms are either chlorophyll- or rhodopsin-based systems(3). Chlorophyll-based photosystems are multi-component pigment-protein complexes (i.e., photosystem I and II) coupled with a series of redox protein complexes to form a photosynthetic electron transport chain, which use light as the energy source to split water, accompanied by the production of ATP and reductants (e.g., NADPH). In comparison, rhodopsin-based photosystems are much simpler with only a light-activated proton pump generating proton motive force (63). There was a lot of evidence suggesting that rhodopsin can support ATP synthesis to enhance inorganic carbon assimilation in the presence of organic electron donors (78). However, rhodopsin cannot solely drive the CO_2 fixation pathway with its proton pumping, due to the lack of electron generation. Microbial rhodopsins as the most widespread proteins in the microbial world are hypothesised to have a significant role in microbial carbon fixation (86, 186). Recently, rhodopsin phototrophy has been shown to generate sufficient energy for reversing electron transfer which can drive NADH synthesis via NADH dehydrogenase (124) and then power CO_2 fixation (187). These findings indicated that the proton gradient generated by rhodopsin can support the regeneration of NAD(P)H via an electron transport chain, providing a driving force for CO_2 reduction (187).

Microbial rhodopsins are widely used as optogenetic tools in synthetic biology and have been successfully expressed in model bacteria such as *Escherichia coli* (25), *Ralstonia eutropha* (187) and *Shewanella oneidensis* (124). Numerous studies (76, 188, 189) demonstrated that the engineered bacteria with rhodopsin can convert light energy into intracellular chemical energy. For example, the engineered *E. coli* with rhodopsin has been shown to improve bioproduction in light (188). Additionally, the expression of rhodopsin in the electroactive bacterium *S. oneidensis* can power the electrosynthesis of reduced products in cathodic conditions (124). Integrating a rhodopsin-based photosystem with chemoautotrophic bacteria represents a promising approach to increase biosynthesis from CO_2. Chemoautotrophic bacteria can utilise inorganic chemicals or an electrode as the electron donor to assimilate CO_2 into valuable

compounds. *R. eutropha* H16, a chemolithoautotroph, is a model microbial chassis, owing to its CO_2 fixation pathway and metabolic versatility. We recently engineered the autotrophic bacterium *R. eutropha* H16 with a *Gloeobacter* rhodopsin (GR) and created a redox loop by integrating it with an external electrode (187). Electrons supplied by the electrode were transferred into the engineered *R. eutropha* to drive CO_2 fixation. The process was mediated by an electron-shuttling molecule such as flavin, and powered by rhodopsins (187). While this system can effectively incorporate CO_2, it displayed a relatively low electron transfer rate and efficiency. We hypothesised that engineering an efficient electron transfer interface on the cell membrane could be a key strategy for improving the electron transport from the electrode to the cells. In the model photosynthetic bacterium *Rhodopseudomonas palustris*, there are cytochromes presented on the outer membrane to enable the electron transfer between intracellular and extracellular electron acceptors and electrons (190). It is hypothesised that artificially combining extracellular electron uptake with intracellular reverse electron transfer could lead to construction of a synthetic photosynthetic electron transport chain in *R. eutropha* H16. In addition, the proton-pumping capacity could be another limiting factor to rhodopsin-based photo-electrosynthesis, which is associated with ATP and NADH synthesis (191). As with *R. palustris*, the proton gradient not only drives ATP production via ATP synthase but also plays a key role in reversing the function of proton-translocating NADH dehydrogenase for regeneration of reducing equivalents (190). Therefore, increasing the proton-pumping activity of rhodopsin may also increase the efficiency of the artificial system.

In this work, *R. eutropha* H16 is engineered to establish a photon and electron harvesting system by the heterologous expression of the outer-membrane conduit MtrCAB complex from *S. oneidensis* MR-1 and the GR protein from *Gloeobacter violaceus*. Natural electroactive bacteria, such as *S. oneidensis* MR-1, use the outer membrane-bound Mtr pathway, facilitating bidirectional electron transfer between extracellular substrates and the quinone pool (192, 193). This synthetic biology design combining the Mtr pathway and rhodopsin-based phototrophy enables the construction of an electrochemically driven photosynthetic electron transport chain, which can be integrated with a solar-driven electrochemical system to achieve artificial photosynthesis (Figure 4.1). As with chlorophyll-based natural photosynthesis, this artificial photosynthesis breaks water into oxygen, protons (hydrogen ions) and

electrons at the anode. The engineered *R. eutropha* can directly take electrons from a cathode through the outer membrane-bound Mtr, connected to the inner membrane-bound electron transport chain. Subsequently, the light-powered rhodopsin in the engineered *R. eutropha* pumps protons and drives the electron transfer to regenerate NAD(P)H for CO_2 fixation and biomass growth (187). The biomass produced by *R. eutropha* is valuable, as it produces high levels of protein, as well as other important nutrients such as essential amino acids and vitamins (161). To enhance CO_2 fixation efficiency, flavin and canthaxanthin are introduced to combine with Mtr and GR, respectively, improving the electron transfer rate and proton pumping capacity. Additionally, a carbonic anhydrase (*can*) is overexpressed to enhance CO_2 fixation (194) by concentrating CO_2 (195). Overall, the artificial photosynthesis developed in this study could help design alternative methods for CO_2 fixation, providing a valuable reference for engineering non-photoelectrosynthetic bacteria into photoelectrotrophs, and offer insights into future investigations of the potential interplay between rhodopsin-based metabolism and extracellular electron transfer, along with their joint effect on microbial CO_2 fixation.

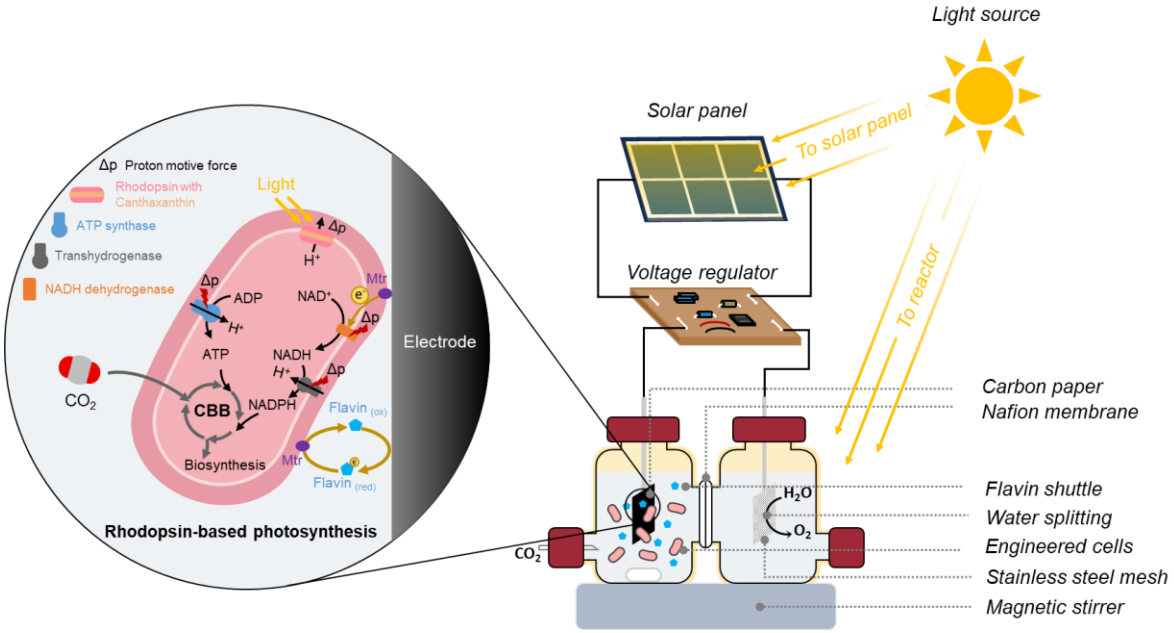


Figure 4.1. Construction of hybrid photosynthesis by combining an electrochemical system with engineered cells expressing rhodopsin and an outer-membrane conduit Mtr.

4.3 Results

4.3.1 Engineering a synthetic Mtr-mediated electron transport chain

A plasmid containing a gene pathway encoding MtrCAB (pLO11a-MtrCAB) was created under the control of an arabinose-inducible P_{BAD} promoter. MtrCAB is a multi-heme protein complex linking the intracellular electron transport chain with extracellular substrates (Figure 4.2a). Cytochrome *c* maturation is required for heme insertion (196). Unlike *E. coli* which cannot express cytochrome *c* aerobically (196), *R. eutropha* H16 can synthesise cytochromes under aerobic conditions, the same as that of electroactive *Shewanella oneidensis* MR-1 cells (Suppl Fig. S4.1). The plasmid pLO11a-MtrCAB was transferred into *R. eutropha* H16 to create *R. eutropha*-Mtr (Table S4.1). After induction by arabinose, the cell pellet of induced *R. eutropha*-Mtr showed a red colour (insets in Figure 4.2b), compared with that of uninduced cells. The red colour was attributed to the expression of MtrCAB complexes on the cell membrane which is consistent with the results reported in *E. coli* (196). Single-cell Raman analysis revealed that Raman spectra of cells expressing Mtr displayed a significant increase in bands associated with the cytochromes (Figure 4.2b and Suppl Fig. S4.2). This is in good agreement with a previous study report that *S. oneidensis* MR-1's cytochromes levels decreased due to the deletion of Mtr genes (197). MtrC and MtrA are c-type cytochromes; thus, the elevated cytochromes suggest the synthesis of Mtr in *R. eutropha*-Mtr. Proteins from whole cell extracts were separated by SDS-PAGE, and heme *c* containing proteins MtrC and MtrA were identified by heme straining (Suppl Fig. S4.3). Collectively the results confirm the expression of the Mtr pathway in *R. eutropha*.

Furthermore, electrochemical tests were performed to confirm the functions of Mtr in *R. eutropha*. Since *R. eutropha* is able to carry out a nitrate-reducing metabolism (198), we hypothesised that in the presence of nitrate as an electron acceptor, the Mtr pathway in *R. eutropha*-Mtr could obtain cathodic electrons for denitrification via native nitrate reductases (Figure 4.2a). The precultured *R. eutropha*-Mtr with and without arabinose induction were incubated in potentiostatic-controlled bioreactors under cathodic conditions (–500 mV vs. Ag/AgCl). After a period of acclimation, 20 mM nitrate was added to the cathodic chamber. We observed that the addition of nitrate accelerated *R. eutropha*-Mtr consuming current with a significant current drop over 6 h, while little

current change was detected in the control group with the Mtr-uninduced strain (Figure 4.2c). The observation indicates that electron flux from a cathode to nitrate reductases was due to the Mtr complex in *R. eutropha*-Mtr. The nitrate respiration pathway is part of the electron transport chain; thus, the expression of the Mtr complex creates an electrical connection between cellular energy metabolism and the electrode.

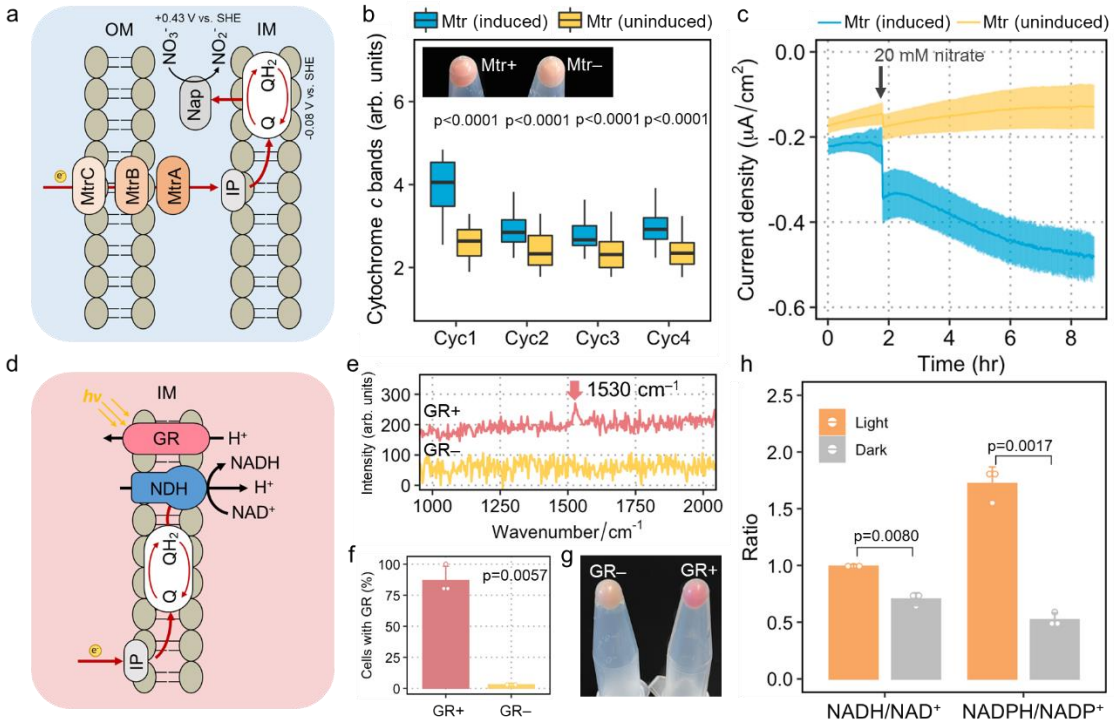


Figure 4.2. Construction of a photosynthetic electron transport chain. (a) The MtrCAB complex mediates inward electron transfer to reduce nitrate (OM: outer membrane; IM: inner membrane; IP: inner-membrane proteins; Nap: nitrate reductases; Q: quinones). (b) Semi-quantification of *c*-type cytochrome levels in cells with or without Mtr complexes at the single-cell level by Raman analysis. Cyc1, Cyc2, Cyc3 and Cyc4 represent the quantification of four bands at 748, 1128, 1312 and 1584 cm^{-1}. The number of measured cells = 234. The lower and upper quartiles are drawn as lines outside the box. The rectangle in the box plots represents the second and third quartiles with a line inside representing the median. The whiskers indicated the minima and maxima. (c) Current consumption by induced and uninduced *R. eutropha*-Mtr with addition of 20-mM nitrate (Data show means ± SD of three biological replicates). (d) Light-activated GR drives NADH dehydrogenase (NDH) in reverse to synthesise NADH from quinone. (e) A typical Raman spectrum of a cell with GR complexes identified by a band at ~1530 cm^{-1} (red) and a typical Raman spectrum with the band intensity below background noise identified as a cell without GR (yellow). (f) The percentage of GR-expressing cells, i.e., with the 1530 cm^{-1} GR band, in induced (number of measured cells n = 297) and uninduced (number of measured cells n = 306) groups. Data show means ± SD of three biological replicates. (g) Uninduced and arabinose-induced cell pellets were yellow and pink, respectively. (h) $NADH/NAD^+$ and $NADPH/NADP^+$ ratios in the engineered cells under light and dark conditions (Data show means ± SD of three biological replicates). Statistics were performed with two-sided Student's t-test (Exact p values are provided in the figures).

4.3.2 Combination of the electron transport chain with a rhodopsin-based photosystem

Reducing power such as NADH and NADPH is the key driving force to power CO_2 fixation. Although the Mtr-mediated electron transfer system can support electron flow inwardly, there is an energy hurdle over intracellular electron transfer. We expect that electrons flow from a cathode to Mtr (−300 mV_{SHE} to +100 mV_{SHE}) (193), then to the quinones pool (−80 mV_{SHE} for menaquinone) mediated by inner-membrane proteins (IPs) and onto NADH dehydrogenase for the generation of NADH (−320 mV_{SHE}). However, the electron transfer from quinol to NAD^+ is thermodynamically unfavourable. Previous studies have demonstrated that introducing a rhodopsin-based proton pump can drive the process by providing extra energy in the form of proton motive force (124, 187). Therefore, in this study, we combined the Mtr pathway with a gene encoding *Gloeobacter* rhodopsin (GR) to form a phototrophic extracellular electron uptake pathway (Figure 4.2d). The GR-based photosystem can harvest light energy around 530 nm (186) and act as a light-activated proton pump. Previous in-vitro studies have demonstrated that holo-GR was able to generate a proton motive force under light and had a two-fold faster turnover rate than other proteorhodopsins (PRs) (167). Hence, a plasmid containing genes encoding both MtrCAB and GR (pLO11a-MtrCAB-GR) was transferred to *R. eutropha* to create *R. eutropha*-GR-Mtr (Table S4.1).

As a consequence of GR expression, arabinose-induced cells in the cell pellet were pink in colour, compared with that of uninduced bacteria (Figure 4.2g). The pink colour was attributed to the presence of GR-retinal complexes on the cell membrane. Single-cell Raman analysis revealed that Raman spectra of cells expressing GR displayed a characteristic rhodopsin band at 1530 cm^{-1} (Figure 4.2e), consistent with the previous report (187). The GR complexes were detected in 87% of the induced cells by examining single-cell Raman spectra of 270 individual cells, and none in the uninduced cells (number of measured cells n = 306) (Figure 4.2f). After establishing the GR-based photosystem with the Mtr pathway, the *R. eutropha*-GR-Mtr strain was employed to investigate the possibility that the extracellular electrons could drive the reducing power generation in *R. eutropha* under light, by incubating the strain in cathodic conditions with an electrode as the electron source. After 2-day incubation, reducing power accumulated in light conditions due to the energy provided by the

functional GR. The NADH and NADPH levels were significantly increased in *R. eutropha*-GR-Mtr under the light compared to that in the dark (Figure 4.2h). Interestingly, in the light, the NADPH/$NADP^+$ ratio was higher than NADH/NAD^+ (Figure 4.2h), indicating that the strain could be more inclined to uptake extracellular electrons for driving NADPH-dependent reactions such as CO_2 fixation.

4.3.3 Light-driven metabolism with CO_2 as the sole carbon source

It is reasonable to assume that the reducing power NADPH would energize the CO_2 fixation pathway (CBB cycle) in *R. eutropha* H16. Biosynthesis requires a catalyst, energy and building blocks (such as CO_2 and H_2O). *R. eutropha*-GR-Mtr was used as a catalyst to harvest light energy for CO_2 fixation. Heavy water D_2O has been employed to probe general cellular metabolic activities (199). We hypothesised that the photoelectro-autotrophic *R. eutropha*-GR-Mtr, in the presence of both CO_2 and reducing power NADH/NADPH, can incorporate D_2O into cell metabolisms, including the regeneration of NAD(P)H and the synthesis of 3-phosphoglycerate (3PG) (Suppl Fig. S4.4a). Thus, in the presence of D_2O, carbon−deuterium (C−D) bond will form only in metabolically active cells, which can be readily detected by single-cell Raman analysis (Suppl Fig. S4.4a).

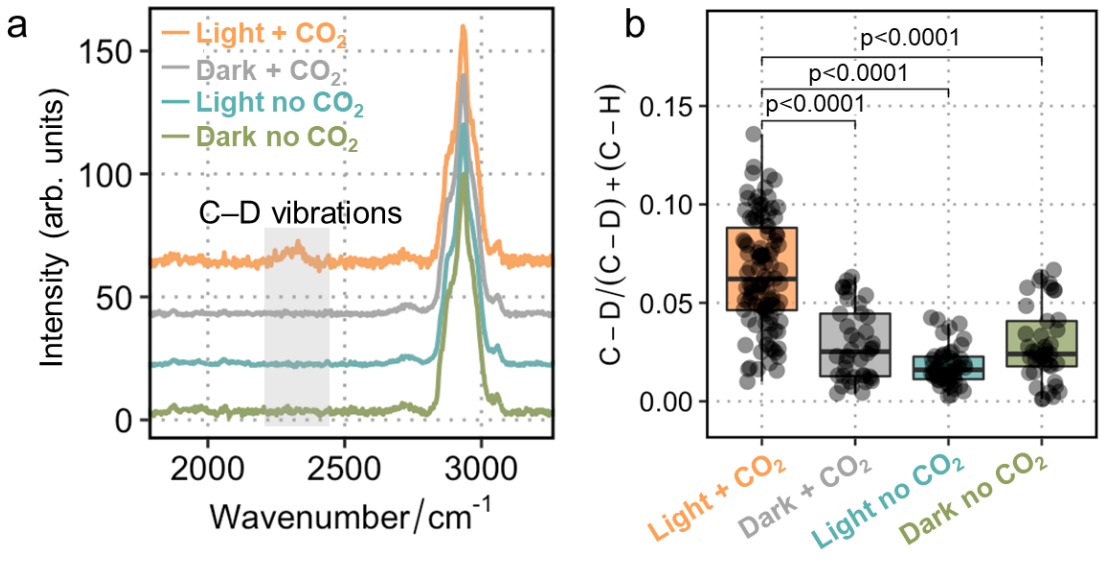


Figure 4.3. Metabolic activities of *R. eutropha*-GR-Mtr probed by Raman C–D vibrations. (a) Averaged single-cell Raman spectra of *R. eutropha*-GR-Mtr cultured with 30% D_2O under different conditions. The Raman band of C–H vibrations was shifted to a C–D band at 2070–2300 cm^{-1}, the extent of which represents the metabolic activities of the cells. (b) Comparison of C–D / (C–D) + (C–H) in the *R. eutropha*-GR-Mtr with and without light and CO_2 supply. The lower and upper quartiles are drawn as lines outside the box. The rectangle in the box plots

represents the second and third quartiles with a line inside representing the median. The whiskers indicated the minima and maxima. Statistics were performed with two-sided Student's t-test ($p < 0.0001$, the number of measured individual cells = 294).

The precultured *R. eutropha*-GR-Mtr was inoculated into cathode chambers which were operated in four conditions: dark and no CO_2, dark with CO_2, light and no CO_2, and light with CO_2. After 2-day incubation, C−D bands originated from newly formed C−D bonds were only observed in the group with light and CO_2 in both averaged Raman spectra (Figure 4.3a) and single-cell analysis (Figure 4.3b; number of measured individual cells = 294), suggesting that *R. eutropha*-GR-Mtr was active to perform light-driven CO_2 fixation. In the case of *R. eutropha*-GR, no significant C−D bands were observed in the presence of light and CO_2 (Suppl Fig. 4.5), indicating the importance of Mtr in extracellular electron transfer. In particular, the single band at 1003 cm^{-1} is characteristic of the phenyl ring of phenylalanine (an aromatic amino acid), which becomes three bands at 987, 975 and 961 cm^{-1} due to the utilisation of D_2O in *R. europha*-GR-Mtr (Suppl Fig. 4b). These isotopic shifts in Raman spectra are in good agreement with the phenylalanine deuteration reported in previous work(200). In addition, the display of a band at 1050 cm^{-1} in Raman spectra from the cells in the dark indicates bicarbonate presence, since the continuous supply of CO_2 without consumption would result in the accumulation of bicarbonate intracellularly in *R. eutropha*-GR-Mtr. These results indicate that the introduction of MtrCBA and GR in *R. eutropha*-GR-Mtr leads to biosynthesis from CO_2. In summary, these observations confirm that *R. eutropha*-GR-Mtr has been converted into a photoelectro-autotrophic bacterium.

4.3.4 Further enhancement of artificial photosynthesis

To achieve photosynthesis with light energy as the sole energy source, we employed a solar panel to drive the electrochemical platform. Instead of using a potentiostat to control the cathode potential, we designed a simple voltage regulator to adjust the applied potential generated by the solar cells (Suppl Fig. S4.6 a and b). The voltage regulator was employed to stabilise the cathode potential in order to avoid cathode potential fluctuations that could harm the cells.

The biomass of *R. eutropha* was chosen as the end product of photosynthesis, as it was qualified by European Union to be used as a safe source of single-cell protein for animal feed (161). The *phaCAB* operon has been knocked out in *R. eutropha* H16 to create *R.*

eutropha Δ*pha* (RHM5) mutant for maximising carbon flux towards biomass instead of polyhydroxyalkanoates (PHA) (Figure 4.4a, Table S4.1). Flavin mononucleotide (FMN) was added as an electron mediator to enhance the electron transfer rate which can react with MtrC (201). Single-cell Raman analysis showed a typical band of FMN at ~1340 cm^{-1} in cells expressing Mtr (Figure 4.4b and Suppl Fig.S4.7), indicating that exogenous FMN could bind to MtrC as the cofactor involved in electron transport. *R. eutropha* RHM5-GR-Mtr strains (Table S4.1) were inoculated in bioelectrochemical reactors with an applied voltage of ~1.7V under light or dark over 5 days (Suppl Fig. S4.6c), whilst CO_2 was continuously pumped in as the sole carbon source. The results showed that cells grew on CO_2 in the presence of light, and all controls in the dark could not grow (Fig. 4.4f). The OD_{600} of the induced RHM5-GR-Mtr increased to 0.237 over 5-day illumination (Fig. 4.4f). The control group did not show biomass production, ruling out the possibility of H_2-mediated electron transfer to support growth. These results suggest that the engineered *R. eutropha* were able to perform photoelectron-autotrophic growth, and fix CO_2 powered by the light-driven electron transport chain. Our previous work demonstrated that the addition of exogenous flavin was effective as an electron shuttle mediating electron transfer between GR-expressing *R. eutropha* and the electrode (Suppl Fig. S4.8) (187). Although the electron-shuttling molecules can pass the outer membrane and deliver electrons to the inner-membrane bound electron transport chain, combining the electron mediator with the outer-membrane bound Mtr proteins created a more efficient electron transfer pathway (Suppl Fig. S4.8). In this study, we compared the effects of MtrCAB on cell doubling time and system faradic efficiency. Supported by the Mtr pathway, the doubling time of *R. eutropha* RHM5-GR-Mtr almost halved, and the faradic efficiency increased to 35.4% from 23.9%, compared to *R. eutropha* RHM5-GR using flavin as an electron mediator (Figure 4.4g and h). The total charge transfer of the photoelectrochemical system with *R. eutropha* RHM5-GR-Mtr increased to 105 coulombs, a 54.4% improvement compared to 68 coulombs achieved by the system with *R. eutropha* RHM5-GR. These results suggest that the expression of the outer membrane-bound MtrCAB establishes an efficient electron transfer path connecting extracellular electrons with central carbon metabolism.

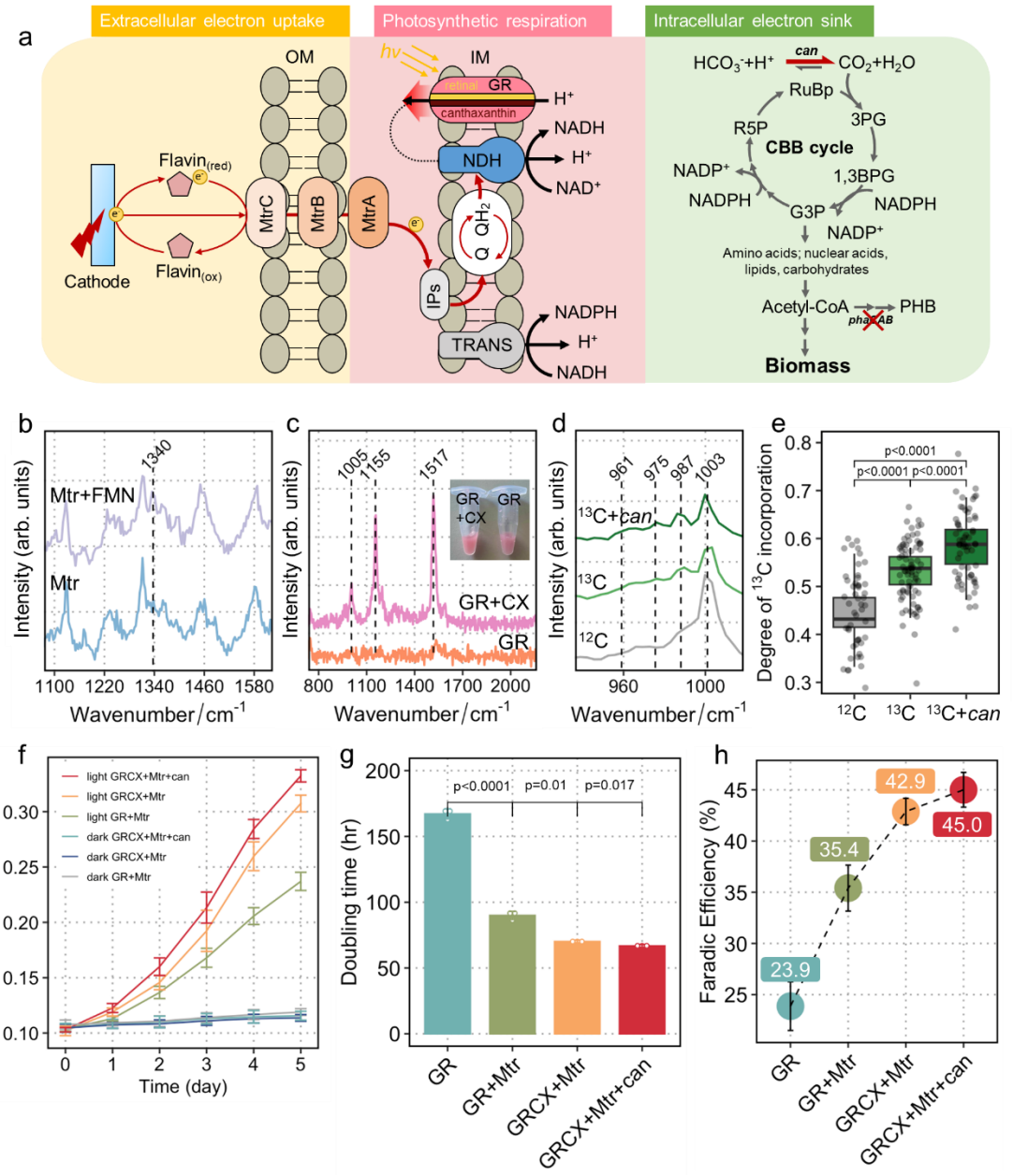


Figure 4.4. Photoelectro-autotrophic growth of RMH5-GR-Mtr. (a) The photoelectrophic system can be divided into extracellular electron uptake, photosynthetic respiration and intracellular carbon sink (OM: outer membrane; IM: inner membrane; IPs: inner-membrane proteins; NDH: NADH dehydrogenase; TRANS: transhydrogenase; Q: quinones). (b) A typical Raman spectrum of an RMH5-GR-Mtr cell with Mtr-bound FMN identified by a band at ~1340 cm^{-1}. (c) A typical Raman spectrum of an RMH5-GR-Mtr cell with canthaxanthin (CX) identified by three bands at ~1005, 1155 and 1517 cm^{-1}. Cell suspensions of induced RHM5-GR-Mtr with and without CX. (d) Cells grown in ^{13}C-bicarbonate exhibited isotopic Raman shifts from 1003 cm^{-1} to 987, 975 and 961 cm^{-1} (e) Comparison of the degree of ^{13}C-bicarbonate incorporation of strains with and without *can* overexpression (the number of measured individual cells = 241). The lower and upper quartiles are drawn as lines outside the box. The rectangle in the box plots represents the second and third quartiles with a line inside representing the median. The whiskers indicated the minima and maxima. (f) Growth profiles of RMH5- GR-Mtr with and without canthaxanthin under light and dark conditions (Data show means ± SD of three biological replicates). (g) Comparison of generation time of strains with GR, GR-Mtr, GR-canthaxanthin complex (GRCX)-Mtr and GRCX-Mtr-*can* (Data show means ± SD of three biological replicates). (h) Comparison of faradaic efficiency of strains with GR,

GR-Mtr, GRCX-Mtr-CX and GRCX-Mtr-*can* (Data show means ± SD of three biological replicates). Statistics were performed with two-sided Student's t-test (Exact p values are provided in the figures).

Proton motive force is the key driver that determines the kinetic rate and overall performance of the system. Therefore, to further increase the proton pumping of the photosystem, canthaxanthin was added as an antenna of GR to improve the capture of light energy (Figure 4.4a). The GR-canthaxanthin complex was reported to possess a 5-fold proton pumping capacity compared to the sole GR (202). We resuspended the *R. eutropha* RHM5-GR strains with or without canthaxanthin in an unbuffered solution and tracked the extracellular proton concentration changes over 1 minute in the light. The presence of canthaxanthin resulted in almost doubling ΔpH compared to the strain with GR alone (Suppl Fig. S4.9). Single-cell Raman analysis revealed bands at 1005, 1155 and 1517 cm^{-1} in the engineered cells when canthaxanthin was introduced, in contrast to the cells without canthaxanthin, and these bands are consistent with the Raman spectra of pure canthaxanthin chemical (Figure 4.4c and Suppl Fig. S4.7). The addition of canthaxanthin changed the colour of the suspension of GR-expressing cells from pink to red (inset in Figure 4.4c), which is consistent with the previous study (202). In the presence of canthaxanthin, the doubling time of the photo-electrotrophic growth decreased by 22% to 70 h (Figure 4.4g) and the efficiency increased by 21% to 42.9% (Figure 4.4h) compared to the control strain with GR only. This suggests that the GR-canthaxanthin complex can significantly enhance light harvesting of photosynthesis in this artificial system.

In addition to the energy generation module, the module of CO_2 fixation can also be improved by overexpressing a native carbonic anhydrase *can* which catalyses the interconversion of bicarbonate and CO_2 (203). A portion of CO_2 combines with water to form bicarbonate which is then transported inwards to cells, the overexpression of *can* is thus expected to accelerate the interconversion between HCO_3^- and CO_2 and increase the CO_2 utilisation rate. When ^{12}C-formate and ^{13}C-bicarbonate were used as the substrates to culture the *can*-expressing RHM5, single-cell Raman analysis showed isotopic shifts of the phenylalanine band at 1003 cm^{-1} to 987, 975, and 961 cm^{-1}, indicating incorporation of ^{13}C from bicarbonate into biomass (Figure 4.4d and Suppl Fig. S4.10). We further calculated the degree of the ^{13}C incorporation and found a higher ^{13}C content in *can*-expressing RHM5 compared to controls (Figure 4.4e). In the photoelectrochemical system, the overexpression of *can* further reduced the generation

time to a minimum of 67.3 h (Figure 4.4f) which is comparable to that of a native anoxygenic phototrophic bacterium *Rhodopseudomonas palustris* under electrochemical conditions (~50 h) (190). The Faradic efficiency of the engineered strain RHM5-GR-Mtr-*can* with additional canthaxanthin can reach 45.0% (Figure 4.4h), indicating that our modular engineering strategies can effectively optimise artificial photosynthesis.

4.4 Discussion

This research demonstrates that an artificial photosynthetic system can be established by redesigning a non-phototrophic bacterium *R. eutropha*. This system can be potentially extended to transform other non-photosynthetic bacteria into photosynthetic forms. The artificial photosynthetic system was inspired by natural photosynthesis. We have developed an electrochemical system powered by light energy, to split water, mimicking the function of photosystem II. To achieve the function of photosystem I for the regeneration of NADH/NADPH, rhodopsin was incorporated to generate proton motive force, facilitating the process of electron transfer (Figure 4.5). Unlike common H_2-mediated microbial electrosynthesis (93), we engineered a transmembrane conduit Mtr complex as an interface between an extracellular cathode and the intracellular electron transport chain. Such electron transfer efficiency, in theory, could be comparable to an H_2-mediated system (204). To rule out hydrogen generation and ensure that the Mtr-mediated electron transfer was the major mechanism, a relatively low potential at ~1.7 V was applied with no evolution of hydrogen detected in the headspace (Suppl Fig. 4.4c). The control condition in the absence of light showed no cell growth (Figure 4.4f), consistent with the previous reports that low potential conditions are insufficient to support cell growth (93, 139). The formation of the photosynthetic electron transport chain designed in this study is fundamentally similar to natural photosynthesis, in which electrons are transferred via a series of redox enzymes accompanied by proton movement, whilst avoiding the generation of intermediates such as H_2 (93) and formate (92). Such electrons and protons interactions drive the photochemical reactions.

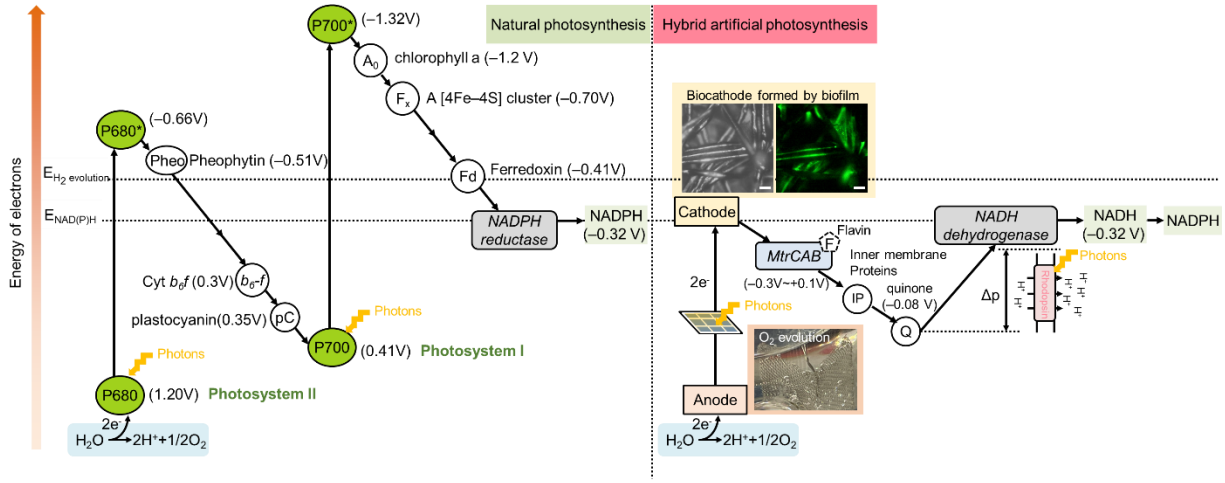


Figure 4.5. Schematic illustration of the light reaction pathways of natural photosynthesis and designed artificial photosynthesis. Potentials for hydrogen evolution reaction ($E_{Hydrogen\ evolution}$) and NAD(P)H ($E_{NAD(P)H}$) synthesis are highlighted by dashes lines. Part of redox enzymes are omitted. Oxygen evolution with O_2 bubbles was observed on the anode, and biofilms were observed on the cathode with brightfield microscopic image and FITC fluorescence image of biofilms attached to the cathode using SYTO™ 9 staining. The Scale bars represent 20 μm.

The engineered photo-electrotrophic *R. eutropha* in this study is similar to the anoxygenic phototroph *Rhodopseudomonas palustris* which is a model bacterium for studying phototrophic extracellular electron uptake (190). Both the genetically engineered *R. eutropha* and the native *R. palustris* are phototrophic; however, their photosystems are unable to solely drive CO_2 fixation due to the absence of photosystem II which is essential for water splitting and electron generation. In the presence of an electrode, both microorganisms are able to harvest electrode-supplied electrons to drive CO_2 fixation pathway in the light. However, the underlying mechanisms of these microbial systems are different. The engineered *R. eutropha* employs rhodopsin to generate proton motive force. We used the synthetic design to couple proton movement with electron transfer to generate the energy required for CO_2 fixation. In contrast, *R. palustris*'s photosystem P_{870} naturally involves electron transfer and can excite electrons in the light (190). Although the synthetic design showed comparable performance in supporting photo-electroautotrophic growth, further investigations are needed to deepen our understanding of the photosynthetic electron transport chain.

In the process of electron transfer in the engineered *R. eutropha*, the native biomolecule plays an important role in obtaining electrons from the Mtr pathway. In the model electroactive bacterium *S. oneidensis* MR-1, the outer-membrane MtrCAB pathway is usually coupled with an inner-membrane protein CymA to involve electron transfer

(205). However, a recent study on the engineered *E. coli* with an Mtr pathway showed that CymA might not be necessary for inward electron transport (206). In addition, several other inner-membrane enzymes such as NapC have been suggested to perform the same function as CymA (196). Furthermore, a recent study of *S. oneidensis* reported hydrogenase can obtain electrons from the Mtr pathway (207). Inspired by the finding in *S. oneidensis* MR-1, we propose that, in the native system of *R. eutropha*, the periplasm-facing membrane-bound hydrogenase could also be involved in Mtr-mediated inward electron transfer. This study demonstrates that the expression of the MtrCAB complex enhances extracellular electron transfer in *R. eutropha*. Nevertheless, the enhancement in electron transfer remains limited compared to other heterologous microorganisms, such as *E. coli* which achieved an approximate 2 to 6-fold increase in the electron transfer efficiency through the Mtr pathway expression (196, 208). This observed limitation could be attributed to relatively low MtrCAB expression in *R. eutropha*. The expression of the Mtr pathway can potentially be improved by optimisation of codon and ribosome binding site, as well as the addition of precursors like 5-aminolevulinic acid (209) for heme synthesis. Additionally, the introduction of additional proteins such as periplasmic small tetraheme cytochrome (STC) may further enhance electron transfer within the periplasmic space (209). The investigation of heterologous Mtr pathway expression in non-native bacteria has received considerable attention in recent years (196, 208, 209). The introduction of Mtr pathway has improved the extracellular electron transfer of *R. eutropha* in this study (Figure 4.4h). However, the exact functionality of the Mtr expression in *R. eutropha* and other heterologous bacteria requires more rigorous verification. For example, there is a remote possibility that MtrCAB may not be directly involved in electron transfer but, instead, might increase membrane permeability, enhancing electron transfer via endogenous electron mediators such as flavins and quinones.

The reversing function of NADH dehydrogenase is a key to regenerating NADH (124). The reverse electron transfer from the quinol pool (with a midpoint potential, E_m, approximately – 0.08 V vs. SHE) to NAD^+ (E_m = –0.32 V vs. SHE) is thermodynamically unfavourable (Figure 4.5). The reversed process requires a highly reduced quinol pool to supply electrons and a high proton motive force to drive protons back through the NADH dehydrogenase in the reverse direction to forward catalysis. In this study, electrons flow inwardly from the external electrode to the Mtr pathway

then leading to the reduction of the quinol pool. The effective potential of the highly reduced quinol pool should be more negative than its electrochemical midpoint potential and approached NADH potential. In the meantime, the proton motive force generated by rhodopsin facilitated the NADH dehydrogenase-mediated reverse electron flow for NADH regeneration. In *R. eutropha*, there are two types of NADH dehydrogenase, namely *nuo* and *ndh* (198). *nuo* is a proton-translocating protein and *ndh* is a non-proton pumping membrane-bound protein. According to a previous study of *S. oneidensis*, *nuo* is critical to inward electron transfer from the electrode for NADH generation (210). In this system, the NADH generation was impeded by the addition of cyanide m-chlorophenyl hydrazone (CCCP), a protonophore (Suppl Fig. S4.11). Therefore, it is logical to reason the significant role of the proton-translocating *nuo* in *R. eutropha* in the process of inward electron transfer for NADH generation.

In this system, the proton motive force primarily relies on the photoreaction of the proton-pumping rhodopsin. There are two strategies for enhancing the proton pumping of rhodopsin. One approach is increasing light intensities, thereby elevating the proton pumping rate of the rhodopsin. We found that increasing light intensities led to enhanced biomass increases in *R. eutropha* RHM5-GR-Mtr (Suppl Fig. S4.12). The other approach is binding an antenna molecule to rhodopsins. In nature, microorganisms cannot control the light intensities of natural light, but they synthesise the antenna molecules to bind with rhodopsin for enhanced energy absorption and energy generation (4). In the system presented here, the exogenous antenna molecule canthaxanthin was introduced which can be potentially biosynthesised. The addition of canthaxanthin did not adversely affect the viability of cells (Suppl Fig. 4.13). Furthermore, the GR-canthaxanthin complex was reported to have higher thermal stability compared to GR (202).

Reactive oxygen species (ROS) are a potential concern in photo-electrosynthesis because of their toxicity to cells (92, 93, 139). In this study, a high proton motive force and reverse electron transfer could be possible factors contributing to ROS generation. To avoid the risk of ROS generation, we employed a dual-chamber electrochemical reactor separated by a Nafion proton exchange membrane (PEM) to reduce the effect of anodic oxygen generation on microbial carbon fixation in the cathodic chamber. This design ensures that oxygen produced from water splitting in the anodic chamber cannot permeate the PEM, thus preventing its entry into the cathode chamber to generate ROS.

In addition, the N_2/CO_2 syngas were continuously pumped into the cathode chamber to maintain an anaerobic condition. Although the anaerobic cathode chamber can effectively avoid ROS generation, it could sacrifice the cellular energy generated via the aerobic respiration pathway. Therefore, a strategic approach might involve controlling the oxygen level while simultaneously enhancing microbial resistance to ROS. Achieving a balance between reducing ROS effects and improving energy generation would be important for the future scaling-up and long-term operation of the system. There are some strategies to reduce ROS when bacteria are exposed to the risk of ROS. For example, engineering bacteria to express lycopene has been shown to improve microbial resistance toward ROS (103). The addition of antioxidants, such as glutathione, has been shown effectively to reduce ROS in the system (148).

This artificial photosynthesis system is relatively simple, in contrast to natural chlorophyll-based photosynthesis which contains complex membrane structures after millions of years of evolution. Calculations can be made with respect to the overall photosynthesis efficiency of this system. But as yet, such calculations will have to be based on so many assumptions that a meaningful number is not yet attainable. Chlorophyll does not absorb photons in the photosynthetically available radiant (PAR) waveband evenly, with only a low degree of absorbance occurring in the green region. In contrast, rhodopsin strongly absorbs green-blue light (~500 nm). The complementary light absorption offers the possibility of integrating chlorophyll and rhodopsin photosystems in either a pure culture (211) or a mixed community (3) to maximise the utilisation of solar energy. The artificial photosynthesis outlined in this research is modularised, allowing for further optimisation. In this study, the addition of flavin and canthaxanthin enhanced the electron transfer rate and the proton pumping rate, respectively. Material engineering such as electrode modification can provide effective approaches to further increasing energy efficiency (212). It is even possible to achieve maximum utilisation of light energy by extending rhodopsin's light absorption to non-visible wavelengths, which has already been shown feasible for the GR photosystem (144).

Many studies have demonstrated that microbial rhodopsins are major contributors to solar energy harvesting in the ocean, compared to chlorophyll (1, 3, 213, 214). Antennas such as canthaxanthin are found binding to rhodopsin and may have an important effect on rhodopsin phototrophy (4). Rhodopsin phototrophy is recognised

as independent of electron transfer and does not involve redox processes. In recent years, the proton motive force generated by rhodopsin has been demonstrated to drive NADH dehydrogenases in reverse, which couples the rhodopsin-based photosystem with the electron transport chain (124, 187). Interestingly, there is evidence showing transmission of Mtr-mediated extracellular electron transfer among oceanic bacteria (215). In addition to the solid-phase electrode, syntrophic metabolisms (216) and inorganic minerals (217) could be used as natural electron sources for bacteria growth if they contain both rhodopsin and Mtr complexes. In nature, the ubiquity of rhodopsins might allow microbes with Mtr pathways to use various electron sources besides just water splitting. Therefore, our demonstration of artificial photosynthesis in *R. eutropha* could guide future research into connecting rhodopsin photosystems to extracellular electron transfer systems at the gene level in oceanic environments. It is plausible to hypothesise that autotrophic microorganisms, equipped with Mtr-like proteins and rhodopsin in nature, could potentially fix CO_2 powered by solar energy.

4.5 Materials and methods

4.5.1 Bacterial strains, culture conditions and plasmid construction

All bacterial strains, plasmids, and primers used in this study are shown in Table S4.1 and Suppl Fig. S4.14. The primers used in this study are shown in Table S4.2. *E. coli* strains were grown in Lysogeny Broth (LB) at 37 °C under aeration by shaking at 200 rpm. *R. eutropha* and *S. oneidensis* strains were grown in LB broth at 30 °C under aeration by shaking at 150 rpm. If required, antibiotics (Sigma-Aldrich) were added as follows: 10 μg ml^{-1} gentamicin and 10 μg ml^{-1} tetracycline for *R. eutropha*; 12.5 μg ml^{-1} tetracycline for *E. coli*. Before the preculture of bio-electrochemical experiments, *R. eutropha* strains were grown in TSB (Tryptic Soy Broth) and minimal medium with fructose as the carbon source. The minimal medium was prepared and filter sterilized, composed of 6.74 g/L $Na_2HPO_4 \cdot 7H_2O$, 1.5 g/L KH_2PO_4, 1.0 g/L $(NH_4)_2SO_4$, 1 mg/L $CaSO_4 \cdot 2H_2O$, 80 mg/L $MgSO_4 \cdot 7H_2O$, 0.56 mg/L $NiSO_4 \cdot 7H_2O$, 0.4 mg/L ferric citrate, 200 mg/L $NaHCO_3$, 1mL/L concentrated metals solution (1.5 g/l $FeCl_2 \cdot 4H_2O$, 0.19 g/l $CoCl_2 \cdot 6H_2O$, 0.1 g/l $MnCl_2 \cdot 4H_2O$, 0.07 g/l $ZnCl_2$, 0.062 g/l H_3BO_3, 0.036 g/l $Na_2MoO_4 \cdot 2H_2O$, 0.025 g/l $Na_2WO_4 \cdot 2H_2O$ and 0.017 g/l $CuCl_2 \cdot 2H_2O$), 10 ml/L concentrated vitamin solution (2 mg/L D-biotin, 2 mg/L folic acid, 10 mg/L pyridoxine

HCl, 5 mg/L thiamine HCl, 5 mg/L nicotinic acid, 5 mg/mL D-pantothenic acid, hexacalcium salt, 0.1 mg/L cobalamin, 5 mg/L p- aminobenzoic acid, 5 mg/L α-lipoic acid and 5mg/L FMN) and 10 mL/L concentrated amino acids solution (2 g/L L-glutamic acid, 2 g/L L-arginine, and 2 g/L D, L-serine), and pH was adjusted to 7. For the anabolic test of the overexpression carbonic anhydrase in *R. eutropha*, *the R. eutropha* mutants with pLO11a-can were pre-grown overnight in the minimal medium with and without 0.1% (w/v) arabinose, respectively, using 20 mM fructose as carbon sources. Then the precultured strains were washed three times with the minimal medium and inoculated in the minimal medium with 20 mM formate and 10 mM ^{13}C-bicarbonate (initial OD = 0.5). After 24 hours of culture, cells were collected for single-cell Raman analysis to investigate the incorporation of bicarbonate.

The plasmid pLO11a-Mtr containing the MtrCAB biosynthesis gene cluster was introduced to synthesise the MtrCAB complex in *R. eutropha* H16-Mtr. The plasmid pLO11a-GR containing the *Gloeobacter* rhodopsin gene (GR) was introduced to make GR in *R. eutropha* H16-GR (187). pLO11a-GR-Mtr containing GR and MtrCAB was introduced to *R. eutropha* Δ*pha* to make RHM5-GR-Mtr. pLO11a-GR-Mtr-*can* containing GR, MtrCAB, and *can* was introduced to make *R. eutropha* Δ*pha* (RHM5) to make RHM5-GR-Mtr-*can*. Induction of strains transformed with the pLO11a expression vector containing the arabinose-inducible P_{BAD} promoter was carried out by growth to log phase and the addition of 0.1% (w/v) L-arabinose (Sigma-Aldrich) and overnight growth at 30 °C for *R. eutropha*. Induction of GR expression was accompanied by the addition of exogenous *trans*-retinal (Sigma-Aldrich) to a final concentration of 5 μg/mL. Exogenous *trans*-canthaxanthin (Sigma-Aldrich) dissolved in dimethyl sulfoxide was added as an antenna for GR with a final concentration of 5 μg/mL. Flavin mononucleotide (FMN) was added at a final concentration of 10 μmol/L to investigate the interaction between outer-membrane cytochrome Mtr and FMN.

Cloning procedures were performed according to standard protocols. Polymerase chain reaction (PCR) was carried out using Q5 DNA polymerase (NEB, UK) and synthesised primers (Sigma-Aldrich) according to the manufacturer's instructions. The construction of plasmid was performed in *E. coli* DH5α using HiFi assembly (NEB, USA). After extraction and purification, the plasmid was transferred into *R. eutropha* strains by conjugation.

4.5.2 Single-cell Raman spectra (SCRS) measurements and analysis

Single bacterial cells, their metabolic profiles and pure standard chemicals were characterized by Raman microspectroscopy. Prior to the measurements, bacterial cells were washed three times with distilled water to remove traces of culture medium and extracellular metabolites. The cells were observed under a microscope after washing. Cells were diluted so that individual bacteria could be observed with a 1.5-µl suspension dropped onto an aluminium-coated slide and air dried. Raman spectroscopic acquisition was performed using a LabRAM HR Evolution confocal Raman microscope using a 100×/0.75 air objective (HORIBA, UK). Single-cell Raman spectra (SCRS) were obtained using a 532-nm neodymium-yttrium aluminium garnet laser with a 300 grooves mm^{-1} diffraction grating and were acquired in the range of 100–3200 cm^{-1}. The laser power was set at ~80 mW which was attenuated by neutral density (ND) filters before focusing onto the samples. Spectra were recorded with LABSPEC 6 software (HORIBA, UK). All raw spectra were pre-processed by cosmic ray correction, polyline baseline fitting and subtraction and vector normalization of the entire spectral region. Linear discriminant analysis (LDA) was used for dimension reduction of single-cell Raman spectroscopy to aid visualization at the single-cell level. All analysis and plotting were done under an R 4.2.2 environment.

4.5.3 Analysis and quantification of intracellular biomolecules

Single-cell Raman spectroscopy was employed to characterise biomolecules of cytochromes, rhodopsin, and canthaxanthin-GR as well as C–D band and phenylalanine band for stable isotope probing. A green incident laser light with a wavelength of 532 nm was employed for our Raman measurements. Importantly, all the biomolecules we characterized with Raman absorb visible light at wavelengths very close to the incident light. For example, cytochromes absorb light at 530 nm (152), rhodopsin at 520 nm (74), and canthaxanthin-GR at 485 nm (202). This proximity in wavelengths results in a resonance effect, which significantly enhances the Raman scattering cross-section and consequently improves the signal-to-noise ratios by orders of magnitude. Furthermore, the phenylalanine band selected for ^{13}C-labelling experiments contains an aromatic ring that also contributes to this resonance effect. The deployment of Raman-deuterated water has been widely applied in probing microbial activities (149) and offers a unique, universally applicable approach for non-destructively measuring single-cell activities

(199).

For characterising cells under induced or uninduced conditions with arabinose, triplicates were performed in each condition and Raman spectra were acquired using a 25% power filter and 3 to 5-second acquisition time with high signal-to-noise ratios. Raman bands at 748 (pyrrole breathing mode), 1128 (υ(CN) stretching vibrations), 1312 (δ (CH) deformations) and 1584 cm^{-1} (υ (CC) skeletal stretches) were attributed to cytochromes. Quantification of cytochrome *c* was achieved by integrating band areas at each of these four band positions. Intracellular phenylalanine was identified and quantified by the phenylalanine band centred at 1003 cm^{-1}. Raman spectra of pure riboflavin 5′-monophosphate sodium salt hydrate (Sigma-Aldrich, UK) in powder as well as in water solution was measured as a standard to identify a band at 1340 cm^{-1} as an indicator for quantification of flavin, which is assigned to the middle ring vibration of the tricyclic isoalloxazine structure of the flavin. GR complex was characterized by Raman microscopy using a 1% power filter and 1-second acquisition time. The low power and short acquisition time were used to prevent photobleaching of the GR chromophores. SCRS of strains with the pLO11a expression vector, either with or without the addition of L-arabinose were measured in triplicates. GR complexes were identified by a band at ~1530 cm^{-1} above the background noise in the SCRS. Quantification of biomolecules was done by integrating the area of the corresponding Raman bands and represented as boxplots. The lower and upper quartiles are drawn as lines outside the box. The rectangle in the box plots represents the second and third quartiles with a line inside representing the median. Sample means were compared by using Welch's two sample t-test for unequal variance.

The degree of ^{13}C incorporation into biomass (200) was determined by calculating the isotopic shifts of phenylalanine from 1003 cm^{-1} to 987, 975, and 961 cm^{-1}. Depending on different ^{13}C substitutions on the phenylalanine ring, a total of four possible Raman positions of the $^{13}C/^{12}C$ mixture existed for possible isotopomers. Due to the symmetric structure, substitutions at only three carbon sites on the phenyl ring can affect the vibrational modes hence the wavenumbers: the bands at 1003 cm^{-1} correspond to structures where all three carbon are ^{12}C; the bands at 987 cm^{-1} occur when any of the three carbon sites are substituted with ^{13}C; the 975-cm^{-1} bands occur when any two of the sites are ^{13}C; and the bands at 961 cm^{-1} only appear when all three carbon sites are ^{13}C and hence occur only with high assimilation from ^{13}C -bicarbonate into biomass.

The degree of ^{13}C incorporation was calculated by the ratio of total ^{13}C to total ^{13}C and ^{12}C as follows, in which A represents the area under the curve centred at a defined wavenumber:

$$\text{Total } ^{13}\text{C incorporation} = \frac{A_{961cm^{-1}} + \frac{2}{3}A_{975cm^{-1}} + \frac{1}{3}A_{987cm^{-1}}}{A_{975cm^{-1}} + A_{987cm^{-1}} + A_{1003cm^{-1}}} \quad (1)$$

4.5.4 Determination of NADH and NADPH levels

For measurements of intracellular reductant levels including NADH and NADPH, cells were harvested from the working chamber and pre-treated according to the manufacturer's instructions. $NADH/NAD^+$ and $NADPH/NADP^+$ ratios were determined using a NAD/NADH Assay Kit (Abcam, USA) and an NADP/NADPH Assay kit (Sigma-Aldrich, UK), respectively. They were measured using a colourimetric assay with a microplate reader (BioTek Corporation, UK) equipped with Tecan SPARKCONTROL Dashboard software to detect the wavelength at 450 nm.

4.5.5 Fluorescence microscopy to visualize biofilm on the electrode

The Raman microscope chassis was modified with an epifluorescence system in consultation with the manufacturer (HORIBA, UK). An LED lamp and a FITC filter block were used to visualize the fluorescence of the engineered cells stained by SYTO™ 9 (Thermo Fisher Scientific, UK) with a 20×/0.4. The final images were processed with background denoising using ImageJ2 (version number: 2.3.0/1.53f).

4.5.6 Microbial photoelectrochemical system

A dual-chamber bioreactor (70 mL of total volume) separated by a Nafion membrane (only allowing proton transfer) was used as a bio-photoelectrochemical system. The microbial photoelectrochemical experiments were performed in a three-electrode configuration on a multichannel potentiostat (PalmSens, Netherlands). For the anode chamber, a stainless-steel mesh was used as the counter electrode. For the cathode chamber, the working electrode was made of 2.5 × 2.5 cm^2 carbon paper (H23, Quintech, UK) and an Ag/AgCl reference electrode (3M KCl, RE-5B, BASi, USA) was installed for measuring the potentials. The anodic electrolyte was made of 50 mM KH_2PO_4 and 50 mM K_2HPO_4 (pH=7.2), and the cathodic electrolyte was the same as the above-mentioned minimal medium. The working chamber was continuously

agitated by a magnetic stirrer at 30 °C. For the photoelectrochemical experiments, 5 m of white LED light strips encircled the exterior of the working chamber to ensure even light distribution during the experiment, and illumination intensity was monitored by a photometer.

4.5.7 Electrochemically driven nitrate reduction

To test electron transfer from the electrode to cells, arabinose-induced and uninduced *R. eutropha*-Mtr were inoculated to the cathode of the photoelectrochemical system. *R. eutropha*-Mtr strains were first activated 24 h in TSB in the presence of 10 μg ml^{-1} tetracycline. Then 200 μL of bacterial cultures were inoculated into 10 mL of the fresh minimal medium on 20 mM fructose with 10 μg ml^{-1} tetracycline. For the Mtr induction group, 0.1% (w/v) L-arabinose was added to induce the gene expression. After overnight preculture in a shaker with 150 rpm at 30 °C, the cells were harvested by centrifugation at 3000 g for 3 min and washed three times with the minimal medium to remove organics. The cell pellets were resuspended in the minimal medium and the OD_{600} was adjusted to ~0.5 before transfer to the working chamber which was continuously bubbled with N_2 gas to maintain an anaerobic environment. Cells were subjected to anodic conditions at +200 mV (vs. Ag/AgCl) for two days to exhaust any potential internal electron storage, such as PHB, and increase cell adhesion to the electrode. After assimilation, the mineral medium in the working chamber was replaced with the fresh medium and planktonic cells were resuspended in the reactor. Then the electrode potential was switched to the cathodic condition at –500 mV (vs. Ag/AgCl). At an intermediate time point, 20 mM of nitrate was added to monitor the current change by a potentiostat (PalmSens, Netherlands).

4.5.8 Electrochemically driven photosynthetic electron transport chain for reductant generation

R. eutropha-GR-Mtr was used to test whether the electrode-supplied electrons could be used to regenerate reducing power NADH and NADPH. The uninduced and induced strains were precultured as above and inoculated into the microbial photoelectrochemical system with an initial OD of ~0.5. During the experiments, the working chambers were poised at –500 mV (vs. Ag/AgCl) and bubbled with N_2. The reactors were illuminated with a white LED light (~150 μmol/s/m^2) or covered with aluminium foil as dark control. After 2 days of *R. eutropha*-GR-Mtr incubation in the

light and dark, cells were harvested from the working chamber for the measurement of NADH and NADPH. To investigate the effect of the proton motive force on the reversing function of NADH dehydrogenase, the induced *R. eutropha*-GR-Mtr strains were incubated in the photoelectrochemical system with illumination for 24 hours and then 100 μM of the proton motive force inhibitor, carbonyl cyanide m-chlorophenyl hydrazone (CCCP) was injected to the working chamber for additional 24-hour incubation. $NADH/NAD^+$ ratios were compared between the CCCP-treated group and the control group with the blank solvent dimethyl sulfoxide.

4.5.9 The use of heavy water (D_2O) to probe phototrophic metabolisms

The *R. eutropha*-GR-Mtr was precultured as described above. The 30% D_2O (v/v) minimal medium was prepared with 99% D_2O (v/v) (Sigma, UK) to replace the spent minimal medium in the working chamber and resuspend the cells pellet. The initial OD was adjusted to ~0.2 before being inoculated into the working chamber which was sparged with N_2 to remove oxygen and then changed to CO_2. After 2 days of incubation, single-cell Raman analysis was used to detect the C−D vibration in the cells.

4.5.10 A hybrid system for light-driven CO_2 fixation into biomass

For light-driven experiments, a two-electrode configuration was performed with the carbon paper as the cathode and platinum as the anode. A commercial polycrystalline solar cell (1.5W, 140 mm×180 mm, RS, UK) was combined with a laboratory-assembled voltage regulator to power the water splitting to generate electrons. To maximise the carbon conversion to biomass, the RHM5 strain, an *R. eutropha* mutant without PHB biosynthetic pathways was used for biomass growth. The precultured RHM5-GR-Mtr strains were treated as above before being inoculated into the cathode chamber. Then cells were pre-grown in the cathode chamber under formatotrophic conditions with 60 mM formate to form a biofilm on the electrode. After 2 days of incubation when the biocathode was established, the spent medium was replaced with fresh medium, and the biomass (OD_{600}) of the planktonic cells was adjusted to ~0.1. The growth experiments were conducted by continuously sparging with an 80:20 mixture of N_2:CO_2 gas under light and dark conditions, gas under light and dark conditions, with induction of GR, GR-Mtr or GR-Mtr-*can*, respectively. Flavin mononucleotide was introduced as an electron mediator to boost electron transfer. ~10 μmol/L of flavin was added at an interval of 24 h to reduce flavin's photochemistry.

4.5.11 Calculations

The electron transfer efficiency ($\eta_{electron}$) of the biomass formation could be calculated by the equation,

$$\eta_{electron} = \frac{nzF}{\text{Charge passed (C)}} \qquad (2)$$

Where *n* is the amount of biomass (using the formula $CH_{1.77}O_{0.49}N_{0.24(93)}$ and 1 OD_{600} corresponding to 0.448 g/L dry biomass) product (mol), *z* is the number of transferred electrons (z = 4 for CO_2 conversion to biomass), *F* is the Faraday constant (96,485 C/mol).

The doubling time (g) of the strains could be calculated by the equation,

$$g = \frac{\ln 2}{\ln(OD_{day5}/OD_{day1})/4} \qquad (3)$$

Where OD_{day5} and OD_{day1} represent the OD values of the planktonic cells on Day 5 and Day 1, respectively.

Data Availability Statement: The data generated in this study are provided in the main text and/or Supplementary information, where the source data are listed in the Source Data file. Source data are provided with this paper.

Acknowledgements

W.E.H. thanks EPSRC (EP/M002403/1 and EP/N009746/1) for financial support. W.E.H gratefully acknowledges funding from EPSRC (EP/M02833X/1) for instrumentation. We thank Prof Kwang-Hwan Jung at Sogang University for providing plasmids of beta-carotene and GR and had helpful discussions. We thank Harris Saeed for making the voltage regulator. We also thank Oliver Lenz at Technische Universität Berlin, Germany for providing wild-type *Ralstonia eutropha* H16 and cloning plasmids.

Author Contributions Statement: W.E.H conceived the original idea; W.T. and W.E.H. designed research; W.T. performed research; I.P.T. contributed new

reagents/analytic tools; W.T., J.X. and W.E.H. analysed data; W.T. and W.E.H. drafted the manuscript, and all authors revised the manuscript.

Competing Interests Statement: W.T., I.P.T., and W.E.H. have filed a provisional patent application (International Patent Application No. PCT/GB2023/052452) with the UK Patent Office related to this work. J.X. has declared no conflict of interest.

Chapter 4 Supplementary Information



Engineering Rhodopsin-Based Artificial Photosynthesis for CO_2 Fixation

Weiming Tu, Jiabao Xu, Ian P. Thompson and Wei E. Huang*

Department of Engineering Science, University of Oxford, Oxford OX1 3PJ, United Kingdom.

*Corresponding author: Wei E. Huang. Email: wei.huang@eng.ox.ac.uk. Tel: +44 1865 283786.

Chapter adapted from publication: ***Nature Communications*** (2023)

DOI: 10.1038/s41467-023-43524-4

Supplementary Methods

Supplementary Method 1

Whole-cell proteins were extracted by FastPrep-24™ Classic Bead Beating Grinder and Lysis System (MP biomedicals). Cell extracts were suspended in lithium dodecyl sulfate. The samples were run in NuPAGE™ 10% Bis-Tris Gel (Invitrogen) at 16 °C. Electrophoresis was initiated at 100 V for 30 minutes and then increased to 180 V for an additional 60 minutes. The 3,3′,5,5′-tetramethylbenzidene (TMBZ) peroxidase stain method was adapted from Thomas (218) to identify cytochromes *c*, as reported by Jensen et al (196). TMBZ was dissolved in methanol to 6.3 mM and mixed in a 3:7 ratio solution with TMBZ solution to 0.25 M Sodium acetate (pH=5). The gel was immersed in the mixture in the dark with periodic mixing for 2 h. Hydrogen peroxide was added to reach a final concentration of 30 mM, and the heme-containing protein bands were visualized 30 min after peroxide addition.

Supplementary Method 2

R. eutropha RHM5-GR-Mtr strains were precultured in TSB medium at 30 °C and induced by 0.1% arabinose, with and without the addition of canthaxanthin, respectively. Then we harvested cells, washed them with unbuffed solution (10 mM NaCl, 10 mM $MgSO_4 \cdot 7H_2O$, and 0.1 mM $CaCl_2$) and resuspended them in the unbuffered solution to obtain an OD_{600} of ~1.5. The cell suspension was placed in the dark until the pH was stabilized, which was measured by Orion Star™ A211 Benchtop pH Meter (ThermoFisher, UK). Following stabilization, the suspension was exposed to illumination with an intensity of ~150 μmol m^{-2} s^{-1} for 1 minute, and the ΔpH was calculated.

Supplementary Method 3

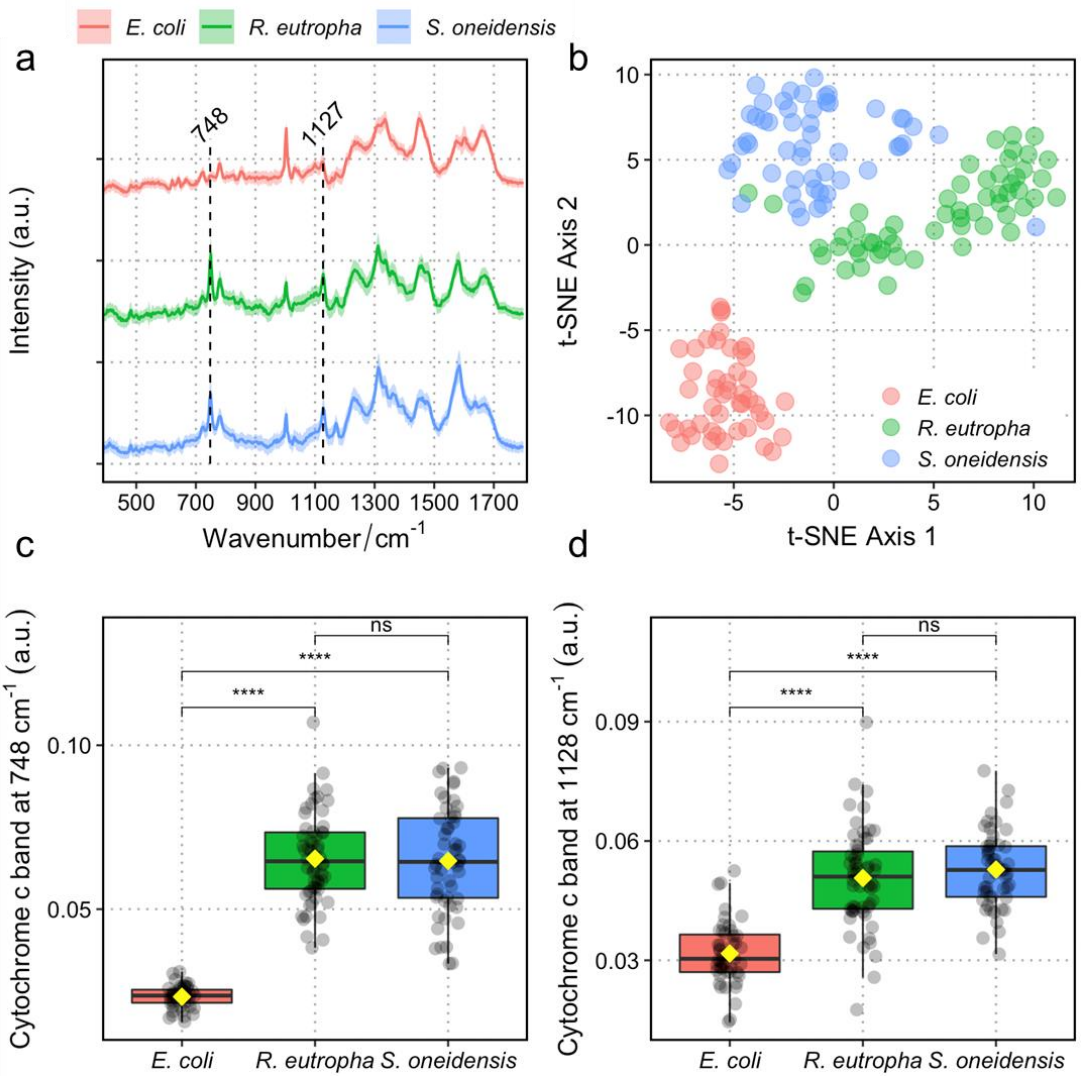
R. eutropha RHM5-GR-Mtr strains were precultured as above, with and without the addition of canthaxanthin, respectively. Subsequently, cells were harvested, washed with phosphate buffer solution (PBS) twice and resuspended in PBS to an OD of 0.6. The cell suspensions were incubated at 30 °C for 120 hours under illumination with an intensity of ~150 μmol/s/m^2, and 100 μL of each dilution was spread on LB agar plates to obtain the Colony-forming unit (CFU) numbers.

Table S4.1. Strains and plasmids used in this study.

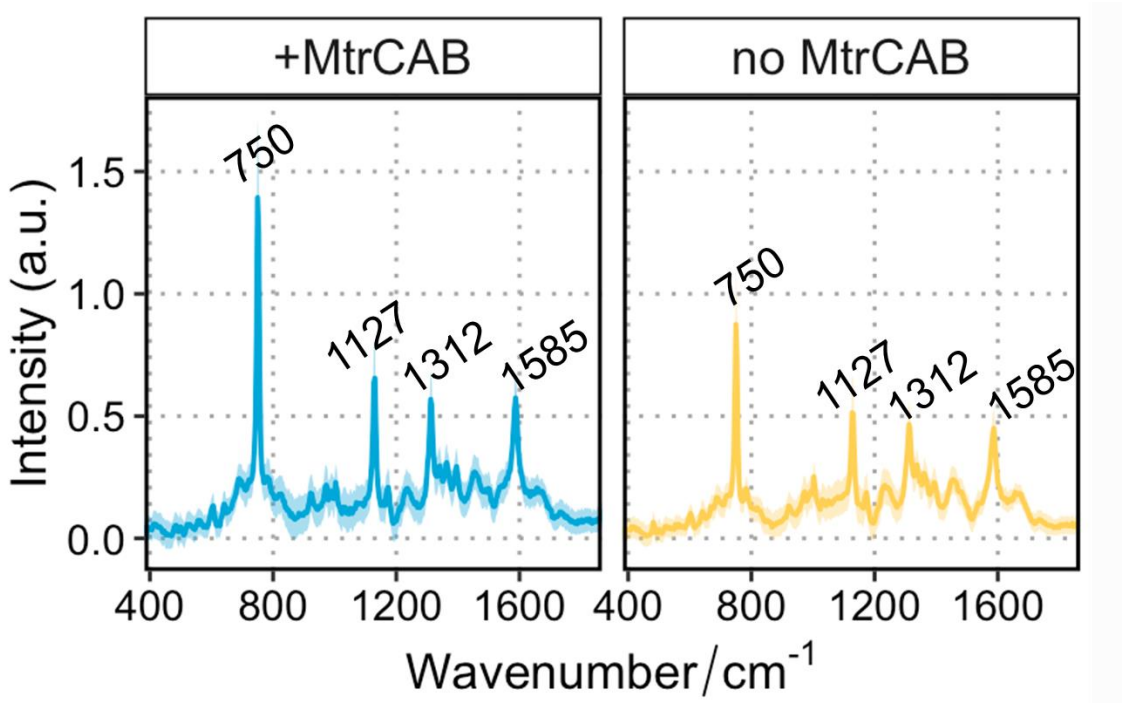
Strains	**Comments**
***E. coli* DH5α**	Commercially obtained (NEW England, UK)
***E. coli* S17**	Commercially obtained (NEW England, UK)
***E. coli* MG1655**	Commercially obtained (NEW England, UK)
***Shewanella oneidensis* MR-1**	Wild-type strain
***Ralstonia eutropha* H16 (ATCC 17699)**	Wild-type strain
***Ralstonia eutropha* H16 Δ*pha* (RHM5)**	Wild-type strain with *phaCAB* operon encoding genes required for conversion of acetyl-CoA to polyhydroxybutyrate (PHB) deleted (gift from Min-Kyu Oh, Korea University, S. Korea).
***R. eutropha*-Mtr**	*Ralstonia eutropha* H16: pLO11a-Mtr
***R. eutropha*-GR**	*Ralstonia eutropha* H16: pLO11a-GR
***R. eutropha*-GR-Mtr**	*Ralstonia eutropha* H16: pLO11a-GR-Mtr
RHM5-*can*	*Ralstonia eutropha* H16 Δ*pha*: pLO11a-*can*
RHM5-GR	*Ralstonia eutropha* H16 Δ*pha*: pLO11a-GR
RHM5--GR-Mtr	*Ralstonia eutropha* H16 Δ*pha*: pLO11a-GR-Mtr
RHM5-GR-Mtr-*can*	*Ralstonia eutropha* H16 Δ*pha*: pLO11a-GR-Mtr-*can*
Plasmids	**Comments**
pLO11a (Tc^r, RK2 *ori*, Mob$^+$)	Expression vector for use in *R. eutropha* with P_{BAD} promoter and downstream cloning sites (gift from Oliver Lenz, Technische Universität Berlin, Germany).
pLO11a-GR [187]	pLO11a containing the gene for GR rhodopsin from *Gloeobacter violaceus* PCC7421
pLO11a-blhDxrCRT-GR [187]	pLO11a containing GR gene and the retinal synthetic gene cluster
pLO11a-Mtr	pLO11a containing *MtrCAB* gene cluster from *Shewanella oneidensis* MR-1
pLO11a-GR-Mtr	pLO11a containing *GR* gene rhodopsin from *Gloeobacter violaceus* PCC7421 and *MtrCAB* gene cluster from *Shewanella oneidensis* MR-1
pLO11a-*can*	pLO11a containing *can* gene from *Ralstonia eutropha* H16
pLO11a-GR-Mtr-*can*	pLO11a containing *GR* gene rhodopsin from *Gloeobacter violaceus* PCC7421, *MtrCAB* gene cluster from *Shewanella oneidensis* MR-1 and *can* gene from *Ralstonia eutropha*

Table S4.2. Primers used in this study.

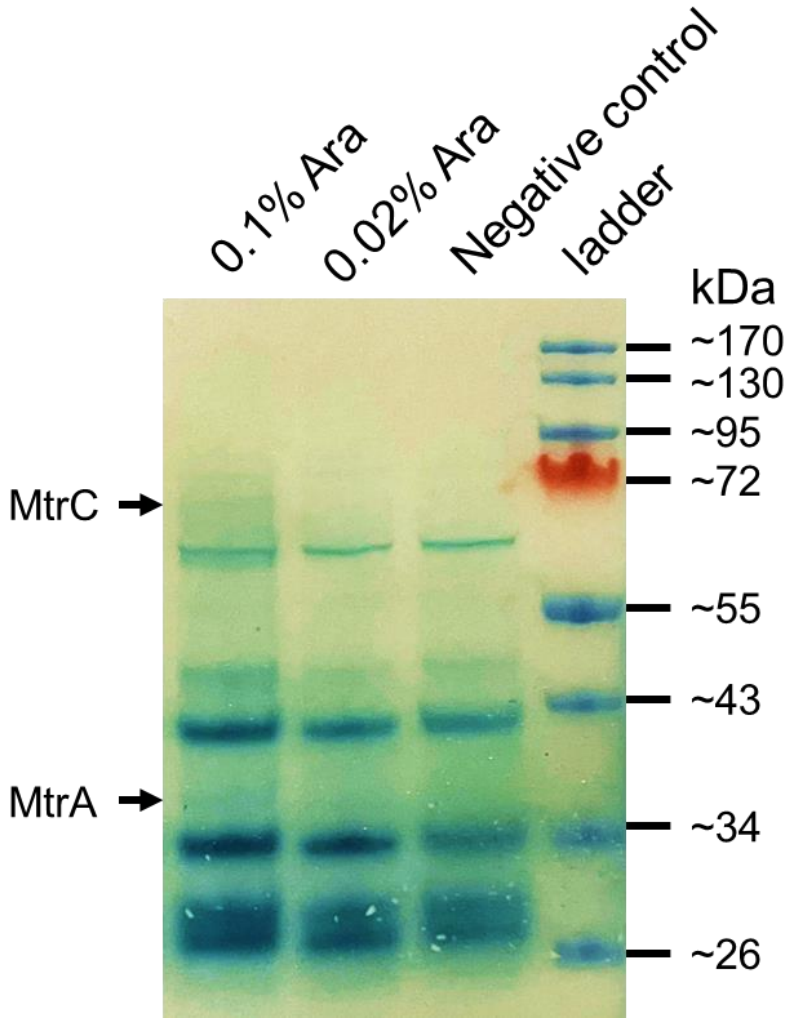
Primer name	Sequence 5’ to 3’
pLO11a-GR1-rv	GCGTTCATCATGGGGTCTCCTCCTTAGCTAG
pLO11a-GR1-fw	CAAACTCTAACGGCCGCAGATCTGC
mtr-rv	AGGAGACCCCATGATGAACGCACAAAAATCAAAAATCG
mtr-fw	TCTGCGGCCGTTAGAGTTTGTAACTCATGCTCAGCATCAG
pLO11a-GR2-rv	CGTCAGTCATGGGGTCTCCTCCTTAGCTAG
pLO11a-GR2-fw	GATCCGCTGACGGCCGCAGATCTGC
can1-rv	ATCTGCGGCCGTCAGCGGATCGACGC
can1-fw	AGGAGACCCCATGACTGACGCCATCGCC
pLO11a-GR3-rv	CGACCCTCCTTCTAGGAGATAAGACTGCCTCCCG
pLO11a-GR3-fw	GATCCGCTGACGGCCGCAGATCTGC
can2-rv	ATCTGCGGCCGTCAGCGGATCGACGC
can2-fw	TTATCTCCTAGAAGGAGGGTCGCATGACTG
pLO11a-Mtr-rv	GAGTGTTGTTCCAGTTTGGA
pLO11a-Mtr-fw	TTATGACAACTTGACGGCTA
pLO11a-blhDxrCRT-GR-rv	TAGCCGTCAAGTTGTCATAA
pLO11a-blhDxrCRT-GR-fw	TCCAAACTGGAACAACACTC



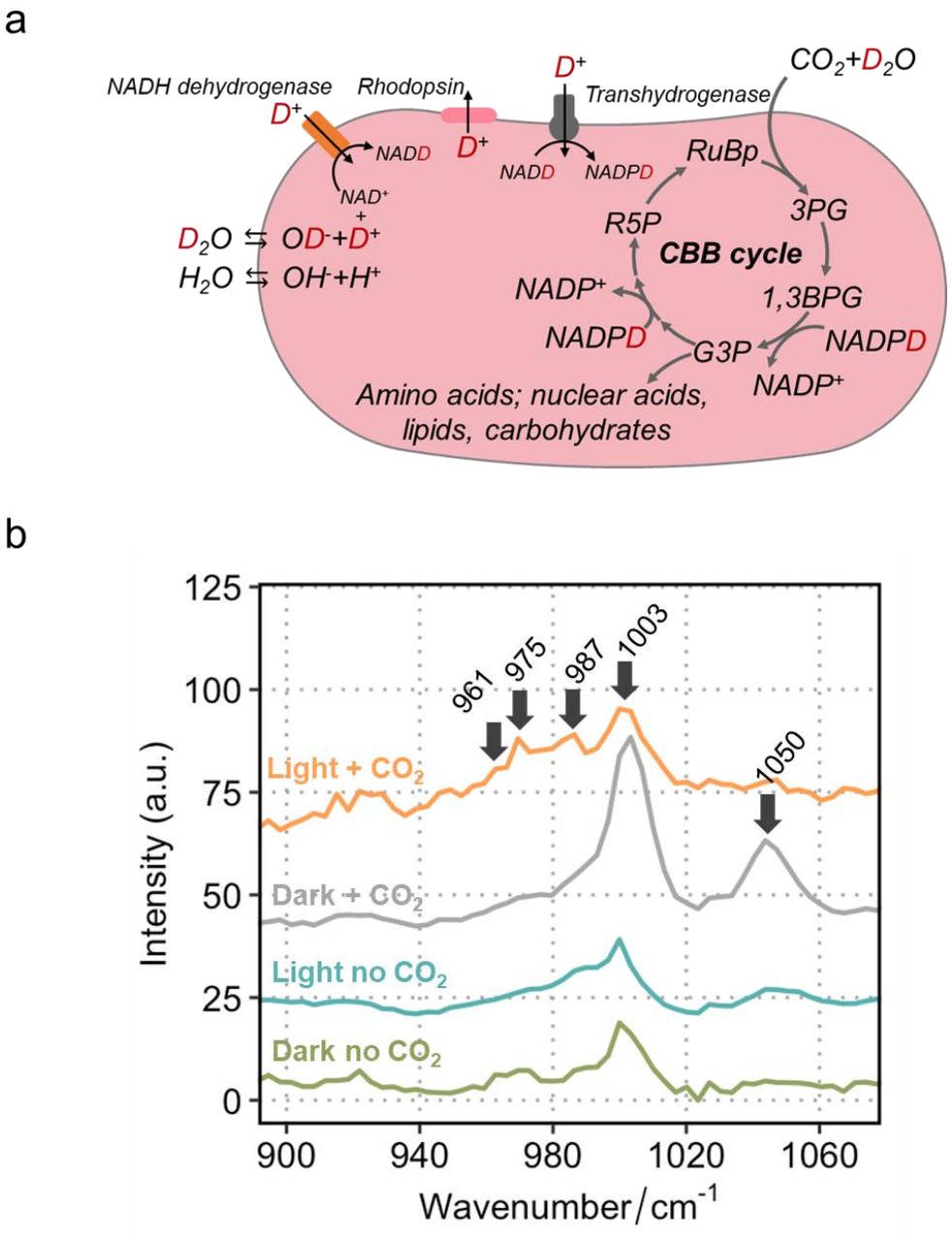
Supplementary figure S4.1. Comparison of average Raman profiles of *E. coli MG*-1655, *R. eutropha* H16 and *S. oneidensis* MR-1. (a) Average single-cell Raman spectrum of *E. coli MG*-1655, *R. eutropha* H16 and *S. oneidensis* MR-1. (b) t-SNE visualization of sing-cell Raman spectrum showing clusters of different strains. (c-d) Semi-quantification of cytochromes levels by integrating Raman bands at (c) 748 and (d) 1128 cm^{-1}. Statistics were performed with two-sided Student's t-test (****: $p < 0.0001$).



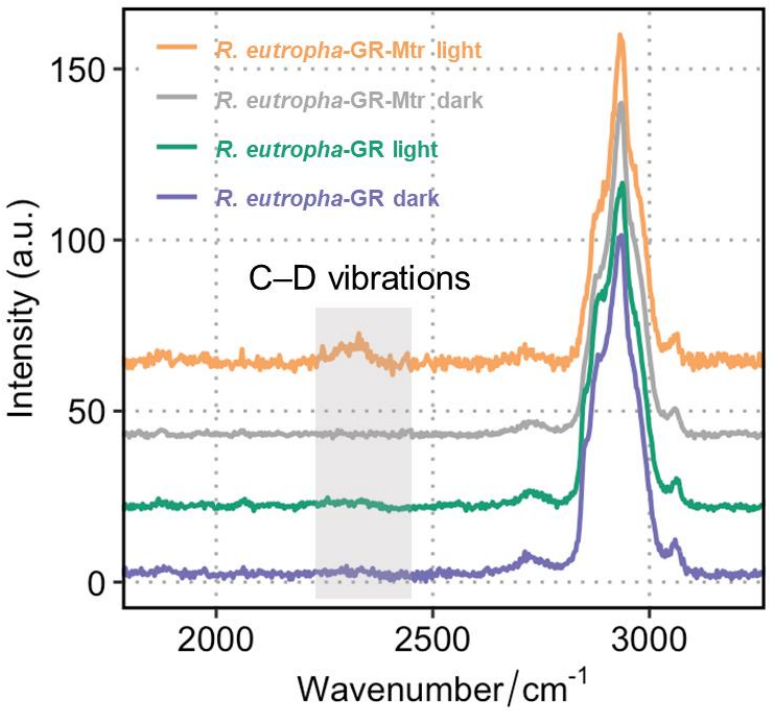
Supplementary figure S4.2. Comparison of induced and uninduced *R. eutropha*-Mtr. Average single-cell Raman spectrum of induced and uninduced strains. Four Raman bands associated with cytochrome c are highlighted at 748, 1128, 1312, and 1585 cm^{-1}.



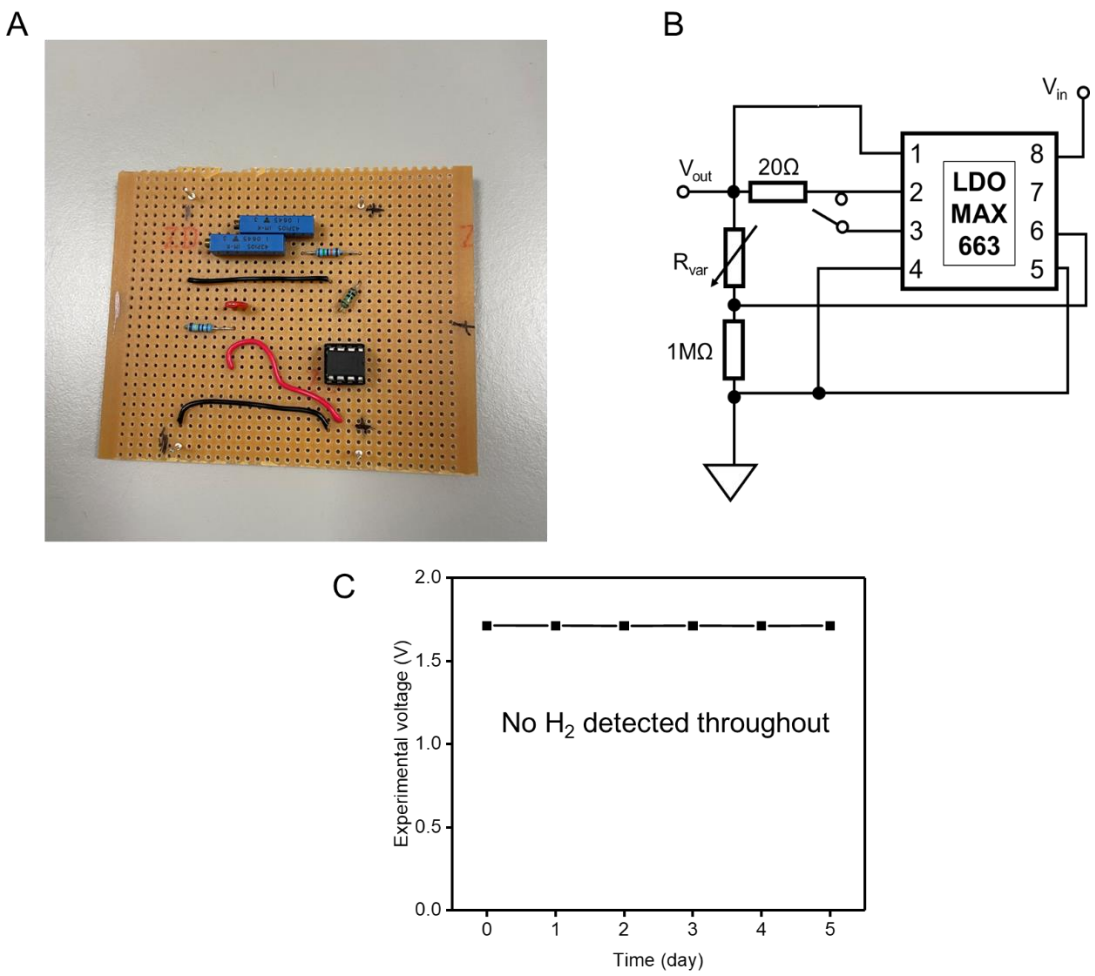
Supplementary figure S4.3. Heme staining of whole cell lysates of *R. eutropha* without expression of Mtr (as the negative control) and *R. eutropha*-Mtr at arabinose (Ara) inducer concentrations of 0.02% and 0.1%. Experiments are repeated twice.



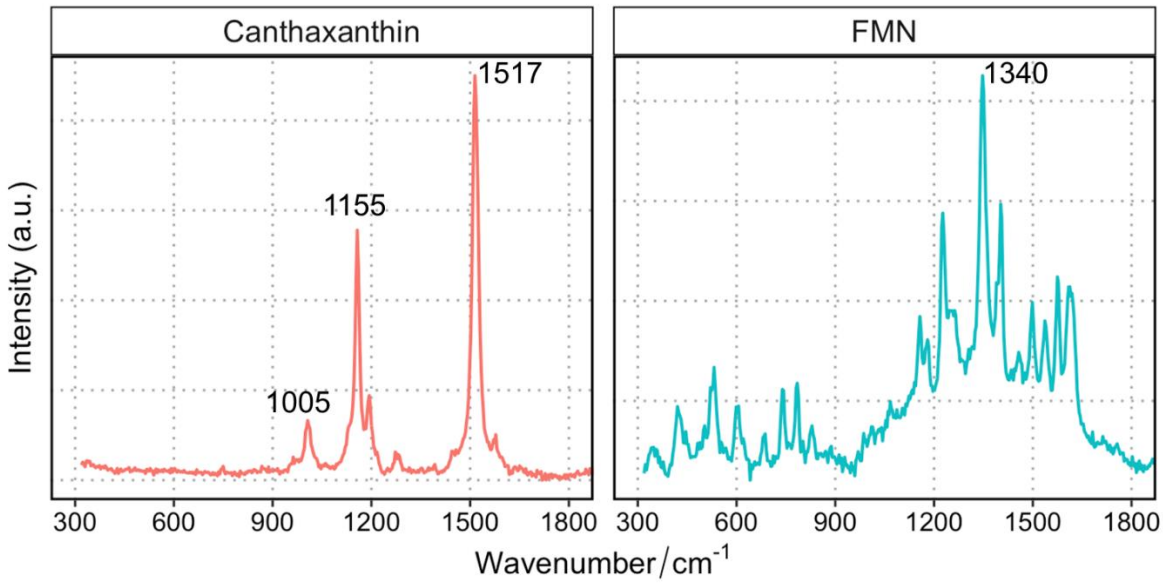
Supplementary figure S4.4. (a) Schematic illustration of D_2O involved in metabolisms based on CO_2 fixation. (b) Averaged single-cell Raman spectra of *R. eutropha*-Mtr-GR cultured with 40% D_2O under different conditions. Raman shifts were observed from 1003 cm^{-1} to 987, 975 and 961 cm^{-1} in the cells incubated with illumination and CO_2. The Raman band associated with bicarbonate is highlighted at 1050 cm^{-1}.



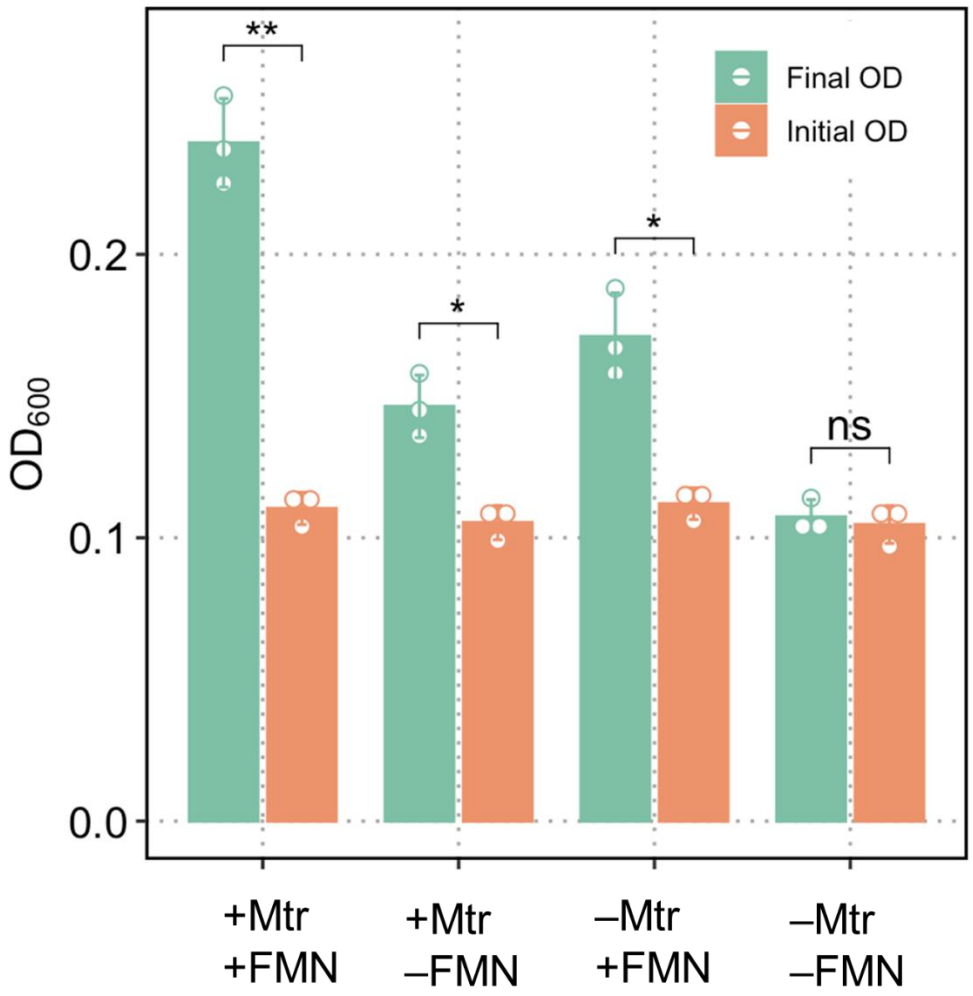
Supplementary figure S4.5. Averaged single-cell Raman spectra of *R. eutropha*-GR-Mtr and *R. eutropha*-GR cultured with 30% D_2O and CO_2 under light and dark conditions.



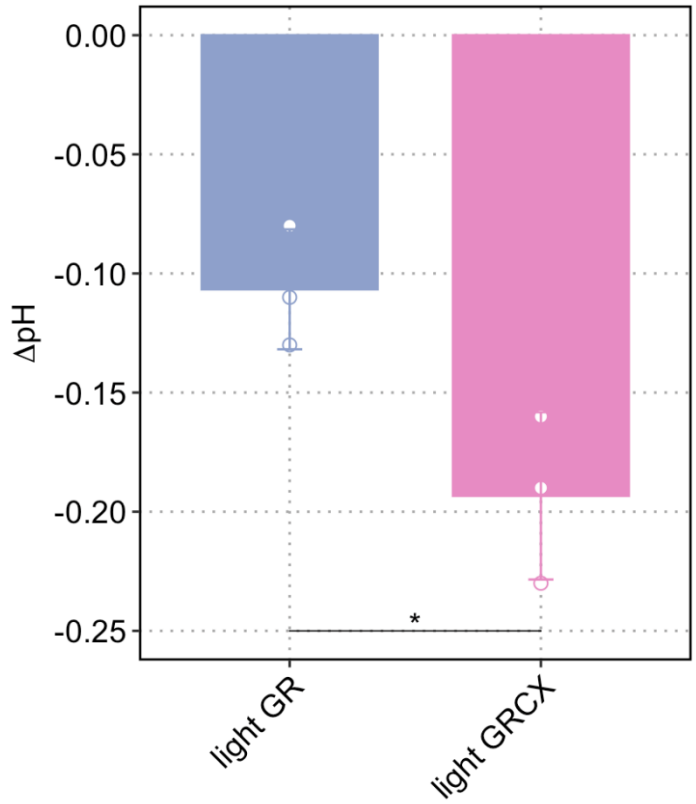
Supplementary figure S4.6. Design of home-made voltage regulator. (a) A picture of the voltage regulator. (b) The circuit diagram of the voltage regulator (c) Volage output controlled by the voltage regulator.



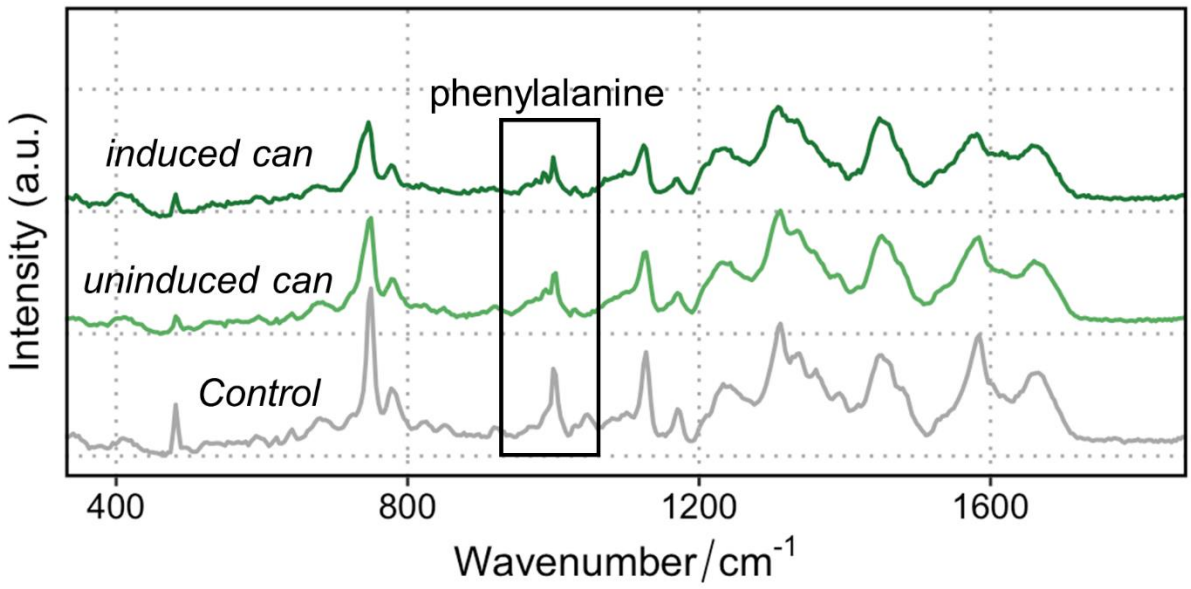
Supplementary figure S4.7. Characterization of pure canthaxanthin and FMN by Raman analysis.



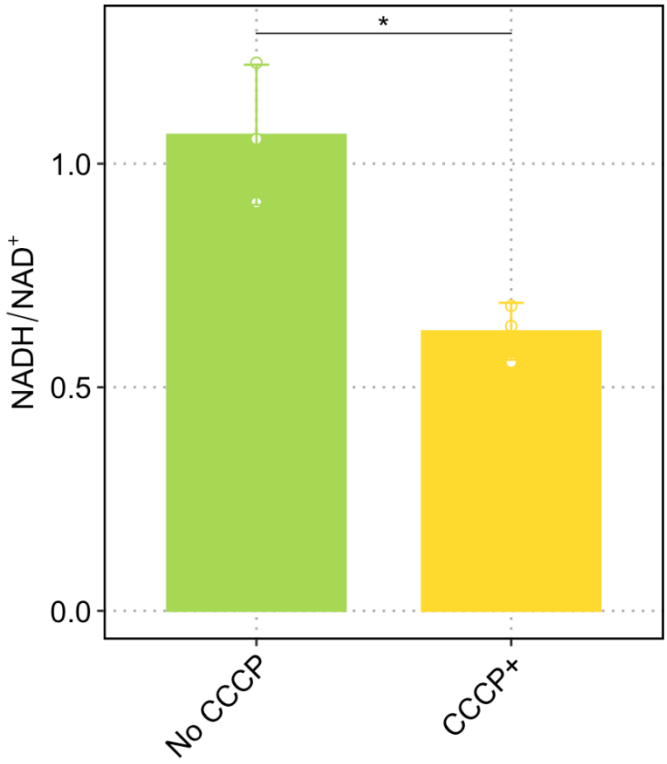
Supplementary figure S4.8. Initial and final optical density (OD_{600}) for the *R. eutropha* RHM5-GR-Mtr strains with and without inducation Mtr pathway after 5 days incubations with and without 50 μM FMN as the mediator (**: $p < 0.01$, *: $p < 0.05$, ns: not significant, data are means ± SD of three biological replicates. Exact p values are 0.00207, 0.00102, 0.0137 and 0.636 for "+Mtr, +FMN", "+Mtr, –FMN", "–Mtr, +FMN" and "–Mtr, –FMN" groups, respectively).



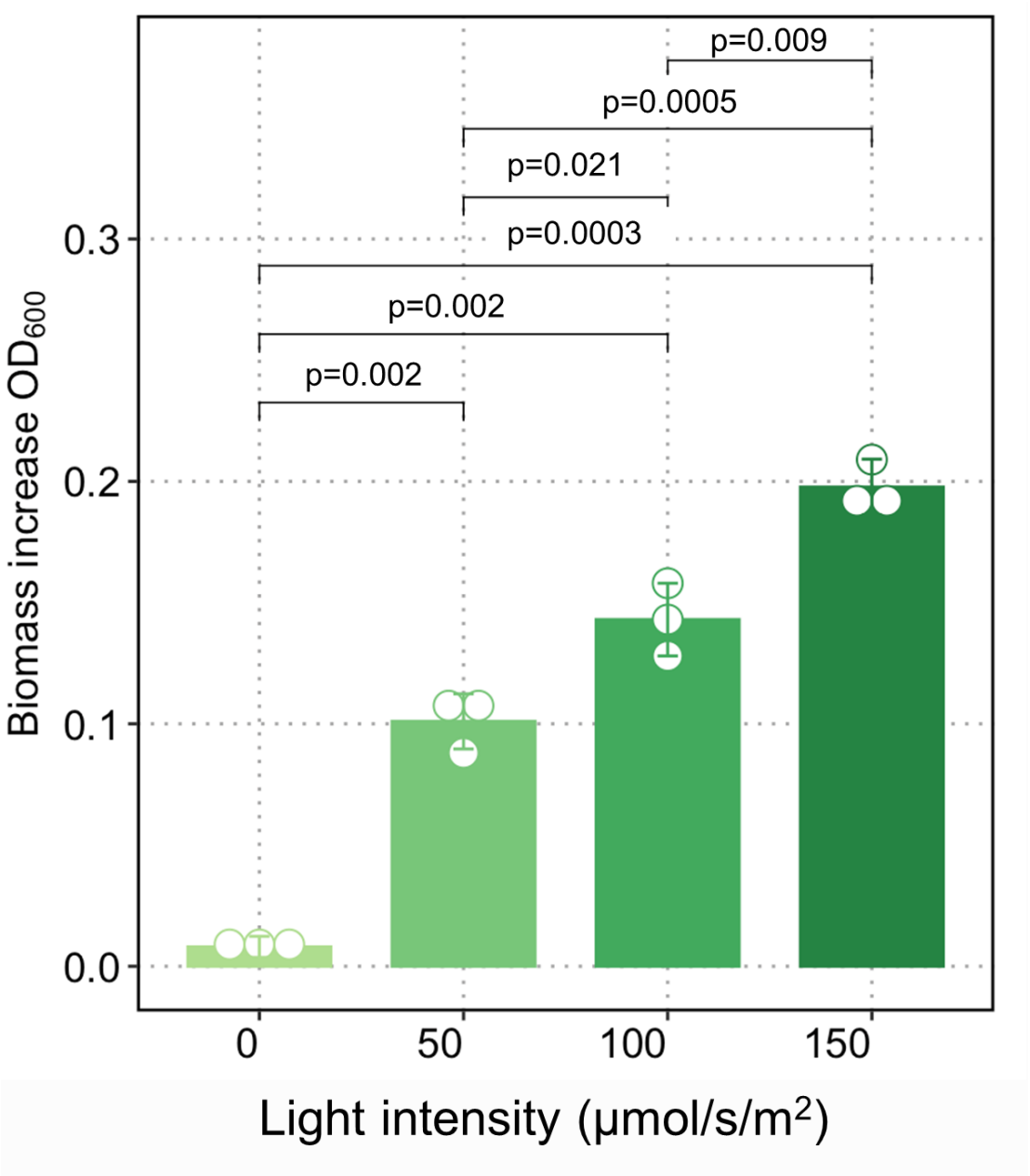
Supplementary figure S4.9. Extracellular proton concentration changes in cell suspensions with GR and GRCX over 1 min. Statistics were performed with Student's t-test (*: $p < 0.05$, data are means ± SD of three biological replicates. Exact p value is 0.0298).



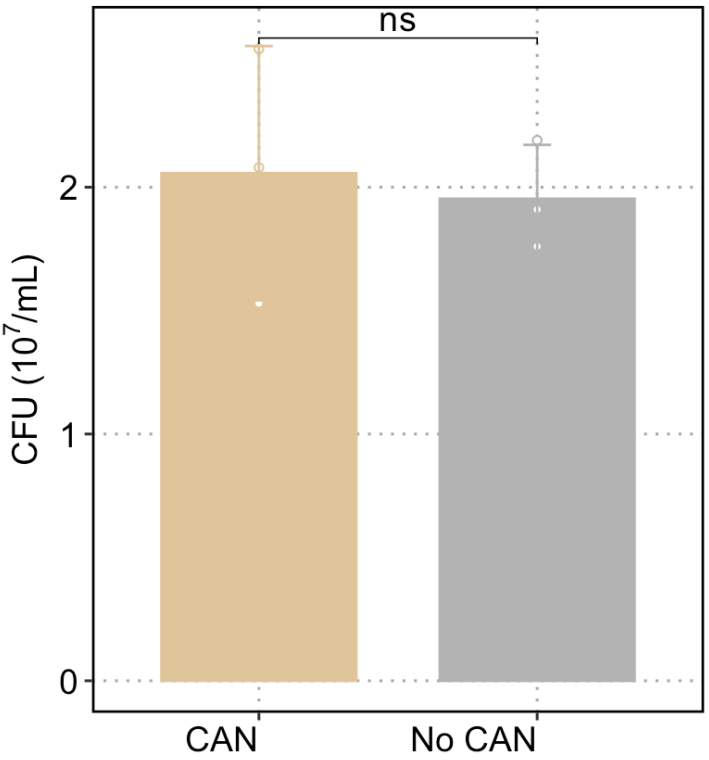
Supplementary figure S4.10. Averaged single-cell Raman spectra of induced or uninduced *R. eutropha* RHM5-GR-can cultured with 20 mM ^{13}C labelled bicarbonate, and phenylalanine is highlighted.



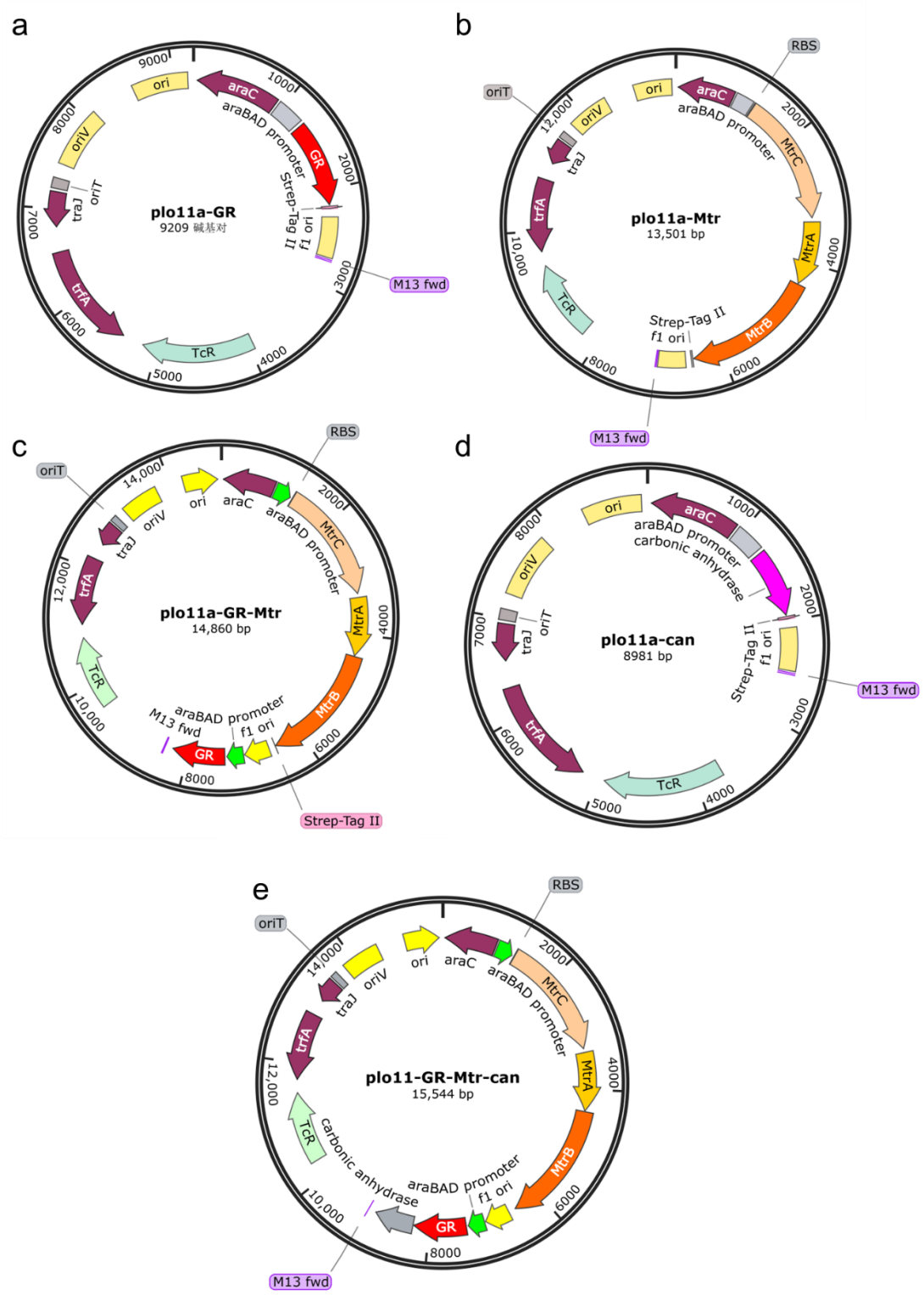
Supplementary figure S4.11. NADH/NAD^+ ratios in the *R. eutropha*-GR-Mtr under photoelectrosynthetic conditions with and without carbonyl cyanide m-chlorophenyl hydrazone (CCCP) treatment. Statistics were performed with Student's t-test (*: $p < 0.05$, data are means ± SD of three biological replicates. Exact p value is 0.0267).



Supplementary figure S4.12. Biomass increases in *R. eutropha* RHM5-GR-Mtr calculated from changes in the OD_{600} over 5 days under different light intensities. Statistics were performed with Student's t-test (data are means ± SD of three biological replicates. Exact p values are shown in the figure).



Supplementary figure S4.13. Comparison of the viability of the engineered cells with and without canthaxanthin after 3-day incubation under illumination. (ns: not significant, data are means ± SD of three biological replicates. Exact p values are 0.772).



Supplementary figure S4.14. Plasmid maps of (a) pLO11a-GR, (b) pLO11a-MtrCAB, (c) pLO11a-GRMtrCAB (d) pLO11a-*can* and (e) pLO11a-GR-Mtr-*can*

Chapter 5

Engineering Bio-nanoreactor in Bacteria for Efficient Hydrogen Production

Weiming Tu, Ian P. Thompson and Wei E. Huang*

Department of Engineering Science, University of Oxford, Oxford OX1 3PJ, United Kingdom.

*Corresponding author: Wei E. Huang. Email: wei.huang@eng.ox.ac.uk. Tel: +44 1865 283786.

Chapter adapted from publication: ***Proceedings of the National Academy of Sciences*** (2024)

DOI: 10.1073/pnas.2404958121

5.1 Summary

This chapter explores the use of a rhodopsin-based light-harvesting photosystem to enhance microbial hydrogen synthesis. Hydrogen production through water splitting is a vital strategy for renewable and sustainable clean energy. In this chapter, we developed a novel approach integrating nano-material engineering and synthetic biology to establish a bio-nanoreactor system as a biocatalyst for efficient cathodic hydrogen production. The periplasmic space (20-30 nm) of an electroactive bacterium, *Shewanella oneidensis* MR-1, was engineered to serve as a bio-nanoreactor to enhance the interaction between electrons and protons, catalysed by hydrogenases for hydrogen generation. To optimise electron transfer, we used the microbially reduced graphene oxide (rGO) to coat the electrode, which improved the electron transfer from the electrode to the cells. Native MtrCAB protein complex on *S. oneidensis* and self-assembled iron sulfide (FeS) nanoparticles acted in tandem to facilitate electron transfer from an electrode to the periplasm. To enhance proton transport, *S. oneidensis* MR-1 was engineered to express *Gloeobacter* rhodopsin (GR) and the light-harvesting antenna canthaxanthin (CAN). This led to efficient proton pumping when exposed to light, resulting in a 35.6% increase in the rate of hydrogen production. The overexpression of native [FeFe]-hydrogenase further improved the hydrogen production rate by 56.8%. The bio-nanoreactor engineered in *S. oneidensis* MR-1 achieved a hydrogen yield of 80.4 μmol/mg protein/day at a potential of −0.75 V. This periplasmic bio-nanoreactor combines the strengths of both nanomaterial and biological components, providing an efficient approach for microbial electrosynthesis.

5.2 Introduction

In response to the global energy crisis and environmental challenges, there is a growing demand for clean energy sources (219). Hydrogen is the quintessential clean energy solution, distinguished by its high energy density and environmentally friendly combustion properties (220). Green hydrogen, generated by water splitting driven by renewable energy sources, is regarded as the most promising energy carrier for a hydrogen economy (221). The quest for economical, stable, and efficient catalysts for cathodic H_2 generation in an electrochemical system has attracted wide interest (222). The cost of hydrogen production is the most important challenge hampering deployment (223). Traditional metal materials, commonly used as the cathode for water electrolysis, often entail substantial cost implications (224). In contrast, biocatalysts, such as microbial cells, offer a cost-effective alternative for catalysing H_2 synthesis under mild conditions (225).

The metal-reducing bacterium, *Shewanella oneidensis* MR-1 is a model electroactive platform, which is commonly employed for microbial fuel cells (123, 226) and microbial electrosynthesis (227, 228) because of its bidirectional extracellular electron transfer pathway (170, 229). *S. oneidensis* MR-1 can be used as a biocatalyst in the electrochemical system for cathodic H_2 production by combining its extracellular electron transfer mechanism and hydrogenase-based metabolism (32). *S. oneidensis* MR-1 has encoded two native hydrogenases, namely, [NiFe]- and [FeFe]-hydrogenases, located in the periplasmic space with the capacity to catalyse the interconversion between protons and hydrogen (230). The electrode as an external electron donor delivers electrons across the outer membrane into hydrogenases reducing protons to hydrogen. Despite theoretical feasibility, the current wild-type *S. oneidensis*-based H_2 electrosynthesis system exhibits unsatisfactorily low hydrogen yield that largely limits the practical applications (32, 207). Hydrogen production is a straightforward reaction, involving the interactions of protons and electrons, catalysed by hydrogenases in the periplasm. We hypothesised that the poor microbial electrosynthesis of H_2 is attributed to inefficient electron transport and suboptimal periplasmic conditions.

Low extracellular electron-transfer rate is a common limiting factor for the electrochemical application of *S. oneidensis* MR-1 (170, 231). Considerable efforts

have been devoted to enhancing the extracellular electron-transfer processes (232, 233). Introducing electron-shuttling molecules such as flavins (234) and iron ions (235) has been widely used to boost the electrochemical performance of *S. oneidensis* MR-1. Recent strategies focus on coupling the nanoparticle with *S. oneidensis* MR-1 which has been reported to significantly promote extracellular electron transfer (231, 232, 236). *S. oneidensis* MR-1 is a well-established bio-nano-factory for synthesising and assembling nanoparticles due to its reducing and detoxification capacities (207, 237). H_2 synthesis of *S. oneidensis* MR-1 takes place in the narrow periplasmic space which yields the opportunity to rationally design the periplasm as a nanoreactor by optimising synergy between nanoparticles and biocomponents (238).

In addition to improving electron transport, a high proton concentration could also facilitate the catalytic reaction from protons to hydrogen. It has been reported that expression of a proton-pumping proteorhodopsin (PR) in *Escherichia coli* with the heterologous hydrogenase increased hydrogen production yield by around 30% under light (77). Microbial rhodopsin is a simple protein which can used as an optogenetic tool to engineer non-native bacteria with light-harvesting capacity (63, 76). Outward proton pumping rhodopsins such as PR (76) and *Gloeobacter* rhodopsin (GR) (187) have been used to enhance microbial energy metabolism while their applications in microbial electrochemical H_2 production remain largely unexplored. Furthermore, the increase of hydrogenase concentration in the periplasm is expected to boost the reaction rate (239).

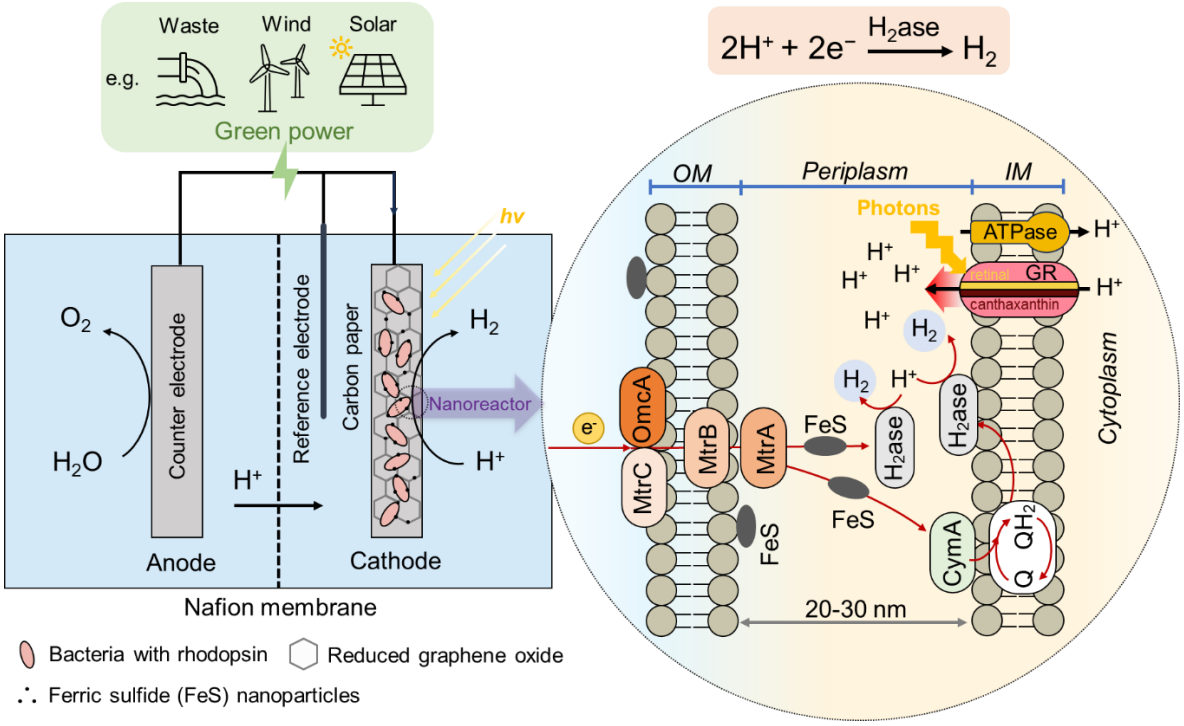


Figure 5.1 Schematic of the sustainable bioprocess for H_2 bioproduction. *Shewanella oneidensis* MR-1 uses hydrogenase to catalyse H_2 synthesis from protons and electrons, powered by light and electricity. Reduced graphene oxide (rGO) and FeS nanoparticles were introduced to enhance the electron transfer. The cells were engineered to express *Gloeobacter* rhodopsin (GR) and its antenna canthaxanthin, which harvest photons to pump protons from cytoplasm to periplasm.

We propose that the efficiency of hydrogen production could be substantially improved by designing a bio-nanoreactor capable of effectively mediating elevated concentrations of protons, electrons, and hydrogenases. In this study, a periplasmic bio-nanoreactor based on *S. oneidensis* MR-1 has been designed for H_2 production (Figure 5.1). The use of biologically reduced graphene oxide (rGO) and native MtrCAB protein complex enhanced electron transfer from the electrode into *S. oneidensis* MR-1. *S. oneidensis* MR-1 was also employed to synthesise iron sulfide (FeS) nanoparticles which are self-assembled and located within the periplasm to mediate the electron transfer. FeS nanoparticles play the role of conductive chain to facilitate the electron transfer from the outer-membrane proteins into hydrogenase at periplasm. In addition, *S. oneidensis* MR-1 was engineered to heterologously express GR and its antenna canthaxanthin (CAN), which is able to harvest light energy to efficiently pump protons from cytoplasm to periplasm. In the periplasm-based bio-nanoreactor, electrons, protons, hydrogenases, as well as conductive FeS are all concentrated into the nanoscale space of periplasm, facilitating an enhanced H_2 synthesis. This rationally designed

system achieved efficient photoelectrochemical hydrogen production. This proof-of-concept study could offer an insight into engineering bacterial catalysts with nanoparticles and genetic reprogramming for efficient microbial electrosynthesis.

5.3 Results

5.3.1 Biogenic FeS nanoparticles assembled in periplasm of *S. oneidensis* MR-1 for enhanced inward electron transfer

S. oneidensis cells, as bio-nano-factories, have been reported to synthesise a variety of multifunctional nanomaterials such as silver (232) and cadmium nanoparticles (207, 240) by reducing metal salts. In this study, *S. oneidensis* MR-1 was employed to synthesise iron sulfide (FeS) nanoparticles because of its highly reductive and unique electrical properties along with easily accessible raw materials (241). Transmission electron microscopy (TEM) image of the cell with synthesised FeS shows that the formed nano-sized particles (15.5 ± 5.8 nm) were mostly located in the periplasmic space with a small number of the nanoparticles attached to the outer membrane of cells (Figure 5.2A, Suppl Figs. S5.1 and S5.2). Raman micro-spectroscopy was used to verify the biosynthesised FeS nanoparticles at the single-cell level (Figure 5.2B). Two characteristic Raman bands at 219 and 282 cm^{-1} were identified in the spectrum of purified FeS biosynthesised by *S. oneidensis* MR-1, and these bands were attributed to the characteristic Fe–S vibrations (242). Single-cell Raman analysis revealed that Raman spectra of the cells assembled with FeS nanoparticles also displayed the bands associated with the Fe–S vibrations (Figure 5.2C), in good agreement with the TEM result of *S. oneidensis* MR-1 cells with self-assembled FeS nanoparticles.

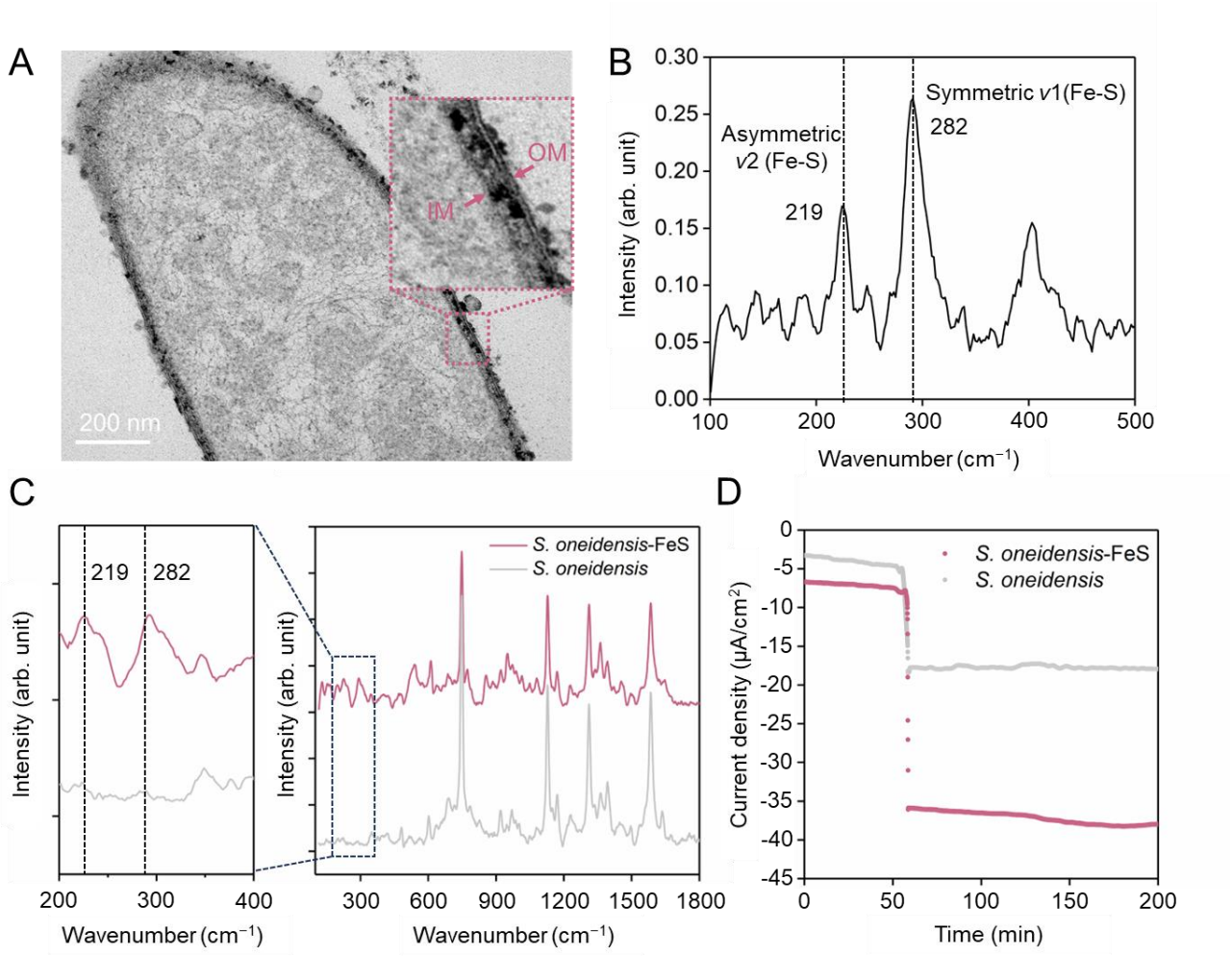


Figure 5.2. The self-assembly of biogenic FeS nanoparticles in the periplasm of *S. oneidensis* MR-1. (A) A TEM image of *S. oneidensis* MR-1 after 2-day incubation with thiosulfate and $FeSO_4$ to form FeS nanoparticles in the periplasm and on the outer membrane. OM: outer membrane; IM: inner membrane. (B) A typical Raman spectrum of FeS nanoparticle synthesised by *S. oneidensis*. (C) Single-cell Raman spectra of cells of *S. oneidensis* with and without FeS nanoparticles. (D) Fumarate reduction test. The biocathode was poised at −0.5 V (vs Ag/AgCl), and 25 mM fumarate was added at ~50 min.

From the TEM image, it can be seen that a large number of FeS nanoparticles were located in the periplasm, which could facilitate the periplasmic electron transfer. Electrochemical tests were performed to evaluate the effect of FeS nanoparticles on the inward extracellular electron transfer of *S. oneidensis*. Fumarate was introduced as an electron acceptor into the *S. oneidensis*-based electrochemical system. Under anaerobic cathodic condition at a potential of −0.5 V (vs. Ag/AgCl), 25 mM fumarate was injected into the cathode chamber containing either *S. oneidensis* or *S. oneidensis*-FeS. The addition of fumarate was expected to enhance electron-transfer processes because *S. oneidensis* contains a periplasmic fumarate reductase catalysing the reduction of fumarate to succinate (170). Monitoring of the current consumption revealed a prompt

decrease in the cathodic current for both *S. oneidensis* with and without FeS nanoparticles (Fig. 5.2D). Notably, the *S. oneidensis*-FeS demonstrated over twofold increase in inward current density (−37 μA/cm^2) compared to *S. oneidensis* without FeS nanoparticles (−17 μA/cm^2). This result suggests that the self-assembled FeS nanoparticles in the *S. oneidensis*-FeS strain could enhance the inward electron transfer rate.

5.3.2 Constructing a biologically reduced graphene oxide with *S. oneidensis* –FeS nanoparticles for H_2 production

S. oneidensis was employed as a biocatalyst to generate H_2 by hydrogenases (32). Linear scanning voltammetry (LSV) analysis was used to measure hydrogen evolution reaction activity for the carbon paper cathode pre-grown with *S. oneidensis* MR-1 at neutral pH. The LSV results show a significant cathodic current with an onset potential of around –0.56 V vs. SHE for the *S. oneidensis* MR-1 biocathode, in contrast to weak reduction currents observed in the control group of the carbon paper-based electrode (Suppl Fig. S5.3A). These results suggest that *S. oneidensis* MR-1-based biocathode should catalyse proton reduction with an overpotential of around 0.15 V, compared to the theoretical hydrogen evolution potential of –0.41 V vs. SHE. When the cathodic potential was set at –0.7 V vs. SHE, the biocathode with *S. oneidensis* MR-1 exhibited significant hydrogen production, in contrast to the negligible amount detected in the control without bacteria. (Suppl Fig. S5.3B).

The microbial electrochemical system can be combined with material engineering to enhance H_2 production. For instance, graphene has been widely applied to enhance the electrochemical properties of the biocathode, due to its high conductivity and large surface area (232, 233). To enhance the electrochemical performance in this study, microbially reduced graphene oxide to coat the electrode was employed. The outer membrane cytochromes of *S. oneidensis* MR-1 have been reported to catalyse graphene oxide (GO) to reduced graphene oxide (rGO) (243). *S. oneidensis* MR-1 cells were mixed with GO and the mixture was incubated for 24 hours at room temperature. Raman spectroscopy was employed to compare the spectra of the *S. oneidensis* MR-1-GO samples before and after the incubation (Figure 5.3A). The initial GO exhibited two sharp bands. The D band (around 1350 cm^{-1}) was associated with the K-point phonons of A_{1g} symmetry, and the G band (around 1580–1600 cm^{-1}) was attributed to

the zone centre phonons of E_{2g} symmetry (244). An obvious red shift of the G band of the samples, transitioning from 1594 to 1581 cm^{-1} was observed after microbial reduction (Figure 5.3A). This shift suggested the formation of rGO from GO, mediated by biological reduction of *S. oneidensis* MR-1. The microbially-reduced graphene oxide was dropped onto the carbon paper to form a thin layer, resulting in an rGO-coated cathode for subsequent microbial H_2 electrosynthesis. An increase in biomass content on the rGO-coated electrode was detected compared to the control carbon paper (Figure 5.3B), which was attributed to the large surface area of graphene. We further compared their electron uptake rates, demonstrating that the current consumption per milligram of cell protein was enhanced from 0.00464 μmol electrons/μg/hour to 0.00636 μmol electrons/μg/hour (Figure 5.3C). This indicated that the introduction of graphene oxide increased conductivity, accelerating the electron-transfer processes between the cells of *S. oneidensis* MR-1 and rGO sheets. The H_2 production yield increased from 7.82 μmol/mg/day to 25.69 μmol/mg/day (Figure 5.3D). Then rGO coated biocathode with *S. oneidensis* MR-1 was further modified by replacing it with FeS nanoparticles functionalised *S. oneidensis* MR-1. In the presence of FeS nanoparticles, the biomass content, electron uptake rate and hydrogen yield were further enhanced to 270.33 μg protein/cm^2, 0.00817 μmol electrons/μg/hour and 43.11 μmol/mg/day (Figure 5.3), respectively, suggesting that nanomaterial engineering significantly enhanced the microbial H_2 electrosynthesis.

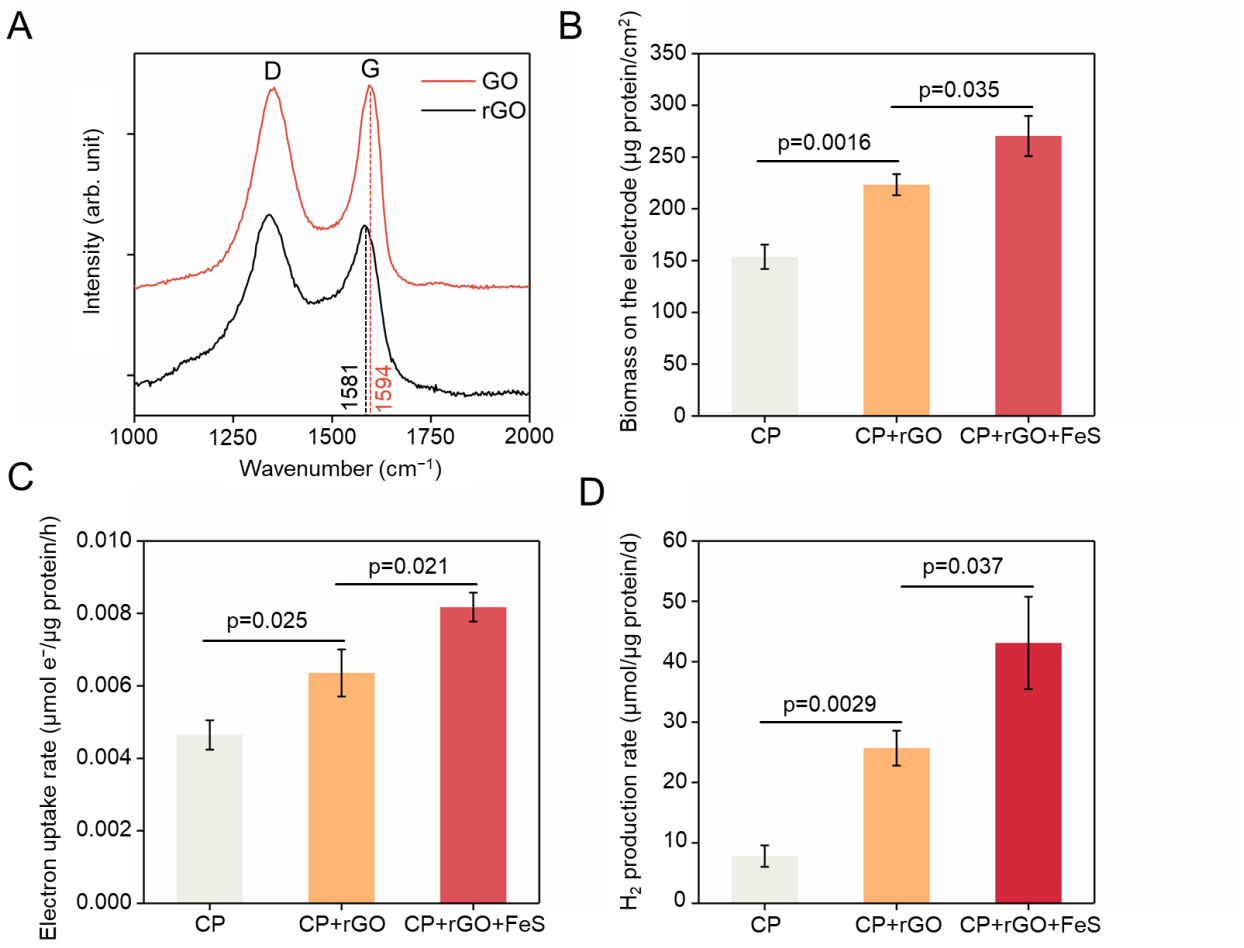


Figure 5.3. The integration of the biogenic reduced GO (rGO) with *S. oneidensis* MR-1 enhanced H_2 production. (A) Raman spectrum of graphene oxide (GO) and rGO due to the reduction reaction by *S. oneidensis* MR-1. (B) The biomass protein on the electrodes based on carbon paper (CP), CP with rGO and CP with rGO and self-assembled FeS nanoparticles. (C) Average current consumption per cell and (D) H_2 production over 72 hours using the bioelectrode based on carbon paper (CP), CP with rGO and CP with rGO and FeS nanoparticles at the cathodic potential of −0.75 V vs. SHE. Statistics were performed with Student's t-test (data are means ± SD, n = 3).

5.3.3 Increasing proton pumping into the periplasm by expression of *Gloeobacter* rhodopsin and canthaxanthin

Outward proton-pumping rhodopsin is the most abundant microbial rhodopsin in nature, which has been widely used as a synthetic biology tool (245, 246). Bacteria with rhodopsin can harvest light energy to pump out protons into the periplasm, generating a proton gradient. Herein, we choose *Gloeobacter* rhodopsin (GR), from *Gloeobacter violaceus* because of its high turnover rate, broad pH range and fast photocycling rate (182). The plasmid pLO11a-GR was transferred into *S. oneidensis* MR-1, resulting in the strain *Shewanella oneidensis* MR-1-GR. The expression of GR was induced by 1

mM arabinose, leading to the cell pellet of the induced group displaying a pink colour, in contrast to the uninduced control (Figure 5.4A). Single-cell Raman spectroscopy identified a distinctive GR band at around 1530 cm^{-1} in arabinose-induced *S. oneidensis* MR-1-GR but not in the uninduced control. This is consistent with the previous reports (74, 187) (Figure 5.4B). At the single-cell level, around 95% of the cell population was counted containing GR (Number of measured cells n=198, Suppl Fig. S5.4A), indicating the gene expression of GR in most *S. oneidensis* MR-1-GR. A plate reader was employed to scan the absorbance of the cell extracts which detected the obvious absorbance at ~540 nm compared to the control group, further confirming a strong light absorption of GR in *S. oneidensis* MR-1-GR (Suppl Fig. S5.5). Previous studies demonstrated that GR could be combined with carotenoids such as canthaxanthin and echinenone to enhance the proton-pumping capacity (245, 247). In this study, *S. oneidensis* was engineered to synthesise canthaxanthin. The expression of canthaxanthin turned the colour of the cell pellet of *S. oneidensis* MR-1-GR-CAN (Table S5.1), shifting it from its initial red colour, characteristic of wild-type *S. oneidensis* (248), to an orange-red colour (Figure 5.4C). Single-cell Raman spectroscopy confirmed the characteristic bands for canthaxanthin at around 1005, 1155, 1517 cm^{-1} (Figure 5.4D) which are consistent with the Raman spectra of the commercially pure canthaxanthin reported by the previous study (245). Single-cell Raman analysis confirms that ~99% population of *S. oneidensis* MR-1-GR-CAN expressed canthaxanthin (Number of measured cells n=198, Suppl Fig. S5.4B). A previous study has demonstrated that the proton pumping capacity of GR was significantly enhanced when assembled with CAN, exhibiting a 1.5-5 times increase compared to GR alone (202). To investigate the proton pumping capacities of cells with GR and GR-CAN, the pH dynamic change of the cell suspension in an unbuffered solution was examined. Light was turned on for 50 seconds and then off when pH remained stable. The proton pumping rate of *S. oneidensis* MR-1-GR-CAN, based on the change in extracellular proton concentration per OD_{600}, was twice that of *S. oneidensis* MR-1-GR (Figure 5.4E). This result suggested that the introduction of canthaxanthin antenna could effectively enhance the proton pumping efficiency of the rhodopsin-expressing cells.

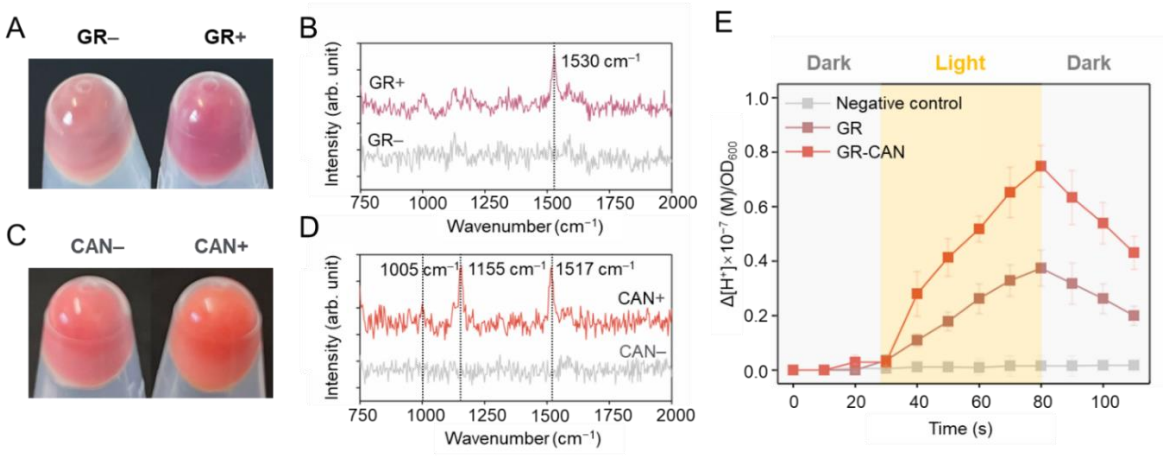


Figure 5.4. The expression of GR and CAN in *S. oneidensis* MR-1-GR-CAN enhanced H_2 production boosted by the light. (A) The pictures of cell pellets with (GR+) and without (GR–) *Gloeobacter* rhodopsin expression. (B) A typical Raman spectrum of a cell with GR complexes identified by a band at ~1530 cm^{-1}. (C) The pictures of cells pellet with (CAN+) and without (CAN–) canthaxanthin expression. (D) A typical Raman spectrum of a cell with canthaxanthin (CAN) identified by a band at ~1005, 1155 and 1517 cm^{-1}. (E) Extracellular proton concentration changes in response to illumination with white light (~200 μmol/m^2/s). Data are means ± SD, n = 3.

5.3.4 Enhanced H_2 production through efficient interactions of reactants within periplasmic nanoreactor

The working electrode was set at a cathodic potential of −0.75 V vs. SHE to investigate the response of the cathode coated with *S. oneidensis* MR-1-GR-CAN to light. The cathode chamber was equipped with white LED lights to activate proton pumping in the GR-CAN complex of *S. oneidensis* MR-1-GR-CAN. The response of the cathodic current to the light was tested by switching on and off the LED lights. In the light, the current consumption was significantly enhanced compared to those in the dark conditions. The current density was boosted from −58 μA/cm^2 to −64 μA/cm^2 within 40 minutes (from 40-80 min in Figure 5.5A), indicating the proton motive force generated by GR enhanced the electron uptake by the engineered cells. To investigate the electron uptake capacity of the engineered cells with *S. oneidensis* MR-1-GR-CAN in the light, strains were pre-grown and inoculated into bioelectrochemical systems with rGO and functionalised with self-assembling FeS nanoparticles (Figure 5.1). Then we compared the hydrogen production in the nano-electrochemical system with and without expression of GR-CAN in *S. oneidensis* MR-1-GR-CAN. At a potential of −0.75 V vs. SHE, the hydrogen yield of the microbial electrochemical system was increased by 35.6% (Figure 5.5B). This was attributed to two major advantages of the

GR-CAN. One was that the proton gradient generated by the GR-CAN complex promoted the electron transfer rate (Figure 5.5A). Secondly, enhanced pumping of protons into the periplasmic nanoscale space created a favourable environment by elevating the concentration of protons and facilitating the hydrogenase-catalysed interaction for H_2 synthesis. Based on thermodynamic analysis of the hydrogen synthesis (Suppl Fig. S5.6), the increased proton concentration led to a decrease of the Gibbs free energy, lowering the energy barrier for the conversion of protons to hydrogen. Therefore, the periplasmic bio-nanoreactor significantly boosted the generation of H_2.

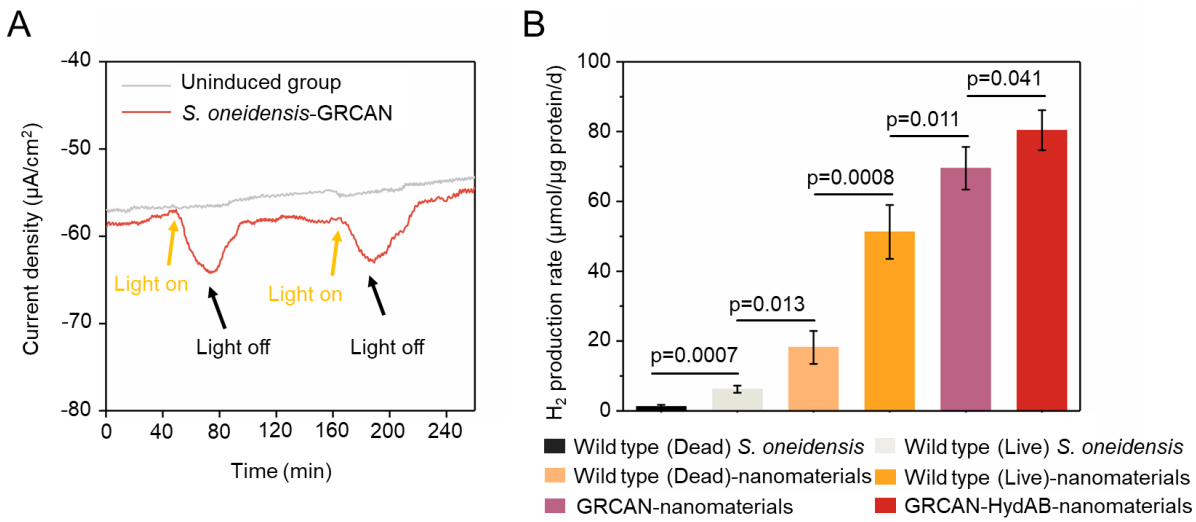


Figure 5.5. The integration of nanomaterial rGO, FeS and biological GR, CAN and [FeFe]-hydrogenase into the periplasmic bio-nanoreactor of *S. oneidensis* MR-1-GR-CAN-HydAB has achieved a high H_2 production. (A) The response of the engineered *S. oneidensis* MR-1-GRCAN to light and dark (B) H_2 production by dead *S. oneidensis* wildtype cells (after 15-min 110 ℃ heat inactivation), wildtype cells, the wild-type cells (dead) with nanomaterial engineering, wild-type cells (live) with nanomaterial engineering, the engineered *S. oneidensis* MR-1-GR-CAN with GR-CAN, and the engineered *S. oneidensis* MR-1-GR-CAN-HydAB with GR-CAN and the overexpression of hydrogenase, at the potential of −0.75 V vs. SHE under illumination. Statistics were performed with Student's t-test (data are means ± SD, n = 4).

Furthermore, the overexpression of enzymes concentrated in the periplasmic environment also accelerated the reaction. Hydrogenases of *S. oneidensis* MR-1 were efficient enzymes for catalytic H_2 turnover (249). Here, the [FeFe]-hydrogenase encoded by *hydA* (the large subunit, ~44kDa) and *hydB* (the small subunit, ~12kDa) were overexpressed, as confirmed by sodium dodecyl sulphate polyacrylamide gel electrophoresis (SDS-PAGE) analysis (Suppl Fig. S5.7), to further improve hydrogen production. The result demonstrates that the hydrogen yield of hydrogenase-

overexpressing strain *S. oneidensis* MR-1-GR-CAN-HydAB achieved 80.4 ± 5.8 μmol/mg protein/d, which is more than 10 times that of 7.8 ± 1.8 μmol/mg protein/d achieved by the wildtype *S. oneidensis* without modification, and more than 4 times than that of 18.2 ± 4.7 μmol/mg protein/d achieved by the abiotic control with FeS and rGO (Figure 5B and Table 5.1). Compared to other similar approaches, this hydrogen production rate surpasses the traditional systems based on bacterial catalysts, as shown in Table 5.1. The bio-nanoreactor significantly outperformed the electrode with a low platinum load (0.03 mg/cm^2 Pt) (FuelCellStore, UK) (Suppl Fig. S5.8). Although there remains a performance gap between the bio-nanoreactor (0.27 mg/cm^2 of proteins) and the traditional platinum electrode (FuelCellStore, UK) loaded with 0.2 mg/cm^2 of platinum catalyst (Suppl Fig. S5.8), the bio-hybrid system offers a cost-effective and sustainable alternative. Its future potential hinges on further enhancements in biocatalytic cell loading density and the efficiencies of electron and proton transport. The Faraday efficiency of this bio-nanoreactor system engineered in *S. oneidensis* MR-1-GR-CAN-HydAB achieved 80.5% ± 6.8% within two days, a significant improvement from 14.0% ± 2.9% efficiency observed in the wild-type strain (Suppl Fig. S5.9). Furthermore, when a potential of −0.85 V was applied, the hydrogen production rate of the bio-nanoreactor increased to 123.55 ± 25.9 μmol/mg protein/d (Table 5.1), despite a minor amount of hydrogen also detected in the abiotic materials (Suppl Fig. S5.10). Notably, the majority of the engineered *S. oneidensis* cells maintained viability under both electrochemical conditions (−0.75 V and −0.85 V) (Suppl Fig. S5.11). Previous research has reported the important role of rhodopsin in enhancing the survival of *S. oneidensis* MR-1 (246). Additionally, it has been demonstrated that the electrode-to-nanomaterial/electron mediator-to-hydrogenase pathway remains functional even in non-viable cells (90, 250), suggesting the robustness and versatility of the bio-hybrid system.

Table 5.1 Comparison to other similar microbial electrochemical systems for H_2 production

Strains	Synthetic biology	Electrode materials	Abiotic materials	Cathode potential (vs. SHE)	H_2 yield	Reference
E. coli BL21	Hydrogenase	Carbon paper	Methylviologen	~−0.9	~7.34 μmol/mg/d *	(90)
S. oneidensis MR-1	/	Carbon felt	/	−0.758	24.5 mL/m^3/d	(32)
S. oneidensis MR-1	/	Carbon felt	/	−0.76	~4.6 μmol/mg/d	(207)
S. oneidensis MR-1	/	Carbon paper	/	−0.75	7.82 μmol/mg/d	This study
S. oneidensis MR-1	GR-CAN, hydrogenase	Carbon paper with rGO	FeS nanoparticles	−0.75	80.37 μmol/mg/d	This study
S. oneidensis MR-1	GR-CAN, hydrogenase	Carbon paper with rGO	FeS nanoparticles	−0.85	123.55 μmol/mg/d	This study

*This result was calculated according to 462.7 μmol/d and 0.3 g wet cells reported in the ref (90)

5.4 Discussion

This study introduces and demonstrates the concept of a periplasmic bio-nanoreactor for sustainable and efficient hydrogen generation through water splitting. By integrating the abiotic nanomaterials and biological components, we have significantly improved biosynthetic reactions within a periplasmic bio-nanoreactor. In some species, such as *Rhodopseudomonas palustris* (251) and *Rhodobacter capsulatus* (252), their metabolic strategies lead to hydrogen synthesis occurring in the cytoplasmic space where cytoplasmic nitrogenases catalyze the reduction of protons with the electrons derived from ferredoxin (251, 252). In contrast, *S. oneidensis* relies on periplasmic hydrogenases for hydrogen synthesis metabolism (230). This approach offers two primary advantages. First, hydrogenases exhibit significantly higher turnover rates than nitrogenases; for example, [FeFe]-hydrogenases can achieve turnover rates up to 1000 times higher than those of nitrogenases (27, 28). Second, the confined space of periplasm facilitates the effective interactions of substrates and enzymes at the nanoscale (238). Moreover, in the bio-nano H_2 production system of this study, the periplasm provides an ideal environment for proton-pumping rhodopsin to significantly enhance hydrogen synthesis. According to the theory of thermodynamics, Gibbs free energy under general conditions (ΔG) is associated with the proton concentration ($[H^+]$),

expressed as:

$$\Delta G = \Delta G^0 + RT \times \ln \frac{1}{[H^+]^2} \qquad (1)$$

, where ΔG^0 is Gibbs free energy under the standard conditions, R is universal gas constant and T is temperature in Kelvin. The volume of the periplasmic space is estimated to be 8-16% of the entire cell (253, 254). Hence, the same amount of protons contributing to the concentration change in the periplasm is 5.2-11.5 times higher than in the cytoplasm. With rhodopsin pumping protons from cytoplasm to periplasm, the elevated proton concentration in the periplasm lowers Gibbs free energy and enhances interactions of hydrogenase with protons for efficient hydrogen synthesis.

In this periplasmic hydrogen synthetic system, both the outer and inner membranes play crucial roles, such as regulating proton movement with distinct permeabilities to protons. Although the outer membrane acts as a barrier to many molecules, including protons, cells can regulate proton transport across the cell envelope through passive diffusion via outer membrane-bound porins, thus maintaining a relatively stable intracellular pH (255). The inner membrane selectively allows proton movement through active transport mechanisms mediated by various membrane proteins such as ion channels, transporters, and ATPases (256, 257). In this study, we propose that the increase in proton concentration in the periplasm, driven by rhodopsin pumping, leads to two significant outcomes (Suppl Fig. S5.12). First, it promotes bacteria to regulate pH via hydrogen synthesis. The consumed periplasmic protons are replenished from the external environment where water splitting serves as a source of proton regeneration. Second, some protons may return to the cytoplasm via inner membrane protein (e.g. ATP synthase) to maintain pH homeostasis. The dynamic pH regulation across the membranes supports proton movement and supply within the periplasm, ensuring the maintenance of the proton gradient. This system could be extended for other reductive hydrogenation reactions in the periplasm such as the synthesis of formate (228) and succinate (258). The abiotic materials used in this work, including the microbially reduced GO and FeS nanoparticles, were synthesised by biological methods, making them more eco-friendly than traditional borohydride reduction approaches.

Biogenic FeS nanoparticles play an important role in enhancing electron-transfer processes (259). *S. oneidensis* MR-1 can naturally synthesise and assemble FeS

nanoparticles, similar to the natural processes observed in sulfate-reducing bacteria (SRB). In nature, 97% of sulfides are produced by SRB (260). Most SRB can synthesise FeS nanoparticles by using ferrous compounds and sulfide (261). SRB assembled with FeS nanoparticles on the membrane and periplasm become electroactive due to their electrical conductivity and interaction with biological components (259). The reductive capability of FeS nanoparticles also makes it a suitable mediator in the microbial electrosynthesis system. In fact, molecular ensembles of iron and sulfide are common in biological systems. For example, iron–sulfur (Fe–S) clusters are involved in important biochemical pathways, such as photosynthesis and respiration (262). Interestingly, the Fe–S clusters are important structures of hydrogenase which act as a connective line to deliver electrons to the central active site (249). Inspired by the natural occurrence of FeS clusters and interconnected chains of Fe–S in hydrogenases, we introduced the FeS nanoparticles to the bio-nano-electrochemical system which showed a significant enhancement in electron transfer and H_2 production by serving as electron transfer chain in periplasm.

The application of synthetic biology to sustainable engineering provides significant means for improving microbial synthesis performance. Microbial rhodopsins represent one of the major photosystems in nature, converting light energy to biochemical energy (3). Among them, outward proton-pumping microbial rhodopsin has become an increasingly popular target for introduction into non-native bacteria to supply energy, by generating a proton gradient across the cell membrane in the light (76, 188, 245). The proton motive force generated by the proton-pumping microbial rhodopsin has been demonstrated to increase intracellular ATP levels (25), survival rate (74), biomass growth (187) and bioproduction yield (76). In this study, by creating an electron sink via H_2 generation, the light-activated GR combined with canthaxanthin not only enhanced the electron uptake rate of cells but also provided favourable conditions in periplasm with elevated proton content. While the introduction of rhodopsin boosted the H_2 synthesis, the underlying mechanism remains elusive. For example, the dynamics of proton flux across the membranes are unclear. A practical application of the microbial photo-electrochemical system may require even more efficient rhodopsins. Therefore, we anticipate using artificial intelligence to support the design of rhodopsins with superior properties, such as high quantum efficiency (68), enhanced pH tolerance (263) and broad spectrum of light absorbance (144).

5.5 Materials and methods

5.5.1 Bacterial strains, culture conditions and plasmid construction

All bacterial strains and plasmids used in this study are shown in Table S5.1. *E. coli* strains were grown in Lysogeny Broth (LB) at 37 °C under aeration by shaking at 200 rpm. *S. oneidensis* strains were grown in LB broth at 30 °C under aeration by shaking at 150 rpm. If required, 25 μg/ml chloramphenicol (Sigma-Aldrich) and 12.5 μg/ml tetracycline (Sigma-Aldrich) were added in the culture medium. All plasmid constructions were performed in *E. coli* DH5α. The plasmid pLO11a-GR contains the *Gloeobacter* rhodopsin gene. The plasmid pLO11a-GR-HydAB (Suppl Fig. S5.13) contains the GR gene and the HydAB genes from *S. oneidensis* MR-1. The plasmid pAC-CANTHipi (Addgene: Plasmid #53301) contains the gene cluster for canthaxanthin synthesis (264). Induction of GR expression was accompanied by the addition of exogenous *trans*-retinal (Sigma-Aldrich) to achieve a final concentration of 5 μg/ml.

5.5.2 Biosynthesis of FeS nanoparticles

S. oneidensis strains were precultured in LB at 150 rpm for 24 hours. The cultured cells were collected by centrifugation at 3000 g for 3 min and washed twice times with phosphate buffer saline (Sigma-Aldrich). Then the cells were incubated in 100 mL anaerobic mineral medium with 0.5 mM $Na_2S_2O_3$ and 20 mM sodium DL-lactate (Thermo Scientific), with an initial OD_{600} of 0.5, at 30 °C, stirring at 150 rpm. After 24 h incubation, 0.5 mM $FeSO_4$ was added, and cultured for another 24 h to form FeS nanoparticles. The anaerobic mineral medium contained 5.85 g/l NaCl, 0.3 g/l NaOH, 1.5 g/l NH_4Cl, 0.1 g/l KCl, 11.91 g/l (4-(2-hydroxyethyl)-1-piperazineethanesulfonic acid) HEPES, and 0.6 g/l $NaH_2PO_4 \cdot H_2O$. The trace mineral minerals solution and amino acids solution were also added, and the compositions can be found in the previous study (229). Unless otherwise stated, all chemicals used above were purchased from Sigma-Aldrich. The FeS nanoparticles formation was operated under anaerobic conditions by pumping in pure nitrogen gas.

5.5.3 Microbial reduction of GO to modify the electrode

For the reduction of graphene oxide, 5 ml of graphene oxide (3 mg/ml) solution was mixed with 10 ml of 100 mL of 20-h culture of *S. oneidensis* MR-1 strains. The mixture

was shaken at 200 rpm, 25 °C. The microbially reduced GO was collected after 24 hours. The rGO composite was washed three times by centrifugation and sonication with distilled water. Subsequently, it was dissolved in 10 ml of ethanol for further utilisation. The carbon paper (FuelCellStore) was cut into pieces with a surface area of 4 cm^2. 2 ml of the microbially-reduced GO solution was dropped on carbon paper and air dried to form a GO-coated electrode. In the subsequent experiments, the biomass on the electrode was quantified by the bicinchoninic acid (BCA) assay kit (Thermo Scientific) (265). The procedure began by immersing the cathode carbon paper in 5 ml of 0.2 M NaOH and vortexing for 1 min. Then samples were heated at 95 °C in a heating block for 30 min to lyse cells. After cooling to room temperature, the samples were mixed with BCA reagents incubated at 37 °C for 30 min and then the absorbance at 562 nm was measured to determine the protein content.

5.5.4 Transmission electron microscope (TEM) characterisation

S. oneidensis MR-1 cells with and without FeS nanoparticles were collected by centrifugation at 3000 g for 3 min, then fixed in 4% formaldehyde (Sigma-Aldrich) and 2.5% glutaraldehyde (Thermo Scientific) in 0.1 M PIPES buffer (Sigma-Aldrich) at pH 7.2 for 1 hour at room temperature ahead of storage at 4 °C. The following day samples were then washed with buffer (0.1 M PIPES buffer, pH 7.2), centrifuged, and the cell pellets enrobed in 2.5% low melting point agarose (Thermo Scientific). Dissected cubes (~1mm^3) of enrobed cells were treated with 50 mM glycine (Sigma-Aldrich) in buffer, then washed again in buffer ahead of secondary fixation with 1% (w/v) osmium tetroxide and 1.5% potassium ferrocyanide (Sigma-Aldrich) in buffer. Samples were washed extensively with Milli-Q water and stained with 0.5% uranyl acetate solution (Electron Microscopy Sciences) then washed again with Milli-Q water. The samples were then dehydrated through an ethanol series and infiltrated with and embedded in TAAB low-viscosity epoxy resin. The samples were then polymerised at 60 °C for 24 hours. Sections of 90 nm were cut from the resin blocks using a Leica UC7 Ultramicrotome and collected onto 3 mm copper grids. The sections were then post-stained with lead citrate and imaged using a JEOL Flash 120kV TEM equipped with a Gatan Rio camera.

5.5.5 SDS-PAGE to validate overexpression of the periplasmic [FeFe]-hydrogenase

S. oneidensis-GR-HydAB strains were grown anaerobically in the anaerobic minimal

medium as descrided above for 48 h at 30°C, using 20 mM sodium DL-lactate (Thermo Scientific) as the electron donor and 10 mM sodium fumarate (Sigma-Aldrich) as the electron acceptor. After the anaerobic culture, cells were harvested and centrifuged (3000 g, 4 °C, 15 min) to an OD_{600} of 5 in 10 mL. Cells were then washed in phosphate buffer saline (Sigma-Aldrich), centrifuged at 3,000 g, 4 °C for 15 min, resuspended in a buffer (100 mM Tris-HCl pH 8, 500 mM sucrose, 0.5 mM EDTA), incubated for 5 min on ice, and centrifuged at 3,000 g, 4 °C for 15 min. For recovery of periplasmic proteins, the pellets were resuspended in 1 mM $MgCl_2$ and incubated for 2 min. The recovered periplasmic proteins were suspended in lithium dodecyl sulfate (Invitrogen). The samples were run in an 8-16% Tris-Glycine Gel (Thermo Scientific) at 16 °C. All samples were standardized to contain 30 μg of protein, as quantified by BCA assay, and loaded in equal volumes of 42 μL. Electrophoresis was operated at 180 V for 50 minutes. Protein bands were stained using the Coomassie Blue staining protocol (266).

5.5.6 Colony forming units (CFU) counting for quantification of viable cells on the electrode

The electrode with biofilm was transferred to a 50 ml Falcon tube filled with 5 ml of sterile 0.9% NaCl solution and vortexed for 2 minutes to disperse the cells. A series of diluted solutions were spread onto LB agar plates, which were then incubated at 30 °C for 36 h before the CFU counting.

5.5.7 Raman spectroscopy characterisation

Single *S. oneidensis* cells and FeS nanoparticles were characterised by Raman microspectroscopy. Before the measurements, samples were washed three times with distilled water to remove traces of culture medium and extracellular metabolites. 1.5-μl suspension was dropped onto an aluminium-coated slide and air dried for subsequent measurements. The cells were observed under a microscope after washing. Raman spectroscopic acquisition was performed using a LabRAM HR Evolution confocal Raman microscope using a 100×/0.75 air objective (HORIBA, UK). Single-cell Raman spectra were obtained using a 532-nm neodymium-yttrium aluminium garnet laser with a 300 grooves mm^{-1} diffraction grating and were acquired in the range of 100–3200 cm^{-1}. The laser power was set at ~80 mW which was attenuated by neutral density filters before focusing onto the samples. Spectra were recorded with LABSPEC 6

software (HORIBA, UK). All raw spectra were pre-processed within LABSPEC 6 software by cosmic ray correction, polyline baseline fitting and subtraction and vector normalization of the entire spectral region.

5.5.8 Linear sweep voltammetry (LSV) analysis

LSV tests were conducted on the carbon paper-based electrode and biocathode with *S. oneidensis* cells. The polarization curves were obtained within a potential range between −0.85 V and −0.25 V vs. SHE with a scanning rate of 1 mV/s. The LSV was controlled by the potentiostat (PalmSens 4-channel Multi EmStat^{3+}, Netherlands). The current was recorded, and the current density was calculated based on the current per square centimetre of the cathode projected area.

5.5.9 Electrochemical test for fumarate reduction

The H-shaped dual-chamber reactor was constructed by connecting two chambers with a proton exchange membrane (PEM) Nafion membrane (Suppl Fig. S5.14). The reference electrode (RE-5B, BASi, USA) was Ag/AgCl in a 3M KCl solution (+0.197 V vs. Standard Hydrogen Electrode, SHE). The working electrode was carbon paper (4 cm^2), and the counter electrode was platinum wire. Precultured *S. oneidensis* suspensions were transferred to 200 ml minimal medium with 20 mM DL-lactate (Thermo Scientific) in 500 ml flasks. After 12-h growth at 30 °C with 150 rpm, the cell suspension concentration was adjusted to an OD_{600} of ~0.5 and injected into the working chamber with a working volume of 50 mL. In contrast, the counter chamber was filled with mineral medium without lactate and bacteria. The working chamber was purged with pure N_2 gas to remove oxygen. The biocathode was imposed at −0.5 V (vs. Ag/AgCl) by the potentiostat (PalmSens, Netherlands). Once the cathodic current stabilized, 25 mM of fumarate was introduced to monitor the current change by the potentiostat (PalmSens 4-channel Multi EmStat^{3+}, Netherlands).

5.5.10 Proton pumping capacity test of engineered cells in light

The precultured *S. oneidensis* strains were harvested and washed with an unbuffered solution containing salts (Sigma-Aldrich) as follows: 10 mM NaCl, 10 mM $MgSO_4 \cdot 7H_2O$, and 0.1 mM $CaCl_2$. Cells were then resuspended in the unbuffered solution to obtain an OD_{600} of ~1.5. The cell suspension was placed in the dark until the pH was stabilized, which was measured by a pH meter (Hanna edge). Following

stabilization, the suspension was exposed to illumination with an intensity of ~200 μmol/m^2/s for 50 seconds. Real-time pH values were recorded, and the corresponding proton concentration differential ($\Delta[H^+]$) was calculated.

5.5.11 Light response test of the electrochemical systems with engineered cells

A photo-electrochemical system was constructed by surrounding the working chamber of the electrochemical system with 5 meters of white LED light strips. The white LED light strips encircled the exterior of the working chamber to ensure even light distribution during the experiment (Suppl Fig. S5.14). The strains with and without induction of GR-CAN complex were precultured as above and formed a biofilm on the electrode. The light was switched on for 40 minutes and then switched off. The currents were measured by the potentiostat (PalmSens 4-channel Multi EmStat^{3+}, Netherlands).

5.5.12 Cathodic hydrogen production

The photo-electrochemical system was constructed as described above. The *S. oneidensis* cells were incubated in the working chamber for 48 hours to form a biofilm on the electrode, with the addition of ~5 μM of riboflavin to facilitate the biofilm formation. Then planktonic cells and mineral medium in the working chamber were removed and replaced with the medium containing 50 mM HEPES (Sigma-Aldrich) and 50 mM NaCl (Sigma-Aldrich). Then working electrode was set at −0.75 vs. SHE for 72 hours. Hydrogen was detected in the headspace using gas chromatography (Shimadzu) equipped with the Carboxen-1010 column. For the light-driven hydrogen synthesis, LED light strips were switched on, providing illumination with a light intensity of approximately 200 μmol/m^2/s. During the hydrogen production, the working chamber was maintained at 25 °C without agitation. For the abiotic control, the biocathode was heat-treated at 110 °C in an oven for 15 min to inactive the *S. oneidensis* MR-1 cells. In addition, the commercial electrodes made of carbon material coated with 0.03 mg/cm^2 of platinum (FuelCellStore, UK) and 0.2 mg/cm^2 of platinum (FuelCellStore, UK), respectively, were used as the cathode for the control experiments. Unless otherwise stated, all hydrogen production experiments were operated using the same electrolyte at 25 °C.

5.5.13 Calculations

Electron uptake rate (μ) of the cells could be calculated by the equation,

$$\mu = \frac{\text{Electrons transferred (μmol)}}{\text{Biomass (μg proteins)} \times \text{Time (hours)}} \qquad (2)$$

Faraday efficiency (η) of the hydrogen formation could be calculated by the equation,

$$\eta = \frac{nzF}{\text{Charge passed (C)}} \qquad (3)$$

where n is the amount of hydrogen (mol), z is the number of transferred electrons (z = 2 for protons conversion to hydrogen), F is the Faraday constant (96,485 C/mol).

Contributions

W.E.H conceived the project; W.T. and W.E.H designed the study; W.T. performed the experiments and collected the data; W.T. analysed the data; W.T. and W.E.H wrote the original paper; W.T., I.P.T., and W.E.H reviewed and edited the paper.

Acknowledgements

W.E.H. thanks EPSRC (EP/M002403/1 and EP/N009746/1) for financial support. W.E.H gratefully acknowledges EPSRC (EP/M02833X/1) for instrumentation. We thank Prof Kwang-Hwan Jung at Sogang University for providing plasmids of GR. We thank Dr. Tanveer Tabish for providing graphene oxide. We thank Dr. Errin Johnson and Dr. Charlotte Melia at Sir William Dunn School of Pathology, University of Oxford, for their help on TEM. We also thank Oliver Lenz at Technische Universität Berlin, Germany for providing cloning plasmid vector pLO11.

Data, Materials, and Software Availability

All study data are included in the article and/or SI Appendix.

Competing Interests Statement

W.T., I.P.T., and W.E.H. have filed a provisional patent application with the UK Patent Office related to this work.

Chapter 5 Supplementary Information

Engineering Bio-nanoreactor in Bacteria for Efficient Hydrogen Production

Weiming Tu, Ian P. Thompson and Wei E. Huang*

Department of Engineering Science, University of Oxford, Oxford OX1 3PJ, United Kingdom.

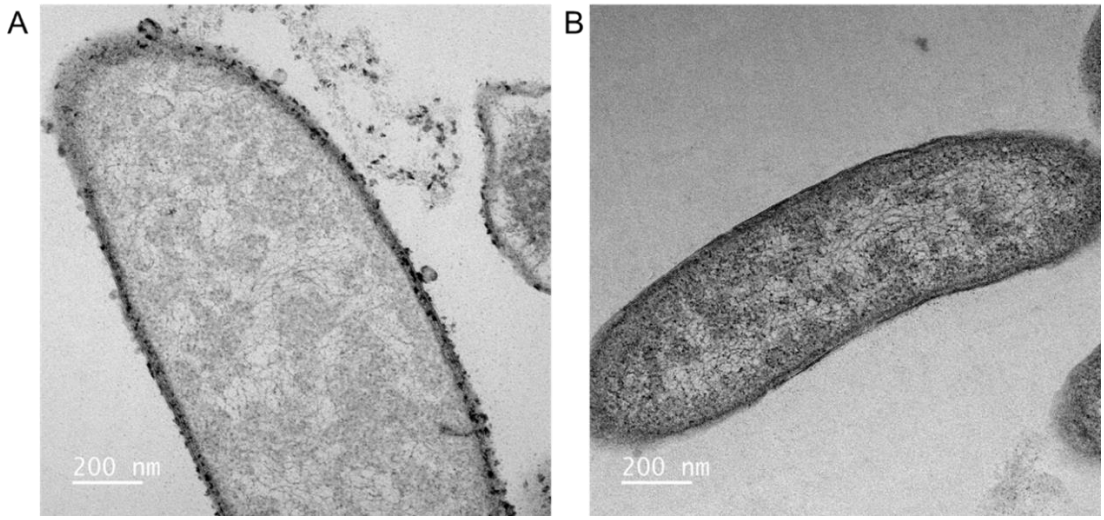
*Corresponding author: Wei E. Huang. Email: wei.huang@eng.ox.ac.uk. Tel: +44 1865 283786.

Chapter adapted from publication: ***Proceedings of the National Academy of Sciences*** (2024)

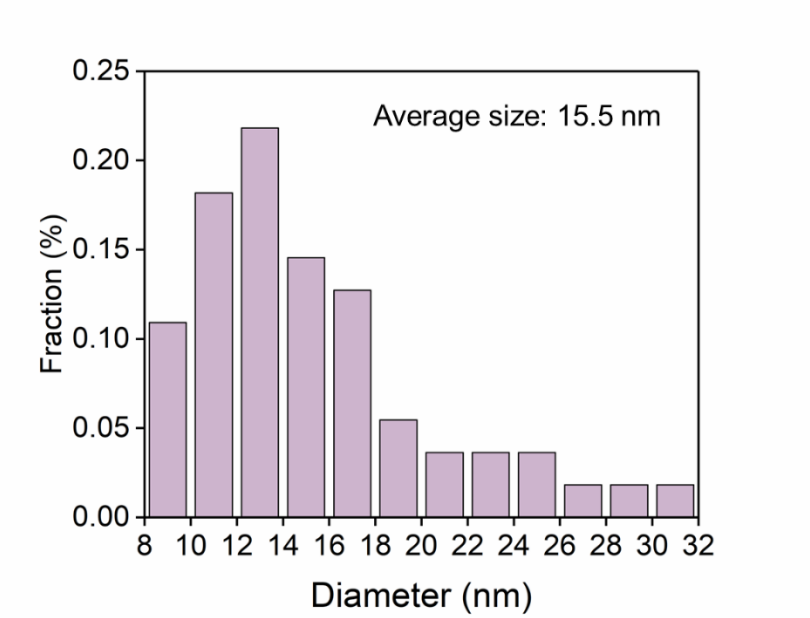
DOI: 10.1073/pnas.2404958121

Table S5.1 Strains and plasmids used in this study

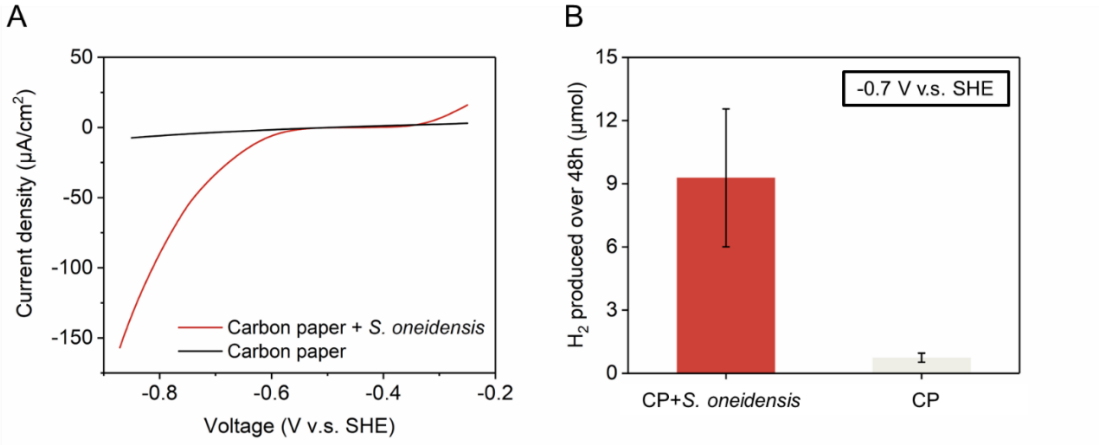
Strains	**Comments**	**Reference**
E. coli DH5α	Commercially obtained (NEW England, UK)	Lab collection
Shewanella oneidensis MR-1	Wild-type strain	Lab collection
Shewanella oneidensis MR-1-GR	*Shewanella oneidensis* MR-1-GR harbouring pLO11a-GR	This study
Shewanella oneidensis MR-1-GR-CAN	*Shewanella oneidensis* MR-1-GR harbouring pLO11a-GR and pAC-CANTHipi	This study
Shewanella oneidensis MR-1-GR-CAN-HydAB	*Shewanella oneidensis* MR-1-GR harbouring pLO11a-HydAB-GR and pAC-CANTHipi	This study
Plasmids	**Comments**	**Reference**
pLO11a (Tc^r, RK2 *ori*, Mob^+)	Expression vector with P_{BAD} promoter and downstream cloning sites (gift from Oliver Lenz, Technische Universität Berlin, Germany).	(187)
pLO11a-GR	pLO11a containing the gene for GR rhodopsin from *Gloeobacter violaceus* PCC7421	(187)
pAC-CANTHipi	pAC-BETAipi with the gene cluster of the canthaxanthin synthetic pathway	(264)
pLO11a-HydAB-GR	pLO11a containing *GR* gene rhodopsin from *Gloeobacter violaceus* PCC7421, *HydA* and *HydB* genes from *Shewanella oneidensis* MR-1	This study



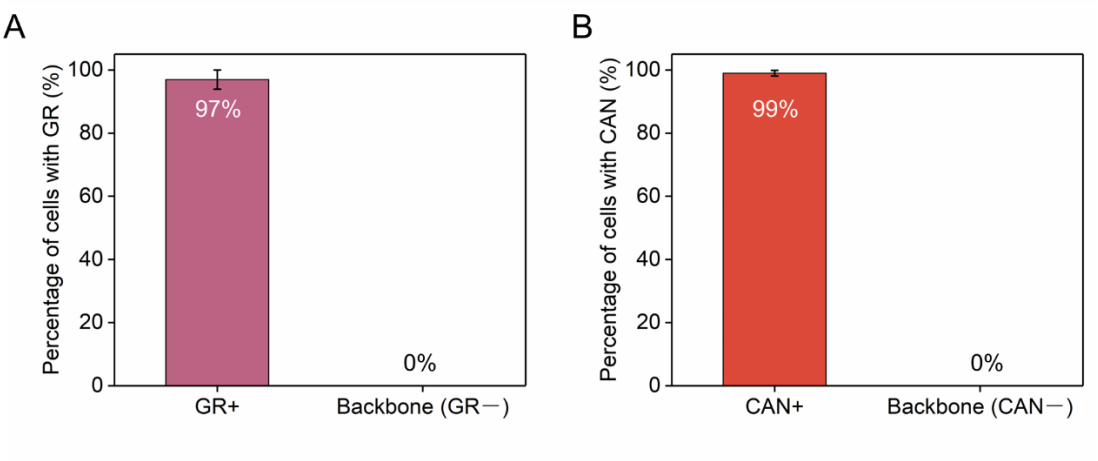
Supplementary figure S5.1. TEM images of (A) *S. oneidensis* MR-1 with FeS nanoparticles, same as Figure 5.2A and (B) the control group without nanoparticles.



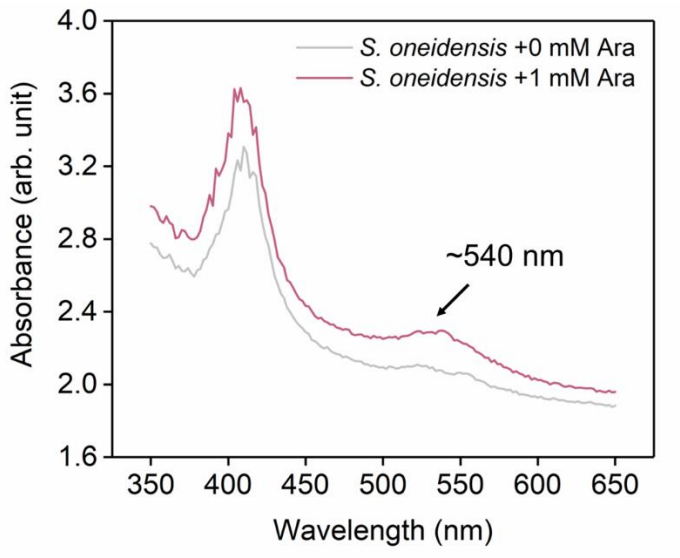
Supplementary figure S5.2. Size distributions of FeS nanoparticles bio-synthesised by *S. oneidensis* MR-1 (n = 55).



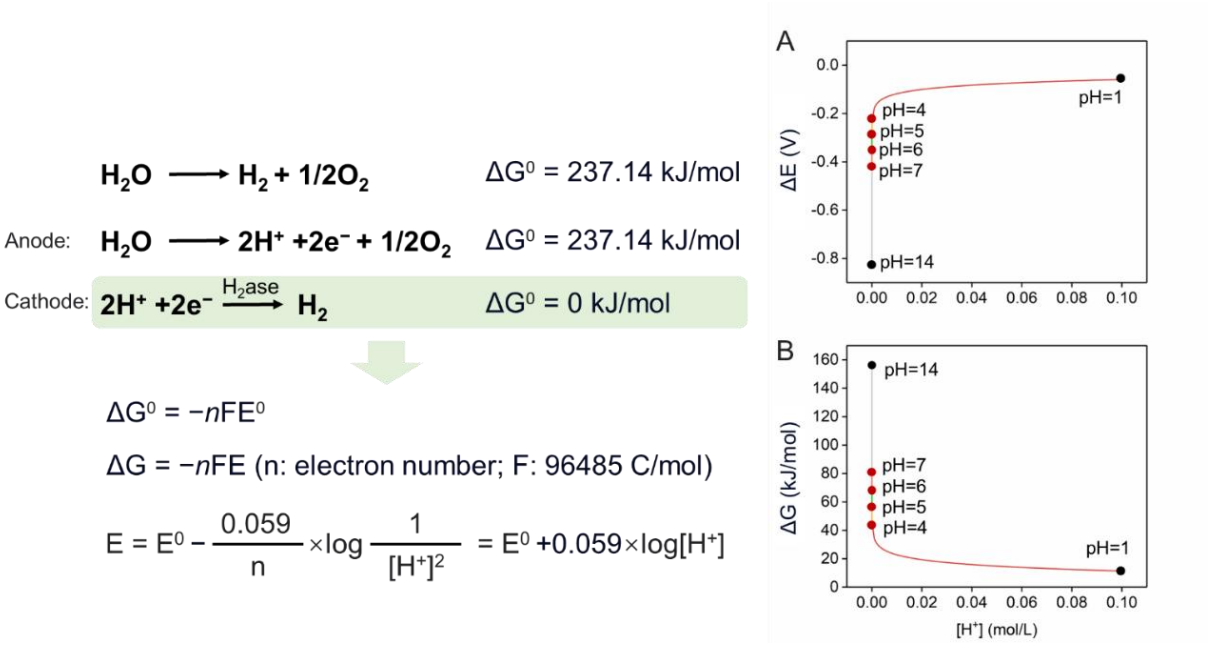
Supplementary figure S5.3. Linear scanning voltammetry (LSV) analysis for the cathode of *S. oneidensis*. (B) Hydrogen production by carbon paper (CP) with and without *S. oneidensis* after 48 hours. Data are means ± SD, n = 3.



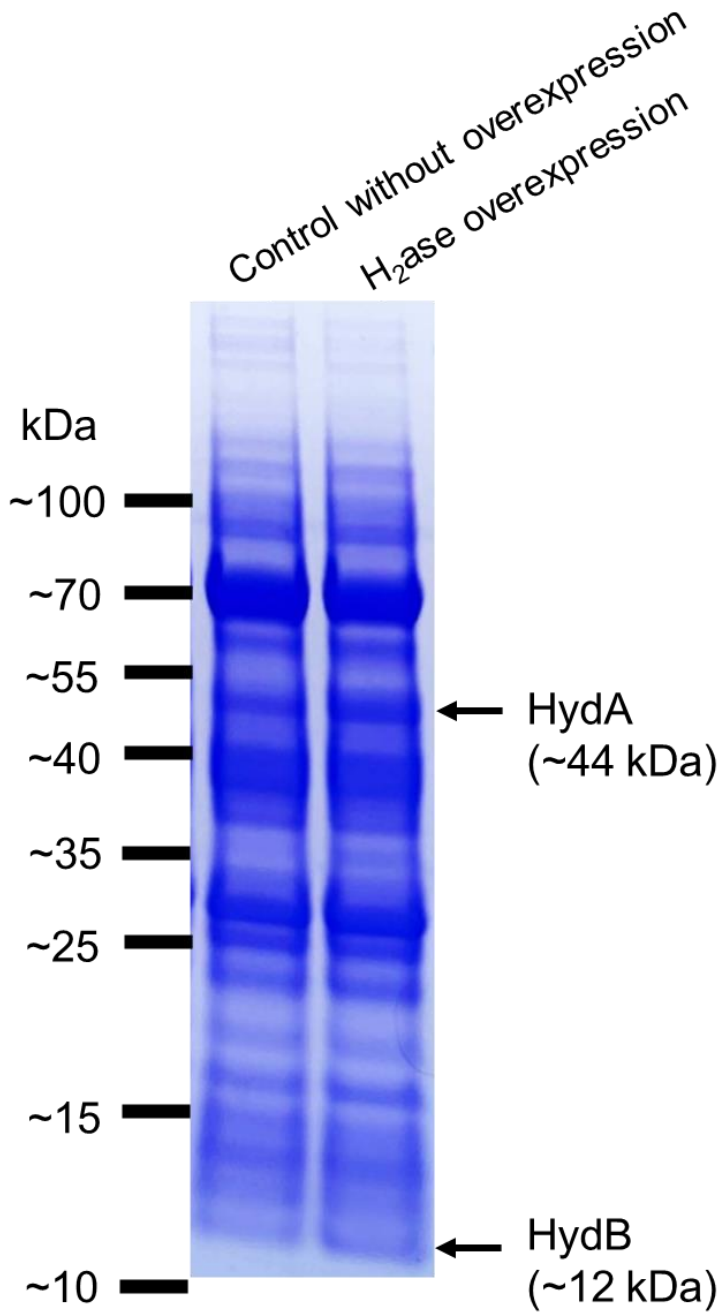
Supplementary figure S5.4. Percentage of the cells expressing GR and canthaxanthin (CAN) in the population. Data are means ± SD, n = 3.



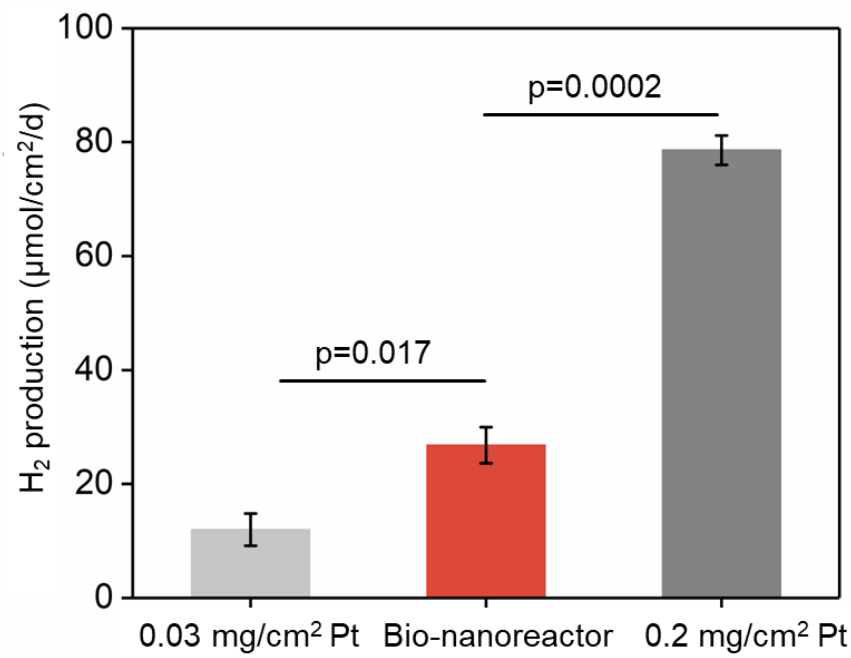
Supplementary figure S5.5. Absorbance scan of the arabinose-induced *S. onidensis*-GR and noninduced cell extracts.



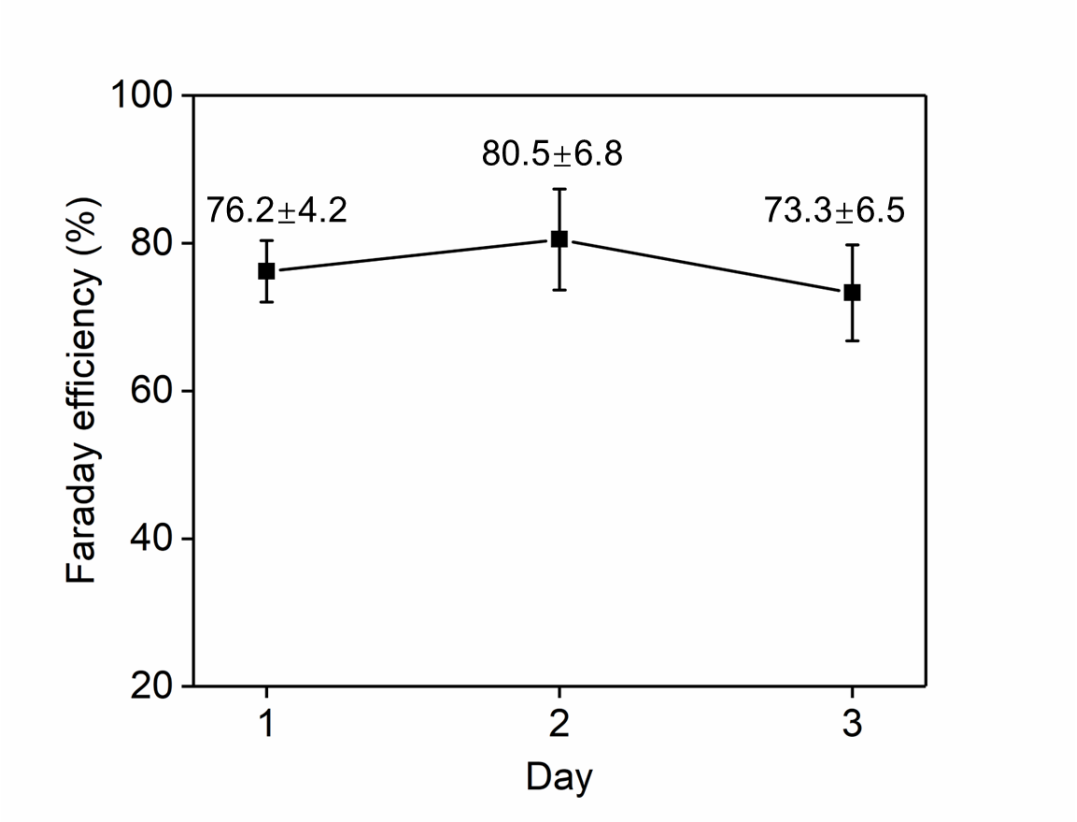
Supplementary figure S5.6. Thermodynamic analysis of redox potential and Gibbs free energy of converting protons to hydrogen.



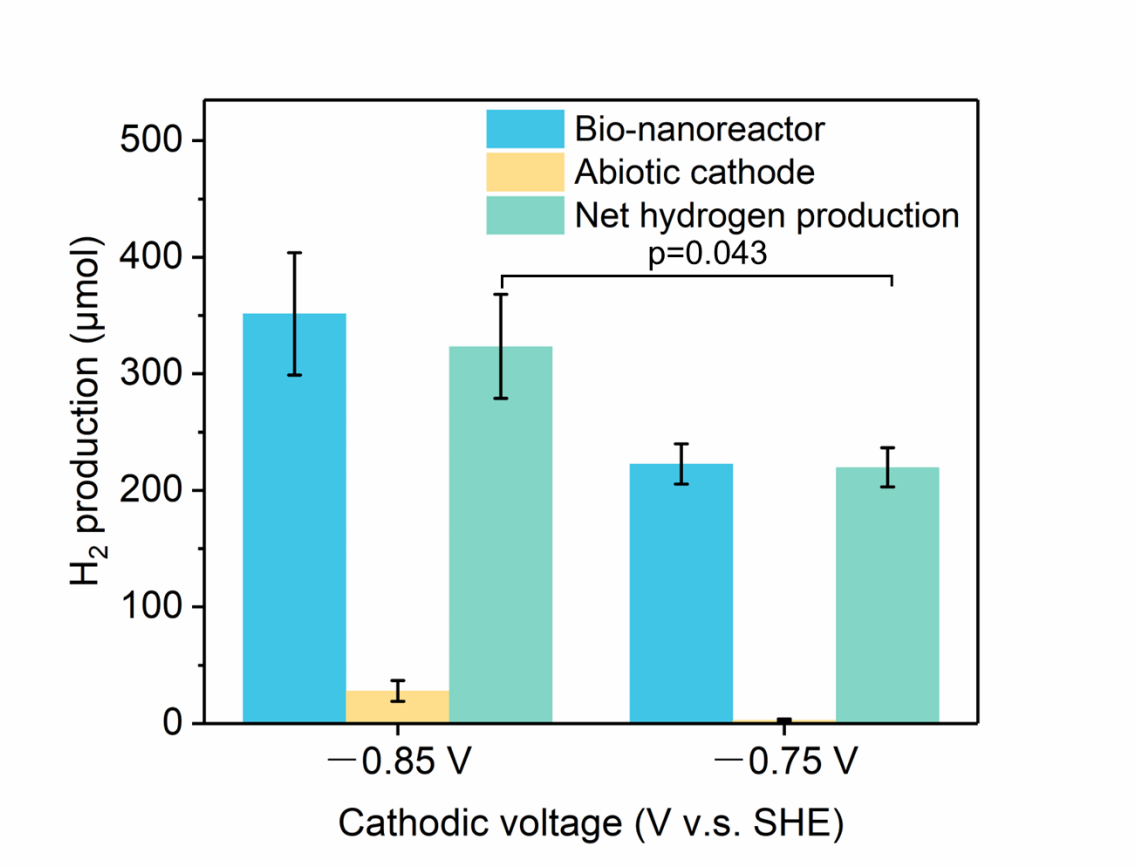
Supplementary figure S5.7. Periplasmic proteins of the arabinose-induced (H_2ase overexpression) and uninduced *S. oneidensis* MR-1-GR-CAN-HydAB. The molecular masses of HydA and HydB peptides are predicted from the amino acid sequence.



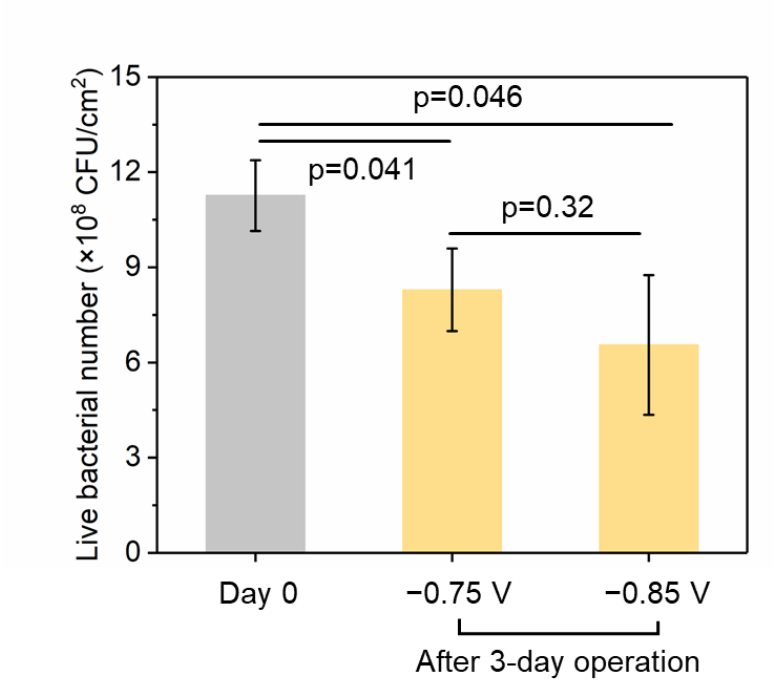
Supplementary figure S5.8. Comparison of hydrogen production between the bio-nanoreactor and the electrodes with varying platinum loadings (0.03 mg/cm^2 Pt and 0.2 mg/cm^2 Pt) at 0.75V vs. SHE, pH 7.



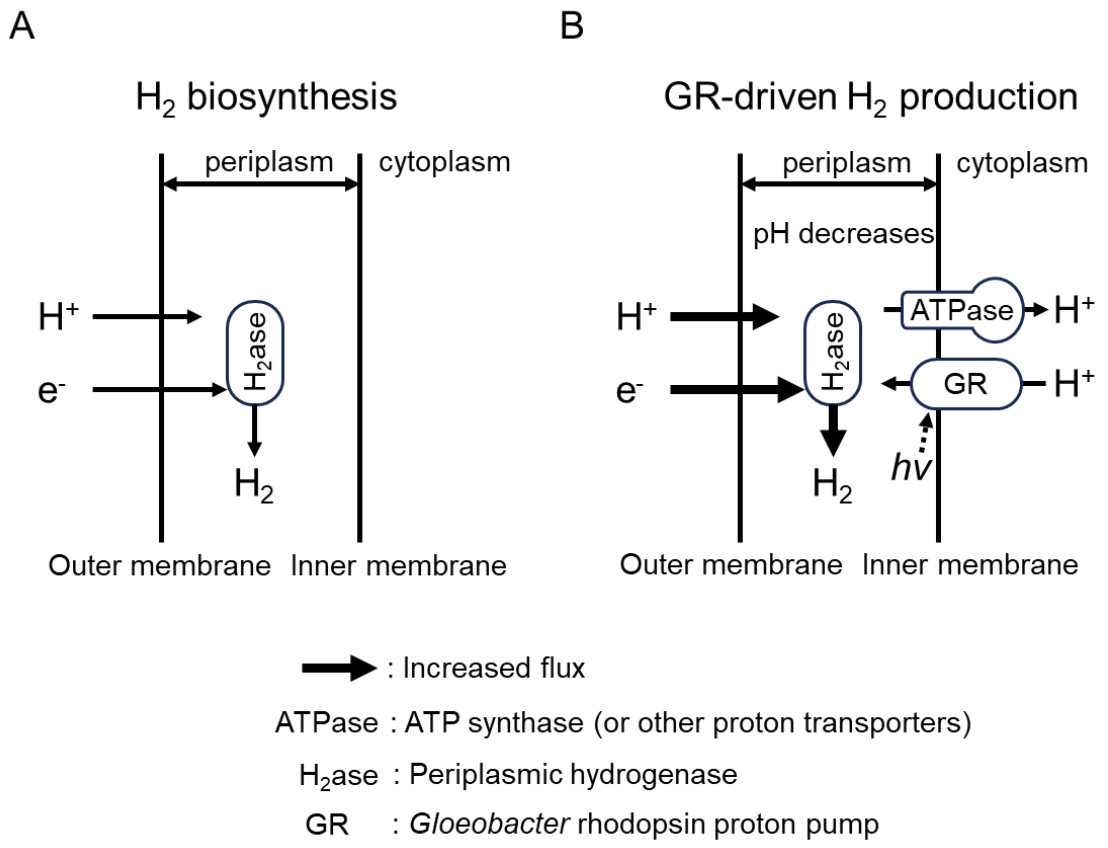
Supplementary figure S5.9. Faraday efficiency of a three-day running of the photoelectrochemical bio-nanoreactor. Data are means ± SD, n = 3.



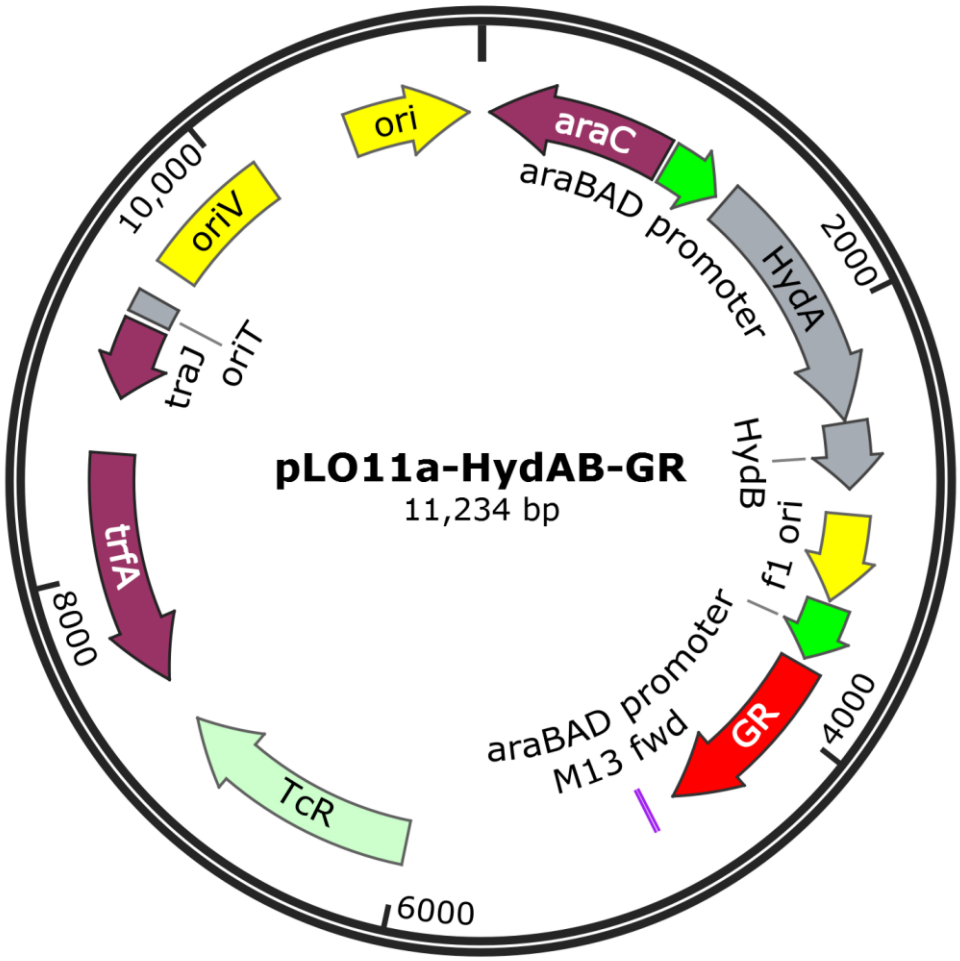
Supplementary figure S5.10. Hydrogen production at the potential of −0.75 V and −0.85 V after three-day operations. Statistics were performed with Student's t-test. Data are means ± SD, n = 3.



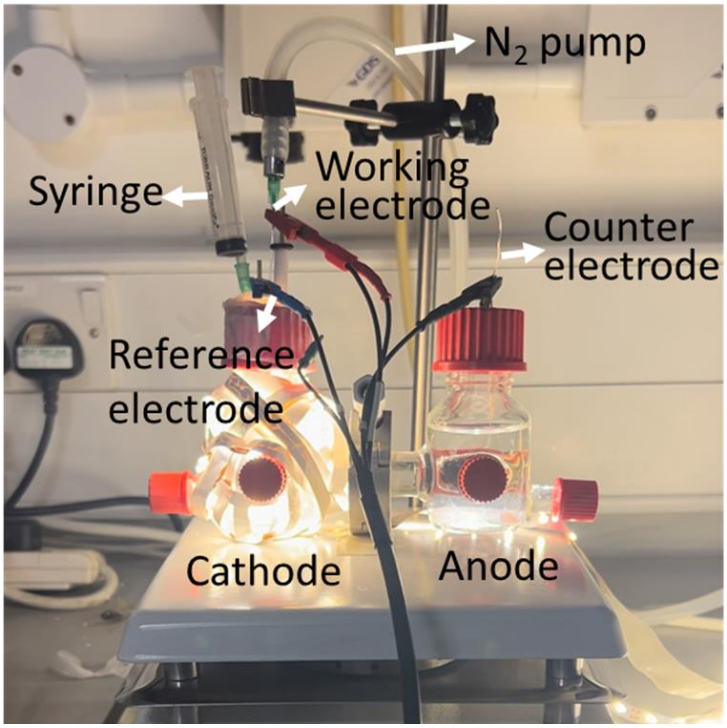
Supplementary figure S5.11. Comparison of viable cells of the engineered *S. oneidensis* before and after three-day operation at different cathodic potentials. Statistics were performed with Student's t-test (Data are means ± SD, n = 3).



Supplementary figure S5.12. Proposed periplasmic proton regulation for enhanced H_2 synthesis induced by GR.



Supplementary figure S5.13. Plasmid map of the pLO11a-HydAB-GR.



Supplementary figure S5.14. Picture of the practical set-up of the water-splitting electrochemical system using *S. oneidensis*-based cathode.

Chapter 6 Summary and Outlook

6.1 Summary

Solar energy is the ultimate source of sustainable energy. One hour of sunlight energy received by the Earth has more energy than humanity consumes in a year. Photosynthetic microorganisms and plants harvest sunlight through photosystems to fix CO_2 and drive the biosynthesis of biomass, which is the foundation of the biosphere. In nature, microbial rhodopsin as a major photosystem plays an important role in capturing light and powering metabolisms. In this thesis, *Gloeobacter* rhodopsin was exploited as an optogenetic tool to engineer rhodopsin-based phototrophy in non-native bacteria, *R. eutropha* H16 and *S. oneidensis* MR-1, for CO_2 fixation and H_2 production (Figure 6.1).

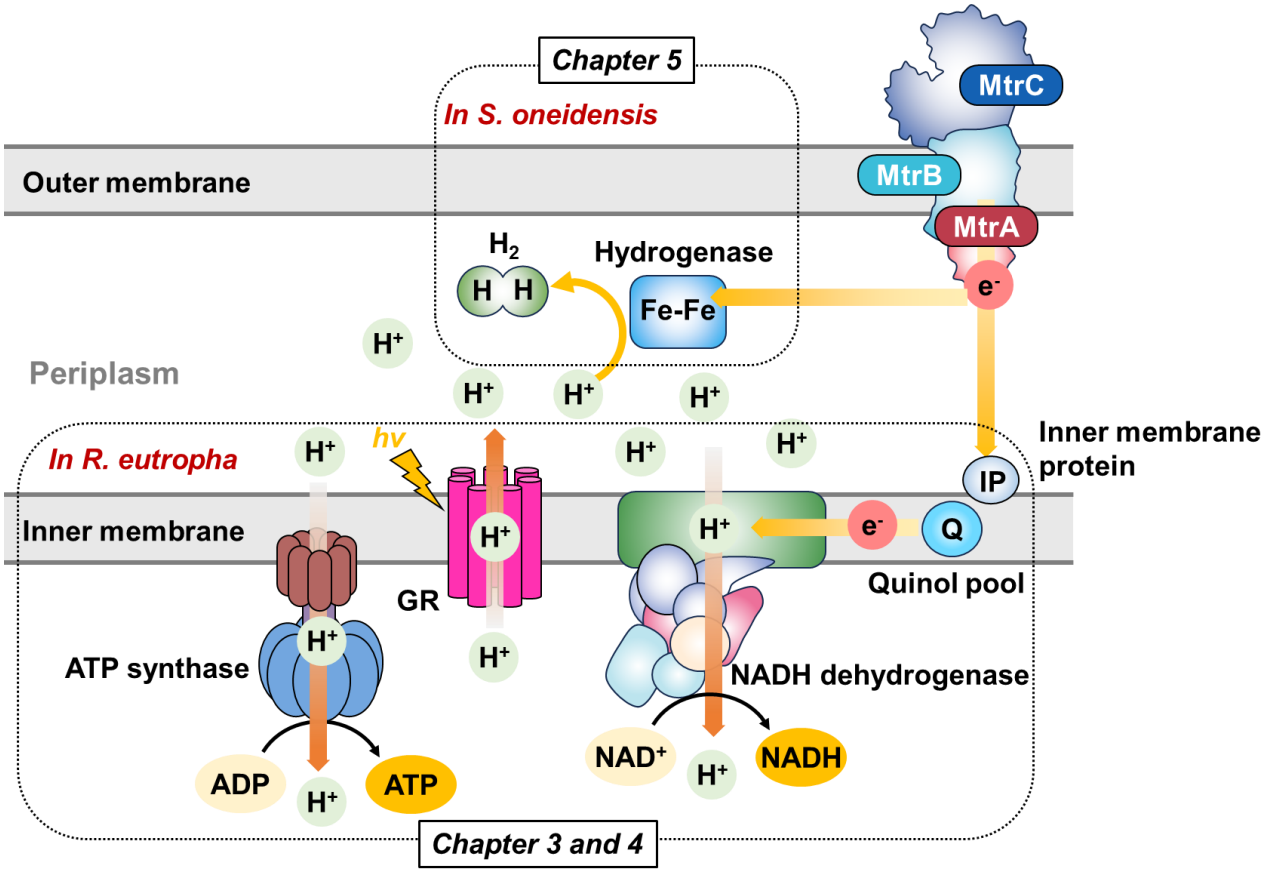


Figure 6.1. Schematic of the rhodopsin-powered hydrogen production in *S. oneidensis* MR-1 and the rhodopsin-based photosynthetic electron transport chain in *R. eutropha* H16.

In Chapter 3, GR was introduced into *R. eutropha* H16 to enhance the biomass growth on formate. The engineered *R. eutropha* H16 showed a 20% increase in biomass (or

OD_{600}) in the light compared to the growth in the dark. Inspired by the natural photosynthesis system, an innovative artificial photosynthesis system was established by integrating a photovoltaic-driven electrochemical system with GR-expressing *R. eutropha* H16. In this artificial photosynthesis system, the electrochemical module emulates photosystem II for water splitting, while the incorporation of rhodopsin substitutes photosystem I to drive the regeneration of ATP and NAD(P)H. In the presence of ATP and reducing equivalents, the CO_2 fixation pathway is activated to drive autotrophic growth.

In Chapter 4, the understanding of rhodopsin-based artificial photosynthesis has been improved from the view of modular engineering. The biological system has been divided into three modules: extracellular electron uptake, photosynthetic respiration module and intracellular electron sink module. This modular partitioning allows for the decoupling of the entire process into components for specific optimisation. An extracellular electron transfer pathway MtrCAB was introduced to improve the electron uptake. Canthaxanthin was added as an antenna to GR to enhance the proton pumping. Additionally, the overexpression of a native carbonic anhydrase and the knockout of PHB synthesis genes directed electron flux towards biomass growth instead of polymer accumulation. In summary, modular engineering offers an effective strategy for efficient CO_2 fixation.

In Chapter 5, the rhodopsin-based photosystem was applied to an electroactive bacterium *S. oneidensis* MR-1 to power H_2 synthesis. The nanoscale periplasmic space (20 to 30 nm) of *S. oneidensis* MR-1 was engineered into a highly effective bio-nanoreactor for H_2 production. The integration of rGO, MtrCAB complex and FeS nanoparticles established an effective electron transfer chain from the electrode to the periplasm. The introduction of GR and CAN boosted proton pumping into the periplasm under light. This system, catalysed by overexpression of [FeFe]-hydrogenase and powered by both electricity and light, achieved a Faraday efficiency of 80% for hydrogen production. This periplasmic bio-nanoreactor marks an advancement in sustainable synthetic biology.

The artificial photosynthesis system established in this thesis provides a safe, cheap, sustainable and energy-efficient approach for energy conversion and CO_2-based bioeconomy. In this electrochemical system, the cathode is constructed from a carbon

cloth, and the biocatalyst is the engineered cells, which is a “self-reproducible factory”. This configuration obviates the need for expensive metal catalysts like platinum and cobalt, leading to considerable cost reductions. In terms of ecological significance, this artificial photosynthesis system offers a new perspective for investigating the role of rhodopsin in environmental microbiology, potentially driving CO_2 fixation and/or H_2 synthesis by harnessing electrons from the environment. Carbon fixation is a cornerstone of the global carbon cycle, while H_2 is an important electron carrier and energy source in marine systems. This work highlights the untapped potential of rhodopsin in the biosphere's carbon and energy cycles.

6.2 Limitations of the work in the thesis

One of the primary limitations in this thesis is the lack of a detailed photosynthesis efficiency analysis. Photosynthetic efficiency is typically calculated by dividing energy output by energy input. In this study, energy output can be directly calculated based on biomass increase. However, there is debate regarding the calculation of solar energy input. Part of the light energy is harvested by rhodopsin while another portion is captured by the solar panel. The solar energy harvested by the solar panel can be estimated from the electricity consumed, assuming a typical solar-to-electricity efficiency of around 0.2. However, the quantum efficiency of rhodopsin has been controversial, yielding a wide range of values, generally between 0.25 and 0.79 (267). The uncertainty of rhodopsin’s quantum efficiency complicates the calculation of overall photosynthetic efficiency in this work. Therefore, to estimate the photosynthesis efficiency of the rhodopsin-based artificial photosynthesis, measuring quantum efficiency for GR in *R. eutropha* will be essential in future efforts.

There are some limitations on experimental measurements. Biomass estimation methods, such as Optical Density at 600 nm (OD_{600}), are commonly used but have inherent drawbacks, particularly when dealing with pigmented cells. Pigments can interfere with accurate OD_{600} readings, leading to unreliable biomass estimates. In this thesis, the pink pigmentation of GR-expressing cells could have affected the accuracy of biomass quantification. Alternative methods such as flow cytometry (FCM), which counts cells directly and provides more precise biomass measurements, may offer a more reliable approach. In addition, the current work did not measure the amount of functional rhodopsin protein present in the system. A previous study has reported that

E. coli, when exogenously supplied with the retinal cofactor, can assemble up to 187,000 holo-proteorhodopsin molecules per cell (74); however, this aspect has been omitted in this thesis. The amount of functional rhodopsin could significantly impact the overall performance of light-driven processes. Quantifying functional rhodopsin would allow for a more accurate assessment of the relationship between protein levels and system efficiency, which remains underexplored in this study.

There are several inherent limitations in the artificial photosynthetic system presented in this thesis. Firstly, the strain used for CO_2 fixation, *Ralstonia eutropha* H16, is not highly robust and does not host multiple plasmids well. Future work should focus on integrating genes directly into the chromosome to ensure stable expression, as well as selecting more suitable industrial strains as the chassis. Secondly, biological electron transfer processes face inherent challenges, characterised by low current densities (0.1–10 mA/cm^2). To overcome the low electron transfer rate, combining biological systems with abiotic materials could enhance electron transfer efficiency.

In Chapter 5, hydrogen was synthesised as an end-product. While hydrogen is a promising clean fuel, it has several limitations. The production, storage, and transport of hydrogen remain challenging, particularly in terms of infrastructure and cost. Hydrogen's low volumetric energy density and the need for high-pressure storage or liquefaction limit its practicality. Additionally, hydrogen's reactivity and flammability present safety concerns, particularly in industrial and transportation settings. These challenges must be addressed before hydrogen can become a widespread fuel solution.

6.3 Outlook

The overarching goal of this thesis is to establish rhodopsin-based artificial photosynthesis for sustainable chemical engineering. It focuses on two carbon-negative applications: CO_2 fixation and H_2 production, both addressed through engineering biology design. As Nobel Laureate Albert Szent-Györgyi said:

"*Life is nothing but an electron looking for a place to rest*."

The artificial photosynthesis of this work has demonstrated that life is driven by Yin (electrons) and Yang (protons) interaction. The redesign of the bacterial electron transport chain powered by proton motive force validated the proton-coupled electron transfer. From a biological perspective, this system is simple and modular, offering the

potential to extend its use to convert any microorganisms into photosynthetic cells, given the ubiquitous expression of rhodopsin in nature's microbes.

Engineering artificial photosynthesis is a long-standing goal. While significant efforts have been devoted to understanding chlorophyll-based photosystems, progress has been slowed progress due to the complexity of the systems. Rhodopsin, as a complementary light-harvesting system, provides a novel approach to reconstructing the photosynthetic electron transport chain in bacteria. Its inherent structural and mechanistic simplicity makes rhodopsin a valuable tool in metabolic engineering, and this simplicity also opens up new possibilities. For example, rhodopsin can be designed to harvest light across a broad spectrum, from blue to red wavelengths (144). In addition, it can be integrated with material engineering to form bio-hybrid systems, enhancing efficiency and controllability in bioproduction (189). Leveraging synthetic biology and material engineering could be the future of artificial photosynthesis. A significant strength of biological systems is their ability to catalyse the production of long-chain carbon compounds, while materials offer high efficiency in one-carbon compound conversion. Integrating these complementary advantages could lead to efficient bioproduction and may represent the future of sustainable chemical engineering.

From the perspective of environmental microbiology, the artificial photosynthesis developed in this thesis offers insights into the role of proton-pumping rhodopsin in natural environments (Figure 6.2). Rhodopsin enhances the growth of heterotrophic organisms by supplying energy through light-driven proton pumping. This phenomenon is observed not only in natural microbes containing rhodopsin but also in engineered strains as demonstrated in Chapter 3. By facilitating more efficient utilisation of organic substrates and ATP synthesis, this process promotes biomass accumulation and overall productivity within microbial communities, granting these rhodopsin-containing organisms a survival advantage in their environments. In addition to enhancing heterotrophic biosynthesis, rhodopsin-driven regeneration of reducing equivalents could be an important mechanism for driving CO_2 fixation in the environment. Rhodopsin-containing microorganisms can obtain electrons from insoluble minerals or through interspecies electron transfer to generate NAD(P)H as a driving force for facilitating CO_2 fixation. However, evidence supporting the relationship between rhodopsin and autotrophic growth in natural environments is still lacking. Metagenomic investigations are needed to explore the connections among

rhodopsin genes, extracellular electron transfer pathway genes, and CO_2 fixation pathway genes.

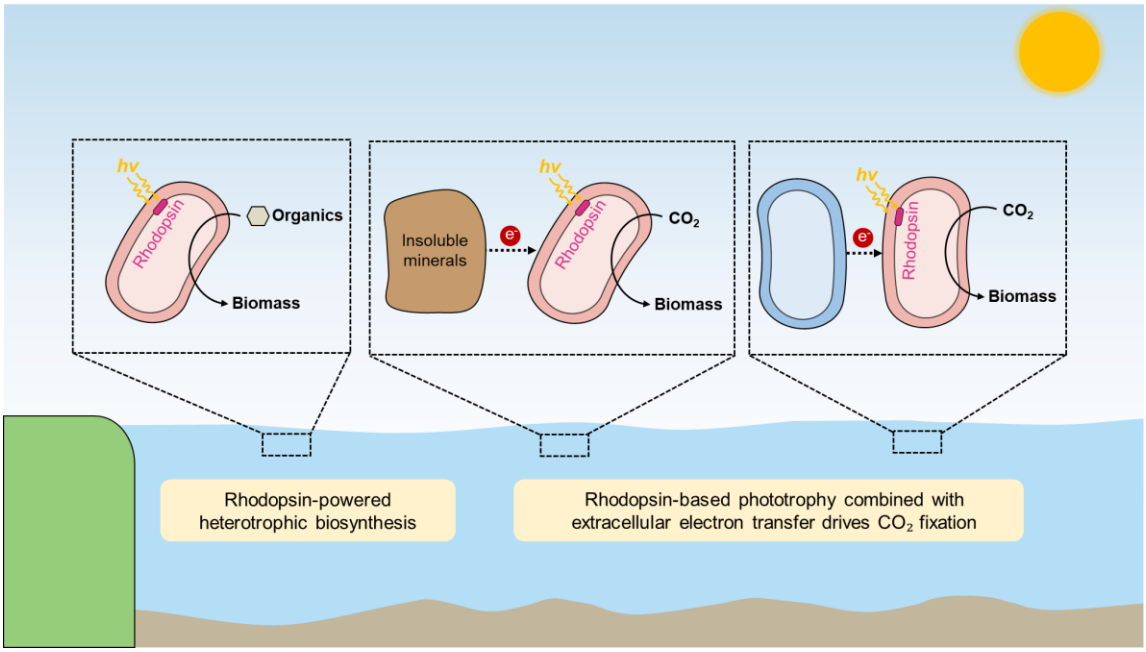


Figure 6.2. Hypothesis on the role of proton-pumping rhodopsin in the carbon cycle based on findings from this thesis.

The sustainable applications of rhodopsin are not limited to artificial photosynthesis. Rhodopsin can also be utilised in solar panels, biosensors, and biocomputing (68, 268, 269) (Figure 6.3). The key to these applications lies in rhodopsin's remarkable photochemical properties which allow it to undergo conformational changes upon light absorption, driving a variety of biological processes. In recent decades, the application of artificial intelligence to rhodopsin design has opened a new frontier for optimising these proteins for specific uses. The integration of biotechnology with artificial intelligence methodologies is having a revolutionising impact to fully unlock the potential of such simple and effective rhodopsin-based light-harvesting systems. As our understanding of these proteins deepens, the exploration of rhodopsin-based applications holds significant promise for addressing global challenges related to energy, food, environment and health, marking a significant stride towards a more sustainable future.

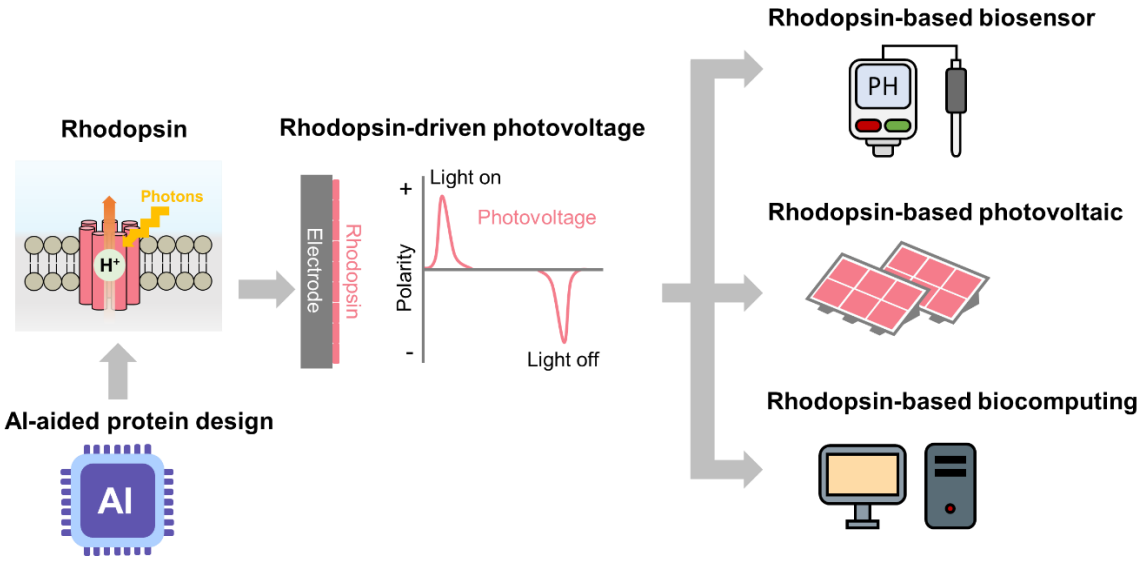


Figure 6.3. The applications of rhodopsin in other sustainable fields.

References

1. O. M. Finkel, O. Béjà, S. Belkin, Global abundance of microbial rhodopsins. *The ISME Journal* **7**, 448-451 (2013).
2. D. A. Bryant, N.-U. Frigaard, Prokaryotic photosynthesis and phototrophy illuminated. *Trends in Microbiology* **14**, 488-496 (2006).
3. L. Gómez-Consarnau *et al.*, Microbial rhodopsins are major contributors to the solar energy captured in the sea. *Science Advances* **5**, eaaw8855 (2019).
4. A. Chazan *et al.*, Phototrophy by antenna-containing rhodopsin pumps in aquatic environments. *Nature* **615**, 535-540 (2023).
5. O. P. Ernst *et al.*, Microbial and animal rhodopsins: structures, functions, and molecular mechanisms. *Chemical Reviews* **114**, 126-163 (2014).
6. M. A. Zahed, E. Movahed, A. Khodayari, S. Zanganeh, M. Badamaki, Biotechnology for carbon capture and fixation: critical review and future directions. *Journal of Environmental Management* **293**, 112830 (2021).
7. H. Schweitzer *et al.*, Innovating carbon-capture biotechnologies through ecosystem-inspired solutions. *One Earth* **4**, 49-59 (2021).
8. E. s. C. H. Page (2019) CO_2.earth https://www.co2.earth.
9. Y. Xu, V. Ramanathan, D. G. Victor, Global warming will happen faster than we think. *Nature* **504**, 30-32 (2018).
10. T. P. Hughes *et al.*, Climate change, human impacts, and the resilience of coral reefs. *Science* **301**, 929 (2003).
11. M. T. Noori, R. Rossi, B. E. Logan, B. Min, Hydrogen production in microbial electrolysis cells with biocathodes. *Trends in Biotechnology* **42**, 815-828 (2024).
12. C. Song *et al.*, Absorption-microalgae hybrid CO_2 capture and biotransformation strategy—A review. *International Journal of Greenhouse Gas Control* **88**, 109-117 (2019).
13. M. Beller, U. T. Bornscheuer, CO_2 fixation through hydrogenation by chemical or enzymatic methods. *Angewandte Chemie International Edition* **53**, 4527-4528 (2014).
14. N. Meunier, R. Chauvy, S. Mouhoubi, D. Thomas, G. De Weireld, Alternative production of methanol from industrial CO_2. *Renewable Energy* **146**, 1192-1203 (2020).
15. D. Y. C. Leung, G. Caramanna, M. M. Maroto-Valer, An overview of current status of carbon dioxide capture and storage technologies. *Renewable and Sustainable Energy Reviews* **39**, 426-443 (2014).
16. M. Sevilla, A. B. Fuertes, CO_2 adsorption by activated templated carbons. *Journal of Colloid and Interface Science* **366**, 147-154 (2012).
17. H. Wang, C. Ma, Z. Yang, X. Lu, X. Ji, Improving high-pressure water scrubbing through process integration and solvent selection for biogas upgrading. *Applied Energy* **276**, 115462 (2020).
18. T. Nguyen, M. Hilliard, G. T. Rochelle, Amine volatility in CO_2 capture. *International Journal of Greenhouse Gas Control* **4**, 707-715 (2010).
19. V. Y. Dindore, D. W. F. Brilman, F. H. Geuzebroek, G. F. Versteeg, Membrane–solvent selection for CO_2 removal using membrane gas–liquid contactors. *Separation and Purification Technology* **40**, 133-145 (2004).
20. H. Salehizadeh, N. Yan, R. Farnood, Recent advances in microbial CO_2 fixation and conversion to value-added products. *Chemical Engineering Journal* **390**, 124584 (2020).
21. T. Cai *et al.*, Cell-free chemoenzymatic starch synthesis from carbon dioxide. *Science* **373**, 1523-1527 (2021).
22. C. Gougoulias, J. M. Clark, L. J. Shaw, The role of soil microbes in the global carbon cycle: tracking the below-ground microbial processing of plant-derived carbon for manipulating carbon dynamics in agricultural systems. *Journal of the Science of Food and Agriculture* **94**, 2362-2371 (2014).

23. P. Branduardi, M. Sauer, Microbial carbon dioxide fixation: new tricks for an old game. *FEMS Microbiology Letters* **365**, fnx269 (2018).
24. S. Gleizer *et al.*, Conversion of *Escherichia coli* to generate all biomass carbon from CO_2. *Cell* **179**, 1255-1263.e1212 (2019).
25. J. M. Walter, D. Greenfield, C. Bustamante, J. Liphardt, Light-powering *Escherichia coli* with proteorhodopsin. *Proceedings of the National Academy of Sciences* **104**, 2408 (2007).
26. J. Xuan, L. He, W. Wen, Y. Feng, Hydrogenase and nitrogenase: key catalysts in biohydrogen production. *Molecules* **28**, 1392 (2023).
27. K. Gärtner, S. Lechno-Yossef, J. Cornish Adam, C. P. Wolk, L. Hegg Eric, Expression of *Shewanella oneidensis* MR-1 [FeFe]-hydrogenase genes in *Anabaena* sp. strain PCC 7120. *Applied and Environmental Microbiology* **78**, 8579-8586 (2012).
28. P. C. Hallenbeck, J. R. Benemann, Biological hydrogen production; fundamentals and limiting processes. *International Journal of Hydrogen Energy* **27**, 1185-1193 (2002).
29. D. Dutta, D. De, S. Chaudhuri, S. K. Bhattacharya, Hydrogen production by cyanobacteria. *Microbial Cell Factories* **4**, 36 (2005).
30. K.-Y. Show, Y.-G. Yan, D.-J. Lee, "Chapter 13 - Biohydrogen production from algae: Perspectives, challenges, and prospects" in Biofuels from Algae (Second Edition), A. Pandey, J.-S. Chang, C. R. Soccol, D.-J. Lee, Y. Chisti, Eds. (Elsevier, 2019), https://doi.org/10.1016/B978-0-444-64192-2.00013-5, pp. 325-343.
31. K. E. Redding *et al.*, Advances and challenges in photosynthetic hydrogen production. *Trends in Biotechnology* **40**, 1313-1325 (2022).
32. Y. Fu *et al.*, Extracellular electron transfer of *Shewanella oneidensis* MR-1 for cathodic hydrogen evolution reaction. *Electrochimica Acta* **305**, 528-533 (2019).
33. L. A. Márquez-Reyes, M. d. P. Sánchez-Saavedra, I. Valdez-Vazquez, Improvement of hydrogen production by reduction of the photosynthetic oxygen in microalgae cultures of *Chlamydomonas gloeopara* and *Scenedesmus obliquus*. *International Journal of Hydrogen Energy* **40**, 7291-7300 (2015).
34. I. Yacoby *et al.*, Photosynthetic electron partitioning between [FeFe]-hydrogenase and ferredoxin:$NADP^+$-oxidoreductase (FNR) enzymes in vitro. *Proceedings of the National Academy of Sciences* **108**, 9396-9401 (2011).
35. F. Gong, H. Zhu, Y. Zhang, Y. Li, Biological carbon fixation: from natural to synthetic. *Journal of CO_2 Utilization* **28**, 221-227 (2018).
36. Z. Liu, K. Wang, Y. Chen, T. Tan, J. Nielsen, Third-generation biorefineries as the means to produce fuels and chemicals from CO_2. *Nature Catalysis* **3**, 274-288 (2020).
37. H. Huber *et al.*, A dicarboxylate/4-hydroxybutyrate autotrophic carbon assimilation cycle in the hyperthermophilic Archaeum *Ignicoccus hospitalis*. *Proceedings of the National Academy of Sciences* **105**, 7851-7856 (2008).
38. I. A. Berg, D. Kockelkorn, W. Buckel, G. Fuchs, A 3-hydroxypropionate/4-hydroxybutyrate autotrophic carbon dioxide assimilation pathway in archaea. *Science* **318**, 1782-1786 (2007).
39. G. STRAUSS, G. FUCHS, Enzymes of a novel autotrophic CO_2 fixation pathway in the phototrophic bacterium *Chloroflexus aurantiacus*, the 3-hydroxypropionate cycle. *European Journal of Biochemistry* **215**, 633-643 (1993).
40. M. Schulman, D. Parker, L. G. Ljungdahl, H. G. Wood, Total synthesis of acetate from CO_2 V. Determination by mass analysis of the different types of acetate formed from $^{13}CO_2$ by heterotrophic bacteria. *Journal of Bacteriology* **109**, 633-644 (1972).
41. M. Evans, B. B. Buchanan, D. I. Arnon, A new ferredoxin-dependent carbon reduction cycle in a photosynthetic bacterium. *Proceedings of the National Academy of Sciences of the United States of America* **55**, 928 (1966).
42. M. Calvin, A. A. Benson, The path of carbon in photosynthesis. *Science* **107**, 476-480 (1948).
43. T. Sumi, K. Harada, Kinetics of the ancestral carbon metabolism pathways in deep-branching bacteria and archaea. *Communications Chemistry* **4**, 149 (2021).

44. T. Zhao, Y. Li, Y. Zhang, Biological carbon fixation: a thermodynamic perspective. *Green Chemistry* **23**, 7852-7864 (2021).
45. Y. Milrad, S. Schweitzer, Y. Feldman, I. Yacoby, Green algal hydrogenase activity is outcompeted by carbon fixation before inactivation by oxygen takes place. *Plant Physiology* **177**, 918-926 (2018).
46. L. Cournac, G. Guedeney, G. Peltier, P. M. Vignais, Sustained photoevolution of molecular hydrogen in a mutant of *Synechocystis* sp. strain PCC 6803 deficient in the type I NADPH-dehydrogenase complex. *Journal of Bacteriology* **186**, 1737-1746 (2004).
47. Z. Gao, H. Zhao, Z. Li, X. Tan, X. Lu, Photosynthetic production of ethanol from carbon dioxide in genetically engineered cyanobacteria. *Energy & Environmental Science* **5**, 9857-9865 (2012).
48. Y. Lu, J. Dai, Q. Wu, Photosynthesis-fermentation hybrid system to produce lipid feedstock for algal biofuel. *Environmental technology* **34**, 1869-1876 (2013).
49. V. H. Work, S. D'Adamo, R. Radakovits, R. E. Jinkerson, M. C. Posewitz, Improving photosynthesis and metabolic networks for the competitive production of phototroph-derived biofuels. *Current Opinion in Biotechnology* **23**, 290-297 (2012).
50. M. Kitajima, W. L. Butler, Excitation spectra for Photosystem I and Photosystem II in chloroplasts and the spectral characteristics of the distribution of quanta between the two photosystems. *Biochimica et Biophysica Acta (BBA) - Bioenergetics* **408**, 297-305 (1975).
51. D. J. Nürnberg *et al.*, Photochemistry beyond the red limit in chlorophyll f–containing photosystems. *Science* **360**, 1210-1213 (2018).
52. H. Kirst, C. Formighieri, A. Melis, Maximizing photosynthetic efficiency and culture productivity in cyanobacteria upon minimizing the phycobilisome light-harvesting antenna size. *Biochimica et Biophysica Acta (BBA) - Bioenergetics* **1837**, 1653-1664 (2014).
53. H. Michel, Editorial: The Nonsense of Biofuels. *Angewandte Chemie International Edition* **51**, 2516-2518 (2012).
54. Y. Tachibana, L. Vayssieres, J. R. Durrant, Artificial photosynthesis for solar water-splitting. *Nature Photonics* **6**, 511-518 (2012).
55. P. C. Sahoo, D. Pant, M. Kumar, S. Puri, S. Ramakumar, Material–microbe interfaces for solar-driven CO_2 bioelectrosynthesis. *Trends in biotechnology* **38**, 1245-1261 (2020).
56. C. M. Lewis *et al.*, Electrochemically Driven Photosynthetic Electron Transport in Cyanobacteria Lacking Photosystem II. *Journal of the American Chemical Society* **144**, 2933-2942 (2022).
57. O. Beja, E. N. Spudich, J. L. Spudich, M. Leclerc, E. F. DeLong, Proteorhodopsin phototrophy in the ocean. *Nature* **411**, 786-789 (2001).
58. X. Jing *et al.*, Raman-activated cell sorting and metagenomic sequencing revealing carbon-fixing bacteria in the ocean. *Environmental Microbiology* **20**, 2241-2255 (2018).
59. B. J. Campbell, L. A. Waidner, M. T. Cottrell, D. L. Kirchman, Abundant proteorhodopsin genes in the North Atlantic Ocean. *Environmental Microbiology* **10**, 99-109 (2008).
60. J. A. Fuhrman, M. S. Schwalbach, U. Stingl, Opinion - Proteorhodopsins: an array of physiological roles? *Nature Reviews Microbiology* **6**, 488-494 (2008).
61. D. B. Rusch *et al.*, The *Sorcerer II* Global Ocean Sampling expedition: Northwest Atlantic through Eastern Tropical Pacific. *Plos Biology* **5**, 398-431 (2007).
62. G. Sabehi *et al.*, New insights into metabolic properties of marine bacteria encoding proteorhodopsins. *Plos Biology* **3**, 1409-1417 (2005).
63. O. Béjà *et al.*, Bacterial Rhodopsin: Evidence for a new type of phototrophy in the sea. *Science* **289**, 1902-1906 (2000).
64. J. Strauss *et al.*, Plastid-localized xanthorhodopsin increases diatom biomass and

ecosystem productivity in iron-limited surface oceans. *Nature Microbiology* **8**, 2050-2066 (2023).
65. D. L. Kirchman, T. E. Hanson, Bioenergetics of photoheterotrophic bacteria in the oceans. *Environmental Microbiology Reports* **5**, 188-199 (2013).
66. D. Boeuf, S. Audic, L. Brillet-Guéguen, C. Caron, C. Jeanthon, MicRhoDE: a curated database for the analysis of microbial rhodopsin diversity and evolution. *Database* **2015** (2015).
67. K. Inoue *et al.*, Exploration of natural red-shifted rhodopsins using a machine learning-based Bayesian experimental design. *Communications Biology* **4**, 362 (2021).
68. K. Kojima, A. Shibukawa, Y. Sudo, The unlimited potential of microbial rhodopsins as optical tools. *Biochemistry* **59**, 218-229 (2020).
69. N. J. Claassens, M. Volpers, V. A. P. M. d. Santos, J. van der Oost, W. M. de Vos, Potential of proton-pumping rhodopsins: engineering photosystems into microorganisms. *Trends in Biotechnology* **31**, 633-642 (2013).
70. L. Steindler, M. S. Schwalbach, D. P. Smith, F. Chan, S. J. Giovannoni, Energy Starved *Candidatus* Pelagibacter Ubique Substitutes Light-Mediated ATP Production for Endogenous Carbon Respiration. *Plos One* **6**, e19725 (2011).
71. L. Gómez-Consarnau *et al.*, Light stimulates growth of proteorhodopsin-containing marine Flavobacteria. *Nature* **445**, 210-213 (2007).
72. L. Gómez-Consarnau *et al.*, Proteorhodopsin light-enhanced growth linked to vitamin-B1 acquisition in marine Flavobacteria. *The ISME Journal* **10**, 1102-1112 (2016).
73. L. Gómez-Consarnau *et al.*, Proteorhodopsin phototrophy promotes survival of marine bacteria during starvation. *Plos Biology* **8**, e1000358 (2010).
74. Y. Song *et al.*, Proteorhodopsin overproduction enhances the long-term viability of *Escherichia coli*. *Applied and Environmental Microbiology* **86**, e02087-02019 (2019).
75. H. A. Kim *et al.*, An evolutionary optimization of a rhodopsin-based phototrophic metabolism in Escherichia coli. *Microbial Cell Factories* **16**, 111 (2017).
76. Y. Toya *et al.*, Optogenetic reprogramming of carbon metabolism using light-powering microbial proton pump systems. *Metabolic Engineering* **72**, 227-236 (2022).
77. J. Y. H. Kim, B. Jo, Y. Jo, H. Cha, Improved production of biohydrogen in light-powered *Escherichia coli* by co-expression of proteorhodopsin and heterologous hydrogenase. *Microbial Cell Factories* **11**, 2 (2012).
78. J. Palovaara *et al.*, Stimulation of growth by proteorhodopsin phototrophy involves regulation of central metabolic pathways in marine planktonic bacteria. *Proceedings of the National Academy of Sciences* **111**, E3650-E3658 (2014).
79. L. Alonso-Sáez, P. E. Galand, E. O. Casamayor, C. Pedrós-Alió, S. Bertilsson, High bicarbonate assimilation in the dark by Arctic bacteria. *The ISME Journal* **4**, 1581-1590 (2010).
80. S. Beier *et al.*, The transcriptional regulation of the glyoxylate cycle in SAR11 in response to iron fertilization in the Southern Ocean. *Environmental Microbiology Reports* **7**, 427-434 (2015).
81. D. L. Kirchman, H. Elifantz, A. I. Dittel, R. R. Malmstrom, M. T. Cottrell, Standing stocks and activity of Archaea and Bacteria in the western Arctic Ocean. *Limnology and Oceanography* **52**, 495-507 (2007).
82. C. Koedooder *et al.*, The role of the glyoxylate shunt in the acclimation to iron limitation in marine heterotrophic bacteria. *Frontiers in Marine Science* **5** (2018).
83. M. A. Moran, W. L. Miller, Resourceful heterotrophs make the most of light in the coastal ocean. *Nature Reviews Microbiology* **5**, 792-800 (2007).
84. J. Pinhassi, E. F. DeLong, O. Béjà, J. M. González, C. Pedrós-Alió, Marine bacterial and archaeal ion-pumping rhodopsins: genetic diversity, physiology, and ecology. *Microbiology and Molecular Biology Reviews* **80**, 929-954 (2016).
85. D. P. Smith *et al.*, Transcriptional and translational regulatory responses to iron limitation in the globally distributed marine bacterium *Candidatus* Pelagibacter ubique. *Plos One* **5**, e10487-e10487 (2010).

86. X. Jing *et al.*, Revealing CO_2-fixing SAR11 bacteria in the ocean by Raman-based single-cell metabolic profiling and genomics. *BioDesign Research* **2022**, 9782712 (2022).
87. K. Rabaey, R. A. Rozendal, Microbial electrosynthesis — revisiting the electrical route for microbial production. *Nature Reviews Microbiology* **8**, 706-716 (2010).
88. J. Philips, K. Verbeeck, K. Rabaey, J. B. A. Arends, "3 - Electron transfer mechanisms in biofilms" in Microbial Electrochemical and Fuel Cells, K. Scott, E. H. Yu, Eds. (Woodhead Publishing, Boston, 2016), https://doi.org/10.1016/B978-1-78242-375-1.00003-4, pp. 67-113.
89. N. J. Kotloski, J. A. Gralnick, D. K. Newman, Flavin electron shuttles dominate extracellular electron transfer by *Shewanella oneidensis*. *mBio* **4**, e00553-00512 (2013).
90. Y. Honda, R. Yuki, R. Hamakawa, H. Fujii, Photo-electro-biochemical H_2 production using the carbon material-based cathode combined with genetically engineered *Escherichia coli* whole-cell biocatalysis. *ChemSusChem* **17**, e202300958 (2024).
91. X. Chen, Y. Cao, F. Li, Y. Tian, H. Song, Enzyme-assisted microbial electrosynthesis of poly(3-hydroxybutyrate) via CO_2 bioreduction by engineered *Ralstonia eutropha*. *ACS Catalysis* **8**, 4429-4437 (2018).
92. H. Li *et al.*, Integrated electromicrobial conversion of CO_2 to higher alcohols. *Science* **335**, 1596 (2012).
93. C. Liu, B. C. Colón, M. Ziesack, P. A. Silver, D. G. Nocera, Water splitting–biosynthetic system with CO_2 reduction efficiencies exceeding photosynthesis. *Science* **352**, 1210-1213 (2016).
94. R. Ganigué, S. Puig, P. Batlle-Vilanova, M. D. Balaguer, J. Colprim, Microbial electrosynthesis of butyrate from carbon dioxide. *Chemical Communications* **51**, 3235-3238 (2015).
95. F. Aulenta, L. Catapano, L. Snip, M. Villano, M. Majone, Linking bacterial metabolism to graphite cathodes: electrochemical insights into the H_2-producing capability of *Desulfovibrio* sp. *ChemSusChem* **5**, 1080-1085 (2012).
96. Q. Liu *et al.*, Multiple syntrophic interactions drive biohythane production from waste sludge in microbial electrolysis cells. *Biotechnology for Biofuels* **9**, 162 (2016).
97. T. Jafary *et al.*, A comprehensive study on development of a biocathode for cleaner production of hydrogen in a microbial electrolysis cell. *Journal of Cleaner Production* **164**, 1135-1144 (2017).
98. E. Touloupakis, A. M. S. Benavides, B. Cicchi, G. Torzillo, Growth and hydrogen production of outdoor cultures of *Synechocystis* PCC 6803. *Algal Research* **18**, 78-85 (2016).
99. J. Chen *et al.*, Engineering a chemoenzymatic cascade for sustainable photobiological hydrogen production with green algae. *Energy & Environmental Science* **13**, 2064-2068 (2020).
100. D. A. Sveshnikov, N. V. Sveshnikova, K. K. Rao, D. O. Hall, Hydrogen metabolism of mutant forms of *Anabaena variabilis* in continuous cultures and under nutritional stress. *FEMS Microbiology Letters* **147**, 297-301 (1997).
101. P. Izadi, J.-M. Fontmorin, A. Godain, H. Y. Eileen, I. M. Head, Parameters influencing the development of highly conductive and efficient biofilm during microbial electrosynthesis: the importance of applied potential and inorganic carbon source. *npj Biofilms and Microbiomes* **6**, 1-15 (2020).
102. T. Lehtinen, H. Virtanen, S. Santala, V. Santala, Production of alkanes from CO_2 by engineered bacteria. *Biotechnology for Biofuels* **11**, 228 (2018).
103. H. Wu *et al.*, Efficient production of lycopene from CO_2 via microbial electrosynthesis. *Chemical Engineering Journal* **430**, 132943 (2022).
104. W. Fu *et al.*, Sugar-stimulated CO_2 sequestration by the green microalga *Chlorella vulgaris*. *Science of the Total Environment* **654**, 275-283 (2019).
105. W. Xiong *et al.*, The plasticity of cyanobacterial metabolism supports direct CO_2 conversion to ethylene. *Nature Plants* **1**, 15053 (2015).

106. P. d. C. C. d. Jesus, M. A. Mendes, E. A. Perpétuo, T. O. Basso, C. A. O. d. Nascimento, Extracellular carotenoid production and fatty acids profile of *Parachlorella kessleri* under increased CO_2 concentrations. *Journal of Biotechnology* **329**, 151-159 (2021).
107. F. E. Liew *et al.*, Carbon-negative production of acetone and isopropanol by gas fermentation at industrial pilot scale. *Nature Biotechnology* **40**, 335-344 (2022).
108. M. E. Martin, H. Richter, S. Saha, L. T. Angenent, Traits of selected *Clostridium* strains for syngas fermentation to ethanol. *Biotechnology and Bioengineering* **113**, 531-539 (2016).
109. H. Löwe, M. Beentjes, K. Pflüger-Grau, A. Kremling, Trehalose production by *Cupriavidus necator* from CO_2 and hydrogen gas. *Bioresource Technology* **319**, 124169 (2021).
110. S. N. Nangle *et al.*, Valorization of CO_2 through lithoautotrophic production of sustainable chemicals in *Cupriavidus necator*. *Metabolic Engineering* **62**, 207-220 (2020).
111. H. Cao, X. Wang, Carbon dioxide copolymers: Emerging sustainable materials for versatile applications. *SusMat* **1**, 88-104 (2021).
112. F. Liew *et al.*, Gas Fermentation—A flexible platform for commercial scale production of low-carbon-fuels and chemicals from waste and renewable feedstocks. *Frontiers in Microbiology* **7** (2016).
113. T. P. Sciarria *et al.*, Bio-electrorecycling of carbon dioxide into bioplastics. *Green Chemistry* **20**, 4058-4066 (2018).
114. T. Zheng *et al.*, Upcycling CO_2 into energy-rich long-chain compounds via electrochemical and metabolic engineering. *Nature Catalysis* **5**, 388-396 (2022).
115. H. Sheng, C. Liu, Spatial decoupling boosts CO_2 electro-biofixation. *Nature Catalysis* **5**, 357-358 (2022).
116. B. L. Adams, The next generation of synthetic biology chassis: moving synthetic biology from the laboratory to the field. *ACS Synthetic Biology* **5**, 1328-1330 (2016).
117. H. Chi *et al.*, Engineering and modification of microbial chassis for systems and synthetic biology. *Synthetic and Systems Biotechnology* **4**, 25-33 (2019).
118. E. Volodina, M. Raberg, A. Steinbüchel, Engineering the heterotrophic carbon sources utilization range of *Ralstonia eutropha* H16 for applications in biotechnology. *Critical reviews in biotechnology* **36**, 978-991 (2016).
119. B. Berla *et al.*, Synthetic biology of cyanobacteria: unique challenges and opportunities. *Frontiers in Microbiology* **4** (2013).
120. J. Bang, S. Y. Lee, Assimilation of formic acid and CO_2 by engineered *Escherichia coli* equipped with reconstructed one-carbon assimilation pathways. *Proceedings of the National Academy of Sciences* **115**, E9271 (2018).
121. O. Kruse *et al.*, Improved photobiological H_2 production in engineered green algal cells. *Journal of Biological Chemistry* **280**, 34170-34177 (2005).
122. S. Wu, R. Huang, L. Xu, G. Yan, Q. Wang, Improved hydrogen production with expression of *hemH* and *lba* genes in chloroplast of *Chlamydomonas reinhardtii*. *Journal of Biotechnology* **146**, 120-125 (2010).
123. F. Li *et al.*, Modular engineering to increase intracellular NAD($H/^+$) promotes rate of extracellular electron transfer of *Shewanella oneidensis*. *Nature Communications* **9**, 3637 (2018).
124. N. M. Tefft, M. A. TerAvest, Reversing an extracellular electron transfer pathway for electrode-driven acetoin reduction. *ACS Synthetic Biology* **8**, 1590-1600 (2019).
125. S. Luo *et al.*, Construction and modular implementation of the THETA cycle for synthetic CO_2 fixation. *Nature Catalysis* **6**, 1228-1240 (2023).
126. Y. Wang *et al.*, Biosynthesis of platform chemical 3-hydroxypropionic acid (3-HP) directly from CO_2 in cyanobacterium *Synechocystis* sp. PCC 6803. *Metabolic Engineering* **34**, 60-70 (2016).
127. Z. Li *et al.*, Engineering the Calvin–Benson–Bassham cycle and hydrogen utilization pathway of *Ralstonia eutropha* for improved autotrophic growth and

polyhydroxybutyrate production. *Microbial Cell Factories* **19**, 228 (2020).
128. C. Leang, T. Ueki, P. Nevin Kelly, R. Lovley Derek, A genetic system for *Clostridium ljungdahlii*: a chassis for autotrophic production of biocommodities and a model homoacetogen. *Applied and Environmental Microbiology* **79**, 1102-1109 (2013).
129. S. Lupacchini *et al.*, Rewiring cyanobacterial photosynthesis by the implementation of an oxygen-tolerant hydrogenase. *Metabolic Engineering* **68**, 199-209 (2021).
130. T. Elman, T. T. Hoai Ho, Y. Milrad, M. Hippler, I. Yacoby, Enhanced chloroplast-mitochondria crosstalk promotes ambient algal-H_2 production. *Cell Reports Physical Science* **3**, 100828 (2022).
131. J. M. Clomburg, A. M. Crumbley, R. Gonzalez, Industrial biomanufacturing: the future of chemical production. *Science* **355**, eaag0804 (2017).
132. P. Durre, B. J. Eikmanns, C1-carbon sources for chemical and fuel production by microbial gas fermentation. *Curr Opin Biotech* **35**, 63-72 (2015).
133. N. Antonovsky *et al.*, Sugar Synthesis from CO_2 in *Escherichia coli*. *Cell* **166**, 115-125 (2016).
134. J. Bang, C. H. Hwang, J. H. Ahn, J. A. Lee, S. Y. Lee, *Escherichia coli* is engineered to grow on CO_2 and formic acid. *Nature Microbiology* **5**, 1459-1463 (2020).
135. J. Panich, B. Fong, S. W. Singer, Metabolic engineering of *Cupriavidus necator* H16 for sustainable biofuels from CO_2. *Trends in Biotechnology* **39**, 412-424 (2021).
136. E. F. DeLong, O. Beja, The light-driven protonpump proteorhodopsin enhances bacterial survival during tough times. *Plos Biology* **8**, e1000359 (2010).
137. D. R. Ort *et al.*, Redesigning photosynthesis to sustainably meet global food and bioenergy demand. *Proceedings of the National Academy of Sciences of the United States of America* **112**, 8529-8536 (2015).
138. A. Pohlmann *et al.*, Genome sequence of the bioplastic-producing "Knallgas" bacterium *Ralstonia eutropha* H16. *Nature Biotechnology* **24**, 1257-1262 (2006).
139. J. P. Torella *et al.*, Efficient solar-to-fuels production from a hybrid microbial–water-splitting catalyst system. *Proceedings of the National Academy of Sciences* **112**, 2337-2342 (2015).
140. A. R. Moise, S. Al-Babili, E. T. Wurtzel, Mechanistic aspects of carotenoid biosynthesis. *Chemical reviews.* **114**, 164-193 (2014).
141. S. Y. Kim, S. A. Waschuk, L. S. Brown, K. H. Jung, Screening and characterization of proteorhodopsin color-tuning mutations in *Escherichia coli* with endogenous retinal synthesis. *Biochim Biophys Acta* **1777**, 504-513 (2008).
142. Y. Nakamura *et al.*, Complete genome structure of *Gloeobacter violaceus* PCC 7421, a cyanobacterium that lacks thylakoids. *DNA Res* **10**, 137-145 (2003).
143. A. R. Choi, L. C. Shi, L. S. Brown, K. H. Jung, Cyanobacterial light-driven proton pump, *Gloeobacter* rhodopsin: complementarity between rhodopsin-based energy production and photosynthesis. *Plos One* **9** (2014).
144. M. K. M. Engqvist *et al.*, Directed evolution of *Gloeobacter violaceus* rhodopsin spectral properties. *Journal of Molecular Biology* **427**, 205-220 (2015).
145. Y. S. Kim, C. S. Park, D. K. Oh, Retinal production from beta-carotene by beta-carotene 15,15'-dioxygenase from an unculturable marine bacterium. *Biotechnol Lett* **32**, 957-961 (2010).
146. T. M. Redmond *et al.*, Identification, expression, and substrate specificity of a mammalian beta-carotene 15,15'-dioxygenase. *Journal of Biological Chemistry* **276**, 6560-6565 (2001).
147. Y. Zhang *et al.*, The Carbon Source Effect on the production of *Ralstonia eutropha* H16 and proteomic response underlying targeting the bioconversion with solar fuels. *Applied Biochemistry and Biotechnology* **194**, 3212-3227 (2022).
148. Y.-A. Na *et al.*, Growth retardation of *Escherichia coli* by artificial increase of intracellular ATP. *Journal of Industrial Microbiology and Biotechnology* **42**, 915-924 (2015).
149. Y. Wang, W. E. Huang, L. Cui, M. Wagner, Single cell stable isotope probing in

microbiology using Raman microspectroscopy. *Current Opinion in Biotechnology* **41**, 34-42 (2016).
150. J. Xu, I. Webb, P. Poole, W. E. Huang, Label-free discrimination of rhizobial bacteroids and mutants by single-cell Raman microspectroscopy. *Analytical Chemistry* **89**, 6336-6340 (2017).
151. F. Adar, M. Erecinska, Spectral evidence for interactions between membrane-bound hemes: resonance Raman spectra of mitochondrial cytochrome b–c_1 complex as a function of redox potential. *FEBS Letters* **80**, 195-200 (1977).
152. M. Okada *et al.*, Label-free Raman observation of cytochrome *c* dynamics during apoptosis. *Proceedings of the National Academy of Sciences* **109**, 28-32 (2012).
153. J. Xu *et al.*, Raman deuterium isotope probing reveals microbial metabolism at the single-cell level. *Analytical Chemistry* **89**, 13305-13312 (2017).
154. M. Raberg *et al.*, Proteomic and transcriptomic elucidation of the mutant *Ralstonia eutropha* $G^{+}1$ with regard to glucose utilization. *Applied and Environmental Microbiology* **77**, 2058-2070 (2011).
155. R. Jia, D. Yang, D. Xu, T. Gu, Electron transfer mediators accelerated the microbiologically influence corrosion against carbon steel by nitrate reducing *Pseudomonas aeruginosa* biofilm. *Bioelectrochemistry* **118**, 38-46 (2017).
156. L. Huang, J. Tang, M. Chen, X. Liu, S. Zhou, Two modes of riboflavin-mediated extracellular electron transfer in *Geobacter uraniireducens*. *Frontiers in Microbiology* **9** (2018).
157. E. Marsili *et al.*, Shewanella secretes flavins that mediate extracellular electron transfer. *Proceedings of the National Academy of Sciences* **105**, 3968-3973 (2008).
158. C. K. Ng *et al.*, Genetic engineering biofilms in situ using ultrasound-mediated DNA delivery. *Microbial Biotechnology* **14**, 1580-1593 (2021).
159. J. B. Jackson, A review of the binding-change mechanism for proton-translocating transhydrogenase. *Biochimica et Biophysica Acta (BBA) - Bioenergetics* **1817**, 1839-1846 (2012).
160. K. Koutsoumanis *et al.*, Update of the list of QPS-recommended biological agents intentionally added to food or feed as notified to EFSA 11: suitability of taxonomic units notified to EFSA until September 2019. *Efsa Journal* **18** (2020).
161. J. Sillman *et al.*, Bacterial protein for food and feed generated via renewable energy and direct air capture of CO_2: Can it reduce land and water use? *Global Food Security* **22**, 25-32 (2019).
162. C. Schäfer, B. Friedrich, O. Lenz, Novel, oxygen-insensitive group 5 [NiFe]-hydrogenase in *Ralstonia eutropha*. *Applied and Environmental Microbiology* **79**, 5137-5145 (2013).
163. K. Nishio *et al.*, Extracellular electron transfer enhances polyhydroxybutyrate productivity in *Ralstonia eutropha*. *Environmental Science & Technology Letters* **1**, 40-43 (2013).
164. T. Tsukamoto *et al.*, Salt bridge in the conserved His-Asp cluster in *Gloeobacter* rhodopsin contributes to trimer formation. *Febs Letters* **587**, 322-327 (2013).
165. S. Hirschi, D. Kalbermatter, Z. Ucurum, T. Lemmin, D. Fotiadis, Cryo-EM structure and dynamics of the green-light absorbing proteorhodopsin. *Nature Communications* **12** (2021).
166. J. Mares *et al.*, The primitive thylakoid-less cyanobacterium *Gloeobacter* is a common rock-dwelling organism. *Plos One* **8** (2013).
167. Q. Chen, J. Arents, S. Ganapathy, W. J. de Grip, K. J. Hellingwerf, Functional Expression of *Gloeobacter* Rhodopsin in *Synechocystis* sp. PCC6803. *Photochemistry and Photobiology* **93**, 772-781 (2017).
168. S. Ganapathy *et al.*, Retinal-Based Proton Pumping in the Near Infrared. *Journal of the American Chemical Society* **139**, 2338-2344 (2017).
169. R. E. Blankenship *et al.*, Comparing Photosynthetic and Photovoltaic Efficiencies and Recognizing the Potential for Improvement. *Science* **332**, 805-809 (2011).

170. Y. Yang *et al.*, Enhancing bidirectional electron transfer of *Shewanella oneidensis* by a synthetic flavin pathway. *ACS Synthetic Biology* **4**, 815-823 (2015).
171. H. M. Lee, B. Y. Jeon, M. K. Oh, Microbial production of ethanol from acetate by engineered *Ralstonia eutropha*. *Biotechnol Bioproc E* **21**, 402-407 (2016).
172. R. Simon, U. Priefer, A. Puhler, A broad host range mobilization system for *in vivo* genetic engineering - transposon mutagenesis in gram-negative bacteria. *Bio-Technol* **1**, 784-791 (1983).
173. S. Green MR, J, *Molecular Cloning: A Laboratory Manual, 4th edition* (Cold Spring Harbor Laboratory Press, Cold Spring Harbor, NY, 2012).
174. R. Patzold *et al.*, In situ mapping of nitrifiers and anammox bacteria in microbial aggregates by means of confocal resonance Raman microscopy. *Journal of Microbiological Methods* **72**, 241-248 (2008).
175. A. Schwarze, M. J. Kopczak, M. Rogner, O. Lenz, Requirements for construction of a functional hybrid complex of photosystem I and [NiFe]-hydrogenase. *Applied and Environmental Microbiology* **76**, 2641-2651 (2010).
176. C. N. Hunter *et al.*, Introduction of New Carotenoids into the Bacterial Photosynthetic Apparatus by Combining the Carotenoid Biosynthetic Pathways of *Erwinia herbicola* and *Rhodobacter sphaeroides*. *Journal of Bacteriology* **176**, 3692-3697 (1994).
177. L. A. Malone *et al.*, Cryo-EM structure of the spinach cytochrome *b*6 *f* complex at 3.6 angstrom resolution. *Nature* **575**, 535 (2019).
178. T. Hasunuma *et al.*, Overexpression of 1-Deoxy-D-xylulose-5-phosphate reductoisomerase gene in chloroplast contributes to increment of isoprenoid production. *J Biosci Bioeng* **105**, 518-526 (2008).
179. J. Hans, B. Hause, D. Strack, M. H. Walter, Cloning, characterization, and immunolocalization of a mycorrhiza-inducible 1-deoxy-d-xylulose 5-phosphate reductoisomerase in arbuscule-containing cells of maize. *Plant Physiol* **134**, 614-624 (2004).
180. J. Jehlicka *et al.*, Potential and limits of Raman spectroscopy for carotenoid detection in microorganisms: implications for astrobiology. *Philosophical Transactions of the Royal Society A* **372** (2014).
181. T. Morizumi *et al.*, X-ray Crystallographic Structure and Oligomerization of *Gloeobacter* Rhodopsin. *Scientific Reports* **9** (2019).
182. M. R. M. Miranda *et al.*, The photocycle and proton tanslocation pathway in a cyanobacterial ion-pumping rhodopsin. *Biophysical Journal* **96**, 1471-1481 (2009).
183. Z. S. Kolber *et al.*, Contribution of aerobic photoheterotrophic bacteria to the carbon cycle in the ocean. *Science* **292**, 2492-2495 (2001).
184. A. Z. Worden *et al.*, Rethinking the marine carbon cycle: factoring in the multifarious lifestyles of microbes. *Science* **347**, 1257594 (2015).
185. C. B. Field, M. J. Behrenfeld, J. T. Randerson, P. Falkowski, Primary production of the biosphere: integrating terrestrial and oceanic components. *Science* **281**, 237-240 (1998).
186. W. Tu, W. E. Huang, Rhodopsin driven microbial CO_2 fixation using synthetic biology design. *Environmental Microbiology* **25**, 126-130 (2023).
187. P. A. Davison *et al.*, Engineering a rhodopsin-based photo-electrosynthetic system in bacteria for CO_2 fixation. *ACS Synthetic Biology* **11**, 3805-3816 (2022).
188. M. Sano *et al.*, Conversion of mevalonate to isoprenol using light energy in *Escherichia coli* without consuming sugars for ATP supply. *ACS Synthetic Biology* **11**, 3966-3972 (2022).
189. G. Hu *et al.*, Light-driven CO_2 sequestration in *Escherichia coli* to achieve theoretical yield of chemicals. *Nature Catalysis* **4**, 395-406 (2021).
190. M. S. Guzman *et al.*, Phototrophic extracellular electron uptake is linked to carbon dioxide fixation in the bacterium *Rhodopseudomonas palustris*. *Nature Communications* **10**, 1355 (2019).
191. M. Volpers *et al.*, Integrated *in silico* analysis of pathway designs for synthetic photo-electro-autotrophy. *Plos One* **11**, e0157851 (2016).

192. A. R. Rowe *et al.*, Tracking electron uptake from a cathode into *Shewanella* cells: implications for energy acquisition from solid-substrate electron donors. *mBio* **9**, e02203-02217 (2018).
193. D. E. Ross, J. M. Flynn, D. B. Baron, J. A. Gralnick, D. R. Bond, Towards electrosynthesis in *Shewanella*: energetics of reversing the Mtr pathway for reductive metabolism. *Plos One* **6**, e16649 (2011).
194. R. Thorbecke *et al.*, The gene dosage effect of carbonic anhydrase on the biosynthesis of poly(3-hydroxybutyrate) under autotrophic and mixotrophic culture conditions. *Polymer Journal* **53**, 209-213 (2021).
195. J. Lu, C. J. Brigham, S. Li, A. J. Sinskey, "Chapter 12 - *Ralstonia eutropha* H16 as a platform for the production of biofuels, biodegradable plastics, and fine chemicals from diverse carbon resources" in Biotechnology for Biofuel Production and Optimization, C. A. Eckert, C. T. Trinh, Eds. (Elsevier, Amsterdam, 2016), https://doi.org/10.1016/B978-0-444-63475-7.00012-1, pp. 325-351.
196. H. M. Jensen *et al.*, Engineering of a synthetic electron conduit in living cells. *Proceedings of the National Academy of Sciences* **107**, 19213-19218 (2010).
197. C. K. Ng *et al.*, Elevated intracellular cyclic-di-GMP level in *Shewanella oneidensis* increases expression of *c*-type cytochromes. *Microbial Biotechnology* **13**, 1904-1916 (2020).
198. R. Cramm, Genomic view of energy metabolism in *Ralstonia eutropha* H16. *Journal of Microbiology and Biotechnology* **16**, 38-52 (2009).
199. D. Berry *et al.*, Tracking heavy water (D_2O) incorporation for identifying and sorting active microbial cells. *Proceedings of the National Academy of Sciences* **112**, E194-E203 (2015).
200. J. Xu *et al.*, Raman Deuterium Isotope Probing Reveals Microbial Metabolism at the Single-Cell Level. *Analytical Chemistry* **89**, 13305-13312 (2017).
201. A. Okamoto *et al.*, Cell-secreted flavins bound to membrane cytochromes dictate electron transfer reactions to surfaces with diverse charge and pH. *Scientific Reports* **4**, 5628 (2014).
202. K. Chuon *et al.*, The role of carotenoids in proton-pumping rhodopsin as a primitive solar energy conversion system. *Journal of Photochemistry and Photobiology B: Biology* **221**, 112241 (2021).
203. C. S. Gai, J. Lu, C. J. Brigham, A. C. Bernardi, A. J. Sinskey, Insights into bacterial CO_2 metabolism revealed by the characterization of four carbonic anhydrases in *Ralstonia eutropha* H16. *AMB Express* **4**, 2 (2014).
204. A. R. Rowe *et al.*, Identification of a pathway for electron uptake in *Shewanella oneidensis*. *Communications Biology* **4**, 957 (2021).
205. Sophie J. Marritt *et al.*, The roles of CymA in support of the respiratory flexibility of *Shewanella oneidensis* MR-1. *Biochemical Society Transactions* **40**, 1217-1221 (2012).
206. M. Baruch, S. Tejedor-Sanz, L. Su, C. M. Ajo-Franklin, Electronic control of redox reactions inside *Escherichia coli* using a genetic module. *Plos One* **16**, e0258380 (2021).
207. H.-X. Han *et al.*, Reversing electron transfer chain for light-driven hydrogen production in biotic–abiotic hybrid systems. *Journal of the American Chemical Society* **144**, 6434-6441 (2022).
208. J. Feng *et al.*, Direct electron uptake from a cathode using the inward Mtr pathway in *Escherichia coli*. *Bioelectrochemistry* **134**, 107498 (2020).
209. M. Mouhib, M. Reggente, L. Li, N. Schuergers, A. A. Boghossian, Extracellular electron transfer pathways to enhance the electroactivity of modified *Escherichia coli*. *Joule* **7**, 2092-2106 (2023).
210. N. M. Tefft, K. Ford, M. A. TerAvest, NADH dehydrogenases drive inward electron transfer in *Shewanella oneidensis* MR-1. *Microbial Biotechnology* **16**, 560-568 (2023).
211. Q. Chen *et al.*, Combining retinal-based and chlorophyll-based (oxygenic) photosynthesis: proteorhodopsin expression increases growth rate and fitness of a ΔPSI

strain of *Synechocystis* sp. PCC6803. *Metabolic Engineering* **52**, 68-76 (2019).
212. C. Catania, A. A. Karbelkar, A. L. Furst, Engineering the interface between electroactive bacteria and electrodes. *Joule* **5**, 743-747 (2021).
213. B. Hassanzadeh *et al.*, Microbial rhodopsins are increasingly favoured over chlorophyll in High Nutrient Low Chlorophyll waters. *Environmental Microbiology Reports* **13**, 401-406 (2021).
214. A. Pushkarev *et al.*, A distinct abundant group of microbial rhodopsins discovered using functional metagenomics. *Nature* **558**, 595-599 (2018).
215. I. R. Baker, B. E. Conley, J. A. Gralnick, P. R. Girguis, Evidence for horizontal and vertical transmission of Mtr-mediated extracellular electron transfer among the bacteria. *mBio* **13**, e02904-02921 (2022).
216. X. Liu *et al.*, Syntrophic interspecies electron transfer drives carbon fixation and growth by *Rhodopseudomonas palustris* under dark, anoxic conditions. *Science Advances* **7**, eabh1852 (2021).
217. S. Kato, Microbial extracellular electron transfer and its relevance to iron corrosion. *Microbial Biotechnology* **9**, 141-148 (2016).
218. P. E. Thomas, D. Ryan, W. Levin, An improved staining procedure for the detection of the peroxidase activity of cytochrome *P*-450 on sodium dodecyl sulfate polyacrylamide gels. *Analytical Biochemistry* **75**, 168-176 (1976).
219. D. E. H. J. Gernaat *et al.*, Climate change impacts on renewable energy supply. *Nature Climate Change* **11**, 119-125 (2021).
220. M. Yue *et al.*, Hydrogen energy systems: A critical review of technologies, applications, trends and challenges. *Renewable and Sustainable Energy Reviews* **146**, 111180 (2021).
221. J. A. Turner, Sustainable Hydrogen Production. *Science* **305**, 972-974 (2004).
222. M. Wang, L. Chen, L. Sun, Recent progress in electrochemical hydrogen production with earth-abundant metal complexes as catalysts. *Energy & Environmental Science* **5**, 6763-6778 (2012).
223. I. E. Agency (2023) Global Hydrogen Review 2023.
224. R. Bashyam, P. Zelenay, A class of non-precious metal composite catalysts for fuel cells. *Nature* **443**, 63-66 (2006).
225. L. Leone *et al.*, Enzymatic and Bioinspired Systems for Hydrogen Production. *International Journal of Molecular Sciences* **24**, 8605 (2023).
226. C. Yang *et al.*, Carbon dots-fed *Shewanella oneidensis* MR-1 for bioelectricity enhancement. *Nature Communications* **11**, 1379 (2020).
227. K. C. Ford, M. A. TerAvest, The electron transport chain of *Shewanella oneidensis* MR-1 can operate bidirectionally to enable microbial electrosynthesis. *Applied and Environmental Microbiology* **0**, e01387-01323.
228. H. Chen *et al.*, A feasible strategy for microbial electrocatalytic CO_2 reduction via whole-cell-packed and exogenous-mediator-free rGO/*Shewanella* biohydrogel. *Chemical Engineering Journal* **460**, 141863 (2023).
229. C. K. Ng *et al.*, Genetic engineering biofilms in situ using ultrasound-mediated DNA delivery. *Microbial Biotechnology* **14**, 1580-1593 (2021).
230. G. Meshulam-Simon, S. Behrens, A. D. Choo, A. M. Spormann, Hydrogen metabolism in *Shewanella oneidensis* MR-1. *Applied and Environmental Microbiology* **73**, 1153-1165 (2007).
231. X. Jiang *et al.*, Nanoparticle facilitated extracellular electron transfer in microbial fuel cells. *Nano Letters* **14**, 6737-6742 (2014).
232. B. Cao *et al.*, Silver nanoparticles boost charge-extraction efficiency in *Shewanella* microbial fuel cells. *Science* **373**, 1336-1340 (2021).
233. T. Lin *et al.*, Engineered *Shewanella oneidensis*-reduced graphene oxide biohybrid with enhanced biosynthesis and transport of flavins enabled a highest bioelectricity output in microbial fuel cells. *Nano Energy* **50**, 639-648 (2018).
234. A. Okamoto, K. Hashimoto, K. H. Nealson, R. Nakamura, Rate enhancement of bacterial extracellular electron transport involves bound flavin semiquinones.

Proceedings of the National Academy of Sciences **110**, 7856-7861 (2013).
235. K. Abuyen, M. Y. El-Naggar, Soluble iron enhances extracellular electron uptake by *Shewanella oneidensis* MR-1. *ChemElectroChem* **10**, e202200965 (2023).
236. X. Wu *et al.*, A role for microbial palladium nanoparticles in extracellular electron transfer. *Angewandte Chemie International Edition* **50**, 427-430 (2011).
237. L.-J. Tian *et al.*, Directed biofabrication of nanoparticles through regulating extracellular electron transfer. *Journal of the American Chemical Society* **139**, 12149-12152 (2017).
238. B. Luo *et al.*, A Periplasmic Photosensitized biohybrid system for solar hydrogen production. *Advanced Energy Materials* **11**, 2100256 (2021).
239. Y.-S. Son *et al.*, Improved bio-hydrogen production by overexpression of glucose-6-phosphate dehydrogenase and FeFe hydrogenase in *Clostridium acetobutylicum*. *International Journal of Hydrogen Energy* **46**, 36687-36695 (2021).
240. E. H. Edwards *et al.*, *Shewanella oneidensis* MR-1 respires CdSe quantum dots for photocatalytic hydrogen evolution. *Proceedings of the National Academy of Sciences* **120**, e2206975120 (2023).
241. Z. Dang *et al.*, Regulating the synthesis rate and yield of bio-assembled FeS nanoparticles for efficient cancer therapy. *Nanoscale* **13**, 18977-18986 (2021).
242. J. Ding *et al.*, Single-Particle Analysis for Structure and Iron Chemistry of Atmospheric Particulate Matter. *Analytical Chemistry* **92**, 975-982 (2020).
243. G. Wang, F. Qian, C. W. Saltikov, Y. Jiao, Y. Li, Microbial reduction of graphene oxide by Shewanella. *Nano Research* **4**, 563-570 (2011).
244. A. C. Ferrari, J. Robertson, Interpretation of Raman spectra of disordered and amorphous carbon. *Physical Review B* **61**, 14095-14107 (2000).
245. W. Tu, J. Xu, I. P. Thompson, W. E. Huang, Engineering artificial photosynthesis based on rhodopsin for CO_2 fixation. *Nature Communications* **14**, 8012 (2023).
246. E. T. Johnson *et al.*, Enhancement of survival and electricity production in an engineered bacterium by light-driven proton pumping. *Applied and Environmental Microbiology* **76**, 4123-4129 (2010).
247. K. Chuon, J.-g. Shim, S.-G. Cho, M. Song, K.-H. Jung, Natural selection of carotenoid binding in *Gloeobacter* rhodopsin. *Algal Research* **74**, 103232 (2023).
248. T. E. Meyer *et al.*, Identification of 42 possible cytochrome *c* genes in the *Shewanella oneidensis* genome and characterization of six soluble cytochromes. *OMICS: A Journal of Integrative Biology* **8**, 57-77 (2004).
249. W. Lubitz, H. Ogata, O. Rüdiger, E. Reijerse, Hydrogenases. *Chemical Reviews* **114**, 4081-4148 (2014).
250. M. Lorenzi *et al.*, Light-driven [FeFe] hydrogenase based H_2 production in *E. coli*: A Model Reaction for Exploring E. coli Based Semiartificial Photosynthetic Systems. *ACS Sustainable Chemistry & Engineering* **10**, 10760-10767 (2022).
251. J. J. Huang, E. K. Heiniger, J. B. McKinlay, C. S. Harwood, Production of hydrogen gas from light and the inorganic electron donor thiosulfate by *Rhodopseudomonas palustris*. *Applied and Environmental Microbiology* **76**, 7717-7722 (2010).
252. H. Ooshima *et al.*, Production of hydrogen by a hydrogenase-deficient mutant of *Rhodobacter capsulatus*. *Journal of Fermentation and Bioengineering* **85**, 470-475 (1998).
253. H. P. Erickson, How teichoic acids could support a periplasm in gram-positive bacteria, and let cell division cheat turgor pressure. *Frontiers in Microbiology* **12** (2021).
254. L. L. Graham, T. J. Beveridge, N. Nanninga, Periplasmic space and the concept of the periplasm. *Trends in Biochemical Sciences* **16**, 328-329 (1991).
255. H. Nikaido, Molecular Basis of Bacterial Outer Membrane Permeability Revisited. *Microbiology and Molecular Biology Reviews* **67**, 593-656 (2003).
256. P. Lund, A. Tramonti, D. De Biase, Coping with low pH: molecular strategies in neutralophilic bacteria. *FEMS Microbiology Reviews* **38**, 1091-1125 (2014).

257. J. C. Wilks, J. L. Slonczewski, pH of the Cytoplasm and Periplasm of *Escherichia coli*: Rapid Measurement by Green Fluorescent Protein Fluorimetry. *J Bacteriol* **189**, 5601-5607 (2007).
258. G. Quek, R. J. Vázquez, S. R. McCuskey, F. Lopez-Garcia, G. C. Bazan, An n-type conjugated oligoelectrolyte mimics transmembrane electron transport proteins for Enhanced Microbial Electrosynthesis. *Angewandte Chemie International Edition* **62**, e202305189 (2023).
259. X. Deng, N. Dohmae, A. H. Kaksonen, A. Okamoto, Biogenic iron sulfide nanoparticles to enable extracellular electron uptake in sulfate-reducing bacteria. *Angewandte Chemie International Edition* **59**, 5995-5999 (2020).
260. D. Rickard, *Sulfidic sediments and sedimentary rocks* (Newnes, 2012).
261. A. Picard, A. Gartman, P. R. Girguis, What do we really know about the role of microorganisms in iron sulfide mineral formation? *Frontiers in Earth Science* **4** (2016).
262. C. Ayala-Castro, A. Saini, F. W. Outten, Fe-S cluster assembly pathways in bacteria. *Microbiology and Molecular Biology Reviews* **72**, 110-125 (2008).
263. J.-g. Shim *et al.*, Discovery of a microbial rhodopsin that is the most stable in extreme environments. *iScience* **24**, 102620 (2021).
264. F. X. Cunningham, E. Gantt, A portfolio of plasmids for identification and analysis of carotenoid pathway enzymes: *Adonis aestivalis* as a case study. *Photosynthesis Research* **92**, 245-259 (2007).
265. D. Coursolle, D. B. Baron, D. R. Bond, J. A. Gralnick, The Mtr respiratory pathway is essential for reducing flavins and electrodes in *Shewanella oneidensis*. *Journal of Bacteriology* **192**, 467-474 (2010).
266. H. Schägger, Tricine–SDS-PAGE. *Nature Protocols* **1**, 16-22 (2006).
267. R. Govindjee, S. P. Balashov, T. G. Ebrey, Quantum efficiency of the photochemical cycle of bacteriorhodopsin. *Biophys J* **58**, 597-608 (1990).
268. S. Rao *et al.*, A proteorhodopsin-based biohybrid light-powering pH sensor. *Physical Chemistry Chemical Physics* **15**, 15821-15824 (2013).
269. M. Conrad, Integrated precursor architecture as a framework for molecular computer design. *Microelectronics Journal* **24**, 263-285 (1993).